ABSTRACT

Title of dissertation:	AEROMECHANICAL BEHAVIOR OF TWIST-MORPHING, HIGH-SPEED, SLOWED RPM ROTORS
	Elizabeth Ward, Doctor of Philosophy, 2018
Dissertation directed by:	Professor Inderjit Chopra Professor Anubhav Datta Department of Aerospace Engineering

This thesis describes the first comprehensive analysis of a composite coupled edgewise rotor in high-speed forward flight. The design objective was to use composite coupling, namely extension-torsion coupling, to morph the built-in twist of a UH-60A-like rotor in slowed RPM flight. As a part of this work, this study included the first analysis of a morphing rotor using full 3-D analysis coupled with aeromechanics. The use of 3-D FEM along with an integrated trim solver and aerodynamic modeling was shown to have been key in developing a fundamental understanding of how composite coupling effects rotor performance and the aerodynamics in different flow conditions.

This research shows that extension-torsion composite coupling in the spar of a UH-60A-like rotor can provide a significant increase in the efficiency when the RPM is reduced. This was achieved through a combination of delayed stall drag along the retreating side of the rotor and reduced negative lift along the advancing side, providing an overall improvement in rotor efficiency. A comprehensive analysis was performed using a full 3-D FEA based aeroelastic computational structural dynamics (CSD) solver with the inclusion of a freewake aerodynamics model. A reduction of RPM down to 85% of the nominal hover RPM (which is well within the operational capacity of current turboshaft engines) showed an improvement in the lift-to-drag ratio,

L/D_e, over all blade loadings, C_T/σ. The maximum improvement in efficiency occurred at the peak blade loading, $C_T/\sigma \approx 0.1$. A further RPM reduction to 65NR (65% of nominal RPM), an RPM that future rotorcraft could potentially achieve with improvements in variable drive train design, showed general efficiency improvement at blade loadings below $C_T/\sigma = 0.08$, with no change in the peak efficiency when compared to an uncoupled rotor. A hygrothermally stable Winckler layup was shown to perform just as well as a nominal coupled layup at 85NR, and marginally better at 65NR, in addition to contributing to practical manufacturability of the rotor design. Close study of the strains in the rotor showed that a rotor with an extension-torsion coupled composite spar would be within the realm of practical manufacturability as the axial strains around the azimuth fell well within IM7/8552's allowable tensile strain of 6000 $\mu\varepsilon$. Tensile strain is directly related to the amount of twist change in the rotor and is reduced when the RPM is slowed and the rotor untwists towards its original cold shape.

AEROMECHANICAL BEHAVIOR OF TWIST-MORPHING, HIGH-SPEED, SLOWED RPM ROTORS

by

Elizabeth Ward

Dissertation submitted to the Faculty of the Graduate School of the
University of Maryland, College Park in partial fulfillment
of the requirements of the degree of
Doctor of Philosophy
2018

Advisory Committee:

Professor Inderjit Chopra, Co-Chair
Professor Anubhav Datta, Co-Chair
Professor James Baeder
Professor Olivier Bauchau
Professor Peter Chung, Dean's Representative

Acknowledgments

The work presented in this thesis would not be possible without the aid and support of so many people. I cannot begin to thank everyone, but I do wish to acknowledge some of those that were instrumental in me getting to this point.

I would first like to thank my advisors. Dr. Wereley, as my undergraduate advisor you remained a voice of reason when I announced my intentions of being a Gemstone member, getting a major in Aerospace Engineering, getting a minor in *both* math and music, potentially joining the swim team, and working. Although I didn't follow your advice, I did appreciate all of your wisdom and support through it all.

Next, I would like to thank my graduate advisor, Dr. Chopra. It has been such an honor to have been able to be counted amongst the amazing engineers who have called you their advisor. Thank you for being such a supportive leader throughout the years, encouraging my work in not only engineering, but in growing our community.

Next of course is Anubhav Datta. From when you were still full time at the AFDD to now as a professor at UMD, during these past four years it has been an honor to watch you grow as a mentor, but also as a friend. It is thanks to you that I was able to pursue research in something that I truly felt passionate about. Your patience and guidance helped make me the engineer I am today.

This work would not be possible without the support and sponsorship by the US Army AFDD. To Roger Strawn: thank you for your unending enthusiasm and support. I would like to thank the members of the UMD Vertical Lift Research Center of Excellence

(under grant number W911W61120012) for the generous funding and in particular, Tom Maier, who acted as the technical monitor.

I would also like to thank my friends at the University of Maryland, who made these past years not just bearable, but extremely fun. From my Gamera team I would like to thank Will Staruk, Joe Schmaus, Graham Bowen-Davies, Ben Berry, Mor Gilad, Chen Friedman, Colin Gore, Brandon Gudenius, and numerous others who accompanied me on a journey that not only took us ten feet up, but across the world. Thank you to those members of the Chopra group who sat through my presentations and were supportive and helpful when I ran into problems, including Vikram Hrishikeshevan, Elena Shrestha, Ananth Sridharan, Stacy Sidle, Brandyn Phillips, Lauren Trollinger, and Anand Saxena.

Thank you to the members of my AHS Design Team, whose hard work and dedication was an inspiration: Jaime Reel, Bharath Govindarajan, James Lamel Lankford, Nishan Jain, Ben Jimenez, Erik Levin, Zak Kaler, and Teju Jarugumilli. To the brilliant and passionate women who I worked with in forming WIAA: you are an inspiration and have pushed me to use my voice and helped me to find a confidence that I didn't know I had. And to the other members of my manufacturing building family over the years, thank you for helping to make an old beat down building a fun and vibrant place to work. This is including but of course not limited to Jillian Alfred, Erica Hocking, Kate Thorne, Robbie Vocke, Tom Pillsbury, Steve Sherman, Jon Chambers, Tyler Sinotte, and Peter Oas.

Also I would like to wish the best of luck to the next generation of students. I am excited to see where all of your potential takes you. Dan Escobar, Wanyi Ng, Fred Tsai, James Sutherland-Foggio, Emily Fisler, Chris O'Reilly, and Brent Mills: may you continue to grow and develop on the solid foundation that the students ahead of you built.

To my friends outside of the engineering world, Sarah Green, Kelly Grob, Samantha and Ben Bochinski, Adelina Buganu and Alex Gunnerson, thank you for putting up with my engineering brain, my unanswered texts, and providing me with love and patience over these last years. A special shout out also goes to my godson, Julius Bochinski – I'll make an engineer out of you yet!

Finally I would like to thank my family. From my parents, Christiana and David Weiner, who are still confused as to how I became interested in helicopters in the first place, to my in-laws, Nadine Ritter and Bill Ward, I have been so fortunate to have had the most fantastic cheer squad. Thank you to my siblings Emily, Erica, and Esther Weiner, and Geraden and Skye Ward who don't know what I do, but support me anyways. To my husband, Random: thank you for being an inspiration to me and pushing me to pursue my passions. You have been my best friend and biggest supporter for over 10 years and I could not have done this without your love and support. I am so excited to see where this next chapter in our journey takes us and I wouldn't want anyone except you by my side.

Table of Contents

List of Tables

List of Figures

List of Abbreviations

AFDD	(US Army) Aeroflightdynamics Directorate
AGRF	Alfred Gessow Rotorcraft Center
BET	Blade element theory
BEMT	Blade element momentum theory
CAD	Computer aided design
CAMRAD	Comprehensive Analytical Model of Rotor Aerodynamics and Dynamics
CATIA	
CFD	Computational fluid dynamics
CLPT	Composite Laminated Plate Theory
CMH	Composite Material Handbook
CSD	Computational structural dynamics
CSM	Computational structural mechanics
DoD	Department of Defense
DoF	Degree(s) of freedom
FEA	Finite element analysis
FEM	Finite element method
FVL	Future Vertical Lift
NASA	National Aeronautics and Space Administration
ONERA	*Office National d'Etudes et de Recherches Aerospatiale*
RCAS	Rotorcraft Comprehensive Analysis System
RPM	
SAM	Structural analysis model
SAR	Structural analysis representation
SFC	Specific fuel consumption
TRAM	Tiltrotor Aeroacoustic Model

Nomenclature

a	Speed of sound, [m/s]
c	Chord length, [m]
$\boldsymbol{c_d M^2}$	Sectional drag $\div \frac{1}{2}\rho a^2 c$
c.g.	Center of gravity
$\boldsymbol{C_H}$	Rotor drag coefficient (shaft axis)
$\boldsymbol{C_L}$	Rotor lift coefficient (wind axis)
$\boldsymbol{c_l M^2}$	Sectional lift $\div \frac{1}{2}\rho a^2 c$
$\boldsymbol{c_m M^2}$	Sectional moment $\div \frac{1}{2}\rho a^2 c^2$
$\boldsymbol{C_P}$	Power coefficient
$\boldsymbol{C_T}$	Rotor thrust coefficient (shaft axis)
$\boldsymbol{C_X}$	Rotor propulsive force coefficient (wind axis)
$\boldsymbol{E_1, E_2}$	Orthotropic ply Young's Moduli, [GPa]
$\boldsymbol{\varepsilon_{11}}$	Axial strain, [$\mu\varepsilon$]
$\boldsymbol{G_{12}}$	Orthotropic ply Shear Modulus, [GPa]
$\boldsymbol{K}$	Composite stiffness matrix

L/D_e	Lift to drag ratio, rotor efficiency
M_{ADV}	Advancing tip Mach number
R	Rotor radius, [m]
t_{ply}	Composite ply thickness, [mm]
t_{spar}	Rotor spar wall thickness, [mm]
V_∞	Forward flight speed, [m/s]
α	Shaft tilt angle, [deg], positive tilt back
β_{1c}, β_{1s}	First harmonic flapping motion, [deg]
θ	Global ply orientation, [deg]
μ	Advance ratio
ρ	Air density, [kg/m^3]
σ	Rotor solidity
ν_{12}	Orthotropic ply Poisson's Ratio
ψ	Rotor azimuthal location, [deg]

Chapter 1:Introduction

1.1 Motivation

As new rotorcraft technology is matured, there is always a consistent and important overarching goal: increased speed. Helicopters have an operational niche; with the unique ability to perform and operate in constrained environments they are a vital asset to aviation. However, when compared to other fixed-wing propeller aircraft of the same weight class, they are considered slow and relatively inefficient in forward flight (low lift-to-drag ratio). Higher speed is vital to the success of search and rescue operations, military utility missions, Medevac flights, and disaster relief applications; the faster and more efficient the vehicle, the larger the impact on saving lives. The Department of Defense's Future Vertical Lift (FVL) initiative envisions a 50-100% increase in speed from current generation helicopters, but with the constraint of maintaining the same level of hover performance (power loading and figure of merit).

Historically, helicopter rotor designs compromise efficiency in hover and forward flight in order to strike a balance between peak capabilities in both flight regimes. A rotor optimally designed for hover (with high twist) experiences negative lift at high speeds due to flow asymmetry, and high tip transonic drag and its resulting nose-down pitching moments on the advancing blade. This leads to increased power requirements (low efficiency) and large vibrations. Additionally, conventional helicopters have been limited to approximately 155-160 kts by drag divergence and compressibility effects on the

advancing side. These problems could be alleviated, however, if the rotor is able to reduce its RPM, ideally with minimal performance and loads penalties. Slowing RPM at high speed reduces the problem of drag divergence, but aggravates another – the very high advance ratio, $\mu = V_\infty/\Omega R$, leads to increased flow asymmetry and even more negative lift. The twist required for an efficient rotor at high μ is very different (much lower) from that required in hover [1]: reducing the twist of the rotor in forward flight would improve the rotor efficiency.

In the 1970s, many high-speed compound rotorcraft designs met limited success for a variety of reasons, but an important reason was the need to compromise hover performance with forward flight performance. With the exception of the XH-51A (which encountered dynamic problems), none considered RPM variation. Current production helicopters, with edgewise rotors, mostly have a fixed RPM. However, engine technology has matured to a point where a reduction of 15% RPM is possible from engine speed alone with less than a 5% loss in specific fuel consumption (SFC) [2]. This factor has been a key enabler for modern high-speed compound demonstrators such as the Sikorsky X-2 and the Eurocopter X3. The study of composite coupling in rotor blade has mostly been focused on tiltrotor applications, as tiltrotors already employed a 20% reduction in RPM between hover and cruise modes (412 RPM and 333 RPM respectively). Prior studies have shown that it is difficult to tailor tiltrotor blades to achieve a significant change in twist without an additional weight penalty and careful inertial tuning. This is because these blades have low aspect ratios and are torsionally very stiff (~8/rev).

Today, with the advent of slowed rotor technology, there is a renewed interest in compound helicopter designs. There have also been significant advances in materials and

manufacturing processes to make a case for re-examination of composite tailoring particularly in the context of slowed edgewise rotors.

1.1.1 The Edgewise Rotor vs. Tiltrotor Problem

It is important to first clarify that the edgewise rotor problem cannot be approached in the same way as the tiltrotor problem because there are several key fundamental differences.

1) The required change in twist from hover to forward flight to improve the rotor efficiency is the first difference to note. This is due to the operational flow conditions. As highlighted in Figure 1-1, edgewise rotors operate under vastly different flow conditions than tiltrotor blades in forward flight. In the case of edgewise rotors there is flow asymmetry over the rotor disk, and because of this the rotor requires less twist at high speed in order to improve efficiency. Tiltrotors operate in axial flow and like propellers require more twist in forward flight to improve aerodynamic efficiency.

Figure 1-1. A UH-60A Blackhawk (left) and a V-22 Osprey tiltrotor (right) in forward flight.

2) Due to sizing constraints, tiltrotors have relatively short and thick rotor blades and have a high torsion frequency (~8/rev). This makes them difficult to twist. On the other hand, edgewise rotor blades are softer to accommodate greater dynamic loads on the control system/swashplate due to the flow asymmetry over the rotor disk. They generally have a torsion frequency significantly lower than tiltrotor blades (~3.5-4.5/rev) so they are far easier to twist.
3) Following from the difference in flow regime is the difference in the blade dynamics. Edgewise rotor blades are generally longer and far more flexible (to absorb dynamic loads) which means the changes in blade frequencies have a much greater impact on the rotor dynamics.
4) The geometry of edgewise rotors is also beneficial to the slowed RPM problem: the increased radius (compared to the chord) provides better centrifugal loading authority and thin, slender beams allow more torsional flexibility.

Therefore, the behavior of an edgewise rotor is expected to be very different from the behavior of a tiltrotor under slowed RPM.

Although the conditions seem to indicate that edgewise rotors would vastly benefit from changing twist in forward flight, limited research has been done on self-twisting edgewise rotors. Until the work conducted as a part of this research, prior studies mostly focused on structures alone, i.e. without aeromechanics [3].

1.1.2 Passive vs. Active Twist

Changing the twist of the rotor blade in flight can be accomplished in two different ways: through an active twist approach or through a passive twist approach. Active twist requires the introduction of active materials such as piezoceramics [3] or piezofibers such as Active Fibre Composites (AFC) or Macro Fibre Composites (MFC) [4]. Rodgers et al. built a 1/6th Mach scale CH-47D blade model in the mid 1990's and tested it at Boeing Helicopters (Philadelphia, PA). A collaboration within the European Integrated Project produced a more intensive investigation in which a number of parameter optimization studies were conducted and then implemented in BO-105-like rotor blades [5, 6]. This concept was formalized into an optimization methodology as recently as 2017, by Kovalovs et al. [7]. The one major feature that differentiates active from passive twist rotors is that an active system requires a feedback control mechanism [8] which often requires complicated electronics and control algorithms. Additionally, there are weight penalties associated with the required actuation system and power drawn that negates some of the positive aspects of these designs (for more examples see [9, 10])

Passive twist, if possible, can be mechanically simple and does not require feedback mechanisms (heavy actuation/on-board power conditioning system). The change in blade shape could then be achieved through only a change in the rotor's operational environment, such as a change in the rotor RPM. This method for improving rotor efficiency is attractive as there are no moving parts. This leads to low maintenance designs and therefore a reduction in cost. For these reasons, only passive twist is considered in this research.

1.2 Prior Work

The fundamental basis of the research presented here is composite tailoring and the structural coupling this can introduce. It is therefore important to review past work on the application of composite tailoring in a rotor blade. This work also required a review of how composite properties can be simplified for fast but accurate analysis*-.

1.3 Composite Tailoring of Rotor Blades

There has been widespread use of composite materials in rotor blade design since the early 1960's. This has been in part due to their high specific strength, high stiffness, and superior fatigue life when compared to metals [11, 12, 13]. Composites also provide better corrosion resistance, improved damage tolerance, and allows for more advanced rotor blade geometries. Tailoring the layup of composite materials has been shown to have a favorable influence on the aeroelastic behavior of blades and as such requires a careful planning of ply orientation in the laminate; introducing structural coupling does not require that any additional weight be added to the system.

However, although there is a wealth of analytic research that has shown composite couplings can be beneficial to the performance and aeroelastic stability of the rotor, to date there does not seem to be any production blades that incorporate it in the structural design. What is widely adopted in current production level blades is a balanced laminate – one that negates any structural coupling terms and treats the composite material as a lightweight homogenous material.

One of the reasons for this lack of structural optimization at the production level is a lack of experimental data and a limited understanding of composite failure modes,

particularly in regards to delamination. In order to influence the future of rotor design, careful consideration of the local stresses and strains in the rotor in such a highly dynamic environment is required. This is even more important when considering the inclusion of composite couplings that may impact fatigue life.

The concept of self-twisting rotor blades is not new. Two common coupling methods are discussed here. Extension-torsion coupling is the most widely studied, specifically in the context of tiltrotors. As the name of the coupling implies, twist is induced by a change in axial force. In order to achieve blade twist, there must be axial actuation. This is best achieved through RPM variation, which is an important feature in current tiltrotor operations. The other coupling reviewed here is bending-torsion coupling.

To see an aerodynamic efficiency improvement in edgewise rotors, we require less twist, especially towards the blade tip. However with this coupling, it is difficult to achieve adequate bending moments to cause significant twist in articulated rotors. Additionally, bending-torsion coupling does not generally produce a static change to the overall rotor shape; rather, due to flap/bending variations around the rotor disk this is a dynamic coupling. Therefore bending-torsion coupling is not the ideal solution to the problem that this research aims to address, i.e., reducing the overall twist of the rotor to improve rotor aerodynamic efficiency. However, it should be noted that bending-torsion coupling does have its benefits and is addressed in Section 1.3.1.2.

1.3.1.1 Extension-Torsion Coupling

It is clear that there is not a single twist distribution that is best for a rotor in hover and also in cruise. All helicopter rotors end up with a twist that is a compromise between

the two. Because of this, there has been a plethora of research on methods to improve the performance in both modes of flight. Methods of passively changing the twist started with the characterization and understanding of composite coupling in simple beams and eventually progressed to scaled blade models.

A method of achieving this coupling is by using an antisymmetric layup. Beams with this design have a single ply orientation on the top flange and the equivalent in magnitude but opposite in direction on the bottom flange. When an axial or extensional force is applied to the beam, the opposing shear forces provide the bi-moment required to twist the beam. This is illustrated in Figure 1-2 for both a solid cross-section beam and a box beam.

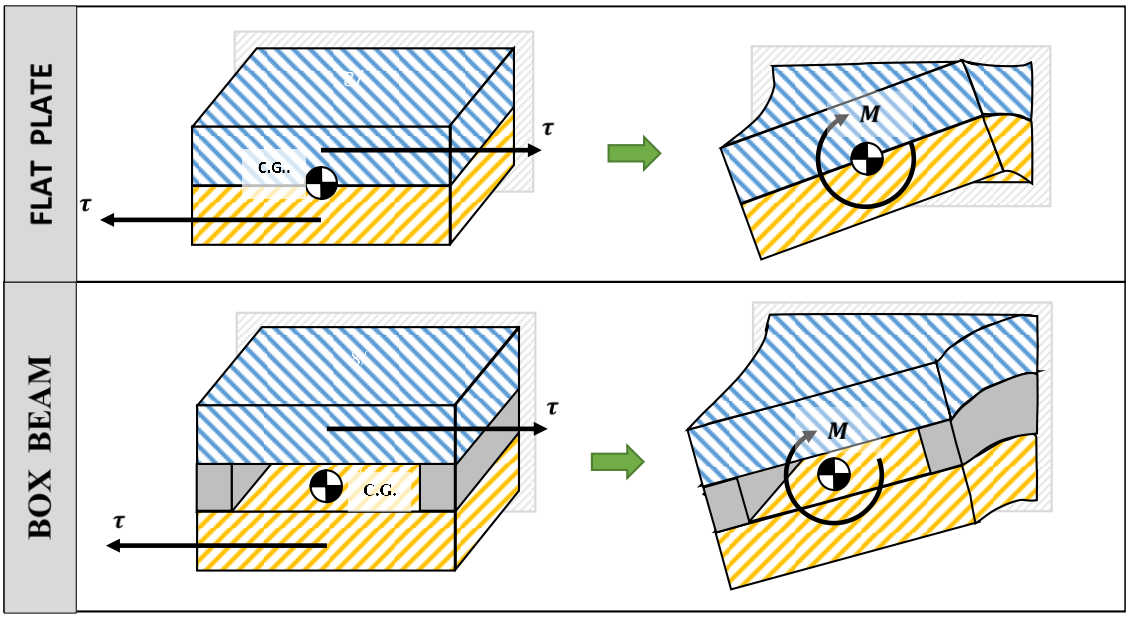

Figure 1-2. Mechanism of Extension-torsion coupling in thin plates and its equivalent

1.3.1.1.1 Extension-Torsion Coupled Beams

Historically, rotor blades have been modeled as one dimensional beams. In order to model them as such requires that the strain energy in the one dimensional beam is about

the same as in a three dimensional blade. Because the out-of-plane warping deformation of a cross section are significantly smaller than deformations in the bending, shear, and twist deflections, it has been accepted that one can separate the three dimensional blade problem into two parts: the two dimensional local deformations in the cross section, and the one dimensional global deformations of the full blade.

In 1988, Rehfield, Hodges, and Atligan [14] extended the work of Rehfield [15] on a linear composite beam theory (which was validated with rotor blade, box beam, and circular tube finite element results [16, 17, 18]). In this work they identified the significance of including non-classical effects in thin-walled composites, namely torsional warping and bending-shear coupling. At this time (1988), Bauchau and Hong also presented a non-linear elastic theory for a box beam with variable twist [19] in which they identified the same non-classical effects as being important. In classical beam theory, the assumption of that there is no deformation in the cross section is crucial, as it simplifies the three dimensional problem into one that can be modeled as a one dimensional beam. However, out of plane warping becomes a significant concern when using anisotropic materials like carbon composites and thus the inclusion of torsional warping in the analysis of extension-torsion coupled beams is important. The inclusion of bending-shear coupling is important as it significantly reduces the effective bending stiffness of a beam, which can in turn strongly influence the blade dynamics, especially lag mode stability (shown also in the later studies of Smith and Chopra [20] and Jung and Kim [21]). Bauchau and Hong also required a small strain assumption, as the requirement for strain levels within the operating environment of the material is important for the fatigue life concerns.

Hong and Chopra [22] further studied the aeroelastic stability of hingeless rotor blades. At the time of this work, there had been a few attempts to analyze composite, hingeless blades; most notable was the work of Mansfield and Sobey [23], who treated the blade as a cylindrical tube. However, the work of Hong and Chopra focused on including composite materials in the finite element formulation of Srinaveri and Chopra [24] which was a single-load-path structure that included the main rotor blade, the flexbeam, and the torque tube. Although the composite rotor model used in this study was relatively simple, is showed that there were benefits of composite tailoring on the aeroelastic stability of the full blade. Chandra, Stemple, and Chopra built simple box beams to experimentally validate the coupling relationships due to different fiber directions [25]. This work was built on in 1991 when Smith and Chopra, recognizing that there were very few cases of extension-torsion coupled experimental validation with the exception of the work done by Nixon and Hodges et al. [26, 16], provided correlation between analysis, experiment, and finite element solutions for a more varied set of ply orientations [27].

1.3.1.1.2 Extension-Torsion Coupled Tiltrotor Blades

There is extensive research on extension-torsion coupled tiltrotors, most of which has come to the same conclusion: in order to achieve an appreciable improvement in performance significant weight must be added to the system. This is due, in part, to the stiff torsional frequency of the rotor (~8/rev). The following cited works provide a brief overview of the scope and breadth of composite coupling research in rotor blades. For a more thorough review, interested readers are also encouraged to reference the book "Nonlinear Composite Beam Theory" [28].

Application of extension-torsion coupling to a rotor started with the XV-15 as early as 1986 when Bauchau et al. [29] considered two designs that analytically provided the required change in torsion to achieve passive twist change. One of the limitations of this study, however, was the requirement to match of the baseline XV-15 stiffness properties (flap, lead/lag, and torsion) and inertial properties (c.g. location and mass distribution). With such rigid design requirements, the first design was only able to achieve 0.5° of twist in response to a 15% reduction in RPM. When the bending and torsion constraints were relaxed, the second design was able to achieve a 2° change in twist over the same RPM variation. However, this analysis did not include aerodynamics.

Two designs were then developed by NASA in 1987 to determine whether the desired twist could be achieved within the material design limits. It was found that the analytical predictions were within 11% at the design limit loads [18]. Further results showed that tip weights up to 60 lbs. could practically improve the rotor performance and reduce the hover and forward flight power requirements by up to 6.1 and 6.5% respectively [30]. It should stressed that this improvement came at the expense of a significant weight increase to the rotor, and therefore is not considered a practicable solution.

In 1994 Lake et al. [31] recognized that the incorporation of advanced composite structures not being included in new production rotorcraft, namely tiltrotors, was in part due to a lack of experimental data. In response to this they developed a four bladed articulated model rotor hub with 42 in. (1.07 m), NACA0012, twisted, rectangular planform, extension-torsion coupled blades. Close agreement was found between the analytical model and the experiment: the inclusion of extension-torsion coupling, even at this scale, allowed for up to 5.6° of elastic twist. In 1996, Kosmatka and Lake [32]

considered a similar problem, however this research focused more on the effect of ply orientation on the blade natural frequency than on the characterization of the variable twist. For cantilevered beams with extension-torsion coupling, it was shown that as the strength of extension-shear coupling is increased, there is a reduction in the bending mode natural frequencies that was highly dependent on the ply orientation (31-46% decrease), and an increase in the torsion natural frequency, although to a lesser extent (5-6% increase).

In 2000, Soykasap and Hodges [33] conducted an analytical study on the effect of introducing composite coupling to a tiltrotor blade. Through a formal optimization process, it was determined that a box beam spar could produce enough extension-torsion coupling to improve performance while passing the Tsai-Wu failure criterion and avoiding any instability, including whirl flutter. Although these results were promising there was no means to validate the results due to a lack of experimental results.

In 2005 Ozbay, et al., considered the possibility of achieving extension-torsion coupling by incorporating a passive twist control in a tiltrotor blade referred to as the Sliding Mass Concept, or SMC [34]. The goal of this study was to increase the effectiveness of extension-torsion coupling without modifying the structural stability characteristics, which in tiltrotors can lead to whirl flutter. Using a nonstructural 1.0 kg/m sliding mass value, analysis showed a 4.4% improvement in hover performance. However, there was negligible improvement in the forward flight performance.

For small scale rotor designs, this coupling may not be strong enough to provide a performance improvement. In 2015, Peng et al. [35] developed 7.87 in. (200 mm) long rotors that incorporated both composite coupling and a tip mass to achieve a passive twist change. While they were able to achieve excellent twist change in hover, they only

achieved 2.4° of their predicted 30° nose-down twist due to RPM limitations in propeller mode.

1.3.1.1.3 Extension-Torsion Coupled Edgewise Rotors

Until recent developments, no edgewise rotor vehicles slowed their RPM at high speed, and so any application of extension-torsion coupling to them has been limited. When this coupling has been considered in the structural design, it has been chosen mainly to modify the rotor natural frequencies for vibration mitigation. Oh, Song, and Librescu expanded on theirs, and others', work on the free vibration problem of rotating beams [36, 37, 38, 39] while including the non-classical effects of composites. Their work culminated in good agreement between their formulation and the available theoretical and experimental predictions of eigenfrequencies. This work also identified trends in the natural frequency changes when modifying ply angle, pre-twist, and preset of the rotor.

In 2011 Mahadev and Dancila [40] considered a novel star-beam airfoil at the tip of the rotor. Although their design was shown to be effective in the lab, it is not yet feasible to implement on realistic rotors or wind turbines. Additionally, this study was purely a structural study; the effects of coupling on the aerodynamics was not considered. Without an aerodynamic and trim solution no clear conclusions can be drawn on rotor performance. In fact, without aerodynamics, the word "edgewise" or "tiltrotor" cease to have any meaning.

1.3.1.2 Bending-Torsion Coupling

Another coupling commonly considered for rotorcraft applications is bending-torsion coupling. This mechanism is usually used to pitch the blade in response to out-of-plane bending (flapping) motion. It could also be used to pitch the blade in response to in-plane (chordwise or lead/lag) bending. In order to introduce bending-torsion coupling, one method is to apply a symmetric layup. In this design the orientation of plies in both the top and bottom of a beam is the same. As shown in Figure 1-3, when a bending (flapping) force is applied, the top of the beam is put into compression and the bottom is in tension. This produces the bi-moment required to twist the rotor.

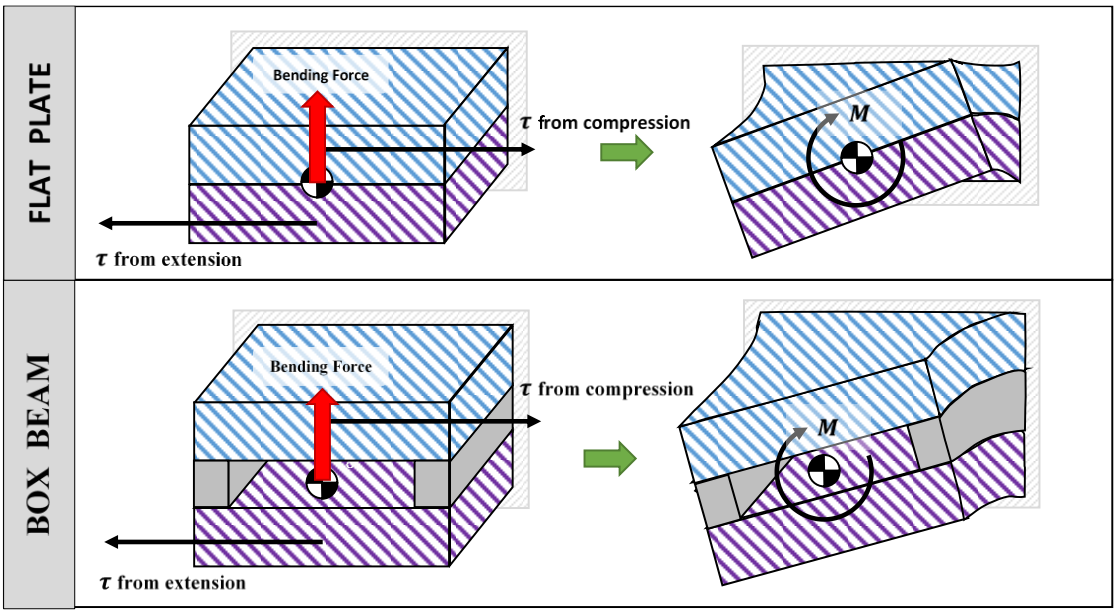

Figure 1-3. Mechanism of Bending-torsion coupling in thin plates and its equivalent representation in a box beam type structure

Although this coupling is often used in the research of wind turbines, there have been several studies using it to modify the vibration loads of rotors in a conventional helicopter orientation.

1.3.1.2.1 Bending-Torsion Coupled Wind Turbines

In operation, wind turbines experience large variations in velocity field and bending-torsion coupling could potentially be employed to reduce bending loads, increase fatigue life, and improve rotor aerodynamic efficiency. In a recent study, in 1999, Goeij, et al. [41] examined whether the mechanical properties of an anisotropic composite material could be utilized to introduce a passive control system for a wind turbine rotor blade. They considered the use of bending-torsion coupling to modify the rotor pitch as wind speeds varied. In order to produce the best torsional response, the composite material was applied as the rotor skin (rather than being incorporated into an internal blade structural element), leading to points of high stress and a likely failure point on the blade's leading edge, where the layup orientation changed abruptly. However, alternative designs in which the coupling was applied to a box beam spar yielded an acceptable response while eliminating the failure points.

Another study by Bottasso, et al. in 2012 [42] considered a composite coupled wind turbine blade through introduction of coupling in the blade skin in conjunction with coupling and thickness optimization in the spar cap. This design yielded performance improvement over the results when either method was used alone. Work by Federov and Berggreen [43], in which they applied unidirectional composite material in the spar flanges showed that purely by changing the coupling (biasing the fibers from the radial axis) one can reduce the blade stiffness by 30-35%. However, applying a single layup along the entire blade span was deemed to be unsafe by Stablein in 2016 [44], as the tower clearance of the blade tip was a restricting design criterion. Therefore it was shown that coupling

only needs to be introduced in key regions of the blade so as to improve the efficiency and avoid tower strikes.

1.3.1.2.2 Bending-Torsion Coupled Edgewise Rotors

There is extensive literature that covers bending-torsion coupling in rotorcraft. In a very recent study (2008) Bao designed and fabricated five rotors with composite couplings to reduce vibrations [45]. With no additional weight, it was found that modifications to the blade spar produced notable changes to the vibratory hub loads, namely the 4/rev vertical hub force. These tests were conducted only up to an advance ratio of $\mu = 0.3$. Characterization of how the coupling improved the aerodynamic efficiency was not documented. However, while bending-torsion coupling has been shown to have a stabilizing effect on the aeroelastic stability of the rotor, it has also been shown to have a negative impact on the ground resonance stability [46].

There were also attempts to achieve bending-torsion coupling through the use of active controls. The implementation of piezoelectric actuators on a rotor tip in conjunction with a composite layup, by Bernhard in 2000 [47], was shown to achieve 2° half peak-to-peak response and if phased correctly was shown to reduce vibrations in the main rotor. Other work (see the work of Bernhard and Chopra [48], Koratkar and Chopra [49], Straub et al. [50], and Cesnik et al. [51]) also showed promising twist response, but practical application to a rotor was difficult as most of these systems or methods resulted in bulky designs and as such were difficult to implement in real systems.

1.3.2 Composite Homogenization

When working with composite structures, the modeling problem often becomes too involved if each individual layer is modeled separately in the analysis. It is important, therefore, to consider ways to simplify the model without losing its fundamental material properties. Composite homogenization allows the designer to model large numbers of plies with a smaller FEA mesh size.

Early work on homogenization studied alternating layers of an isotropic material. The work by White and Angona [52], Postma [53], Rytov [54], Behrens [55], and Salamon [56] used, for the most part, varying wave propagation theories, in which the wave equation is derived from the stress/strain relations and the equation of motion. White and Angona and Salamon used a static approach by assuming specific stresses/strains in the medium. White and Angona used these assumptions to calculate the elastic constants in an alternately layered composite, while Salamon calculated the compliances of stratified rock masses. Rytov and Behrens studied the propagation of elastic waves in a layup using dispersion techniques, calculating phase velocity for different directions of propagation and polarization. However, Chou, Carleone, and Hsu [57] determined that these prior methods, although approached in a variety of ways with differing boundary conditions, yielded identical formulae. Their study provided a more generalized approach to determining the stiffness matrix for an equivalent homogenous material and provided a closed form solution. This approach also allowed for each layer in the lamina to be orthotropic, whereas the previously mentioned methods limited their plies to be isotropic.

The basic assumptions of this method combine the hypotheses of both Voigt (all strain components through the laminate thickness are continuous) and Reuss (all stress

components through the laminate thickness are continuous) to avoid the problems of delamination due to non-uniform stresses at the ply interface and interlaminar shear, respectively. The method adopted in the current work was that of Chou et al and is further discussed in Section 3.1.1. This method is computationally efficient and has been validated by other researchers (see Bogetti, et al. in 1995 [58] for example).

Sun and Li used an approach very similar to that of Chou et al. in 1988 [59]. This study, however, could not be used when there were high stress gradients, so Sun and Liao expanded upon this further in 1990, using a mix of global and local approaches in a laminate [60]. In areas of high stress gradients, such as free edges and at crack locations, a detailed local analysis is used. In areas where stresses are more evenly distributed, the previous method by Sun and Li was used.

In 2000, Pagano and Yuan [61] revisited their work from 1974 in which a three dimensional laminate model was created to predict the response of a laminate in response to thermal and mechanical loading. Like Chou et al., Pagano and Yuan did not limit the material type to isotropic layers, nor did the analysis require repetition or even symmetry. They found that creating representative volume elements led to the potential for severe macrostress gradients so there are limitations when homogenization is used to attempt prediction of detailed failure characteristics. However, using it for general predictions is a good first attempt to characterize patterns and identify high risk areas in the laminate.

1.3.3 Analysis of Composite Rotors

The approach to modeling composite rotors has primarily been to use 1-D beam based analysis, however such analyses may not be able to provide accurate stress/strain

distribution in the blade. They also do not consider the potential for chordwise bending. Future rotorcraft concepts are beginning to consider structures that may require detailed structural analysis. Swept and anhedral tips, radial non-uniformity in materials and geometry, discontinuities in spar shapes, chordwise (along the airfoil) flexibility, and ballistic damage cannot be modeled from first principles using 1-D beams.

1.3.3.1 Beam Analysis in Rotors

The Euler-Bernoulli beam theory has been the most frequently used method of modeling rotor blades. As far back as 1926, when Glauert formulated blade element theory (BET), rotor blades were treated as rigid beams flapping about a hinge at the root [62]. Houbolt and Brooks [63] applied the Euler-Bernoulli assumption to formulate linearized equations of motion for elastic blades experiencing small flap bending, lag bending, and torsional deformations. As rotor designs developed to include hingeless rotors, formulations were refined to include moderate to large deformations. In 1974 Hodges and Dowell established a general moderate-deflection nonlinear theory for coupled flap, lag, and torsion dynamics of rotor blades including second order nonlinear terms [64]. This was followed soon after by work to expand the analysis to include exact kinematics, multiple load paths, and higher order nonlinearities by researchers including Ormiston and Hodges [65], Kvaternik and Kirshna [66], Rosen and Friedmann [67], and Johnson [68].

The beam formulation by Timoshenko [69] differs from Euler-Bernoulli in that the assumption that a cross section remains perpendicular to the beam axis is not needed, i.e. transverse shear cannot be considered negligible. This theory provides better results for beams that are short and when the wavelengths of higher modes approach the beam

thickness. This theory is also better for composite materials where extension-shear coupling can be a key design element. For example, Chandra and Chopra [38], Smith and Chopra [27], and Jung et al. [39] all verified that in the analysis of composite beams neglect of transverse shear deformations would produce incorrect results. It was shown by Cortinez and Piovan that shear deformations and torsional warping only really effect the beam frequencies when analyzing a closed cross section [70]. There is a vast literature on composite beams, including many review papers and books (see Hodges' Nonlinear Composite Beam Theory for rotorcraft oriented treatment [28] and the historical review of aeroelasticity in rotors by Friedmann and Hodges [71]).

1.3.3.2 Shell Finite Elements in Rotors

Shell elements, an intermediate compromise, are used by researchers in the wind turbine community, such as the work by Bazilevs et al. in 2011 [72], but gyroscopic terms are not very pronounced in wind turbines. Shell elements have also been used in the work of Bauchau and Bottasso [73, 42], and explored by Kang et al. in the development of the RCAS comprehensive analysis [74]; however, finding a way to obtain shell properties (like beam properties) is a problem in and of itself.

1.3.3.3 Solid/3-D Finite Elements in Rotors

There has been very limited work on the dynamic analysis of rotors with three dimensional models because for most classical configurations, beam models were found to be adequate. 3-D models are routinely used for static stress analysis based on previous flight test measured loads and/or dynamic loads from lower order beam analyses, but have

so far not integrated with aerodynamics and trim due to their unacceptable computational run times.

The design of advanced rotors with radially changing cross sections requires us to consider full 3-D FEA modeling, similar to what is used in static analysis, but now with dynamics. For this research, X3D, a new next-generation 3-D FEA based computational structural dynamics solver for rotor aeromechanics is used. X3D includes structural dynamics, aerodynamics, and rotor trim. These are briefly discussed in the next two sections and more thoroughly in Chapter 4.

1.4 Structural Dynamics in X3D

Development of X3D (an abbreviation for Experimental 3-Dimensional dynamic analysis of rotors) began in 2008 at AFDD within the umbrella of the US Department of Defense (DoD) High Performance Computing Modernization Program (HPCMP) Computational Research and Engineering Acquisition Tools and Environments – Aviation (CREATE-AV) program. Since its original presentation in 2009 by Datta and Johnson, X3D was shown to be parallelizable [75], capable of being unified with multibody dynamics [76], and fully integrated with 3-D CFD [77] in 2014.

As a part of this work, an idealized UH-60A-like blade mesh with an articulated root flap/lag/torsion hinge and a pitch link for control was developed. It was then coupled with Helios, a next generation rotorcraft CFD simulation tool. The coupled airloads were compared to measured experimental data for a high speed test [78]. The baseline rotor model used in this thesis is based on this original UH-60A-like model. A rotor trim solution

with lower order lifting line aerodynamics (2-D table lookup with freewake) is also available.

Analysis in X3D uses 3-D finite element models, usually generated using a computer aided design (CAD) software and meshed with Cubit, a mesh preprocessing software developed by Sandia National Laboratories [79]. This is a departure from classical rotor analysis as it does not require the calculation of beam cross sectional properties such as EI and GJ. Development of a formal CAD based method for modeling, meshing, and morphing complex real rotors was conducted by Staruk, Ward (nee Weiner), and Chopra starting in 2013. This work, the subject of a number of subsequent papers cataloguing its progress [80, 81, 82, 83, 84, 85], produced a methodology, the first of its kind, for creating CAD-based 3-D models of generic rotor blades and was applied to an advanced tiltrotor specifically released by NASA. This model was then coupled with Helios to simulate conversion mode flight (the transition of the tiltrotor nacelles from their hover to cruise position) to identify numerous unique and complex loading mechanisms. The material modeling component of that work is a part of this dissertation (see Chapter 3:). In addition, the morphing piece of that work focused on a UH-60A-like rotor and forms the central investigation of this thesis. The work presented in this dissertation used X3D to understand how modifying an original UH-60A-like rotor to a composite rotor effected the performance in slowed-rotor, high-speed, forward flight regime and to understand if the blade could be seamlessly morphed into a different twisted distribution depending on RPM [86, 87, 88, 89].

1.5 Aerodynamic Modeling and Trim Solution in X3D

In addition to the structural dynamics, morphing rotors require aerodynamic modeling and trim capabilities, just like any other rotor. The aerodynamic model in X3D includes blade element momentum theory (BEMT) for hover and a free-vortex wake option in general. In forward flight the wake can be modeled using linear inflow or the Maryland Freewake free-vortex wake [90] (linear inflow uses the elementary models of Coleman, Feingold and Stempin, Drees, and the more recent White and Blake model for low speed flight [91]).

1.6 Specific Objectives of this Thesis

The objective of this thesis is to investigate the variation of built-in twist in a helicopter rotor blade during flight by changing rotor speed (or revolutions per minute, RPM) in conjunction with extension-torsion composite coupling. In the context of this research, this is defined as "self-twisting" of the rotor blade. Using composite coupling is a passive phenomenon, requiring no active actuation in the blade; the only requirement is that the blades be designed with composites/extension-torsion coupling and the rotor be capable of variable RPM.

The composite coupling in this research aims to reduce the twist of the rotor so as to reduce the drag and negative lift in high speed forward flight. This leads to an improvement in rotor efficiency, or lift-to-drag ratio (L/D_e).

The incorporation of tailored composite materials in rotors introduces inherent design concerns, such as manufacturing complexity, but it is assumed that addressing these

concerns is a natural step to changing the design methodology and advancing the state-of-the-art in structural composition for future rotor blades.

There are three overarching objectives of this research:

1. To develop an integrated modeling methodology for self-twisting rotors that includes:
    a. Computational Structural Mechanics (CSM)
    b. Aerodynamics and trim solution
    c. Integrated stress/strain analysis
2. To quantify the potential for performance improvement
3. To identify key criteria for the design and fabrication of self-twisting rotors

The specific questions that this work aims to answer are:

1. Can extension-torsion coupling be introduced into a rotor spar in order to tailor twist distribution in response to RPM variation?
2. What range of RPMs provides improved aerodynamic efficiency?
3. To what extent can the aerodynamic efficiency be improved as a result of reduced twist in slowed-rotor high-speed forward flight?
4. What are the mechanisms that contribute to an improvement in aerodynamic efficiency?
5. Do practical manufacturability concerns limit the strength of extension-torsion coupling in a rotor?
6. Are composite materials capable of withstanding the stresses/strains experienced by a rotor in high speed forward flight?

1.7 Test Data

The analyses performed in this work were validated with experimental data. Validation was carried out using a number of different data sets, as indicated in Table 1-1, the principle data set being that of the full-scale UH-60A test data acquired recently in 2011 as a part of a comprehensive and intricate test program including high μ, slowed RPM tests where the rotor was taken up to $\mu = 1.0$ and slowed to 40% of the nominal RPM (NR). This unique data set is perfectly suited to validate predictions.

Table 1-1. Test data requirements and their corresponding source

Validation	Experimental Data Test Set
Composite Box Beams	Chandra and Chopra, 1990 [25] Smith and Chopra, 1991 [27],
Material Homogenization	Chandra and Chopra, 1990 [38] TRAM
Rotor Validation, incl.: Shank drag validation Performance measurements	UH-60A test data, 2013 [78]
Hygrothermally Stable Layups	Winckler, 1985 [92] Haynes and Armanios, 2009 [93]

1.8 Contributions

There are many contributions from this work that enhance the state-of-the-art in rotor modeling and design; they fall into two major categories. The first, is the contribution of analytical predictions for future validation of self-twisting rotors. These include:

- The first comprehensive 3-D structural aeromechanical analysis of an extension-torsion coupled, slowed RPM, edgewise rotor. The fundamental rotor geometry can be changed based on the operating state – here where the twist morphs in response to a change in RPM
- This integrated analysis provides detailed performance results (L/D_e, power, trim angles), airloads ($C_l M^2$, $C_d M^2$, $C_m M^2$), and stress/strain distribution of morphing rotor blades. In the context of this research, integrated means there is no isolated piecewise integration of cross-sectional analysis, aeroelastic analysis, and stress/strain recovery with artificial constraints on each piece or iteration in the workflow. The use of X3D allowed for a single integrated analysis. It should be noted that no formal optimization was carried out (even though analysis is naturally suited for such).

Through this research, several key contributions were made in regards to the fundamental understanding of how rotor performance is effected by modifying the composite-induced twist in variable RPM, high-speed cruise conditions. This work presented the first detailed aeromechanical explanation of the performance improvement due to the reduced twist of an edgewise rotor in high speed forward flight. The following observations were also made:

1) A maximum efficiency (L/D_e) improvement of 20% over the baseline was observed with a 15% reduction in RPM.
2) At 85NR it was observed that the rotors with extension-torsion coupling (both the nominally coupled layup and with a hygrothermally stable layups) was more

efficient than an uncoupled rotor at all blade loadings (C_T/σ). This has important implications with respect to the current status of engine/drive train technology as a 15% reduction in engine speed is currently available with minimal SFC losses.

3) This study showed the first application of a hygrothermally stable spar design on the aeromechanical analysis of rotor blades. At 85NR the rotor with the Winckler layup was equally as efficient as the purely academic antisymmetric layup with the added improvement of practical manufacturability.
4) This work showed that a full aeromechanical solution is required to characterize the rotor performance. Twist change due to RPM variation alone (without the inclusion of aerodynamics), did not reveal insight into performance trends observed in the full rotor solution.
5) When the RPM was further reduced to 65NR extension-torsion coupling provided no significant improvements in maximum efficiency over the baseline case, however at low blade loadings the coupled rotors still outperformed the uncoupled baseline. The maximum improvement seen at 65NR was 15%.

1.9 Organization of the Dissertation

The work presented here focuses on the integration of composite coupling capabilities with an edgewise rotor in high-speed forward flight. Chapter 1 presented the basis for this research and a discussion of prior work in a variety of research areas: beam analysis, composite coupling, composite modeling, and the integration of these key areas.

Chapter 2 provides the methodology used to determine preliminary cross sectional properties. This process was used to form a fundamental understanding of how composite

coupling effects static deflections of a beam. The properties calculated as a part of this methodology were not extended to the full composite rotor, but rather allowed for basic generalizations and characterization of composites in multi-cell beams/rotors. Chapter 3 presents the methodology for calculating homogenized material properties. This chapter includes verification and validation of the chosen method which was key for the simplification of rotor meshes.

Chapter 4 presents the methodology for modeling the UH-60A-like rotor used as the base rotor model in this thesis. This included the establishment of an appropriate shank drag correction term required for validation of the baseline structural model against slowed-rotor experimental test data. This work included the development of several different rotor meshes, and established the baseline design criterion for the analysis of rotors with modified material properties.

Chapter 5 presents the key results of analysis of the twist-morphing rotor. Here forward flight airloads and structural blade loads are examined for a variety of rotor models. Careful comparisons are made between uncoupled and coupled rotors to determine how a change in built-in rotor twist (as a result of reduced RPM) effects the aerodynamic efficiency and what the mechanisms that contribute to this result are. The dynamic strains experienced by the morphing rotors are also taken into consideration. Chapter 6 provides concluding remarks as well as recommendation for future work.

Chapter 2: Thin-Walled 2-D Cross-Sectional Analysis

Thin-walled composite beams are often used in the fabrication of helicopter rotor blades. Therefore, as a part of this work, calculating the cross-sectional properties of such beams was necessary for a fundamental understanding of how composite materials and layup selection could impact the dynamics of the rotor. This chapter describes a simplified cross-sectional analysis that was employed for this purpose and to understand the effects of composite couplings on the dynamics of beams.

2.1 Methodology

This methodology is based on the Rehfield method [15]. This methodology also assumes St. Venant torsion: the cross section rotates as a rigid body and there is no distortion in the plane of the cross-section. Warping is not constrained and is uniform along the span of the beam [94].

2.1.1 Coordinate systems and cross-sectional displacements

Figure 2-1 shows a cross section of a thin-walled beam. In the description of the beam deformations and for deriving the strains in the beam, several sets of frames will be used. The orthogonal Cartesian frame has axes (x, y, z) are fixed in space with $y - z$ in the

plane of the undeformed section and the *x*-axis, defining the beam reference axis, perpendicular to it.

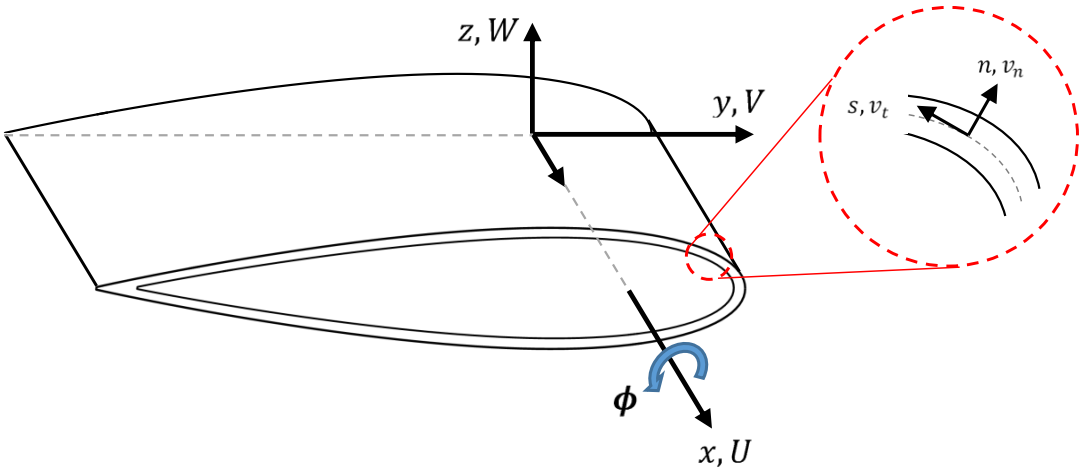

Figure 2-1. Cross sectional geometry and coordinate system

A second frame is the orthogonal curvilinear frame with axes (x, s, n) along the wall of the cross-section. The s-coordinate is along the local tangent to the midline of the walls and the n-coordinate along the tangent normal. For the purpose of cross-sectional analysis, the beam section will be treated as a curved shell structure.

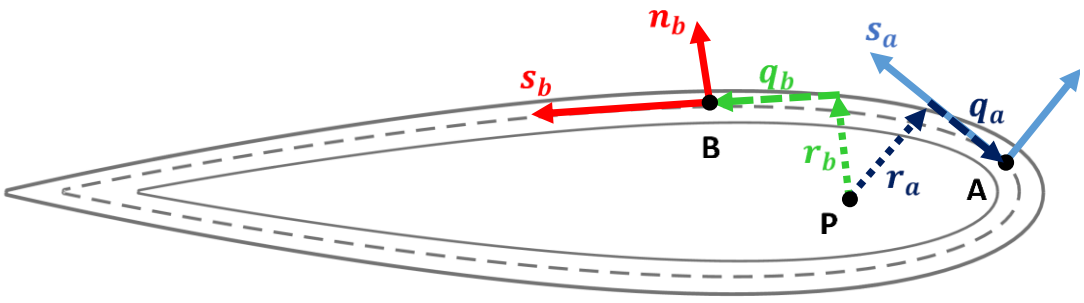

Figure 2-2. Orthogonal curvilinear coordinates. The pole, P, and the coordinates in (r, q) for point A and B are also shown.

The origin of the Cartesian coordinate system can be chosen arbitrarily, but for convenience is assumed to be at the center of rotation of the cross section. This point, P, is set to $y = z = 0$. The *r*-coordinate is the normal distance to the tangent at any given point on the mid-line of the wall from point P. The q-coordinate is the distance to the normal at the same point from P. The *r*- and *q*-coordinates for two points, *A* and B, on the mid-line of the wall are also illustrated in Figure 2-2.

Also shown in Figure 2-1 are the translations *U*, *V*, and *W* of the origin of the Cartesian frame along the *x*-, *y*-, and *z*-axes respectively. The global torsional deformation about the *x*-axis is a rotation by angle ϕ. These deformations (the three translations and rotation) result in the wall deformations (u, v_t, v_n) along the x-, s-, and n-axis respectively. The midline deformations of the wall are denoted by (u^0, v_t^0, v_n^0).

The assumptions of Euler-Bernoulli theory for bending state that cross-sections of the beam that were plane and normal to the undeformed beam axis (x-axis) remain plane and normal to the deformed beam axis and that the Poisson effects are negligible and the cross-section retains its shape after bending. The assumptions of both the St. Venant theory and Vlasov's theory also state that the cross-section does not deform and that it rotates as a rigid body. Therefore, the only strains in the wall of the beam cross section are the axial strain ε_{xx} and the shear strain γ_{xs}.

2.1.2 Relation between (y, z), (r, q), and (s, n) coordinates

Figure 2-2 shows the cross-section of a thin-walled beam and also the (y, z), (r, q), and (s, n) coordinates. The midline of the shell is chosen as the reference curve.

The differential relations between the coordinates can be derived considering a point $A(y,z)$ on the reference curve as shown in Figure 2-3. The tangent to the reference curve makes an angle θ with the y-axis and also defines the direction of the s-coordinate at A; this means that θ is a function of s. Consider an adjacent point $A'(y+dy, z+dz)$. The coordinates of A' can also be written as $A'(r+dr, q+dq)$ or $A'(s+ds, n+dn)$. As shown in Figure 2-3, the following relations can be derived for the differential quantities:

$$ds = rd\theta + dq \qquad dr = qd\theta$$

$$dy = ds\cos\theta \qquad dz = ds\sin\theta \qquad \text{2-1}$$

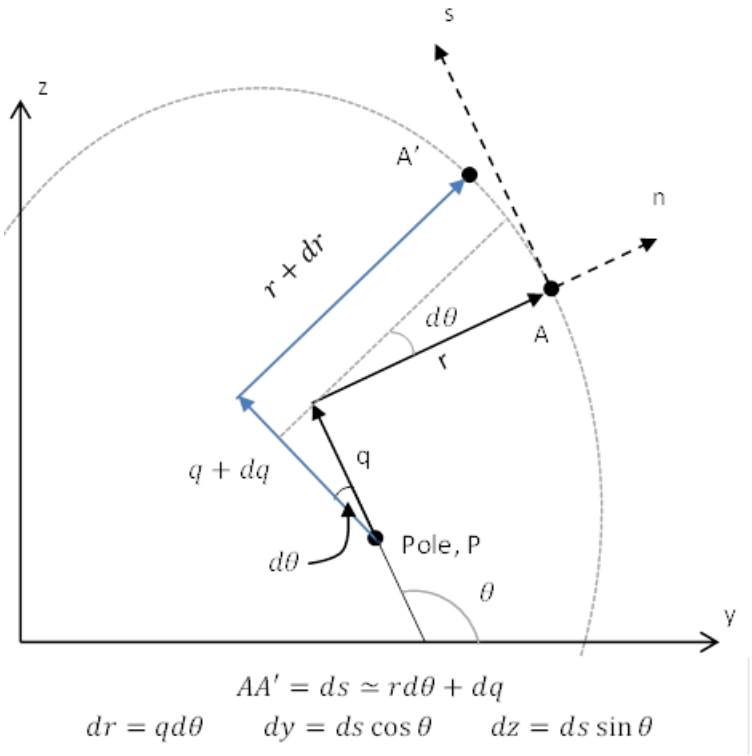

Figure 2-3. Cross section showing $A(y,z)$ after a small rotation about the pole, P

In Equation 2-1, θ is the angle between the positive *y*-axis and the positive *s*-axis. The following notation will be used:

$$(\dots)_{,s} = \frac{\partial(\dots)}{\partial s} \quad (\dots)_{,ss} = \frac{\partial^2(\dots)}{\partial s^2}$$

The following differential relations between the (y, z) coordinates and the *s* coordinate can be derived from Equation 2-1:

$$y_{,s} = \cos\theta \quad z_{,s} = \sin\theta \tag{2-2}$$

Setting $y_1 = z_1 = 0$, the relationship between the (y, z) and (r,q) coordinates are:

$$y = y_1 + r\sin\theta + q\cos\theta = rz_{,s} + qy_{,s}$$

$$z = z_1 - r\cos\theta + q\sin\theta = -ry_{,s} + qz_{,s} \tag{2-3}$$

From Equation 2-3, r and q can be related to $\boldsymbol{y}$ and $\boldsymbol{z}$ through:

$$r = yz_{,s} - zy_{,s}$$

$$q = yy_{,s} + zz_{,s} \tag{2-4}$$

Additionally, Equation 2-3 can be rearranged to show the relationship between the (x, y, z) and (x, r, q) coordinates as:

$$\begin{Bmatrix} x \\ y \\ z \end{Bmatrix} = \begin{bmatrix} 1 & 0 & 0 \\ 0 & \sin\theta & \cos\theta \\ 0 & -\cos\theta & \sin\theta \end{bmatrix} \begin{Bmatrix} x \\ r \\ q \end{Bmatrix} \tag{2-5}$$

The quantities $r_{,s}$ and $q_{,s}$ can be calculated using Equations 2-2 and 2-4:

$$r_{,s} = y_{,s}z_{,s} + yz_{,ss} - z_{,s}y_{,s} - zy_{,ss} = yz_{,ss} - zy_{,ss}$$

$$q_{,s} = y_{,s}y_{,s} + yy_{,ss} + z_{,s}z_{,s} + zz_{,ss} = 1 + yy_{,ss} + zz_{,ss} \qquad 2\text{-}6$$

2.1.3 Strain – Displacement relations for the cross-sectional wall

Figure 2-4 shows the beam displacements; U along the x-axis and $V$and W along the y- and z-axes respectively. The center of rotation is the Pole, P, and the angle of twist, ϕ, is about the x -axis.

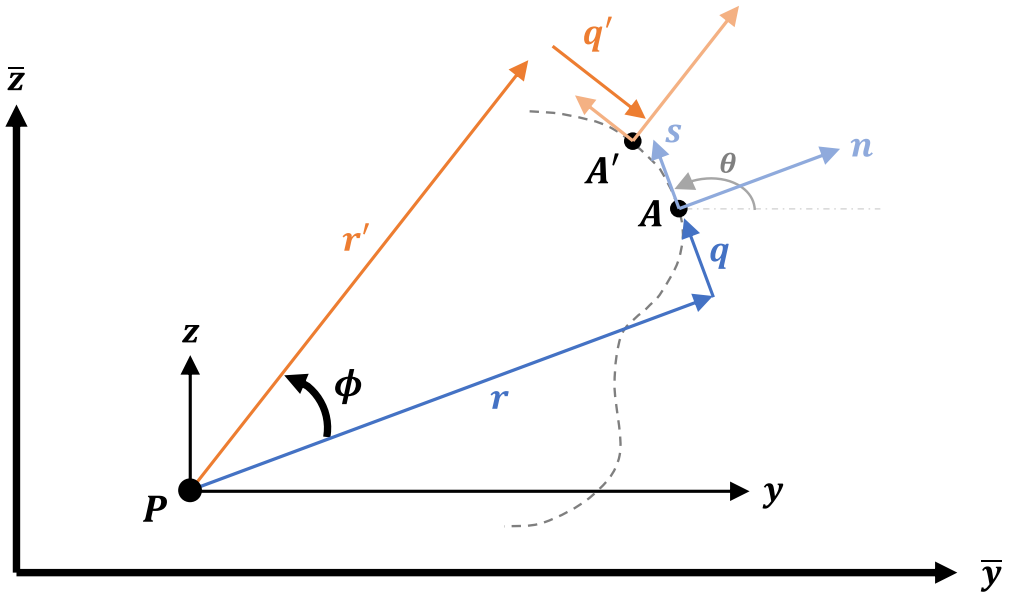

$$v_t = s = V\cos(\theta) + w\sin(\theta) + r\phi$$
$$v_n = n = V\sin(\theta) - W\cos(\theta) - q\phi$$

Figure 2-4. Kinematics of bending and rotation for global bending displacements *V* and *W*

The axial deformation of the point A is composed of the following:

- Extension due to axial force:
$$u_1(x, y, z) = U(x)$$

- Deformation due to bending about z-axis:
$$u_2(x, y, z) = -yV_{,x}(x)$$

- Deformation due to bending about y-axis:
$$u_3(x, y, z) = -zW_{,x}(x)$$

- Deformation due to torsion related warping:

$$u_4(x, y, z) = \psi(y, z)\phi_{,x}(x)$$

where, $\psi(y, z)$ is the warping function

Due to axial force, bending moments about the y- and z-axes, and torsion, the total axial deformation at a point on the midline of the shell is:

$$u^0 = U - yV_{,x} - zW_{,x} + \psi\phi_{,x} \qquad 2\text{-}7$$

The axial deformation pattern or warping function $\psi(y, z)$ is due to the application of a torsional moment. When the ends of the beam are not constrained, the cross-sections are not restrained from warping and therefore the beam is allowed to deform out of plane. This is called warping due to Free Torsion or St. Venant Torsion. If, however, one or both ends of the beam are restrained, $\phi_{,x}$ is not constant, $u_{4_{,x}} \neq 0$, which means axial stresses/strains arise which result in modifying the torsion response. This is called Restrained Torsion or Vlasov Torsion. Vlasov torsion is essential for thin cross sections that are open. It is not particularly significant for closed cross-sections.

As shown in Figure 2-4, the tangential and normal displacements of the wall at point A are given by:

$$v_t^0 = Vy_{,s} + Wz_{,s} + r\phi$$
$$v_n^0 = Vz_{,s} - Wy_{,s} - q\phi \qquad 2\text{-}8$$

Using a small strain assumption, the midline strain, ε_{xx}^0,is given by

$$\varepsilon_{xx}^0 = u_{,x}^0 = U_{,x} - yV_{,xx} - zW_{,xx} + \psi\phi_{,xx} \qquad 2\text{-}9$$

As an example, for a beam of rectangular cross-section, Figure 2-5 shows the shear strains γ_{xy} and γ_{xz}. For a beam with a curved cross-section, Figure 2-6 shows the membrane shear strain γ_{xs},always along the midline of the wall. The relationships between γ_{xs}, γ_{xy}, and γ_{xz} are:

$$\gamma_{xs} = \gamma_{xz}\cos\theta + \gamma_{xz}\sin\theta = \gamma_{xy}y_{,s} + \gamma_{xz}z_{,s}$$
$$\gamma_{xy} = \gamma_{xs}\cos\theta = \gamma_{xs}y_{,s} \qquad 2\text{-}10$$
$$\gamma_{xz} = \gamma_{xs}\sin\theta = \gamma_{xs}z_{,s}$$

The shear strain in the midline of the wall is written using the small strain assumption:

$$\gamma_{xs}^0 = u_{,s}^0 + v_{t,x}^0 \qquad 2\text{-}11$$

where $u^0_{,s} = -y_{,s}V_{,x} - z_{,s}W_{,x} + \psi_{,s}\phi_{,x}$

$$v^0_{t,x} = V_{,x}y_{,s} + W_{,x}z_{,s} + r\phi_{,x}$$

$$\gamma^0_{xs} = (\psi_{,s} + r)\phi_{,x}$$

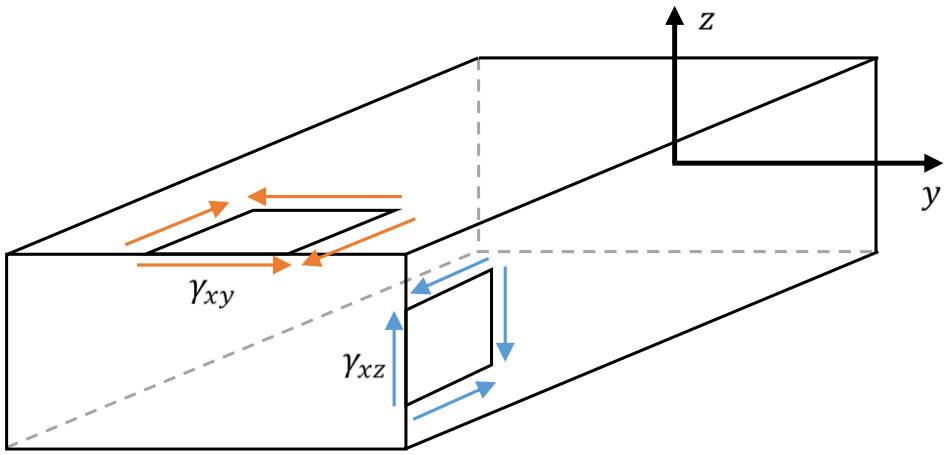

Figure 2-5. Shear strains in the wall of a rectangular beam

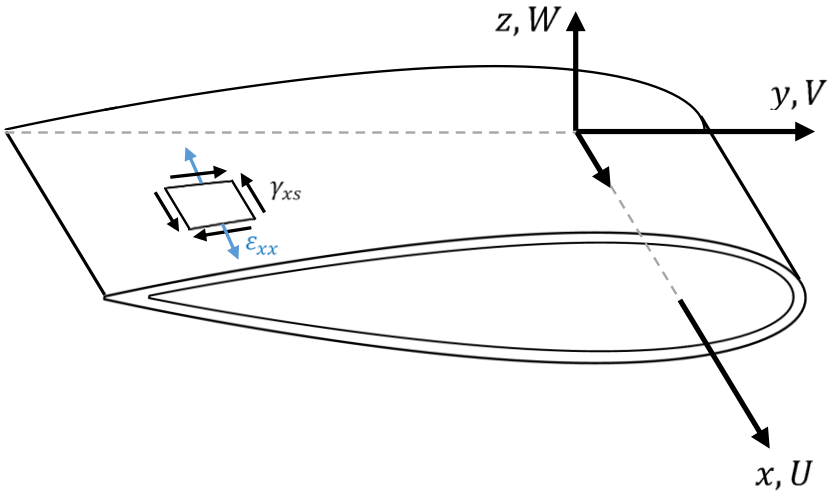

Figure 2-6. Axial strain and shear strains in the wall of a thin walled beam

This is the membrane shear strain. For thin-walled beams, the thickness or transverse shear strain, γ_{sn}, can be neglected. The strain-displacement relations for small strains and small deflections are summarized below:

$$\varepsilon_{xx}^{0} = U_{,x} - yV_{,xx} - zW_{,xx} + \psi\phi_{,xx}$$

$$\gamma_{xs}^{0} = \left(\psi_{,s} + r\right)\phi_{,x} \qquad 2\text{-}12$$

2.1.4 Torsion Related Warping

2.1.4.1 Shear Flow

The result of applying a twisting moment, M_x, to the cross section is a shear stress, τ_{xs}, in the shell wall. The shear flow, q_s, is then defined as

$$q_s = \tau_{xs} t \qquad 2\text{-}13$$

where t is the wall thickness. For thin-walled beams, the shear flow can be assumed to be constant through the thickness. The shear strain, γ_{xs}, is related to the shear stress through:

$$\tau_{xs} = G\gamma_{xs} \qquad 2\text{-}14$$

$$q_s = Gt\gamma_{xs}$$

where G is the shear modulus.

Substituting in the expression for shear strain from Equation 2-12 and using Equations 2-13 and 2-14 the relationship between shear flow and shear strain can be written as

$$q_s = (G\gamma_{xs})t = Gt\left[\left(\psi_{,s} + r\right)\phi_{,x}\right]$$

$$\psi_{,s} = \frac{q_s}{Gt\phi_{,x}} - r \qquad 2\text{-}15$$

The twisting moment can also be expressed in terms of the shear flow as

$$M_x = \oint q_s r ds \qquad 2\text{-}16$$

2.1.4.2 Torsion Related Warping Deformation

Recall from Equation 2-11 the definition for shear strain in a thin wall:

$$\gamma_{xs} = u_{,s} + v_{t,x}$$

St. Venant's theory of torsion assumes that the cross section rotates as a rigid disc about its pole. For a point a distance r from the pole, the expression for the tangential displacement of the shell wall due to torsion (from Equation 2-8) plugged into the shear strain definition yields the expression

$$\gamma_{xs} = u_{,s} + r\phi_{,x} \qquad 2\text{-}17$$

Assuming continuous axial displacement around the profile, Equation 2-17 can be rearranged to yield

$$\phi_{,x} = \frac{\oint \gamma_{xs} ds - \oint u_{,s} ds}{\oint r ds} = \frac{\oint \gamma_{xs} ds}{\oint r ds} \qquad 2\text{-}18$$

An expression for the torsion related warping function, ψ, can now be constructed using Equations 2-15 and 2-18.

$$\begin{aligned} \psi_{,s} &= \frac{q_s}{Gt\phi_{,x}} - r \\ \psi &= \int_0^s \frac{q_s}{Gt\phi_{,x}} ds - \int_0^s r ds \\ &= \int_0^s \frac{q_s}{Gt}\left[\frac{\oint r ds}{\oint \gamma_{xs} ds}\right] ds - \int_0^s r ds \end{aligned} \qquad 2\text{-}19$$

It should be noted that the calculation of cross-sectional warping is important for open cross sections and neglecting it underestimates the beam's twist distribution. However, for thin walled cross sections, the warping is considered local, and is small enough that it can be neglected. An example of calculating the warping term for a single celled cross section is shown in Section 2.4.3.1.

2.2 A Review of Classical Laminated Plate Theory

A composite ply or lamina consists of two parts: fibers and a matrix. The most common composite materials are unidirectional, where all fibers are aligned in one direction. Another common form is a fabric ply, which is made up of fibers woven together. For simplicity, this research only considers unidirectional plies. A laminate is an assembly of plies defined by how the fibers in each layer are oriented in relation to a reference axis.

The orientation of a single layer is denoted by θ_k. Therefore, a laminate made up of n plies is designated as

$$[\theta_1\backslash\theta_2\backslash\theta_3\backslash\ ...\backslash\theta_n]$$

The stresses and strains are related through a generalized Hooke's law:

$$\begin{bmatrix}\sigma_1\\ \sigma_2\\ \sigma_3\\ \tau_{23}\\ \tau_{31}\\ \tau_{12}\end{bmatrix} = \left[\begin{array}{c|c} \textit{Normal Stress as a function of Normal Strain} & \textit{Normal Stress as a function of Shear Strain} \\ \hline \textit{Shear Stress as a function of Normal Strain} & \textit{Shear Stress as a funciton of Shear Strain}\end{array}\right]\begin{bmatrix}\varepsilon_1\\ \varepsilon_2\\ \varepsilon_3\\ \gamma_{23}\\ \gamma_{31}\\ \gamma_{12}\end{bmatrix}$$

$$\begin{Bmatrix}\sigma_1\\ \sigma_2\\ \sigma_3\\ \tau_{23}\\ \tau_{31}\\ \tau_{12}\end{Bmatrix} = \begin{bmatrix} C_{11} & C_{12} & C_{13} & C_{14} & C_{15} & C_{16} \\ & C_{22} & C_{23} & C_{24} & C_{25} & C_{26} \\ & & C_{33} & C_{34} & C_{35} & C_{36} \\ & & & C_{44} & C_{45} & C_{46} \\ & SYM & & & C_{55} & C_{56} \\ & & & & & C_{66}\end{bmatrix}\begin{Bmatrix}\varepsilon_1\\ \varepsilon_2\\ \varepsilon_3\\ \gamma_{23}\\ \gamma_{31}\\ \gamma_{12}\end{Bmatrix}$$

Table 2-1. Definition of material properties required for characterization of an orthotropic composite material

Parameter	
E_1	Young's Modulus in principle/fiber direction
E_2	Young's modulus in transverse direction
G_{12}	Shear modulus in the 1-2 plane
ν_{12}	Poisson's Ratio: Load in principle direction, strain in transverse direction
$\nu_{21} = \frac{E_2\nu_{12}}{E_1}$	Poisson's Ratio: Load in transverse direction, strain in principle direction

A single ply or lamina is orthotropic (or transversely isotropic). The plies considered here are assumed as such. This means that the material has two orthogonal planes of symmetry and requires only five independent constants (Table 2-1) to populate

the C matrix. Assuming a state of plane stress in an individual ply (which is typically the case), the stress-strain relationship for a ply becomes:

$$\begin{Bmatrix}\sigma_1\\ \sigma_2\\ \tau_{12}\end{Bmatrix} = \begin{bmatrix}Q_{11} & Q_{12} & 0\\ Q_{12} & Q_{22} & 0\\ 0 & 0 & Q_{66}\end{bmatrix}\begin{Bmatrix}\varepsilon_1\\ \varepsilon_2\\ \gamma_{12}\end{Bmatrix}$$

where $$\begin{bmatrix}Q_{11} & Q_{12} & 0\\ Q_{12} & Q_{22} & 0\\ 0 & 0 & Q_{66}\end{bmatrix} = \begin{bmatrix}\frac{E_1}{1-\nu_{12}\nu_{21}} & \frac{\nu_{21}E_1}{1-\nu_{12}\nu_{21}} & 0\\ \frac{\nu_{12}E_2}{1-\nu_{12}\nu_{21}} & \frac{E_2}{1-\nu_{12}\nu_{21}} & 0\\ 0 & 0 & G_{12}\end{bmatrix}$$

Rotation of the ply properties along the fiber axis to the global frame is accomplished using the following transformation.

$$\begin{Bmatrix}\sigma_x\\ \sigma_y\\ \tau_{xy}\end{Bmatrix}_k = \begin{bmatrix}c^2 & s^2 & 2cs\\ s^2 & c^2 & -2cs\\ -cs & cs & c^2-s^2\end{bmatrix}^{-1}\begin{bmatrix}Q_{11} & Q_{12} & 0\\ Q_{12} & Q_{22} & 0\\ 0 & 0 & Q_{66}\end{bmatrix}\begin{bmatrix}c^2 & s^2 & cs\\ s^2 & c^2 & -cs\\ -2cs & 2cs & c^2-s^2\end{bmatrix}\begin{Bmatrix}\varepsilon_x\\ \varepsilon_y\\ \gamma_{xy}\end{Bmatrix}_k$$

$$= \begin{bmatrix}\bar{Q}_{11} & \bar{Q}_{12} & \bar{Q}_{16}\\ \bar{Q}_{12} & \bar{Q}_{22} & \bar{Q}_{26}\\ \bar{Q}_{16} & \bar{Q}_{26} & \bar{Q}_{66}\end{bmatrix}\begin{Bmatrix}\varepsilon_x\\ \varepsilon_y\\ \gamma_{xy}\end{Bmatrix} \qquad 2\text{-}20$$

where $c = \cos(\theta_k)$ and $s = \sin(\theta_k)$

and:

$$\bar{Q}_{11} = c^4Q_{11} + 2c^2s^2(Q_{12} + 2Q_{66}) + s^4Q_{22}$$

$$\bar{Q}_{12} = c^2s^2(Q_{11} + Q_{22} - 4Q_{66}) + (c^4 + s^4)Q_{12}$$

$$\bar{Q}_{22} = s^4 Q_{11} + 2c^2 s^2 (Q_{12} + Q_{66}) + s^4 Q_{11}$$

$$\bar{Q}_{16} = c^3 s (Q_{11} - Q_{12} - 2Q_{66}) + cs^3 (Q_{12} - Q_{22} + 2Q_{66})$$

$$\bar{Q}_{26} = cs^3 (Q_{11} - Q_{12} - 2Q_{66}) + c^3 s (Q_{12} - Q_{22} + 2Q_{66})$$

$$\bar{Q}_{66} = c^2 s^2 (Q_{11} + Q_{22} - 2Q_{12} - 2Q_{66}) + (c^4 + s^4) Q_{66}$$

Using these relations, the generalized Hooke's law for the entire laminate can be written as:

$$\begin{Bmatrix} \sigma_1 \\ \sigma_2 \\ \sigma_3 \\ \tau_{23} \\ \tau_{31} \\ \tau_{12} \end{Bmatrix} = \begin{bmatrix} [A] & [B] \\ [B] & [D] \end{bmatrix} \begin{Bmatrix} \varepsilon_1 \\ \varepsilon_2 \\ \varepsilon_3 \\ \gamma_{23} \\ \gamma_{31} \\ \gamma_{12} \end{Bmatrix}$$

$$\text{where} \quad A_{ij} = \sum_{k=1}^{n} \{Q_{ij}\}_n (z_k - z_{k-1})$$

$$B_{ij} = \frac{1}{2} \sum_{k=1}^{n} \{Q_{ij}\}_n (z_k^2 - z_{k-1}^2)$$

$$D_{ij} = \frac{1}{3} \sum_{k=1}^{n} \{Q_{ij}\}_n (z_k^3 - z_{k-1}^3)$$

2.3 Derivation of Cross-section Stiffness Matrix

The global beam deformations (U, V, W, and ϕ) result in the local deformations of the shell wall (u^0, v_t^0, v_n^0). These, in turn, lead to strains and stresses in the shell wall that

resist the applied loads. The resultants of these wall stresses should be equal to the applied loads and moments acting on the cross-section.

2.3.1 Material Law

Figure 2-7 shows an element of the shell wall and the stress resultants acting on that element. The assumption of thin walls implies that the shell wall acts as a membrane and that the contributions of the bending stiffness (as in Kirchoff theory) and the transverse shear stiffness (as in Mindlin theory) to the cross-section stiffness of the thin-walled beam are negligible. Therefore, only the axial stress resultant (σ_{xx}) and the shear stress resultant (τ_{xs}) need to be considered in the analysis.

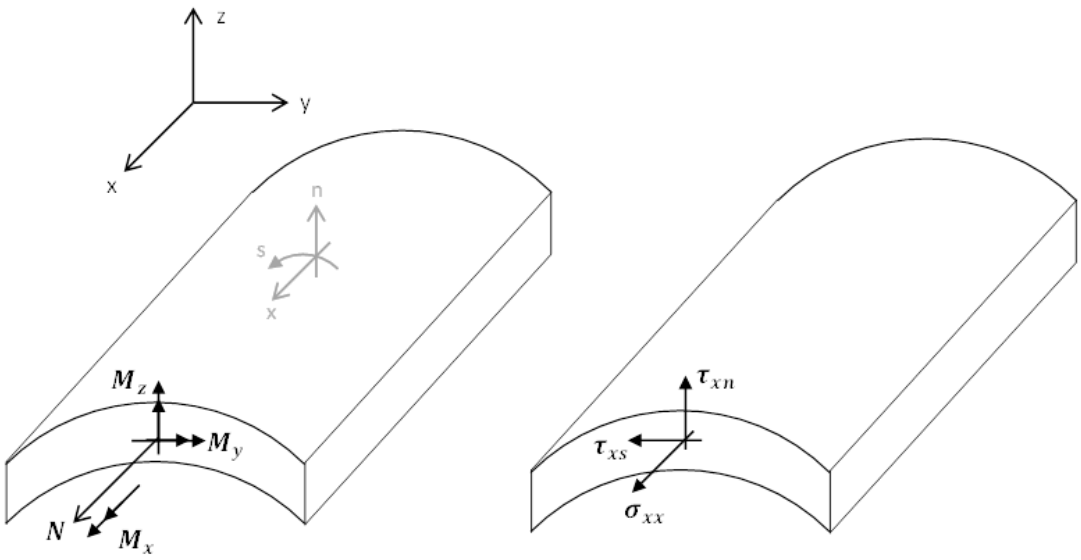

Figure 2-7. Laminate stress resultants acting on an element of the wall

Recall from before the simplified Hooke's law for an orthotropic material from Equation 2-20. Integrating through the wall thickness yields:

$$\oint \begin{Bmatrix} \sigma_{xx} \\ \sigma_{xs} \\ \tau_{xs} \end{Bmatrix} dn = \begin{Bmatrix} N_{xx} \\ N_{ss} \\ N_{xs} \end{Bmatrix} = \begin{bmatrix} \bar{A}_{11} & \bar{A}_{12} & \bar{A}_{16} \\ \bar{A}_{12} & \bar{A}_{22} & \bar{A}_{26} \\ \bar{A}_{16} & \bar{A}_{26} & \bar{A}_{66} \end{bmatrix} \begin{Bmatrix} \varepsilon_{xx} \\ \varepsilon_{ss} \\ \gamma_{xs} \end{Bmatrix}$$

Expanded out we get the following three equations:

$$N_{xx} = \bar{A}_{11}\varepsilon_{xx} + \bar{A}_{12}\varepsilon_{ss} + \bar{A}_{16}\gamma_{xs}$$

$$N_{ss} = \bar{A}_{12}\varepsilon_{xx} + \bar{A}_{22}\varepsilon_{ss} + \bar{A}_{26}\gamma_{xs}$$

$$N_{xs} = \bar{A}_{16}\varepsilon_{xx} + \bar{A}_{26}\varepsilon_{ss} + \bar{A}_{66}\gamma_{xs}$$

The zero hoop stress assumption tells us that $N_{ss} = 0$ such that

$$0 = \bar{A}_{12}\varepsilon_{xx} + \bar{A}_{22}\varepsilon_{ss} + \bar{A}_{26}\gamma_{xs}$$

$$\varepsilon_{ss} = -\frac{\bar{A}_{12}}{\bar{A}_{22}}\varepsilon_{xx} - \frac{\bar{A}_{26}}{\bar{A}_{22}}\gamma_{xs}$$

This equation can now be inserted back into the expressions for N_{xx} and N_{xs} to yield

$$\begin{Bmatrix} N_{xx} \\ N_{xs} \end{Bmatrix} = \begin{bmatrix} \left(\bar{A}_{11} - \frac{\bar{A}_{12}^2}{\bar{A}_{22}}\right) & \left(\bar{A}_{16} - \frac{\bar{A}_{12}\bar{A}_{26}}{\bar{A}_{22}}\right) \\ \left(\bar{A}_{16} - \frac{\bar{A}_{12}\bar{A}_{26}}{\bar{A}_{22}}\right) & \left(\bar{A}_{66} - \frac{\bar{A}_{26}^2}{\bar{A}_{22}}\right) \end{bmatrix} \begin{Bmatrix} \varepsilon_{xx} \\ \gamma_{xs} \end{Bmatrix} \qquad 2\text{-}21$$

where we can use the notation:

$$\begin{bmatrix} A_{11} & A_{16} \\ A_{16} & A_{66} \end{bmatrix} = \begin{bmatrix} \left(\bar{A}_{11} - \frac{\bar{A}_{12}^2}{\bar{A}_{22}}\right) & \left(\bar{A}_{16} - \frac{\bar{A}_{12}\bar{A}_{26}}{\bar{A}_{22}}\right) \\ \left(\bar{A}_{16} - \frac{\bar{A}_{12}\bar{A}_{26}}{\bar{A}_{22}}\right) & \left(\bar{A}_{66} - \frac{\bar{A}_{26}^2}{\bar{A}_{22}}\right) \end{bmatrix}$$

The cross-section stress resultants are:

$$N = \int_s \int_n \sigma_{xx} dn\, ds \qquad \text{Axial force}$$

$$M_z = -\int_s \int_n \sigma_{xx} y\, dn\, ds \qquad \text{Bending moment (lag) about the z-axis}$$

$$M_y = -\int_s \int_n \sigma_{xx} z\, dn\, ds \qquad \text{Bending moment (flap) about the y-axis} \qquad 2\text{-}22$$

$$M_x = \int_s \int_n \tau_{xs}(\psi_{,s} + r) dn ds \qquad \text{Torsion about the x-axis}$$

These are the resultant forces and moments arising out of the stresses in the shell wall and are in equilibrium with the applied static loads on the cross-section.

The cross-section stress resultants shown in Equation 2-22 are expanded using the material law from Equation 2-20 and the strain-displacement relations from Equation 2-12.

$$\begin{aligned} N &= \int_s \int_n \sigma_{xx} dn\, ds \\ &= \int_s A_{11} U_{,x} - y A_{11} V_{,xx} - z A_{11} W_{,xx} + A_{16}(\psi_{,s} + r)\phi_{,x} + \psi A_{11} \phi_{,xx} \end{aligned} \qquad 2\text{-}23$$

In Equations 2-23 and 2-24 the global strains have been rearranged as axial strain, bending about the z-axis, bending about the y-axis, the rate of twist, and the restrained warping $(U_{,x}, V_{,xx}, W_{,xx}, \phi_{,x}, \phi_{,xx})$. The other cross-section stress resultants can be evaluated in a way similar to Equation 2-23.

$$M_y = -\int_s \int_n \sigma_{xx} z \, dn \, ds$$

$$= \int_s -zA_{11}U_{,x} + yzA_{11}V_{,xx} + z^2A_{11}W_{,xx} - zA_{16}(\psi_{,s} + r)\phi_{,x} - z\psi A_{11}\phi_{,xx}$$

$$M_z = -\int_s \int_n \sigma_{xx} y dn \, ds$$

$$= \int_s -yA_{11}U_{,x} + y^2A_{11}V_{,xx} + yzA_{11}W_{,xx} - yA_{16}(\psi_{,s} + r)\phi_{,x} - y\psi A_{11}\phi_{,xx} \qquad 2\text{-}24$$

$$M_x = \int_s \int_n \tau_{xs}(\psi_{,s} + r) dn \, ds$$

$$= \int_s \Big((\psi_{,s} + r)A_{16}U_{,x} - y(\psi_{,s} + r)A_{16}V_{,xx} - z(\psi_{,s} + r)A_{16}W_{,xx} + (\psi_{,s} + r)^2 A_{66}\phi_{,x} + \psi(\psi_{,s} + r)A_{16}\phi_{,xx} \Big) ds$$

Equations 2-23 and 2-24 can be arranged in matrix form as:

$$\begin{Bmatrix} N \\ M_y \\ M_z \\ M_x \end{Bmatrix} = [K] \begin{Bmatrix} U_{,x} \\ W_{,xx} \\ V_{,xx} \\ \phi_{,x} \end{Bmatrix} \qquad 2\text{-}25$$

where $[K]$ is a 4x4 symmetric cross-section stiffness matrix.

The beam strain measures are:

$U_{,x}$	Axial strain
$W_{,xx}$	Bending curvature about y-axis (beamwise bending)
$V_{,xx}$	Bending curvature about the z-axis (edgewise bending)
$\phi_{,x}$	Rate of twist (St. Venant torsion measure)
$\phi_{,xx}$	Change of rate of twist with x (Vlasov torsion measure)

The elements of the (symmetric) stiffness matrix are identified as:

$K(1,1) = \oint A_{11} ds$	Axial stiffness	
$K(1,2) = K(2,1) = \oint -zA_{11}\, ds$	Extension-bending coupling	
$K(1,3) = K(3,1) = \oint -yA_{11} ds$	Extension-bending coupling	
$K(1,4) = K(4,1) = \oint A_{16}(\psi_{,s} + r) ds$	Extension-torsion coupling	2-26
$K(2,2) = \oint -z^2 A_{11}\, ds$	Bending stiffness	
$K(2,3) = K(3,2) = \oint -yzA_{11}\, ds$	Bending-bending coupling	
$K(2,4) = K(4,2) = \oint -zA_{16}(\psi_{,s} + r) ds$	Bending-torsion coupling	

$$K(3,3) = \oint -y^2 A_{11}\, ds \qquad \text{Bending stiffness}$$

$$K(3,4) = K(4,3) = \oint -y A_{16}(\psi_{,s} + r) ds \qquad \text{Bending-torsion stiffness}$$

$$K(4,4) = \oint (\psi_{,s} + r)^2 A_{66} ds \qquad \text{Torsion stiffness}$$

2.4 Example: Chandra-Chopra Box Beam

In order to validate this methodology, it was applied first to a thin-walled, composite box beam, modeled after the experiments of Chandra and Chopra in 1992 [38]. This example has been widely studied including analysis performed by Popescu and Hodges [95], Bauchau and Hodges [96], and Smith [27].

Table 2-2. Material properties of composite material used in Chandra-Chopra box beam experiments

	IM7/8552
$\boldsymbol{E_1, GPa\ (psi)}$	142 (20.59e6)
$\boldsymbol{E_2, GPa\ (psi)}$	9.79 (1.42e6)
$\boldsymbol{G_{12}, GPa\ (psi)}$	6.14 (0.89e6)
$\boldsymbol{\nu_{12}}$	0.42
$\boldsymbol{t_{ply}, mm\ (in.)}$	0.183 (0.005)

2.4.1 Definition of Chandra-Chopra Box Beam

The Chandra-Chopra box beam, illustrated in Figure 2-8 has an exterior width of 0.953 inches and an exterior height of 0.537 inches. The walls are made up of 6 layers of anisotropic carbon fiber composite, the material properties of which are listed in Table 2-2.

The example considered in this work is an uncoupled box beam, in which the layers of composite material are all arranged at 0°.

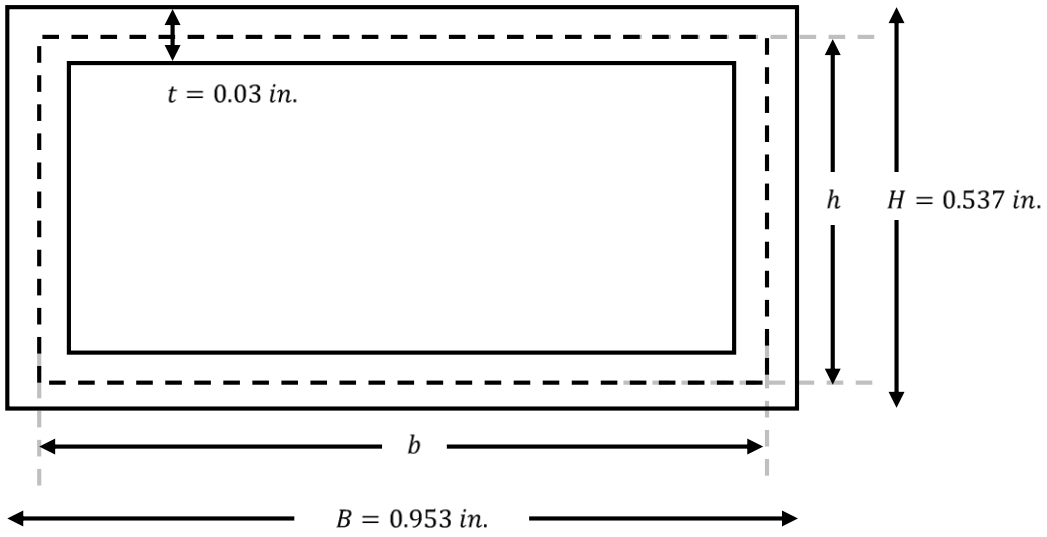

Figure 2-8. Dimensions of Chandra-Chopra box beam cross section

2.4.2 Cross Section Idealization

For this analysis, calculation of the cross-sectional stiffness coefficients was done through integration along the midline of the four walls. This is illustrated in Figure 2-9 as a rectangle with the updated dimensions of 0.923 in. in width and 0.507 in. in height.

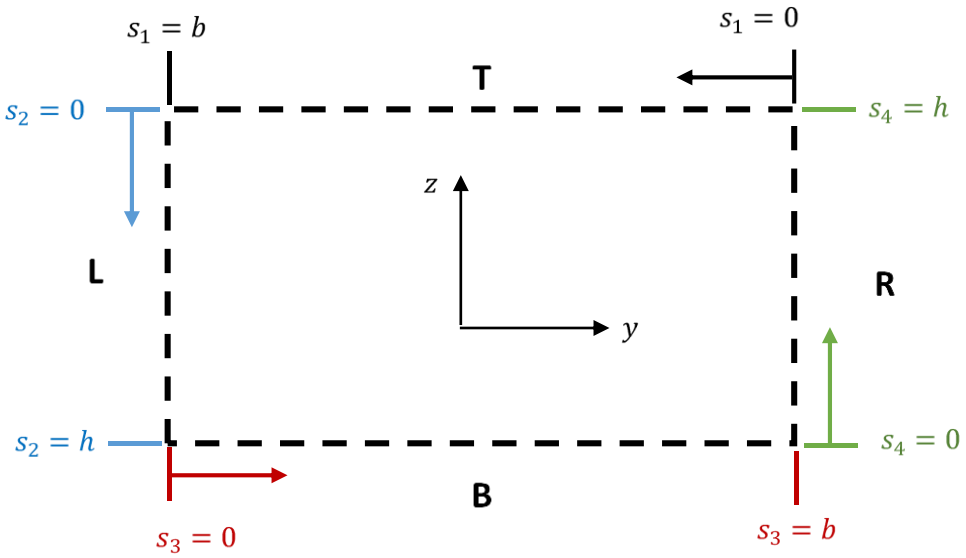

$b = 0.923\ in.$ $h = 0.507\ in.$

Figure 2-9. Idealization of box beam cross-section, where integrated area is within the beam wall centerlines. The four walls are designated as T, R, B, and L for top flange, right web, bottom flange, and left web.

Table 2-3. Calculated values of $\bar{A}$ for a layups defined by $[0°]_6$

	Value
$\bar{A}_{11}$	625307.19
$\bar{A}_{12}$	18112.35
$\bar{A}_{16}$	0
$\bar{A}_{22}$	43124.63
$\bar{A}_{26}$	0
$\bar{A}_{66}$	26700
$A_{11} = \bar{A}_{11} - \frac{\bar{A}_{12}^2}{\bar{A}_{22}}$	617700
$A_{16} = \bar{A}_{16} - \frac{\bar{A}_{12}\bar{A}_{26}}{\bar{A}_{22}}$	0
$A_{66} = \bar{A}_{66} - \frac{\bar{A}_{26}^2}{\bar{A}_{22}}$	26700

2.4.3 Uncoupled – All walls $[0°]_6$

As previously stated, in this example all six layers of composite material are oriented at 0° from the beam axis. Values of $\bar{A}_{ij} = \sum \bar{Q}_{ij}$ for $[0°]_6$ are shown in Table 2-3. These are the same for all four sides of the box.

2.4.3.1 Cross-section Stiffness coefficients

The cross-sectional stiffness values are calculated based on the values in Table 2-3.

$$K(1,1) = \oint A_{11} ds = \int_0^b A_{11}^T ds + \int_0^b A_{11}^L ds + \int_0^b A_{11}^B ds + \int_0^b A_{11}^R ds$$

$$= b(A_{11}^T + A_{11}^B) + h(A_{11}^R + A_{11}^L)$$

$$= 0.923(2)(617700) + 0.507(2)(617700)$$

$$= 1766622$$

$$K(1,2) = K(2,1) = -\oint A_{11} z ds$$

$$= -\int_0^b \left(\frac{h}{2}\right) A_{11}^T \, ds - \int_0^h A_{11}^L \left(\frac{h}{2} - s\right) ds - \int_0^b \left(-\frac{h}{2}\right) A_{11}^B ds - \int_0^h A_{11}^R \left(-\frac{h}{2} + s\right) ds$$

$$= -b\left(\frac{h}{2}\right)(A_{11}^T - A_{11}^B) = 0$$

Note: Because A_{11} is the same for all sides of the beam, $\oint z ds = 0$

$$K(1,3) = K(3,1) = -\oint A_{11} y \, ds$$

$$= -\int_0^b \left(\frac{b}{2} - s\right) A_{11}^T \, ds - \int_0^h A_{11}^L \left(-\frac{b}{2}\right) ds - \int_0^b \left(-\frac{b}{2} + s\right) A_{11}^B ds$$
$$- \int_0^h A_{11}^R \left(-\frac{h}{2}\right) ds$$

$$= -b\left(\frac{h}{2}\right)(-A_{11}^L + A_{11}^R) = 0$$

Note: Because $A_{11}$is the same for all sides in this problem, $\oint y ds = 0$

$$K(1,4) \quad = \oint A_{16}(\psi_{,s} + r) ds = \oint A_{16}\psi_{,s} ds + \oint A_{16} r ds$$

$$= b(A_{16}^T + A_{16}^B) + h(A_{16}^L + A_{16}^R) = 0 \quad \textbf{NO extension-torsion coupling}$$

$$K(2,2) \quad = \oint A_{11} z^2 ds$$

$$= \int_0^b \left(\frac{h}{2}\right)^2 A_{11}^T ds + \int_0^h A_{11}^L \left(\frac{h}{2} - s\right)^2 ds + \int_0^b \left(-\frac{h}{2}\right)^2 A_{11}^B ds$$
$$+ \int_0^h A_{11}^R \left(-\frac{h}{2} + s\right)^2 ds$$

$$= b\left(\frac{h^2}{4}\right)(A_{11}^T + A_{11}^B) + \frac{h^3}{12}(A_{11}^L + A_{11}^R) = 86693.4$$

$$K(2,3) = \oint A_{11} yz \, ds$$

$$= \int_0^b \left(\frac{b}{2} - s\right)\left(\frac{h}{2}\right) A_{11}^T ds + \int_0^h A_{11}^L \left(-\frac{b}{2}\right)\left(\frac{h}{2} - s\right) ds$$

$$+ \int_0^b \left(-\frac{b}{2} + s\right)\left(-\frac{h}{2}\right) A_{11}^B ds + \int_0^h A_{11}^R \left(\frac{b}{2}\right)\left(-\frac{h}{2} + s\right) ds$$

$$= A_{11}^T \left[\left(\frac{h}{2}\right)(0)\right] + A_{11}^L \left[\left(-\frac{b}{2}\right)(0)\right] + A_{11}^B \left[\left(-\frac{h}{2}\right)(0)\right] + A_{11}^R \left[\left(\frac{b}{2}\right)(0)\right]$$

$$= 0$$

$$\oint A_{16} z ds = \int_0^b A_{16}^T \left(\frac{h}{2}\right) ds + \int_0^h A_{16}^L \left(\frac{h}{2} - s\right) ds + \int_0^b A_{16}^B \left(-\frac{h}{2}\right) ds$$

$$+ \int_0^h A_{16}^R \left(-\frac{h}{2} + s\right) ds$$

$$= \frac{hb}{2}(A_{16}^T - A_{16}^B) = 0$$

$$K(2,4) = \oint -z A_{16}(\psi_{,s} + r) ds = \oint -z A_{16} \psi_{,s} ds - 2A_e \oint z A_{16} ds = 0$$

where A_e is the area contained within the midline of the cross section's wall

$$K(3,3) = \oint A_{11} y^2 \, ds$$

$$= \int_0^b \left(\frac{b}{2} - s\right)^2 A_{11}^T ds + \int_0^h \left(-\frac{b}{2}\right)^2 A_{11}^L ds + \int_0^b \left(-\frac{b}{2} + s\right)^2 A_{11}^B ds$$

$$+ \int_0^h \left(\frac{b}{2}\right)^2 A_{11}^R ds$$

$$= \frac{b^3}{12}(A_{11}^T + A_{11}^B) + \frac{b^2 h}{4}(A_{11}^L + A_{11}^R) = 216825.4$$

$$\oint A_{16} y\, ds = \int_0^b \frac{A_{16}^T}{A_{66}^T}\left(\frac{b}{2} - s\right) ds + \int_0^h \frac{A_{16}^L}{A_{66}^L}\left(-\frac{b}{2}\right) ds + \int_0^b \frac{A_{16}^B}{A_{66}^B}\left(-\frac{b}{2} + s\right) ds + \int_0^h \frac{A_{16}^R}{A_{66}^R}\left(\frac{b}{2}\right) ds$$

$$= \frac{hb}{2}\left(\frac{A_{16}^R}{A_{66}^R} - \frac{A_{16}^L}{A_{66}^L}\right) = 0$$

$$K(3,4) = \oint -yA_{16}(\psi_{,s} + r) ds = \oint -yA_{16}\psi_{,s} ds - 2A_e \oint yA_{16} ds = 0$$

$$K(4,4) = \oint (\psi_{,s} + r)^2 A_{66} ds$$

$$= \oint \left(\frac{q_s}{Gt\phi_{,x}}\right)^2 A_{66} ds$$

$$= \oint \left(\frac{q_s}{A_{66}} \cdot \frac{\oint r ds}{\oint \gamma_{xs} ds}\right)^2 A_{66} ds$$

$$= \oint \left(\frac{q_s}{A_{66}} \cdot \frac{2A_e}{q_s \oint \frac{ds}{A_{66}}}\right)^2 A_{66} ds$$

$$= \frac{4A_e^2}{\oint \frac{ds}{A_{66}}} = \frac{4(0.923 \cdot 0.507)^2}{1.0812E-04} = 8177.6$$

It was shown by Smith that $Gt = A_{66}$ [27].

These results are summarized in Table 2-4, as well as compared to other analyses [95]. For this uncoupled composite cross section, it can be seen that there is excellent agreement between all analyses.

Table 2-4. Results of current methodology compared to results from other analyses for an uncoupled Chandra-Chopra box beam

	NABSA	VABS	PRESENT
K(1,1)	$0.177E07$	$0.177E07$	**0.177E07**
K(2,2)	$0.869E05$	$0.869E05$	**0.867E05**
K(3,3)	$0.215E06$	$0.215E06$	**0.217E06**
K(4,4)	**0.816E04**	**0.819E04**	**0.818E04**

2.4.4 Example: Single-Cell Warping

Recall from Equation 2-19

$$\psi = \int_0^s \psi_{,s} ds = \int_0^s \left(\frac{q_s}{A_{66}} \left[\frac{\oint r ds}{\oint \gamma_{xs} ds} \right] - r \right) ds$$

$$= \int_0^s \frac{q_s}{A_{66}} \left[\frac{\oint r ds}{\oint \gamma_{xs} ds} \right] ds - \int_0^s r ds$$

For a closed cross section, $\oint r ds = 2A_e$, where A_e is the cross-sectional area. For a single cell section, the shear flow, q_s, is constant. Therefore the expression for warping can be rewritten as:

$$\int_0^s \psi = \frac{2A_e}{\left[\oint \frac{1}{A_{66}} ds \right]} \int_0^s \frac{1}{A_{66}} ds - 2A_e$$

When integrating warping around a closed loop, we must have

$$\oint \psi ds = 0$$

Based on this we can calculate the cross-sectional warping terms for the box beam:

$$K(1,5) = \oint \psi A_{11}\, ds = 0$$

$$K(2,5) = \oint z\psi A_{11}\, ds$$

$$= A_{11}\left[\frac{2A_e}{\left[\oint \frac{1}{A_{66}} ds\right]} \int_0^b \frac{\left(\frac{h}{2}\right)}{A_{66}} ds - 2A_e\right]^T$$

$$+\left[\frac{2A_e}{\left[\oint \frac{1}{A_{66}} ds\right]} \int_0^h \frac{\left(\frac{h}{2} - s\right)}{A_{66}} ds - 2A_e\right]^L$$

$$+\left[\frac{2A_e}{\left[\oint \frac{1}{A_{66}} ds\right]} \int_0^b \frac{\left(-\frac{h}{2}\right)}{A_{66}} ds - 2A_e\right]^B$$

$$+\left[\frac{2A_e}{\left[\oint \frac{1}{A_{66}} ds\right]} \int_0^h \frac{\left(-\frac{h}{2} + s\right)}{A_{66}} ds - 2A_e\right]^R = 0$$

$$K(3,5) = \oint y\psi A_{11}\, ds =$$

$$= A_{11}\left[\frac{2A_e}{\left[\oint \frac{1}{A_{66}} ds\right]} \int_0^b \frac{\left(\frac{b}{2} - s\right)}{A_{66}} ds - 2A_e\right]^T$$

$$+\left[\frac{2A_e}{\left[\oint \frac{1}{A_{66}} ds\right]} \int_0^h \frac{\left(-\frac{b}{2}\right)}{A_{66}} ds - 2A_e\right]^L$$

$$+\left[\frac{2A_e}{\left[\oint \frac{1}{A_{66}} ds\right]} \int_0^b \frac{\left(-\frac{b}{2} + s\right)}{A_{66}} ds - 2A_e\right]^B$$

$$+\left[\frac{2A_e}{\left[\oint \frac{1}{A_{66}} ds\right]} \int_0^h \frac{\left(-\frac{h}{2}\right)}{A_{66}} ds - 2A_e\right]^R = 0$$

$$K(4,5) = \oint \psi\left(\psi_{,s} + r\right) A_{16} ds = 0$$

For the calculation of $K(5,5)$ it is easier to determine the warping in a piecewise manner based on the specific cross-sectional geometry being analyzed.

Recall from Equation 2-19:

$$\psi = \frac{2A_e}{\oint \frac{ds}{A_{66}}} \int_0^s \frac{ds}{A_{66}} - \int_0^s r ds$$

For a rectangular cross section this can be rewritten using the dimensions of the cross section.

Here $A_e = bh$

and $\oint \frac{ds}{A_{66}} = \frac{2(b+h)}{A_{66}}$

so $\psi = \int_0^s \left(\frac{bh}{b+h} - r\right) ds$

For the right, left, top, and bottom segments, it can be shown that

$$\psi_R = \psi_L = -\beta \frac{bh}{4}$$

$$\psi_T = \psi_B = \beta \frac{bh}{4}$$

where $\beta = \frac{b-h}{b+h}$

The torsional stiffness can now be easily written as

$$K(5,5) = \left(\beta \frac{bh}{4}\right)^2 \oint A_{11} ds = \left(\beta \frac{bh}{4}\right)^2 K(1,1)$$

2.4.5 Extension-Torsion Coupled Beam

An antisymmetric layup introduces tension-torsion coupling to a box beam. Here, the top and bottom flanges of the box beam have the same ply angle, but applied in opposite directions. The left and right webs are maintained quasi-isotropic by alternating between $+15°$ and $-15°$ layups.

Table 2-5. Calculated values of $\bar{A}$ for an antisymmetric Chandra-Chopra box beam

	$[\mathbf{15°}]_6$	$[\mathbf{-15°}]_6$	$[\mathbf{+15°/-15°}]_3$
A_{11}	553470.4		
A_{12}	50950.3		
A_{16}	129649.8	-129649.8	0
A_{22}	49285.5		
A_{26}	15895.8	-15895.8	0
A_{66}	59537.9		

The results of this cross-sectional analysis are summarized and compared against other analyses in Table 2-6. Here is can be seen that there are fairly significant errors in the bending and lag stiffness values (K_{22} and K_{33}).

Table 2-6. Results of current methodology compared to results from other analyses for an antisymmetric Chandra-Chopra box beam

	NABSA	VABS	PRESENT
K(1,1)	0.137E07	0.137E07	**0.143E07**
K(2,2)	0.608E05	0.608E05	**0.703E05**
K(3,3)	0.143E06	0.143E06	**0.102E06**
K(4,4)	0.173E05	0.174E05	**0.172E05**
K(2,4)	0.180E05	0.180E05	**0.179E05**

This is due to the initial assumptions made in the formulation of these expressions. From the kinematic formulation we assumed a form for the shear flow (q_s, Equation 3-14). From the material law (Equation 2-21) this holds only if $A_{16} = 0$. Therefore for the uncoupled example, the solution for lag and bending stiffness is near exact but in the case of a coupled beam, the A_{16} terms begins to play a part and we get larger errors in the leg and bending stiffness. The axial stiffness, K_{11}, however is within a 5% error, and the torsional stiffness, K_{44}, and extension-torsion coupling term, K_{24} are within a 1% error or less.

Using the Mixed Method for calculating the cross-sectional stiffness values will help to reduce these errors and can be seen in Appendix I.

2.5 Example: Multi-Cell Cross Section

In most aerospace applications the cross sections being considered have multiple cells. Accounting for the shear flow is an important part of correctly calculating the cross-sectional stiffness values. In this section we consider two examples: a simple two-celled box beam to show how shear flow is accounted for and the tilt-rotor aeroacoustic model (TRAM rotor) for methodology validation of an aerodynamic structure with multiple cells.

2.5.1 Two-Cell Box Beam

Calculation of the cross-sectional stiffness values follows the same formulation as before. However calculation of the shear flow for both cells must now be considered. This example shows how the shear flow and twist rate are calculated. Consider a box beam as shown below:

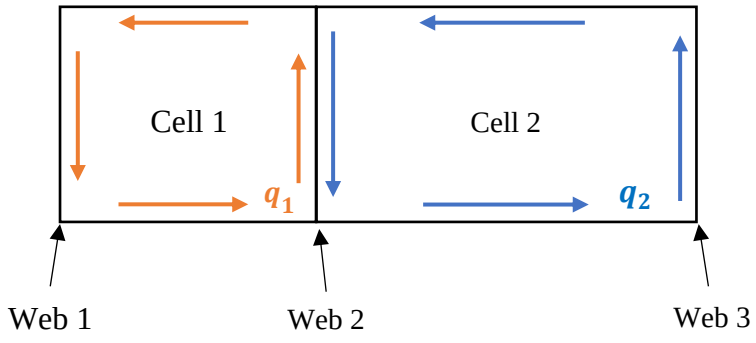

Figure 2-10. Two-cell box beam with shear flow

Note that the shear flow is q_1 in Web 1, q_2 in Web 3, and $(q_2 - q_1)$ in Web 2. For this problem we have three unknowns: $q_1, q_2, \phi_{,x}$

For each cell, the following is true:

$$2A_i\phi_{,x} = q_i \oint \frac{ds}{A_{66}}$$

For this particular problem:

$$2A_1\phi_{,x} = q_1 \int_{Cell\ 1} \frac{ds}{Gt} - q_2 \int_{Web\ 2} \frac{ds}{Gt} = \delta_{11}q_1 - \delta_{12}q_2$$

$$2A_2\phi_{,x} = -q_1 \int_{Web\ 2} \frac{ds}{Gt} + q_2 \int_{Cell\ 2} \frac{ds}{Gt} = -\delta_{21}q_1 + \delta_{22}q_2$$

This can then be represented as:

$$\begin{bmatrix} \delta_{11} & -\delta_{12} \\ -\delta_{21} & \delta_{22} \end{bmatrix} \begin{Bmatrix} q_1 \\ q_2 \end{Bmatrix} = (2\phi_{,x}) \begin{Bmatrix} \bar{A}_1 \\ \bar{A}_2 \end{Bmatrix}$$

Shear flow can then be easily solved for:

$$q_1 = \frac{\delta_{22}\bar{A}_1 + \delta_{12}\bar{A}_2}{\Delta}(2\phi_{,x}) \qquad q_2 = \frac{\delta_{12}\bar{A}_1 + \delta_{11}\bar{A}_2}{\Delta}(2\phi_{,x})$$

$$\text{where} \quad \Delta = \delta_{11}\delta_{22} - \delta_{12}^2$$

Unfortunately there is still one unknown: $\phi_{,x}$. For an isotropic beam, the axial strain, $U_{,x}$, will not play a part, and in order to simplify this analysis we will consider that the moment, $M_{,x}$, is only affected by the St. Venant torsion, $\phi_{,x}$ such that

$$M_x = K(4,4)\phi_{,x}$$

From Equation 2-16

$$M_x = \sum 2\bar{A}_i q_i = 2A_1q_1 + 2A_2q_2$$

so

$$M_x = 2(A_1 q_1 + A_2 q_2) = 4\left[\frac{\delta_{22}\bar{A}_1^2 + 2\delta_{12}\bar{A}_1\bar{A}_2 + \delta_{11}\bar{A}_2^2}{\Delta}\right]\phi_{,x} = K(4,4)\phi_{,x}$$

$$\phi_{,x} = \frac{M_x}{4}\left[\frac{\Delta}{\delta_{22}\bar{A}_1^2 + 2\delta_{12}\bar{A}_1\bar{A}_2 + \delta_{11}\bar{A}_2^2}\right]$$

Plugging this expression in we get the shear flow as

$$q_1 = \frac{\delta_{22}\bar{A}_1 + \delta_{12}\bar{A}_2}{\delta_{22}\bar{A}_1^2 + 2\delta_{12}\bar{A}_1\bar{A}_2 + \delta_{11}\bar{A}_2^2}\left(\frac{M_x}{2}\right)$$

$$q_2 = \frac{\delta_{12}\bar{A}_1 + \delta_{11}\bar{A}_2}{\delta_{22}\bar{A}_1^2 + 2\delta_{12}\bar{A}_1\bar{A}_2 + \delta_{11}\bar{A}_2^2}\left(\frac{M_x}{2}\right)$$

2.5.2 Example: TRAM Blade

The tilt-rotor aeroacoustic model (or TRAM) rotor is an experimental 1/4-scale model of the V-22 tiltrotor developed by NASA. Based on old engineering drawings, cross sections were modeled at eight radial stations to calculate the bending (flapwise and lagwise) and torsional stiffnesses. These values were then compared with documented experimental results.

Figure 2-11 shows that there is generally good agreement for the flapwise (K_{22}) and torsional (K_{44}) rigidity. However this method over-predicted the chordwise bending stiffness (K_{33}). While it was shown before that this cross-sectional methodology a strong coupling value for A_{16} can introduce errors into the cross-sectional stiffness values for lag and bending. However, the extent of these errors are far smaller for the box beam than what was calculated for the TRAM rotor. It is suspected that incomplete material property information contributes to the discrepancy in the lag stiffness. The materials listed in the

original drawings are either no longer in production or no material properties were available. Best estimates were used based on the material information contained in the Composite Materials Handbook (CMH-17) [97].

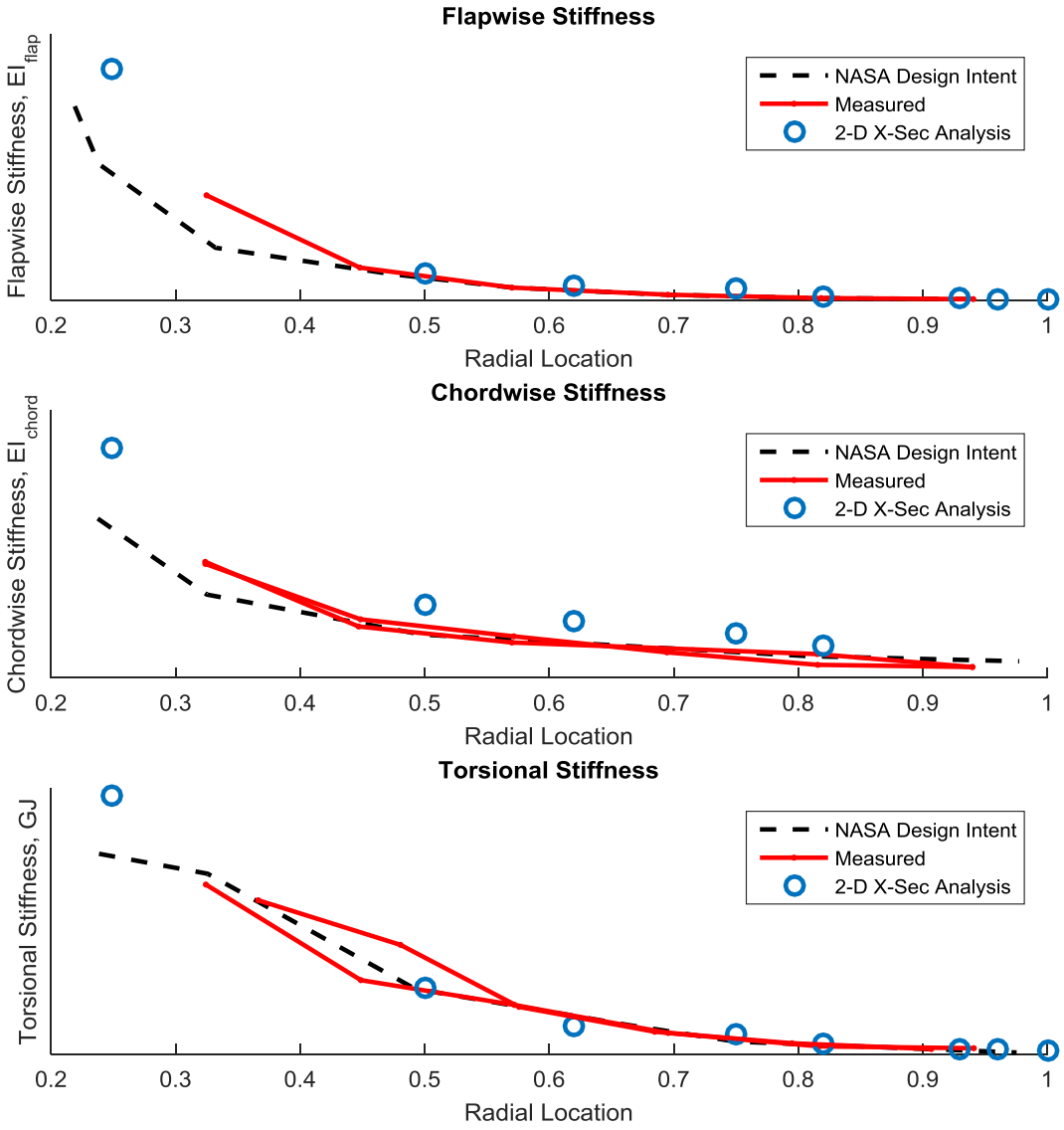

Figure 2-11. Flapwise (K_{22}), Chordwise (K_{33} and Torsional (K_{44}) stiffness of the TRAM rotor at eight radial locations

Chapter 3: 3-D Material Modeling

3.1 Importance

In most applications resolving each layer of a laminate (defined as a stack of laminae or plies) results in a significant increase in the size of analysis. The use of composites in 3-D FEA required the consideration of how to effectively model all plies while keeping the problem size within an acceptable level. Therefore, in order to simplify the problem material homogenization becomes a necessary step in meshing.

The material homogenization method used in this research is based on the work of Chou and Carleone [57] and combines the assumptions of Voigt and Reuss. Employing this method allows for the design of simpler meshes with minimal effect on performance results, as will be shown later. The resolution of some interlaminar stresses, however, must be compromised.

3.1.1 Homogenization Method

Material homogenization is a method to combine a number of composite layers and effectively smear the properties into a single homogenous anisotropic solid layer. In order to do this, it is important to take into account the elastic moduli of the composite material, the volume fraction of each layer, and the orientation of each ply in the laminate.

For any material, the linear stresses and strains are related by Hooke's Law:

$$\begin{Bmatrix} \sigma_{11} \\ \sigma_{22} \\ \sigma_{33} \\ \sigma_{23} \\ \sigma_{31} \\ \sigma_{12} \end{Bmatrix}^{[k]} = [C^k] \begin{Bmatrix} \varepsilon_{11} \\ \varepsilon_{22} \\ \varepsilon_{33} \\ \varepsilon_{23} \\ \varepsilon_{31} \\ \varepsilon_{12} \end{Bmatrix}^{[k]} \quad \textbf{or} \quad \begin{Bmatrix} \sigma_1 \\ \sigma_2 \\ \sigma_3 \\ \sigma_4 \\ \sigma_5 \\ \sigma_6 \end{Bmatrix}^{[k]} = [C^k] \begin{Bmatrix} \varepsilon_1 \\ \varepsilon_2 \\ \varepsilon_3 \\ \varepsilon_4 \\ \varepsilon_5 \\ \varepsilon_6 \end{Bmatrix}^{[k]} \qquad 3\text{-}1$$

where k refers to the k^{th} ply of the laminate. Homogenization aims to find a similar constituent matrix, $[C]$, that represents the entire laminate, within which the ply orientation can vary.

Prior to the work of Chou and Carleone [57], material homogenization was carried out using one of three assumptions: 1) the rule of mixtures, 2) Voigt's hypothesis, and 3) Reuss' hypothesis. Well defined in the Classical Laminated Plate Theory (CLPT) literature, the rule of mixtures is a simple method that volume averages the Young's Moduli of the different composite plies. Unfortunately, this method is not applicable to any other elastic constants, and is only true if the composite structure is flat and loaded uniaxially. In order to model 3-D composite structures and account for out of plane effects, CLPT is not acceptable.

Voigt's hypothesis made the assumption that all six of the strain components throughout the laminate are uniform. However, this assumption means that the stresses at the ply interfaces are not in equilibrium which would lead to delamination of the laminate, as illustrated by Figure 3-1. Reuss' hypothesis acted as the counterpoint to Voigt's and assumed that all of the stress components throughout the laminate are uniform. If one were

to use this hypothesis, then the strains at the ply interfaces would not be in equilibrium and would be too large for the material to remain bonded. This would cause a shearing of the lamina. This is illustrated by Figure 3-2.

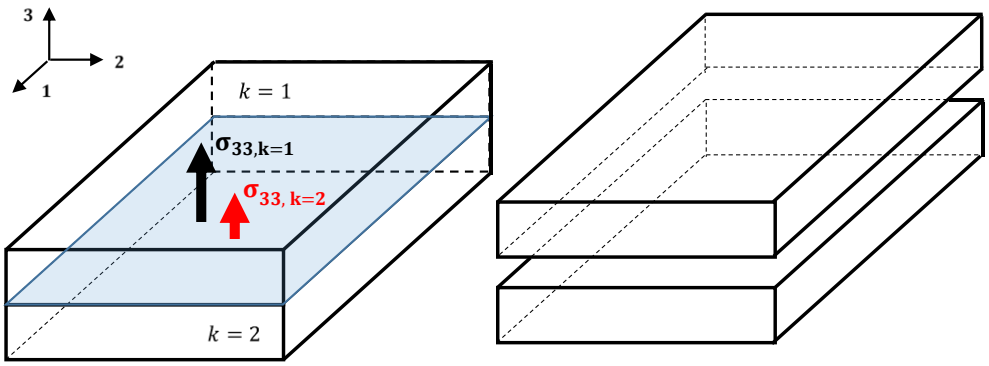

Figure 3-1. Voigt's hypothesis leads to an imbalance in normal stresses and potential delamination of plies

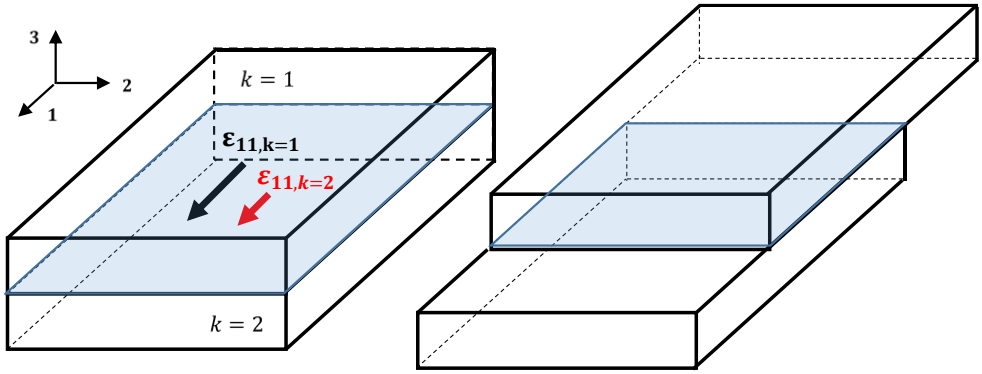

Figure 3-2. Reuss' hypothesis leads to an imbalance in in-plane strains and potential shearing of plies

The present work employs a method that mixes the two material homogenization hypotheses discussed above. Now normal strains in the individual ply fiber plane (the 1- and 2- direction), and the shear strain in the plane of the plies are assumed to be equivalent to the corresponding strains in the homogenous element:

$$\varepsilon_i = \varepsilon_i^k \ \ (i = 1,2,6, k = 1, \dots, n) \qquad 3\text{-}2$$

where the subscript, i, corresponds to the vector elements indicated in Equation 3-1. To ensure there is stress continuity at the ply interfaces, it is also assumed that the ply level normal stresses perpendicular to the plane (out-of-plane stresses) are equivalent to the corresponding stresses in the homogenous element:

$$\sigma_i = \sigma_i^k \ \ (i = 3,4,5, k = 1, \dots, n) \qquad 3\text{-}3$$

Equations 3-2 and 3-3 represent a total of $6n$ linear equations (3 of the 6 stresses and 3 of the 6 strains). The three remaining stresses and three remaining strains, are then assumed to be volume averaged, i.e.

$$\varepsilon_i = \sum_{k=1}^{n} V^k \varepsilon_i^k \ \ (i = 3,4,5)$$
$$\sigma_i = \sum_{k=1}^{n} V^k \sigma_i^k \ \ (i = 1,2,6) \qquad 3\text{-}4$$

where V^k is the volume of the material or ply k relative to the total volume of the laminate (the volume fraction).

Using Equations 3-2 through 3-4 and the assumption that each ply is at least monoclinic in nature (which is always true for the current study as we consider only orthotropic or transversely isotropic materials), i.e.,

$$[C^k] = \begin{bmatrix} C_{11} & C_{12} & C_{13} & 0 & 0 & C_{16} \\ & C_{22} & C_{23} & 0 & 0 & C_{26} \\ & & C_{33} & 0 & 0 & C_{36} \\ & & & C_{44} & C_{45} & 0 \\ & SYM & & & C_{55} & 0 \\ & & & & & C_{66} \end{bmatrix}$$

one can solve for the 36 constituent constants, C_{ij} $(i = 1-6, j = 1-6)$, for the entire laminate. Note that Hooke's Law provides the assumption of symmetry

$$C_{ij}^k = C_{ji}^k, i \neq j$$

as well as an additional $12n$ linear equations:

$$\sigma_i^k = C_{ij}^k \varepsilon_j^k$$

This yields the solution

$$C_{ij} = C_{ji} = 0 \ \ (i = 1,2,3,6; j = 4,5)$$

$$C_{ij} = \sum_{k=1}^{n} V^k \left[C_{ij}^k - \frac{C_{i3}^k C_{3j}^k}{C_{33}^k} + \frac{C_{i3}^k \sum_{l=1}^{n} \frac{V^l C_{3j}^l}{C_{33}^l}}{C_{33}^k \sum_{l=1}^{n} \frac{V^l}{C_{33}^l}} \right] \ (i,j = 1,2,3,6)$$

$$C_{ij} = \frac{\sum_{k=1}^{n} \frac{V^k}{\Delta_k} C_{ij}^k}{\sum_{k=1}^{n} \sum_{l=1}^{n} \frac{V^k V^l}{\Delta_k \Delta_l} \left(C_{44}^k C_{55}^l - C_{45}^k C_{54}^l \right)}, \qquad \Delta_k = \begin{vmatrix} C_{44}^k & C_{45}^k \\ C_{45}^k & C_{55}^k \end{vmatrix} \ (i,j = 4,5)$$

There is one significant downside to using this method – the order in which the plies are layered has no impact on the homogenized constants. Therefore when deciding on groups of plies to be homogenized, care needs to be taken so that any desired coupling is not lost.

For example, consider a hygrothermally stable laminate, defined by Winckler [92], where θ is an arbitrarily chosen ply orientation.

$$[\theta, (\theta + 90)_2, \theta, -\theta, (-\theta + 90)_2, \theta]$$

It can be shown using CLPT that this layup has a non-zero extension-torsion coupling term for all θ. If this layup were to be homogenized into a single element using the present methodology, however, the effect of the antisymmetric layup would be cancelled out. The properties of opposing ply orientations (θ vs $-\theta$ and $(\theta + 90)$ vs $(-\theta + 90)$) would eliminate any coupling. This is because a finite element with smeared material properties takes on the material characteristics of a homogenous material, which by definition cannot be coupled. Therefore to preserve the coupling of a layup like this, the laminate would have to be divided into two elements: one for the top four plies and one for the bottom four plies.

3.1.2 De-Homogenizing Process

While homogenization simplifies the problem and dramatically reduces computational time, detailed stress and strain information is lost at a ply level. One of the main problems of composite laminates is the danger of delamination. It is important, therefore, to accurately predict interlaminar stresses and strains, or at least achieve a close approximation. In the following section we consider a 2-D finite element with homogenized material properties and how stresses and strains would be calculated at points through the laminate's thickness.

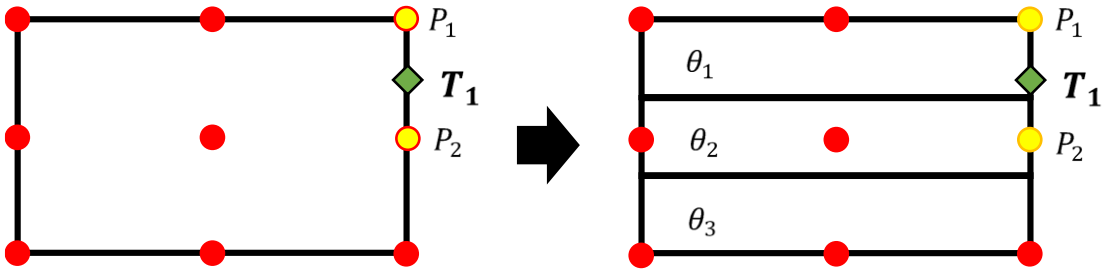

(a) Homogenized/Coarse mesh **(b) Ply resolved mesh**

Figure 3-3. A solid homogenized element representing an original 3 ply layup

The solid elements used for meshing the present analysis are 2nd order, 27-noded, hexahedral elements. The analysis outputs all 6 stresses and 6 strains at each node in the component mesh. Figure 3-3 (a) shows a representative face of a homogenized element, with 9 nodes indicated by red dots, representing a notional composite laminate composed of three plies at three different orientations, θ_1, θ_2, and θ_3.

Sun and Liao [60] proposed a solution for calculating the stresses and strains at the ply level. Consider nodes P_1 and P_2 in Figure 3-3. From the analysis we know all 6 stresses and 6 strains at these points in the homogenized mesh. Say we would like to determine the stresses and strains at a point T_1. Recall from Equation 3-2 and 3-3 that the in-plane stresses (σ_{11}, σ_{22}, and σ_{12}) and out-of-plane strains (ε_{33}, ε_{23}, and ε_{31}) calculated by the analysis are the same at the nodes whether we are considering the homogenized mesh, or the ply resolved mesh. That leaves us with 6 unknown ply resolved stresses/strains: σ_{33}, σ_{23}, σ_{31}, and ε_{11}, ε_{22}, ε_{12}. Recall from Hooke's Law the relationship between the stresses and strains for the entire laminate is related by

$$\begin{Bmatrix}\sigma_{11}\\ \sigma_{22}\\ \sigma_{33}\\ \sigma_{23}\\ \sigma_{31}\\ \sigma_{12}\end{Bmatrix} = [C]\begin{Bmatrix}\varepsilon_{11}\\ \varepsilon_{22}\\ \varepsilon_{33}\\ \varepsilon_{23}\\ \varepsilon_{31}\\ \varepsilon_{12}\end{Bmatrix}$$

Hooke's Law applies to each individual ply as well, with the constituent matrix $[C^k]$ defining the individual ply properties, which vary based on the fiber orientation θ. Expanding three of the six equations from Hooke's Law yields the following:

$$\sigma_{33} = C_{31}^k\varepsilon_{11} + C_{32}^k\varepsilon_{22} + C_{33}^k\varepsilon_{33} + C_{34}^k\varepsilon_{23} + C_{35}^k\varepsilon_{31} + C_{36}^k\varepsilon_{12}$$

$$\sigma_{23} = C_{41}^k\varepsilon_{11} + C_{42}^k\varepsilon_{22} + C_{43}^k\varepsilon_{33} + C_{44}^k\varepsilon_{23} + C_{45}^k\varepsilon_{31} + C_{46}^k\varepsilon_{12}$$

$$\sigma_{31} = C_{51}^k\varepsilon_{11} + C_{52}^k\varepsilon_{22} + C_{53}^k\varepsilon_{33} + C_{54}^k\varepsilon_{23} + C_{55}^k\varepsilon_{31} + C_{56}^k\varepsilon_{12}$$

Or written in matrix form:

$$\begin{Bmatrix}\sigma_{33}\\ \sigma_{23}\\ \sigma_{31}\end{Bmatrix} = \begin{bmatrix}C_{33}^k & C_{34}^k & C_{35}^k\\ C_{43}^k & C_{44}^k & C_{45}^k\\ C_{53}^k & C_{54}^k & C_{55}^k\end{bmatrix}\begin{Bmatrix}\varepsilon_{33}\\ \varepsilon_{23}\\ \varepsilon_{31}\end{Bmatrix} + \begin{bmatrix}C_{31}^k & C_{32}^k & C_{36}^k\\ C_{41}^k & C_{42}^k & C_{46}^k\\ C_{51}^k & C_{52}^k & C_{56}^k\end{bmatrix}\begin{Bmatrix}\varepsilon_{11}\\ \varepsilon_{22}\\ \varepsilon_{12}\end{Bmatrix} \quad \text{3-5}$$

During homogenization, it was assumed that the out-of-plane stresses $(\sigma_{33}, \sigma_{23}, \sigma_{31})$ and the in-plane strains $(\varepsilon_{11}, \varepsilon_{22}, \varepsilon_{12})$ are the same between plies (at the interlaminar surface) so that plies will not delaminate or de-bond from one another. Therefore, these are known for Equation 3-5. To maintain a smooth distribution through the thickness of the ply (to avoid stress or strain discontinuities), the calculated stresses and strains at points not located at a ply interface, such as T_1, are linearly interpolated using the known values at P_1 and P_2.

Equation 3-5 can then be rearranged to calculate the out of plane strains (ε_{33}, ε_{23}, ε_{31}).

$$\begin{Bmatrix}\varepsilon_{33}\\ \varepsilon_{23}\\ \varepsilon_{31}\end{Bmatrix} = \begin{bmatrix}C_{33}^k & C_{34}^k & C_{35}^k\\ C_{43}^k & C_{44}^k & C_{45}^k\\ C_{53}^k & C_{54}^k & C_{55}^k\end{bmatrix}^{-1} \begin{Bmatrix}\sigma_{33}\\ \sigma_{23}\\ \sigma_{31}\end{Bmatrix} - \begin{bmatrix}C_{31}^k & C_{32}^k & C_{36}^k\\ C_{41}^k & C_{42}^k & C_{46}^k\\ C_{51}^k & C_{52}^k & C_{56}^k\end{bmatrix} \begin{Bmatrix}\varepsilon_{11}\\ \varepsilon_{22}\\ \varepsilon_{12}\end{Bmatrix} \quad 3\text{-}6$$

From these, the laminar in-plane stresses (σ_{11}, σ_{22}, σ_{12}) can be calculated using Hooke's Law.

This method of determining the interlaminar stresses and strains is straightforward when considering regular 2-D quadrilateral elements (all corners are right angles). However the models used in this research are not made of regular quadrilateral elements but rather irregular tetrahedral elements. Tetrahedral interpolation of stresses and strains, as required to move from Equation 3-5 to 3-6, poses a non-trivial problem that is outside the scope of the present work.

3.2 Validation

Validation of the composite homogenization model was required before application of composite coupling to a rotor. Validation was carried out on two vastly different structures: a box beam, and a solid flexbeam. Validation of the beam model was performed using the experimental results produced by Chandra, et al. [25]. Three antisymmetric layups were considered. Two of the beams tested were defined by a $[0/\theta]_3$ layup and the third by a $[\theta]_6$ layup. These experiments provide reliable static deflection data to validate the material homogenization employed to simplify the structural model.

Table 3-1. Material properties of composite materials used in Chandra and Haynes extension-torsion coupled beam experiments

	IM7/8552	T300/976
$E_1, GPa\ (psi)$	142 (20.59×10^6)	125 (18.13×10^6)
$E_2, GPa\ (psi)$	9.79 (1.42×10^6)	8.45 (1.23×10^6)
$G_{12}, GPa\ (psi)$	6.14 (0.89×10^6)	4.3 (0.62×10^6)
ν_{12}	0.42	0.328
$t_{ply}, mm\ (in.)$	0.183 (0.005)	0.152 (0.006)

3.2.1 Chandra-Chopra Box Beam

For the Chandra-Chopra layups, the thin walled box beams were composed of 6 layers of IM7/8552 graphite-epoxy, the material properties of which are listed in Table 3-1. Two meshes were created for this case. The first, Figure 3-4 (a) is a fine or ply resolved mesh. In this case each element represented only a single ply's thickness. In contrast to this is the coarse, or homogenized, mesh (Figure 4-4 (b)). A cross section of the ply resolved mesh contained 960 elements. The homogenized mesh contained 60 elements. All elements are 27-noded, isoparametric, second order, Lagrangian hexahedral elements. Each model was designed to match the dimensions of the box beams built by Chandra et al. [25].

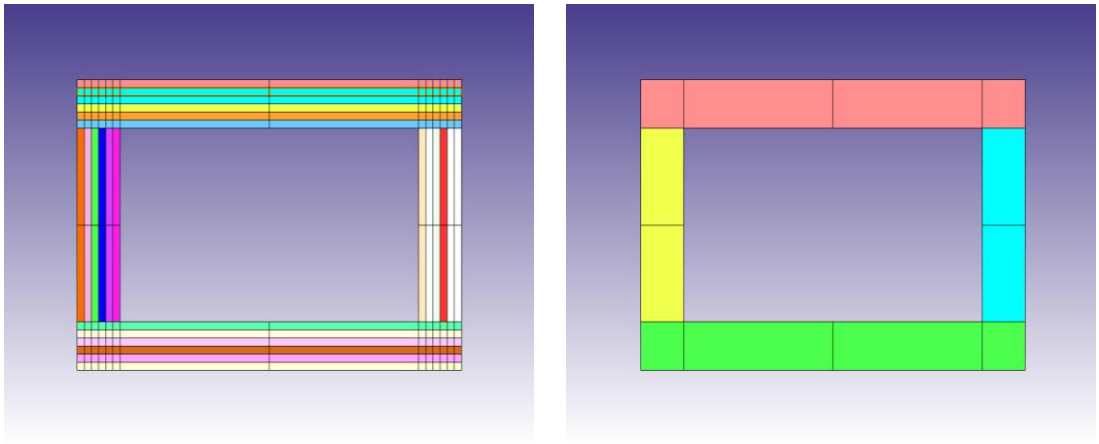

(a) Ply resolved or fine box beam mesh **(b) Homogenized or coarse box beam mesh**

Figure 3-4. Cross section of two box beam meshes created to validate homogenization method

Figure 3-5 shows the twist induced along the beam span due to an axial tip force of 1 lb for three different layups with both the ply resolved and homogenized meshes. For the exception of the $[15°]_6$ case, homogenization has minimal impact on the results. In general, predictions match the experimental data for the $[0°/30°]_3$ and $[0°/45°]_3$ cases extremely well.

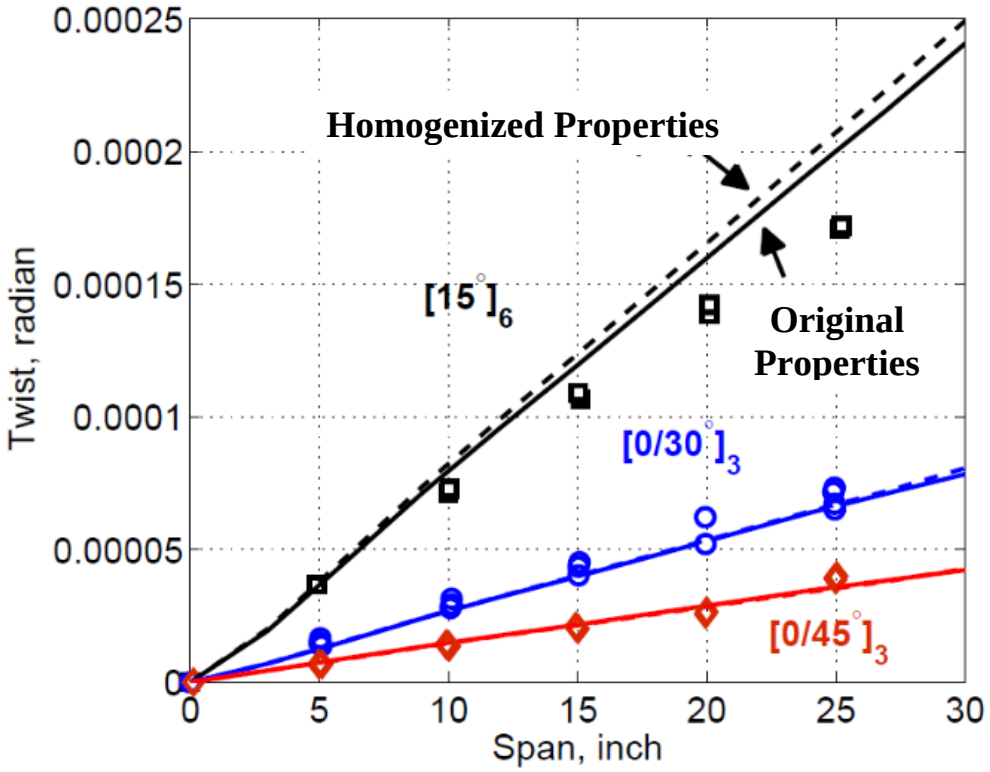

Figure 3-5. Twist due to a tip axial force of 1 lb for three nominal antisymmetric box beams

3.2.2 TRAM Rotor/Flexbeam

The TRAM rotor flexbeam experimental data was provided to the University of Maryland by NASA. The flexbeam acts as the primary flapping hinge and is rigidly attached to the gimbaled hub, as illustrated in Figure 3-6.

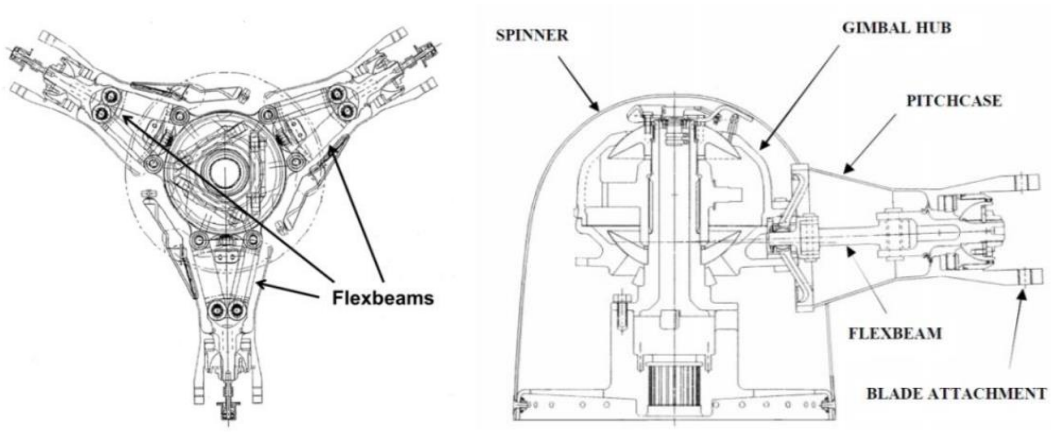

Figure 3-6. TRAM hub cross section top view and side view

Two different structural meshes were created to model the flexbeam: a fine, ply resolved mesh consisting of 32,225 nodes and 3,660 elements, and a coarse, homogenized mesh made up of 4,515 nodes and 30 elements. Structural analysis was carried out on the fine flexbeam, and the beamwise deflections matched experimental data well. It was found to be significantly stiffer in the chordwise direction [98] which was assumed to be due to uncertainty in material properties, as indicated in Section 2.5.2.

Although the structural properties were not exact to the experimental data, this model can still be used to determine the effects of homogenization on the stress/strain calculations. Figure 3-7 through Figure 3-18 show a side by side comparison of the fine and coarse flexbeams for all 6 stresses and all 6 strains.

From these figures it can be seen that the ply resolved mesh naturally has more local stress bands and concentrations, most notably on the top surface. Part of this is due to the fact that in the ply resolved mesh, there were more regions in which the number of plies changed (there was more variation in the thickness of the flexbeam that was eliminated in the simplified coarse mesh). The homogenized mesh, however, was able to

capture the peak positive and negative magnitude stresses and strain. These figures also show that the stress/strain distribution is very 3-dimensional in nature, with independent variation along the span, chord, and thickness of the structure.

The largest differences between the two meshes occurs in the shear stresses and strains, most noticeably in ε_{13}, even though the general patterns are similar. The homogenization was carried out over a substantial thickness containing many plies of many materials (details cannot be provided due to proprietary restrictions), so it is expected that the shear stresses and strains differ more substantially than the in-plane stresses and strains. Additionally, although there were no attempts to recover the individual ply stresses and strains, this example was chosen to understand the stress/strain patterns for a structure with known static deflection data. The pattern of 3-D stresses and strains in the homogenized mesh as well as the maximum amplitudes appear to be well captured.

For the rotor used in this research, the thickness of the structure is significantly lower and the number of plies over which homogenization is carried out is greatly reduced.

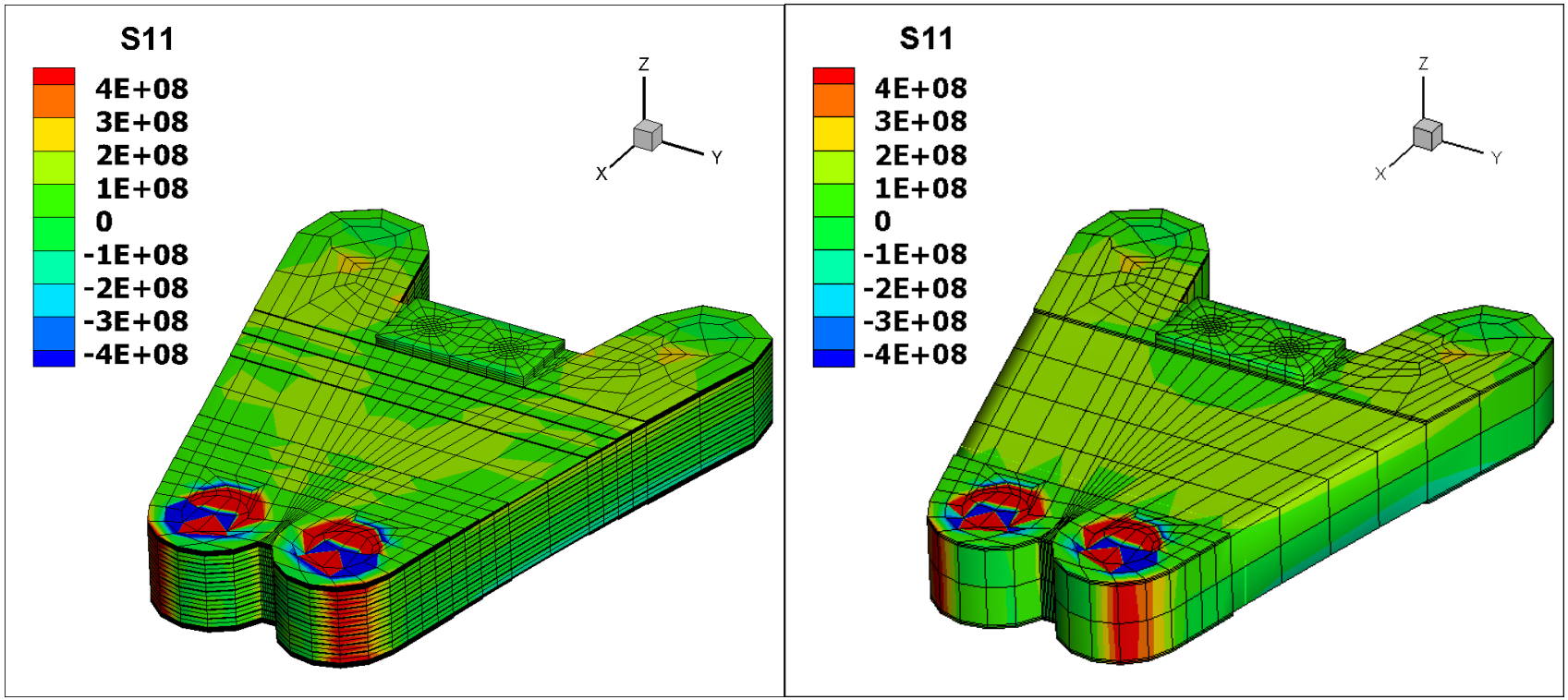

Figure 3-7. Principle stress (in Pa) in the radial or x-direction for a ply resolved and homogenized TRAM flexbeam due to a static bending load

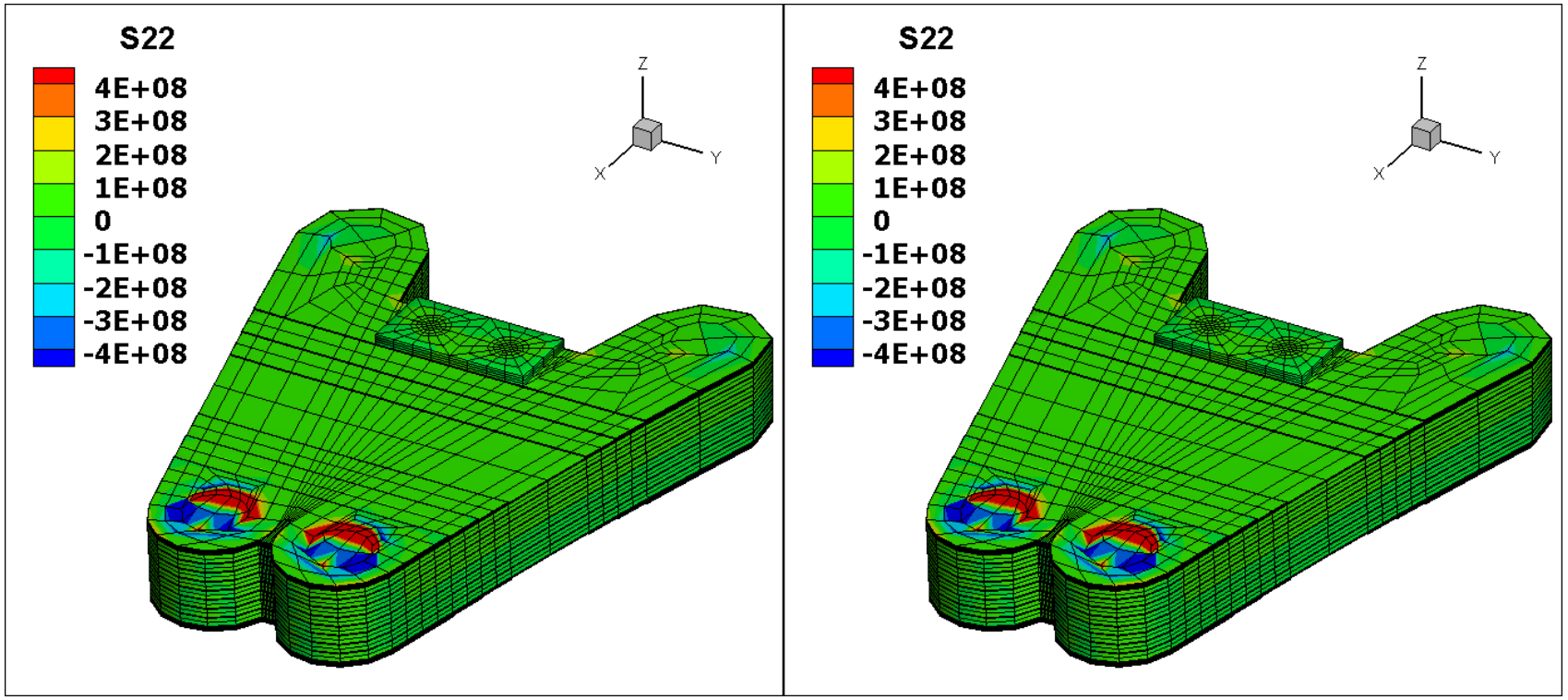

Figure 3-8. Principle stress (in Pa) in the lagwise or y-direction for a ply resolved and homogenized TRAM flexbeam due to a static bending load

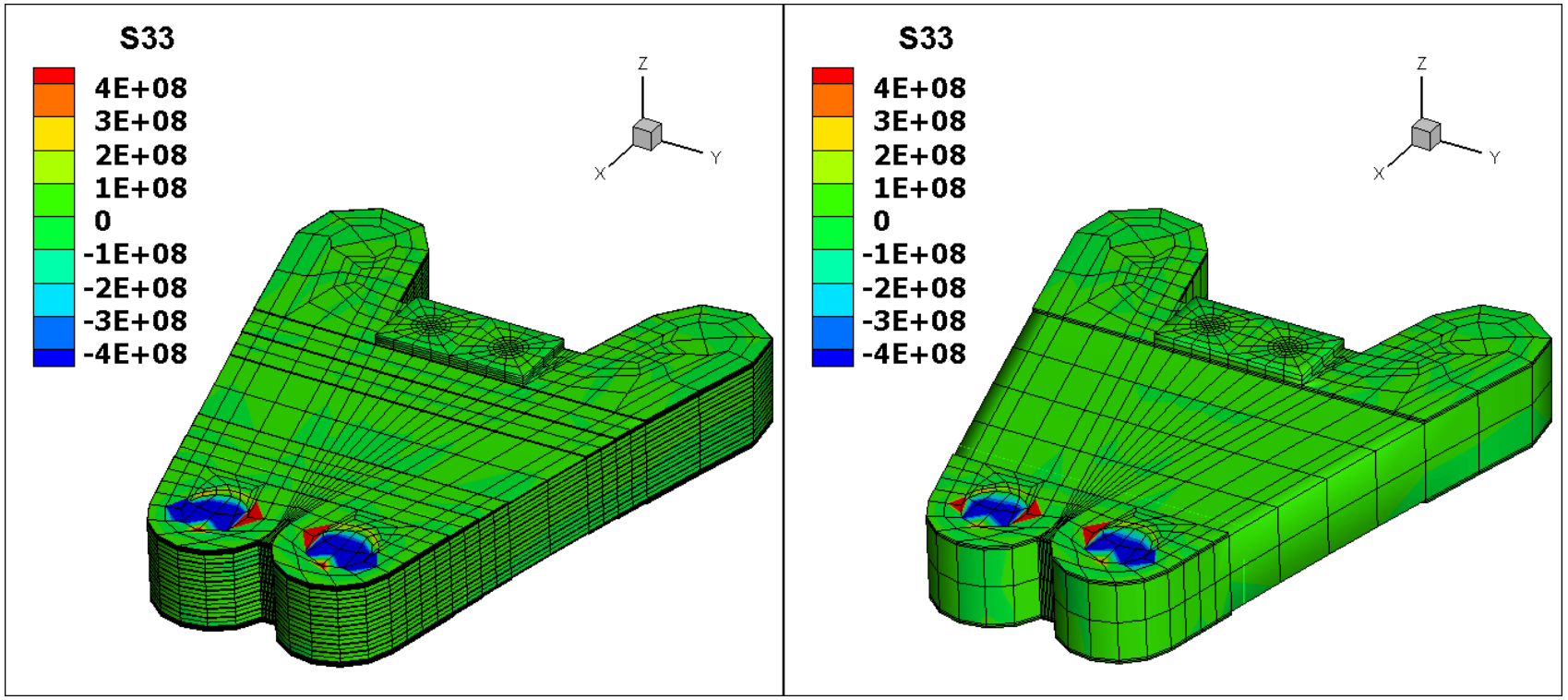

Figure 3-9. Principle stress (in Pa) in the flapwise or z-direction for a ply resolved and homogenized TRAM flexbeam due to a static bending load

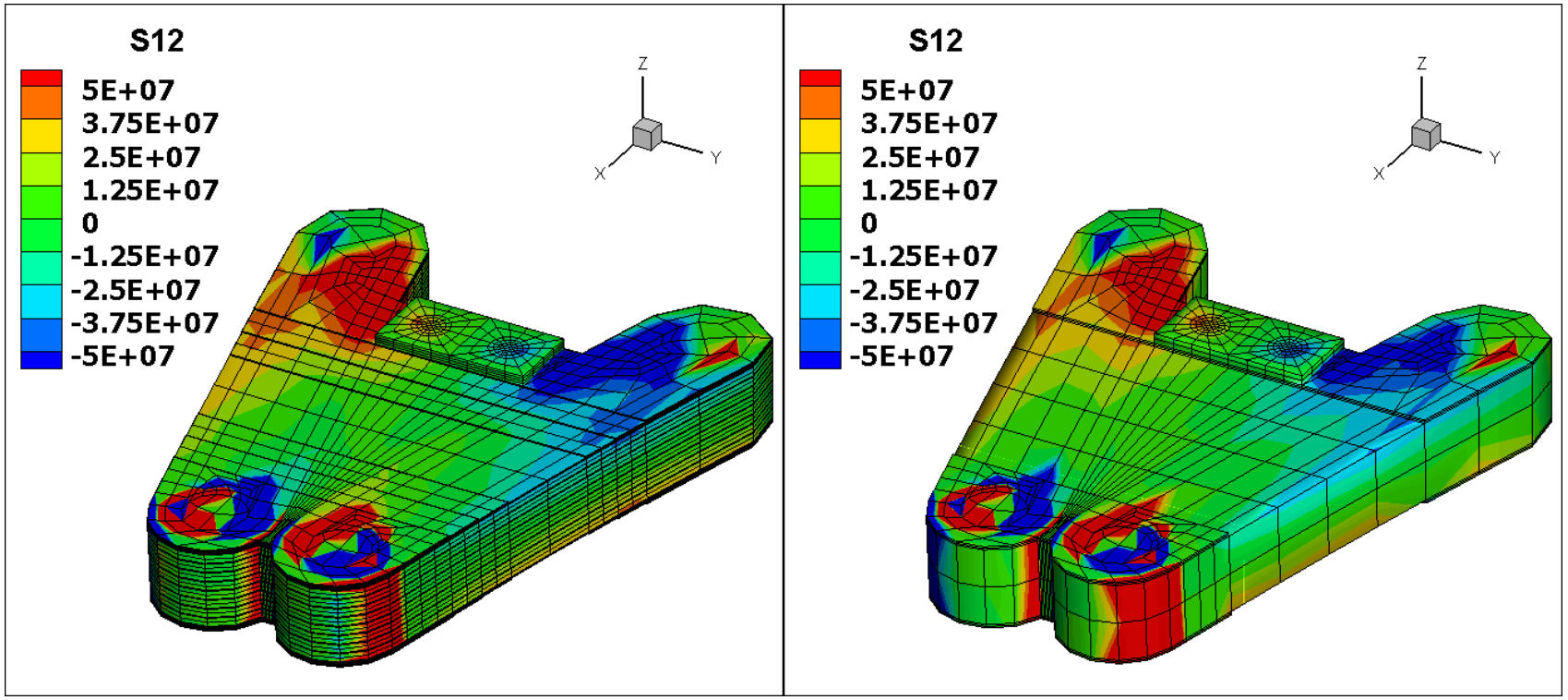

Figure 3-10. Shear stress (in Pa) in the x-y plane for a ply resolved and homogenized TRAM flexbeam due to a static bending load

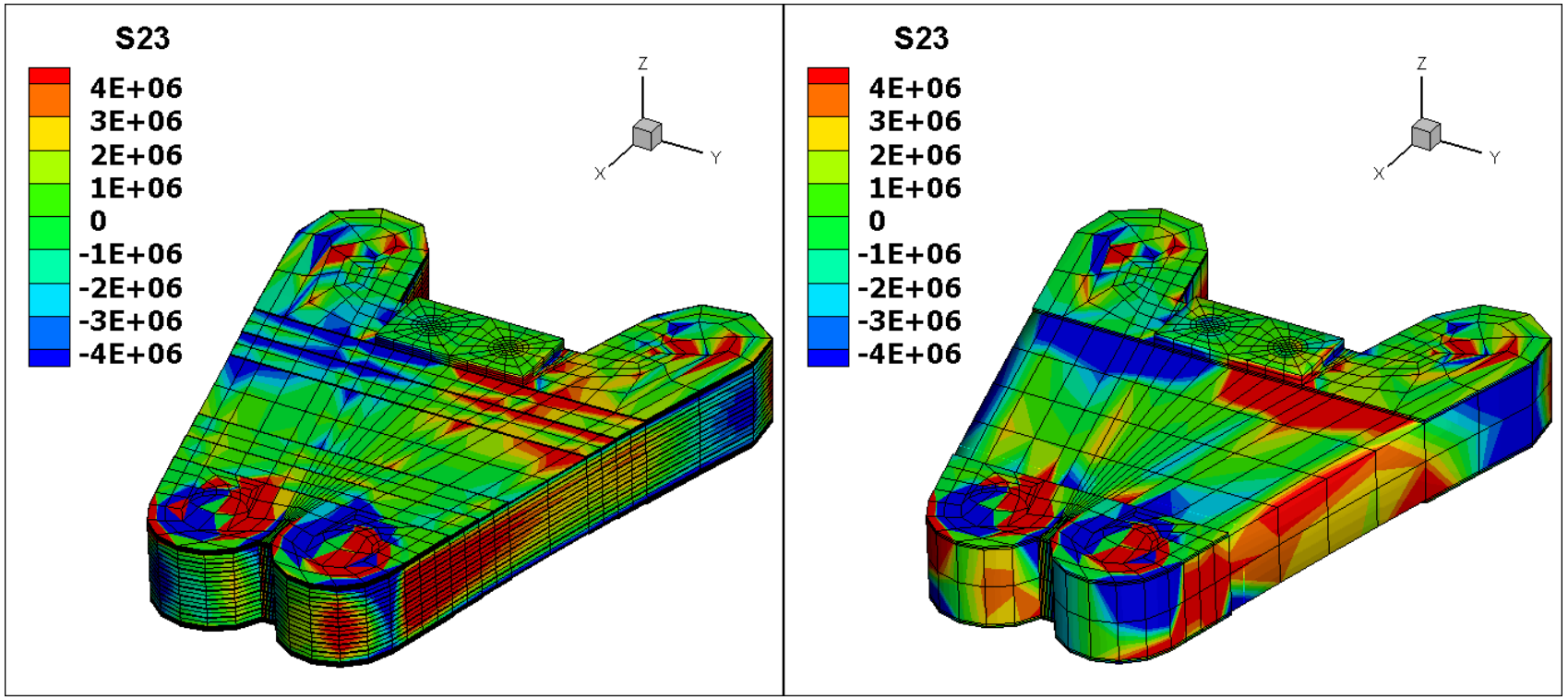

Figure 3-11. Shear stress (in Pa) in the y-z plane for a ply resolved and homogenized TRAM flexbeam due to a static bending load

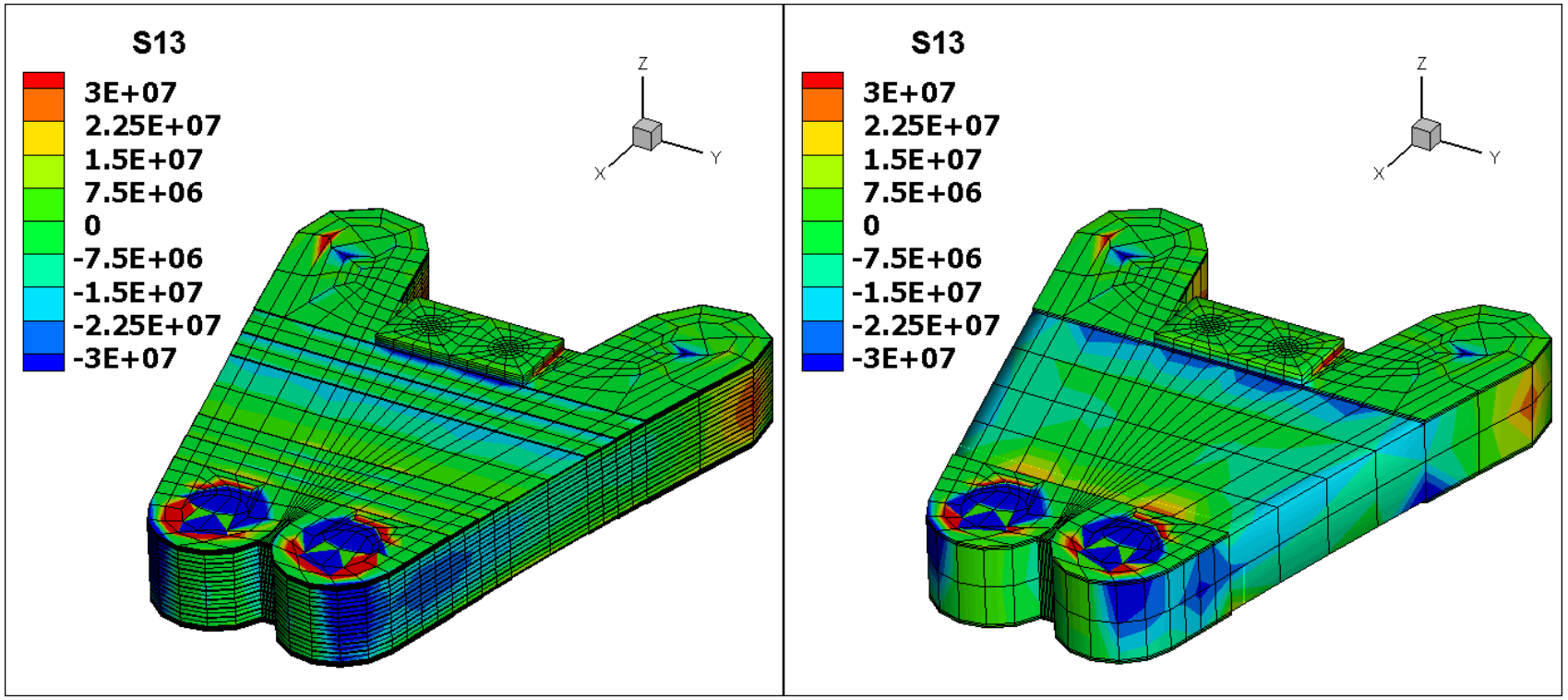

Figure 3-12. Shear stress (in Pa) in the x-z plane for a ply resolved and homogenized TRAM flexbeam due to a static bending load

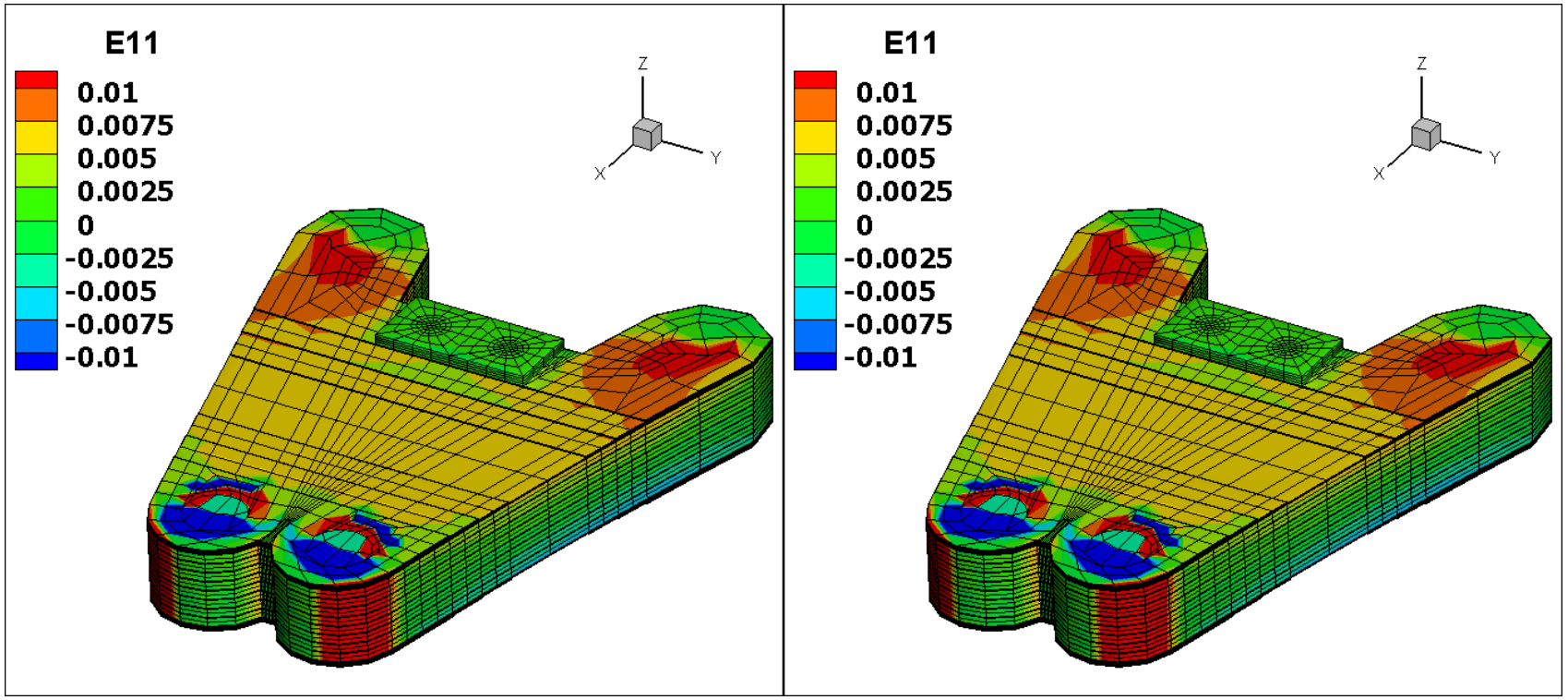

Figure 3-13. Principle strain (in Pa) in the radial or x-direction for a ply resolved and homogenized TRAM flexbeam due to a static bending load

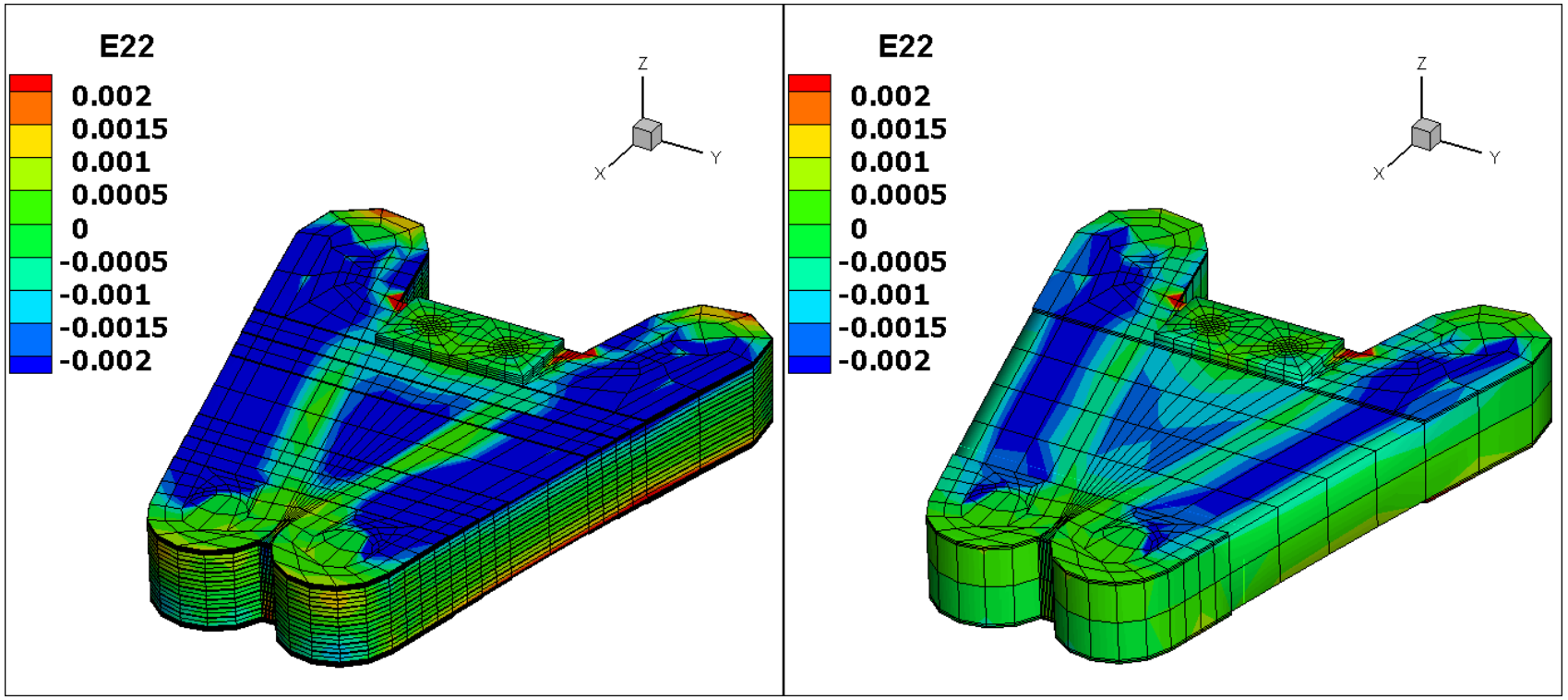

Figure 3-14. Principle strain (in Pa) in the lagwise or y-direction for a ply resolved and homogenized TRAM flexbeam due to a static bending load

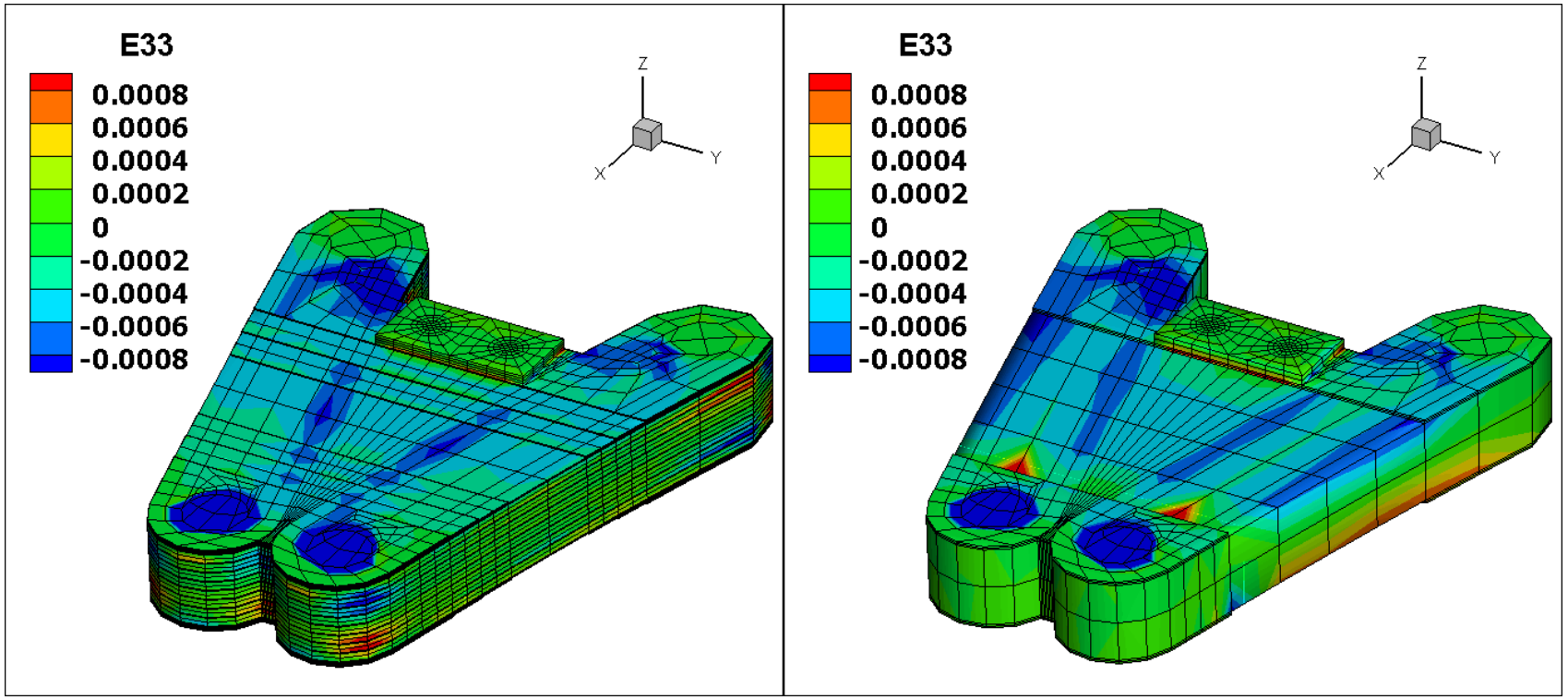

Figure 3-15. Principle strain (in Pa) in the flapwise or z-direction for a ply resolved and homogenized TRAM flexbeam due to a static bending load

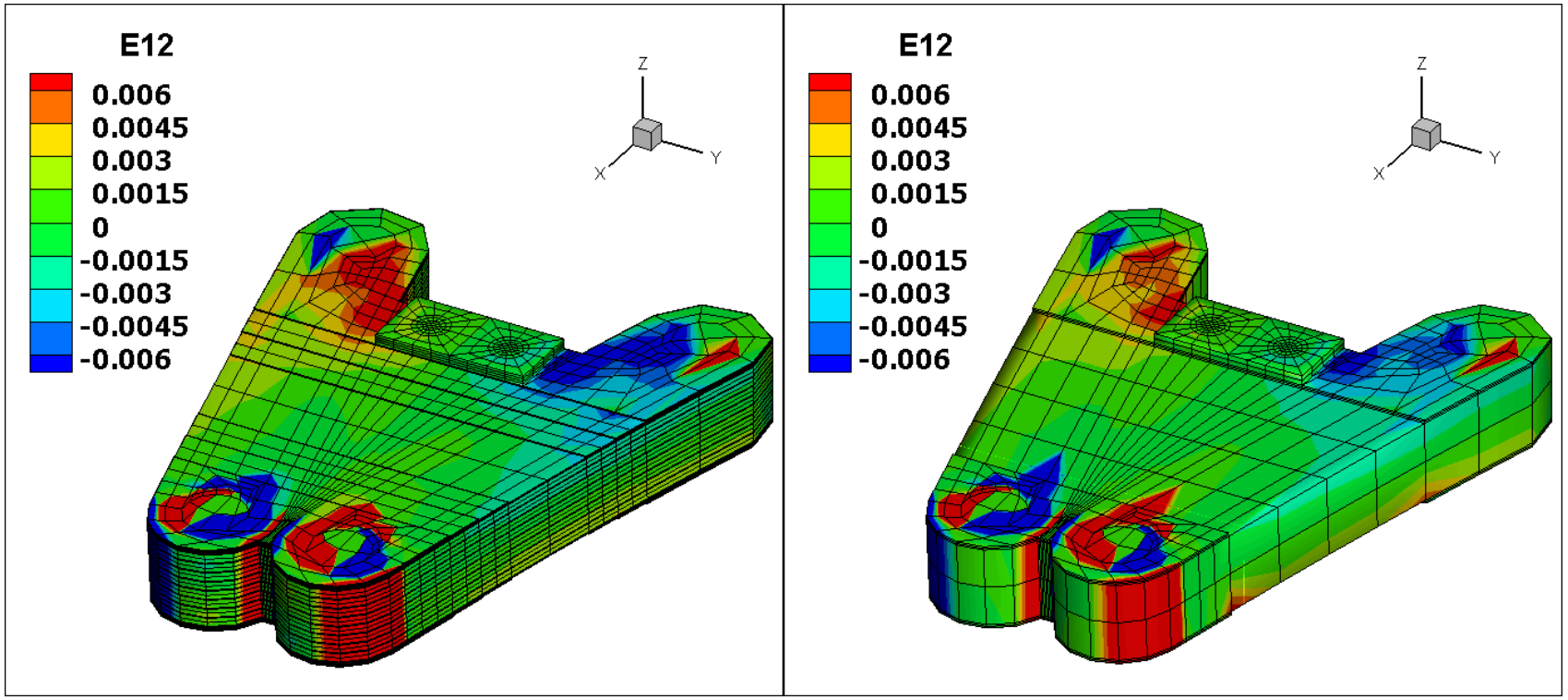

Figure 3-16. Shear strain (in Pa) in the x-y plane for a ply resolved and homogenized TRAM flexbeam due to a static bending load

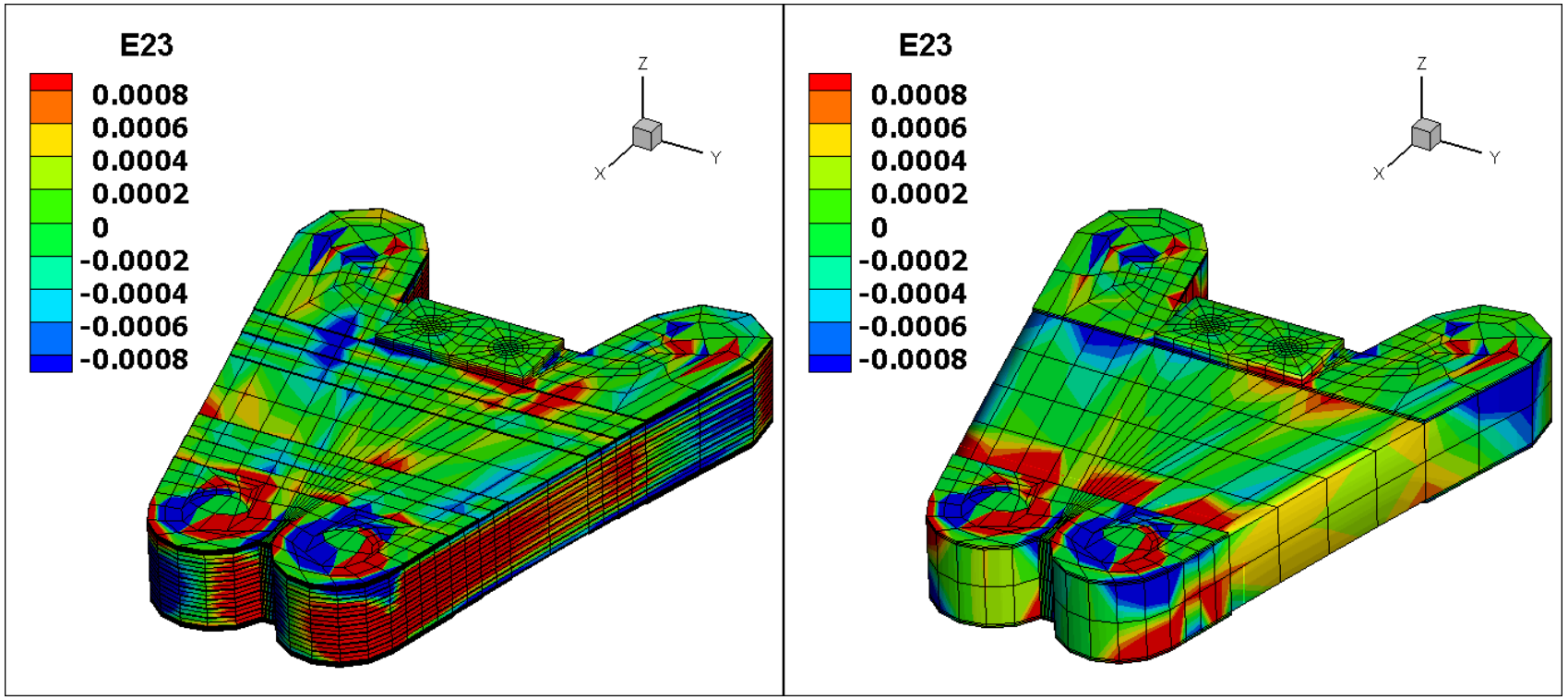

Figure 3-17. Shear strain (in Pa) in the y-z plane for a ply resolved and homogenized TRAM flexbeam due to a static bending load

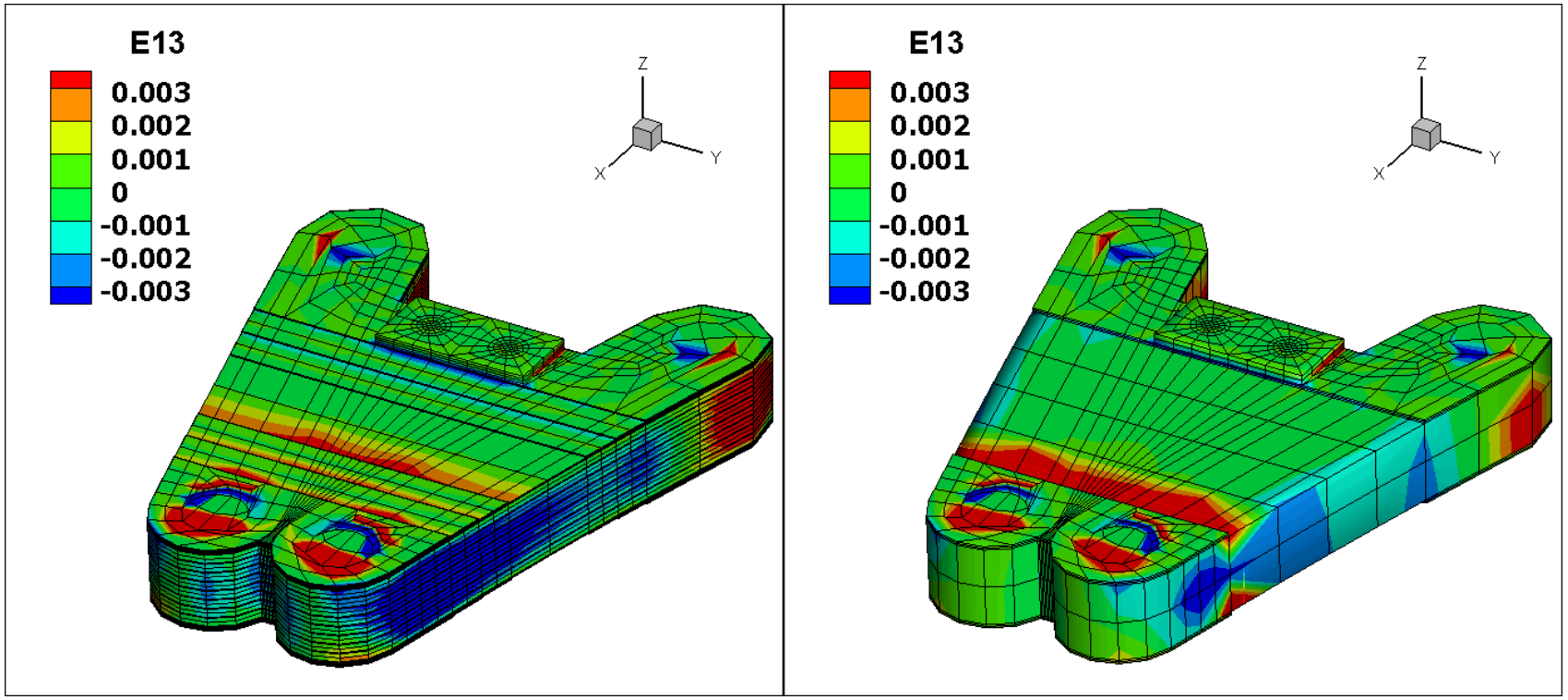

Figure 3-18. Shear strain (in Pa) in the x-z plane for a ply resolved and homogenized TRAM flexbeam due to a static bending load

3.3 Stress/Strain Analysis

Calculation of stresses and strains was also evaluated before launching into the analysis of morphing rotors. To demonstrate this, two examples were considered: a simple, rectangular-section, cantilevered beam subject to a tip shear force, and the Chandra-Chopra box beam.

3.3.1 80 Ply Cantilevered Beam

For this problem, a short, thick, rectangular cantilevered beam made up of 80 plies was considered. Here the orthotropic plies are arranged in the 4 layer pattern $[-45°/+45°/0°/90°]$, repeating 10 times, mirrored about the centerline. The dimensions of this beam are listed in Table 3-2. This beam was cantilevered and subjected to a 1 lb tip vertical force (unit shear force) in the z-direction.

Table 3-2. 80 ply beam dimensions

	MINIMUM DIMENSION (IN.)	*MAXIMUM DIMENSION (IN.)*	
X-AXIS	0	5	$x = 5.0$
Y-AXIS	-0.125	0.125	$b = 0.5$
Z-AXIS	-0.5	0.5	$h = 1.0$

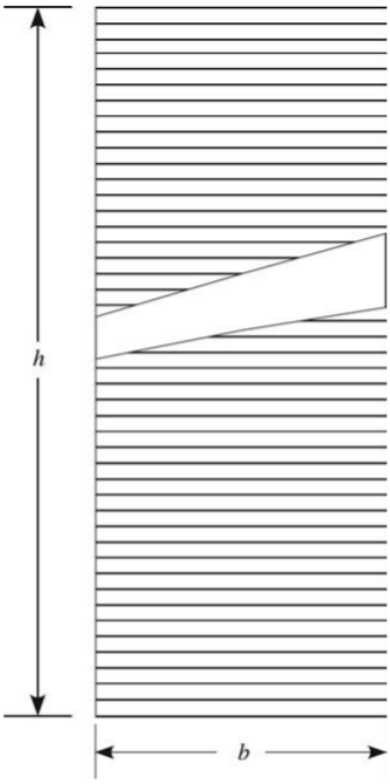

Figure 3-19. Schematic of 80 ply rectangular beam cross section

The mesh created for this problem modeled every single ply in this beam and contained Figure 3-20 and Figure 3-21 show the stress components, σ_{13} and σ_{12} respectively, through the beam thickness at the midspan of the beam ($x = 2.5$ in) compared to ANSYS results. It can be seen here that the transverse shear stress σ_{12} is nearly indistinguishable from the ANSYS results. The transverse shear stress σ_{13} is shown to be slightly overpredicted, but by a margin of less than 2%. These results are on par with the results obtained from VABS (see [28]) and shows that X3D agree with other detailed analysis tools. Additionally, Figure 3-21 shows that the simplification of the beam into 10 elements (each element representing 8 plies with an associated homogenized material definition) provides very similar results, slightly overpredicting the magnitude of σ_{13} but capturing the proper distribution trend.

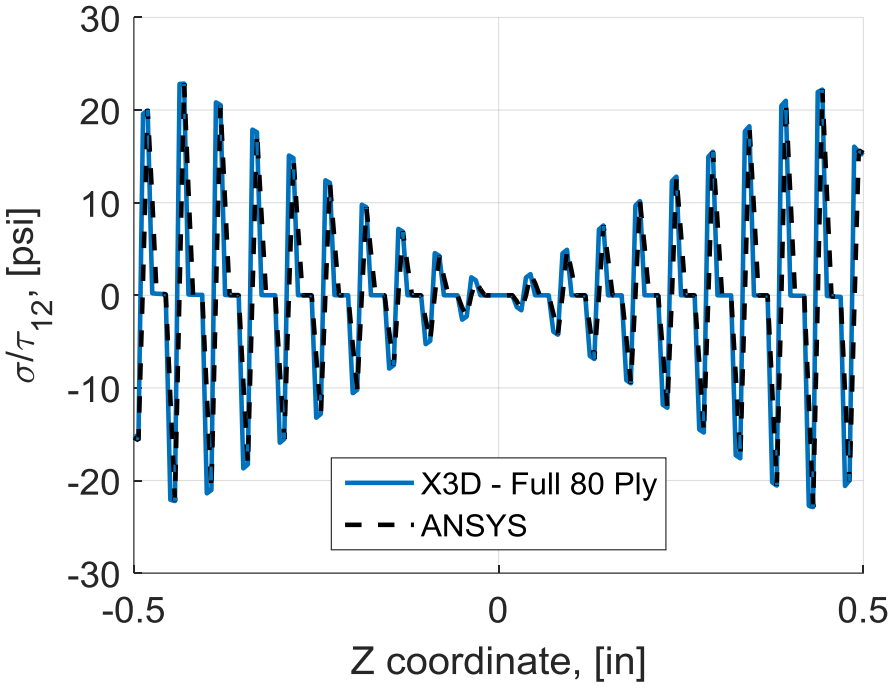

Figure 3-20. Transverse shear stress σ_{12} of an 80 ply beam through the thickness, at midspan

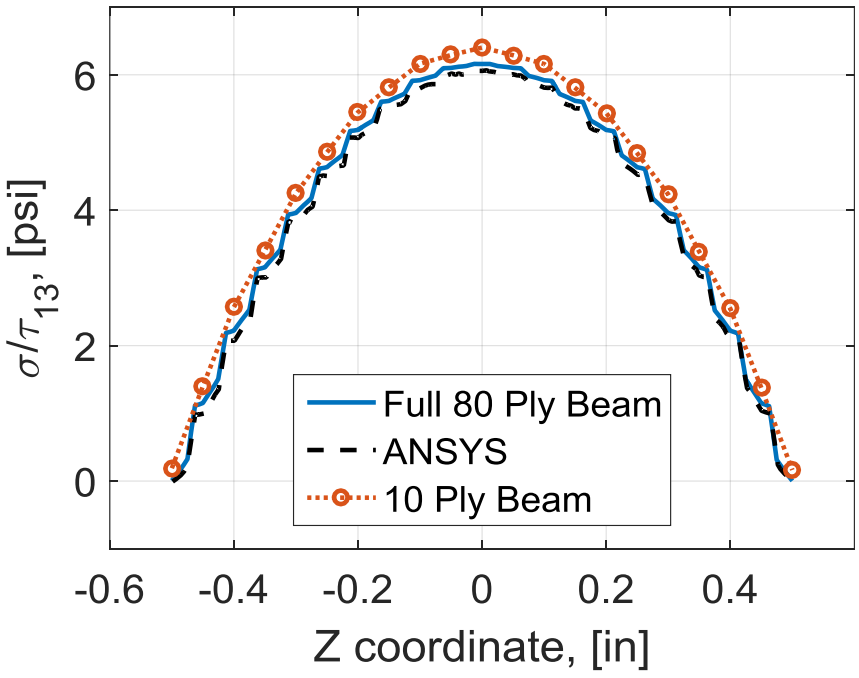

Figure 3-21. Transverse shear stress σ_{13} of an 80 ply beam through the thickness, at midspan

3.3.2 Chandra-Chopra Box Beam

One of the current limitations to using X3D is that the calculated stresses and strains are in the global beam axis. However, when considering composite materials, it is more important to consider the stresses and strains along the fiber direction (the fiber or material axis), to be indicated here by the prime superscript. In this section we consider the same Chandra-Chopra box beam that was defined in 3.2.1. For the box beam considered in this example, we consider the same six-layer webs and sides as before.

The transformation relationships for the strains and stresses from the global axis to the fiber axis are given in Equations 3-7 and 3-8, respectively.

$$\begin{Bmatrix} \varepsilon_{x'} \\ \varepsilon_{y'} \\ \gamma_{x'y'} \end{Bmatrix} = \begin{bmatrix} c^2 & s^2 & cs \\ s^2 & c^2 & -cs \\ -2cs & 2cs & c^2 - s^2 \end{bmatrix} \begin{Bmatrix} \varepsilon_x \\ \varepsilon_y \\ \gamma_{xy} \end{Bmatrix} \tag{3-7}$$

$$\varepsilon'_x = \varepsilon_x \cos^2(\theta) + \varepsilon_y \sin^2(\theta) + \gamma_{xy} \sin(\theta)\cos(\theta)$$

$$\varepsilon'_y = \varepsilon_x \sin^2(\theta) + \varepsilon_y \cos^2(\theta) - \gamma_{xy} \sin(\theta)\cos(\theta)$$

$$\gamma_{x'y'} = 2(\varepsilon_y - \varepsilon_x)\sin(\theta)\cos(\theta) + \gamma_{xy}[\cos^2(\theta) - \sin^2(\theta)]$$

where $c = \cos(\theta)$ and $s = \sin(\theta)$

$$\begin{Bmatrix} \sigma_{x'} \\ \sigma_{y'} \\ \tau_{x'y'} \end{Bmatrix} = \begin{bmatrix} c^2 & s^2 & 2cs \\ s^2 & c^2 & -2cs \\ -cs & cs & c^2 - s^2 \end{bmatrix} \begin{Bmatrix} \sigma_x \\ \sigma_y \\ \tau_{xy} \end{Bmatrix} \tag{3-8}$$

$$\sigma'_x = \sigma_x \cos^2(\theta) + \sigma_y \sin^2(\theta) + 2\tau_{xy} \sin(\theta)\cos(\theta)$$

$$\sigma_y' = \sigma_x \sin^2(\theta) + \sigma_y \cos^2(\theta) - 2\tau_{xy} \sin(\theta)\cos(\theta)$$

$$\tau_{x'y'} = (\sigma_y - \sigma_x)\sin(\theta)\cos(\theta) + \tau_{xy}[\cos^2(\theta) - \sin^2(\theta)]$$

Six different meshes were created. As indicated in Table 3-3, three used homogenized material definitions (1, 2, and 3 plies through the wall thickness), and three were fully resolved (6, 12, and 18 plies through the wall thickness). This was done to determine if homogenization significantly affected the ply resolved stresses and strains and to see if a finer mesh (more than one element through a single ply's thickness) is required to converge to a final solution. Figure 3-23 and Figure 3-24 show all 6 stresses and strains, respectively, for all six box beam meshes at 50%R through the top web's center thickness, as indicated in Figure 3-22.

Table 3-3. Total nodes and elements for Chandra-Chopra beams designed for stress/strain validation

Plies through spar thickness	Nodes	Elements
1	2952	240
2	7872	800
3	11808	1280
6	23616	2720
12	47232	5600
18	70480	8480

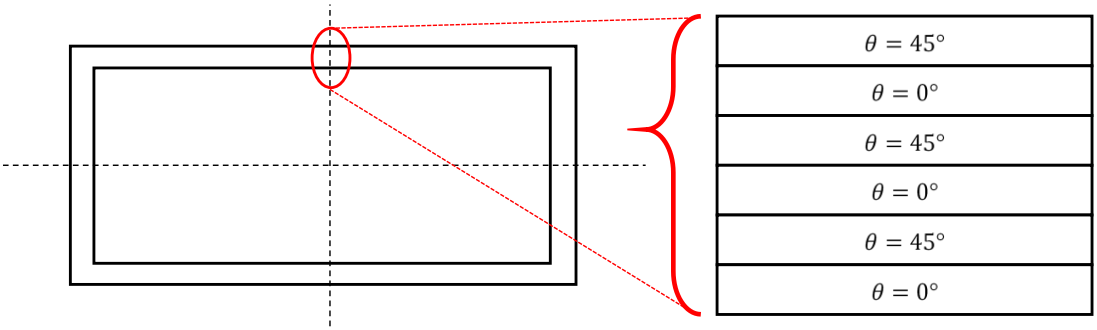

Figure 3-22. Location of plotted stresses and strains

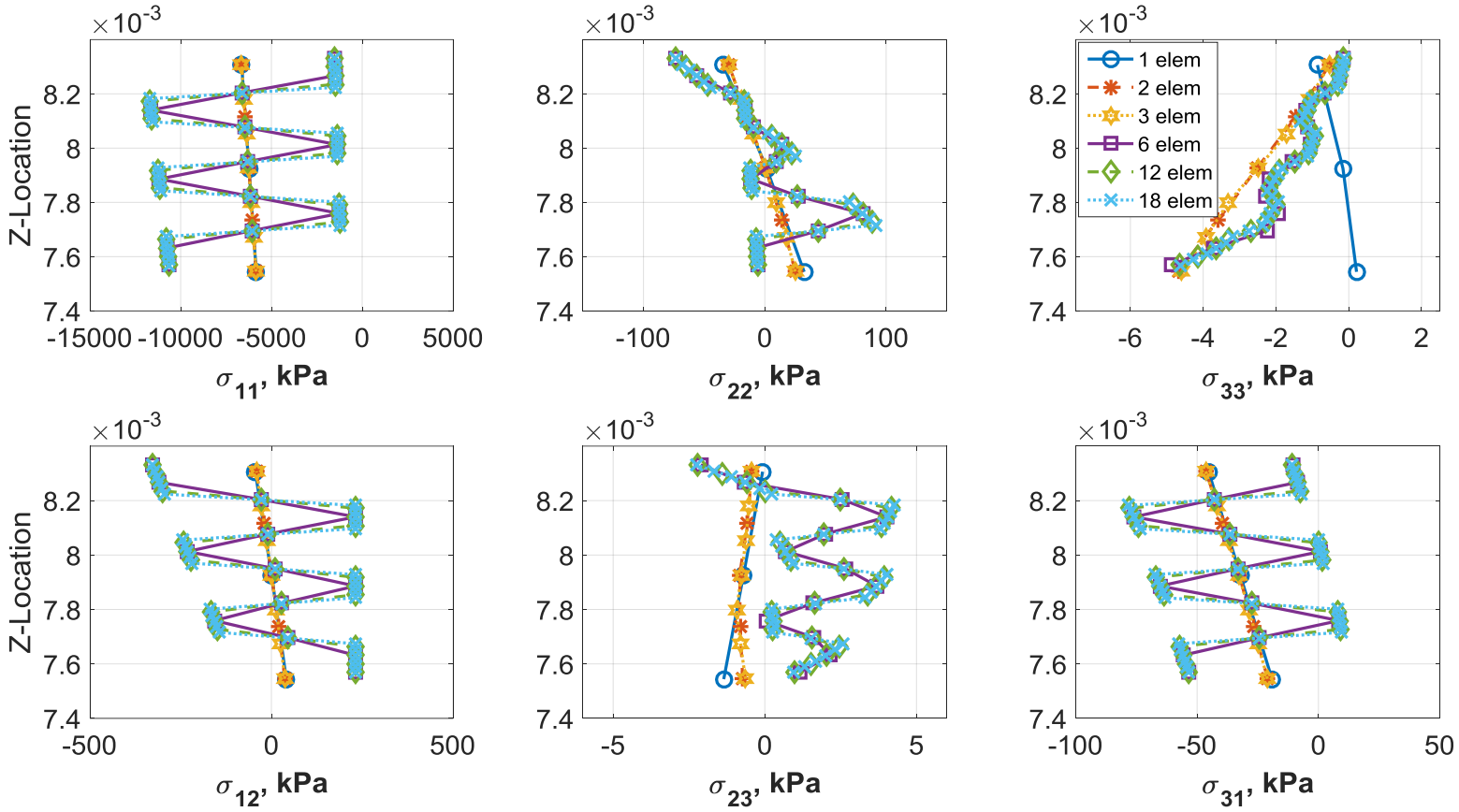

Figure 3-23. Global stresses for Chandra-Chopra box beam with alternating layers of 0° and 45° oriented composite material at 50%R and the center, top flange due to a unit axial tip load

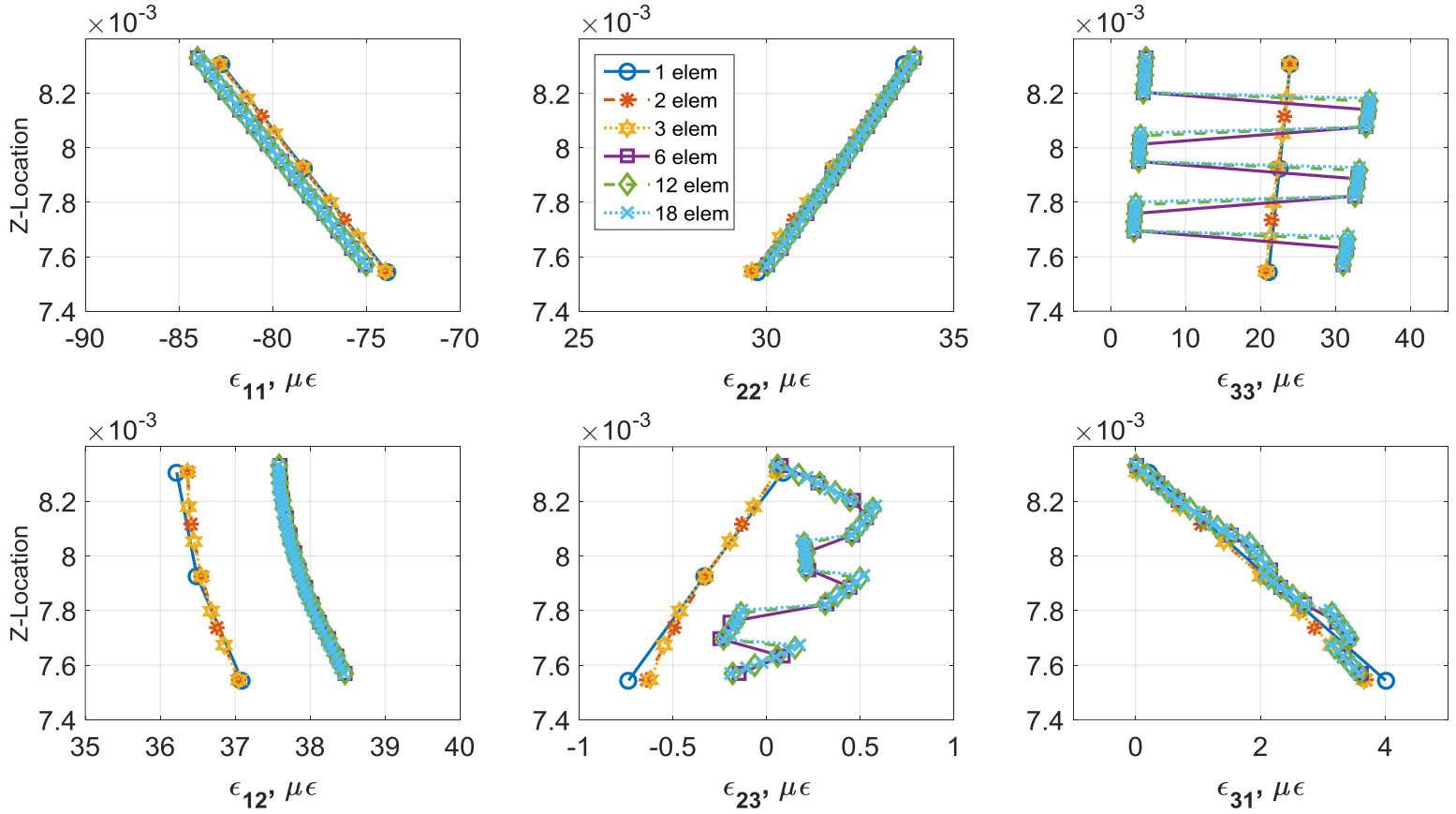

Figure 3-24. Global strains for Chandra-Chopra box beam with alternating layers of 0° and 45° oriented composite material at 50%R and the center, top flange due to a unit axial tip load

As with the flexbeam example, it can be seen that regardless of the material resolution (homogenized or ply resolved) the stresses and strains follow the same general trends. The differences between the homogenized and ply resolved results are small enough that we have confidence in the dynamic stresses and strains calculated as a part of the final rotor calculation. Additionally, resolving the mesh more than the thickness of an individual ply does not change the solution to any significant degree. This is an advantage of second order elements with internal nodes.

The stresses and strains can be transformed to the fiber axis. Figure 3-25 and Figure 3-26 show the strain in the principle fiber directions (ε_{11} and ε_{22}) based on Equation 3-7. Because the factors contributing to the fiber oriented strains ($\varepsilon_x, \varepsilon_y, \gamma_{xy}$) are nearly identical for all six meshes, the fiber oriented strains ($\varepsilon'_x, \varepsilon'_y, \gamma'_{xy}$) fall within the same range of strains. In fact, the maximum and minimum strains shown in Figures 3-23 and 3-24 are practically identical, regardless of mesh size. This is important as the allowable tensile and compressive strains of a composite material are based on fiber orientation. This shows that homogenization does not lead to a loss in strain information.

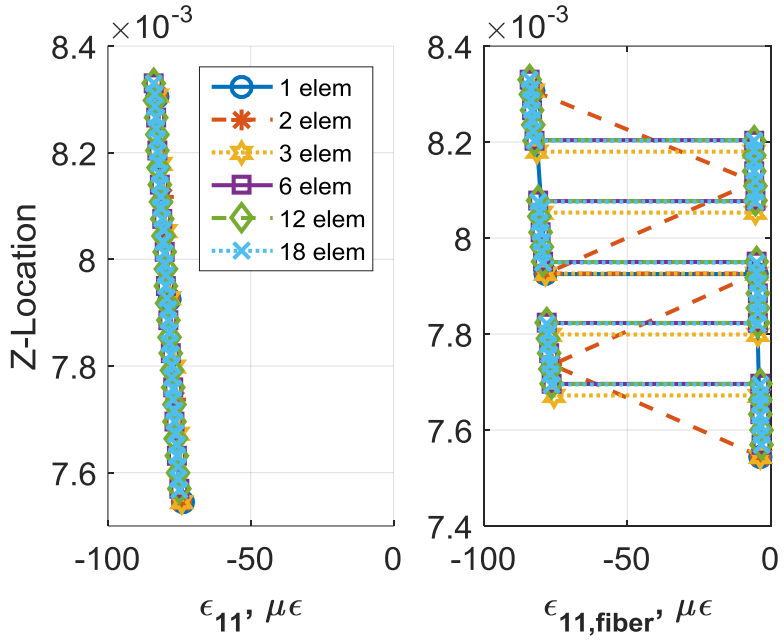

Figure 3-25. Strain in the global radial axis compared to strain in the fiber orientation

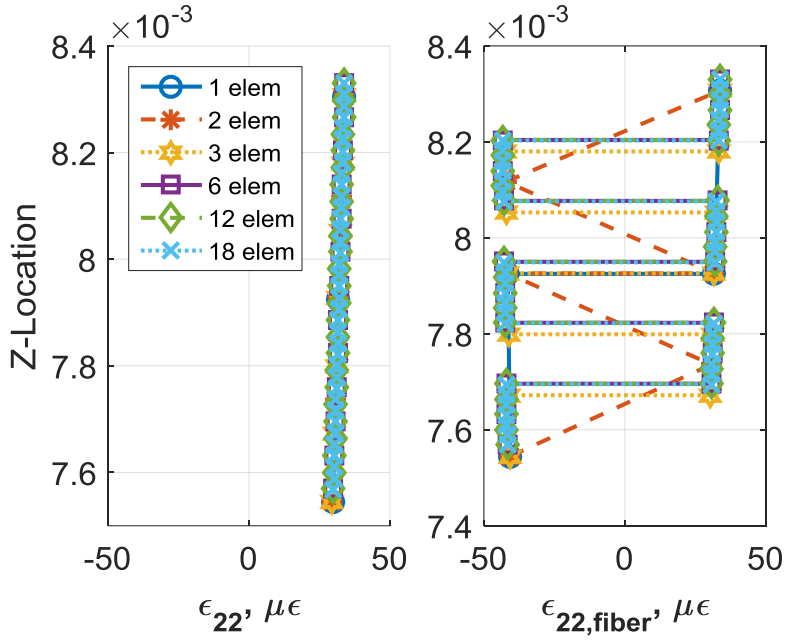

Figure 3-26. Strain in the global lag axis compared to strain in the transverse fiber orientation

Chapter 4: Rotor Modeling

Special care was taken to model a rotor in 3-D elements. For the structure, three different rotor meshes were constructed (with one, three, and four plies through the spar) to represent several composite layup schemes. Five different material models were considered for the rotor spar:

1. Titanium
2. Uncoupled (quasi-isotropic) composite (balanced structure)
3. Nominally (extension-torsion) coupled composite
4. Hygrothermally stable Winckler layup composite
5. Hygrothermally stable Haynes layup composite

4.2 Baseline Structural Model

An idealized UH-60A-like blade with a titanium box-beam-like spar was used for the baseline rotor model, identical to that validated in Reference [99]. The model matches the first three modes of the UH-60A blade exactly and the next three modes approximately at the operating RPM (hover) of 258 (27 rad/s). The model has the UH-60A aerodynamic geometry based on the data provided in the NASA Ames Master Database [100]. The rotor model is treated as fully articulated with a coincident flap and lag hinge located at 4.66%R,

a non-linear built in twist of $-16°$, and a tip sweep in the outer 6.9% of the blade span reaching a maximum of $20°$ at 94.5%R. The rotor has four identical blades with a total rotor solidity of $\sigma = 0.0826$. For the trim solution, only one blade needs to be modeled. The torque offset is included.

Only the internal construction is idealized: a rectangular spar is used (based on public domain drawings). The geometric profile is kept SC1095 throughout (the aerodynamic modeling accounts for SC1094 R8 from 49-82%R). The inner profile is also consistent throughout, so it has the same mass per length and stiffness properties only twisted about its beam axis. The locus of the beam axis (along the ¼ chord line) is described precisely in the model.

The spar is the box-beam-like section in Figure 4-1 and is the only part of the blade where composite material properties were applied, when the blade is modified. For the modified blades, the baseline titanium spar was replaced with IM7/8552 graphite-epoxy oriented in either an uncoupled or a coupled layup. Although composite material weighs significantly less than titanium, the blade mass and CG were kept constant through the addition of weight in the front and rear webs. The elements defining the webs were not altered; their material density was increased to account for weight balance. This maintained uniform mass and c.g. properties between models, but changed the moments of inertia. The total blade mass is always kept constant, regardless of the spar's material. With total mass and c.g. remaining constant, with the c.g. ahead of the quarter-chord line, and torsion frequency not altered drastically, the aeroelastic stability is not expected to change.

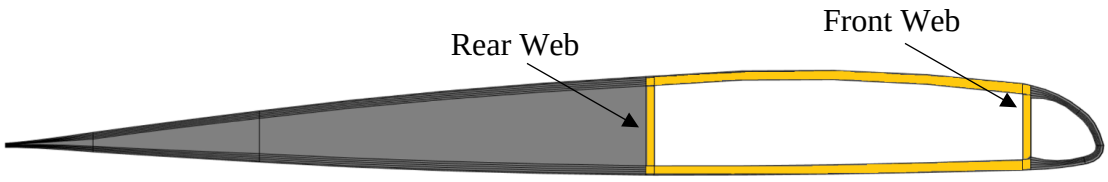

Figure 4-1. Idealized UH-60A blade cross section with highlighted spar

The baseline (titanium spar) rotor model was validated with experimental results from a full-scale, slowed RPM, UH-60A rotor tested in the Ames high-μ, 40 ft x 8ft full-scale wind tunnel in 2010 [78].

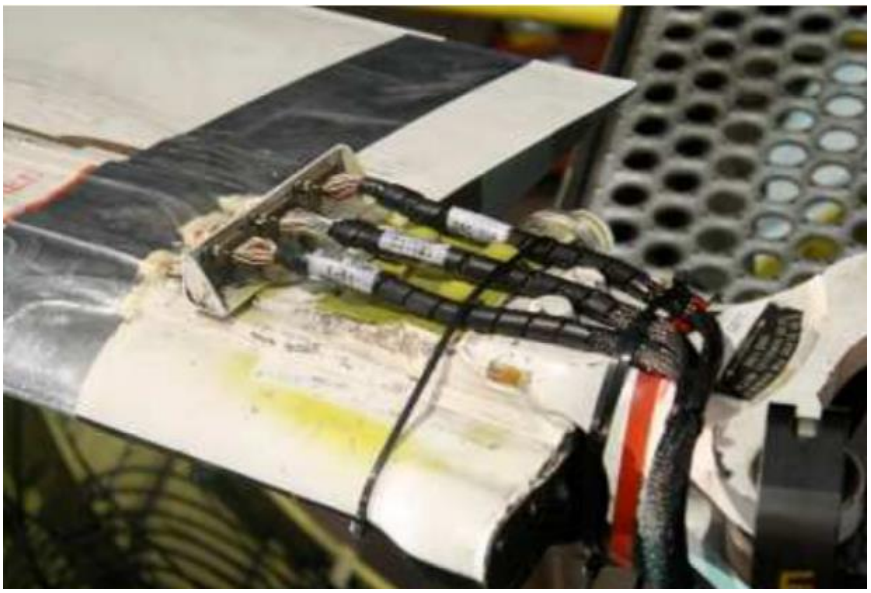

Figure 4-2. UH-60A instrumented blade shank

4.3 Aerodynamic Model

The aerodynamic model has no assumptions and is the same for all cases presented in this dissertation. The exact geometry and airfoil decks are included. The blade is made up of two airfoils: SC1095 from 20-49%R and 82-100%R, and SC1094 R8 from 49-82%R.

Between 8-20%R, there are no airfoils; this area is considered the blade shank. Special consideration is needed to model this shank particularly in high advance ratio regimes where this shank provides a significant amount of drag. Validation at high-μ required careful consideration of the highly instrumented blade root end, or the shank, shown in Figure 4-2.

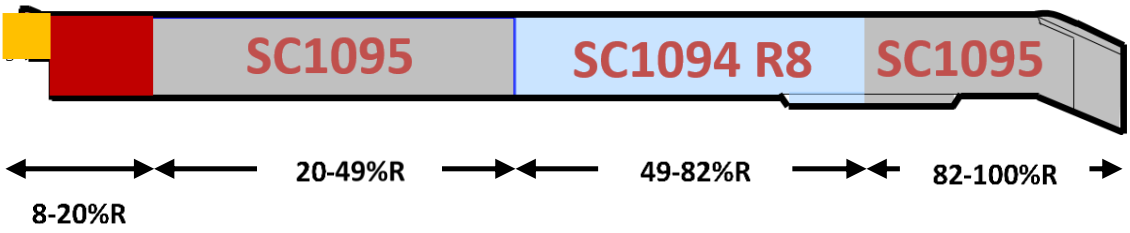

Figure 4-3. Distribution of airfoils along rotor span

The blade shank is an unfaired drag producing structure extending from 8-13%R, with a transition to blade airfoils from 13-20%R. The nominal blade airfoils were shown in Figure 4-3. The shank has been accounted for in the analysis by a correction to the drag table of the nominal SC1095 airfoil.

Contemporary analyses report significant deficiencies in predicted performance without the use of a shank drag correction. However, the magnitude of the corrections are ad hoc and depend strongly on the comprehensive code. Yeo [101] used a shank drag coefficient of 0.4 for 8-13%R and 0.02 for 13-20%R to match measured performance at high-μ. Ormiston [102] assigned a drag coefficient of 1.5 across both segments. Potsdam modeled the blade shank using a first principles approach (CFD) which resulted in a drag coefficient between 0.14-0.18, however drag on the non-aerodynamic blade could not be

calculated [103]. The current analysis found that a shank drag coefficient of 0.75 across both segments provided good correlation of rotor efficiency at the highest advance ratio: $\mu = 1.0$. Figure 4-4 shows the predicted and measured rotor efficiency, L/D_e, compared at different thrust levels. Rotor efficiency, L/D_e, is defined by Equation 1 and assumes zero shaft angle ($C_L = C_T$ and $C_X = -C_H$). The L/D_e match well at high advance ratios and acceptably at low advance ratios. However, the analysis consistently over-predicts the maximum L/D_e and the range of C_T/σ before stall experienced by the rotor at all advance ratios.

$$\frac{L}{D_e} = \frac{C_L}{\frac{C_P}{\mu} - C_X} = \frac{C_T}{\frac{C_P}{\mu} + C_H} \tag{1}$$

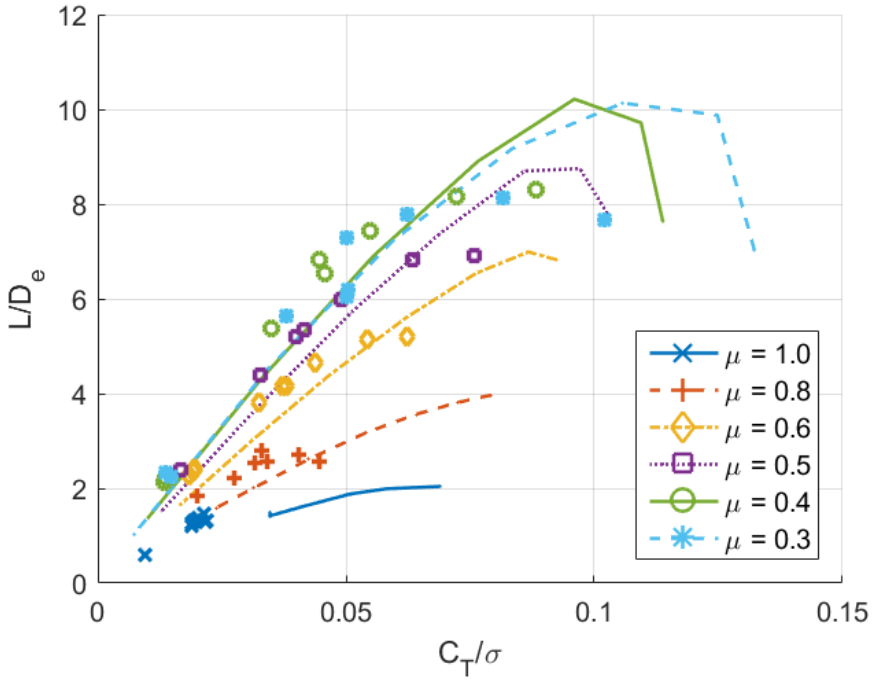

Figure 4-4. Analytical vs. experimental results for rotor efficiency vs. blade loading for a UH-60A rotor with a titanium spar at an RPM of 10.8 rad/s and various advance ratios

Figure 4-5, Figure 4-6, and Figure 4-7 respectively show the prediction of thrust (C_T/σ), drag (C_H/σ), and power (C_P/σ) – the contributing components of L/D_e – varying with collective. The predictions show the correct trends at least up to $\mu = 0.6$ and provide adequate confidence in the aerodynamic model. Note that an exact match is not expected as the rotor is representative only, not an exact model of the UH-60A. The validation ensures the fundamental aeromechanical behavior of a slowed RPM, high μ, articulated rotor is included in the model.

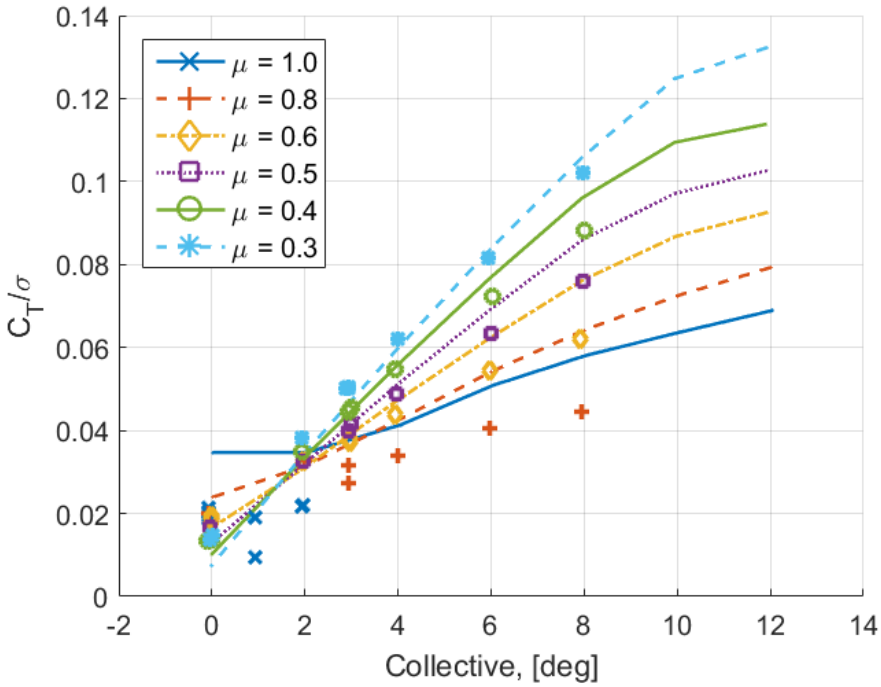

Figure 4-5. Analytical vs. experimental results for C_T/σ as a function of collective for a UH-60A rotor with a titanium spar at an RPM of 10.8 rad/s and various advance ratios

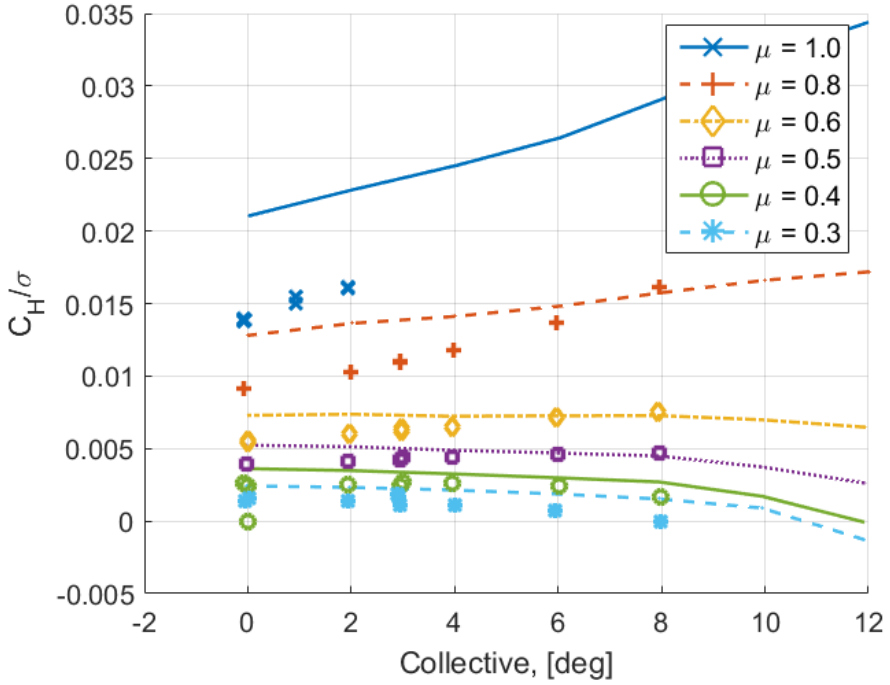

Figure 4-6. Analytical vs experimental results for C_H/σ as a function of collective for a UH-60A rotor with a titanium spar at an RPM of 10.8 rad/s and various advance ratios

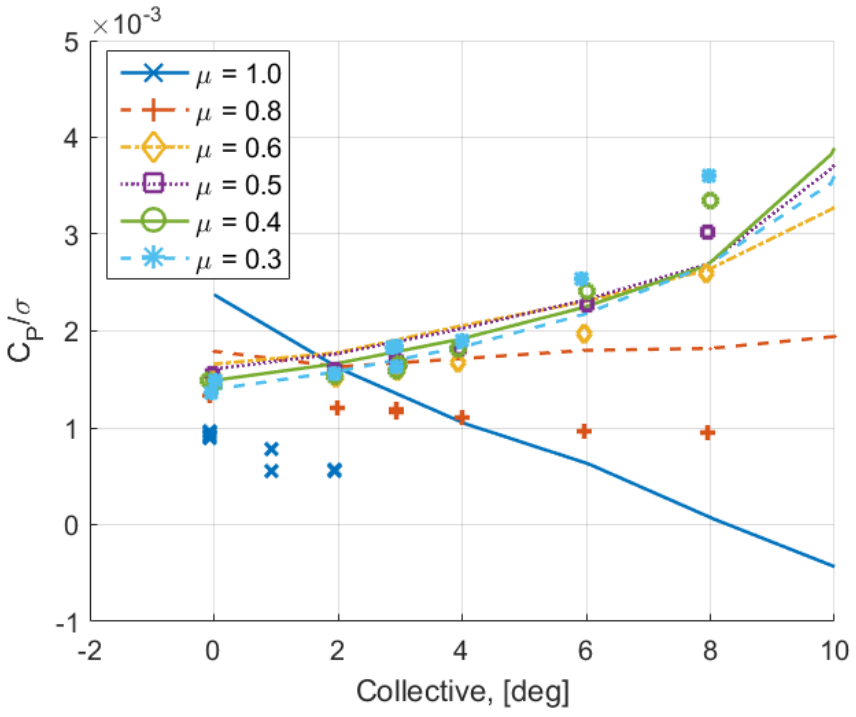

Figure 4-7. Analytical vs. experimental results for C_P/σ as a function of collective for a UH-60A rotor with a titanium spar at an RPM of 10.8 rad/s and various advance ratios

Figure 4-8 shows the top view of the rotor wake over two turns at four different advance ratios: 0.96, 0.8, 0.6, and 0.4. Here it can be seen that at high μ the wake washes backwards by over 10 rotor radii and there is no significant distortion. As the advance ratio is decreased, the distance traveled by the wake significantly decreases to the point where we see at a normal helicopter operating μ=0.4 the wake is only washed back by approximately 5 rotor radii.

Viewing the rotor wake from behind, as in Figure 4-9, and from the side, Figure 4-10, shows more clearly how the rotor wake is distorted based on the operational μ. It is clear from these figures that as the advance ratio decreases, the wake becomes more distorted.

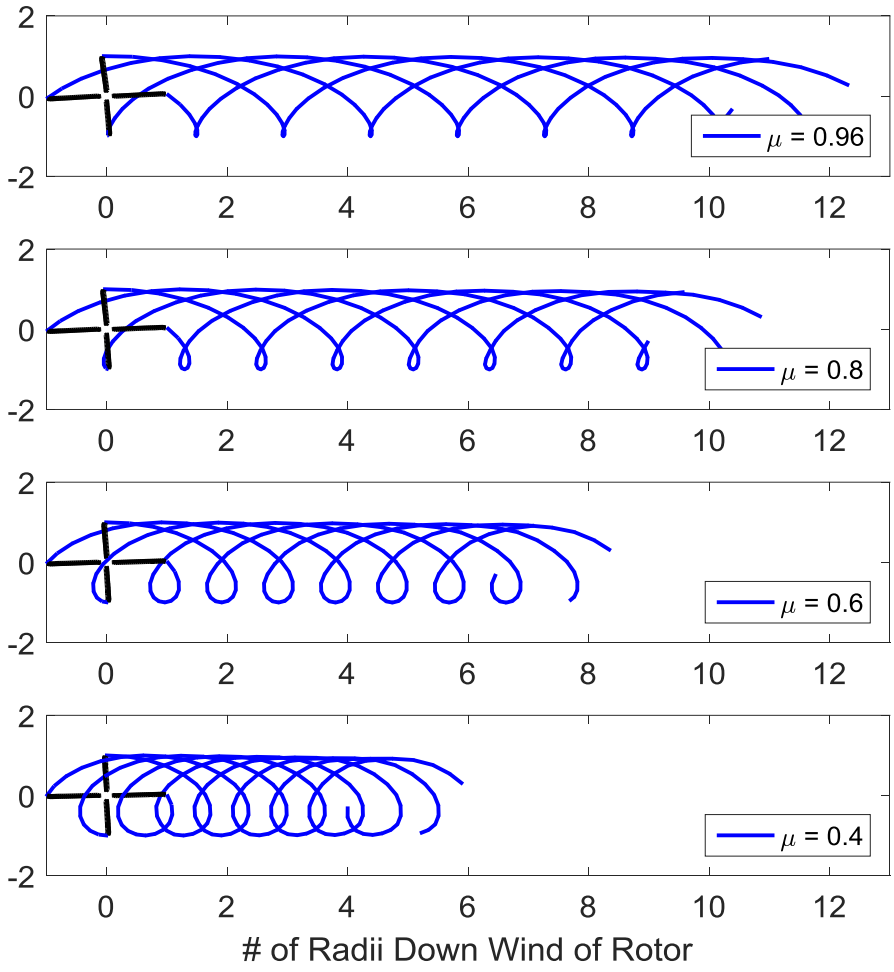

Figure 4-8. Top view of rotor wake trajectory for advance ratios of $\mu = 0.4$ to $\mu = 0.96$

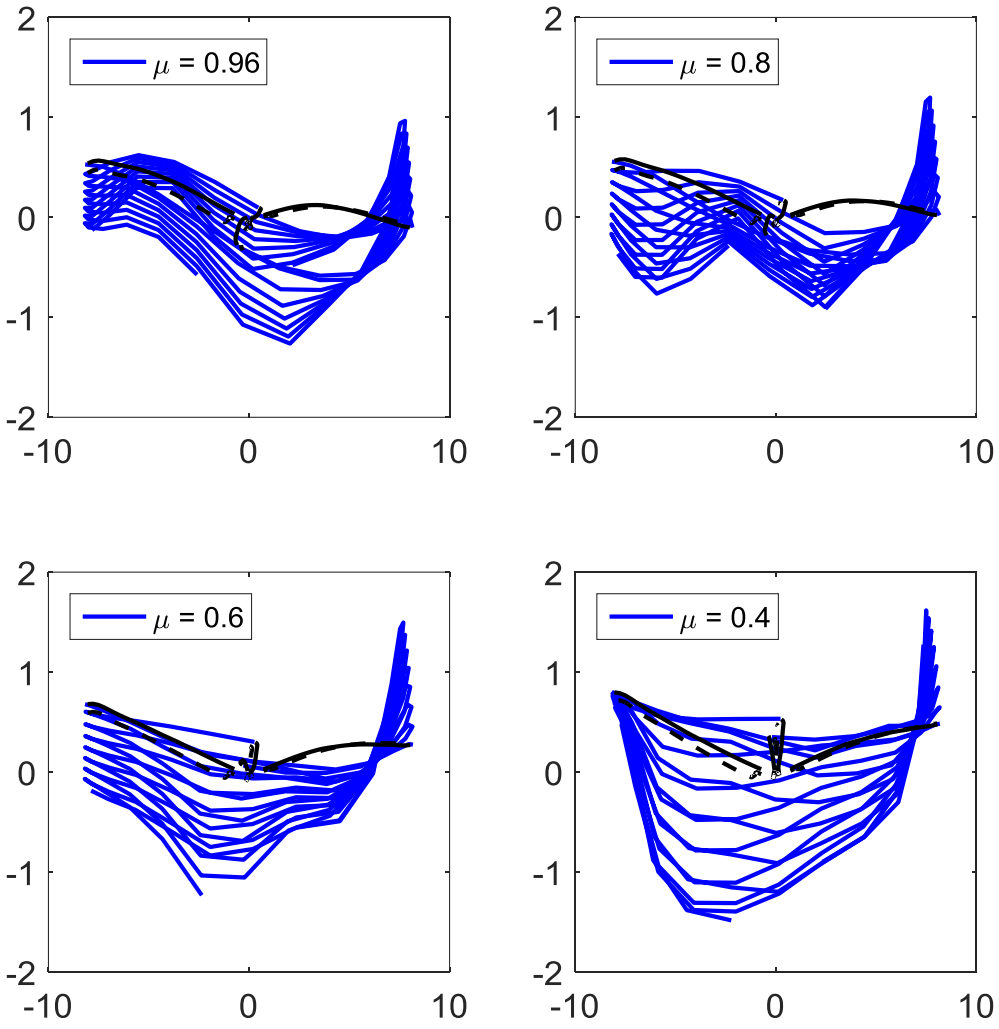

Figure 4-9. Rear view of rotor wake trajectory for advance ratios of $\mu = 0.4$ to $\mu = 0.96$

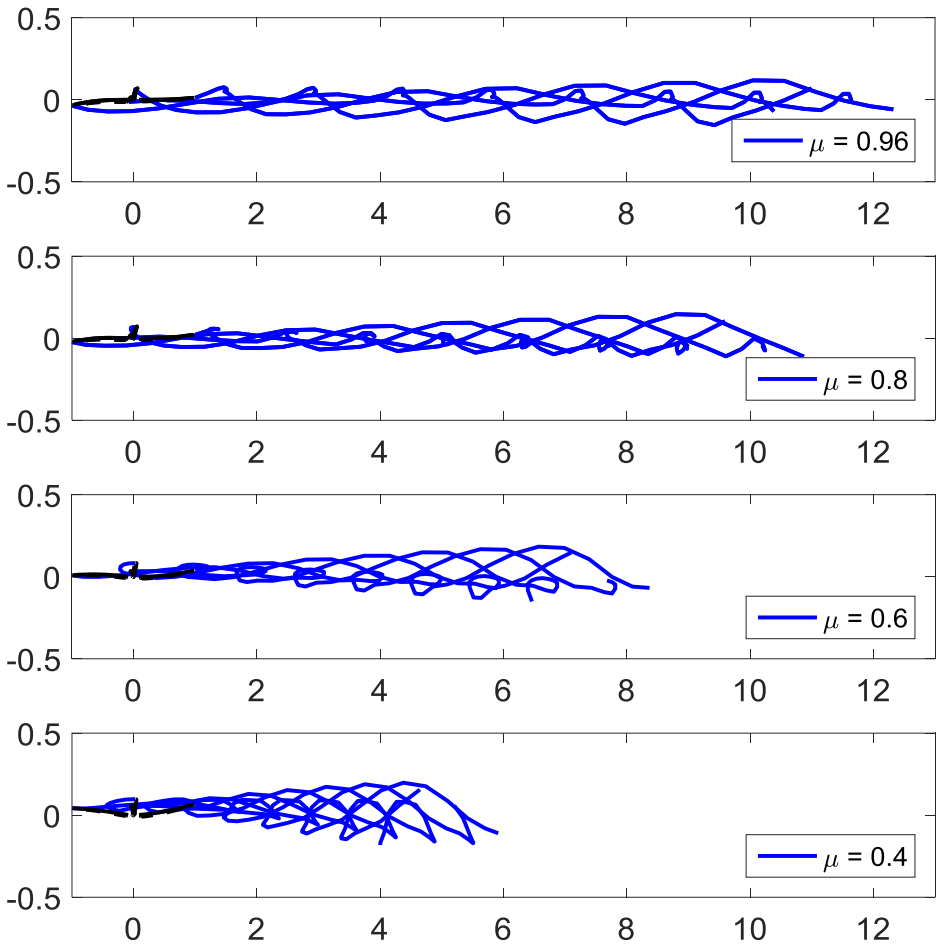

Figure 4-10. Side view of rotor wake trajectory for advance ratios of $\mu = 0.4$ to $\mu = 0.96$

For each case considered in this research, the same computational constants were used. The time step that was chosen for structural and aerodynamic computation was $\Delta\psi = 7.5°$. As can be seen in Figure 4-11 (a) and (b), there are slight differences in the results at time steps larger than 15°, but the results quickly converged as the time steps were reduced. The choice of $\Delta\psi = 7.5°$ was chosen for accuracy as well as speed. Other important inputs were that the induced tip loss factor was set to 1.15, the free-wake model

was initialized using linear inflow for the first two turns, and a single free tip vortex was used, rolling up from 50% radius outboard, with a core size of 0.2 times the tip chord.

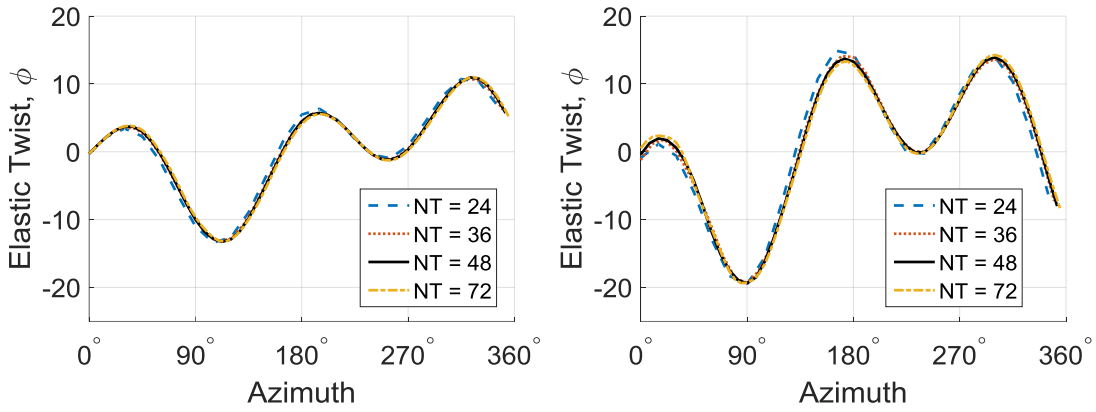

(a) $\mu = 0.3$ (b) $\mu = 1.0$

Figure 4-11. Elastic twist variation due to computational time step for low and high advance ratios

4.4 Composite Layup Designs

In order to down-select to the most effective layup for the rotor model, a simple cross-sectional analysis was used to understand the effect of ply angle on the stiffness properties of the rotor spar. Equation 4-1 shows the linear relationship between axial force and torsion moment and axial strain and rate of elastic twist. For no moments, $M_x = 0$, Equation 4-2 gives the relationship between axial force, F_x, and twist rate, ϕ'. While $K_{1,4}$ represents the extension-torsion coupling, the actual twist produced by a given extension force – the twist sensitivity – is determined also by the torsional stiffness, $K_{4,4}$, that allows the blade to twist, and the extensional stiffness, $K_{1,1}$, that induces twist.

$$\begin{Bmatrix} F_x \\ M_x \end{Bmatrix} = \begin{bmatrix} K_{1,1} & K_{1,4} \\ K_{1,4} & K_{4,4} \end{bmatrix} \begin{Bmatrix} u_e' \\ \phi' \end{Bmatrix} \quad 4\text{-}1$$

$$\phi' = \frac{K_{1,4}}{K_{1,1}K_{4,4} - K_{1,4}^2} F_x \quad 4\text{-}2$$

The composite layups were only applied to the top and bottom flanges of the rotor spar. An uncoupled [0°/90°] layup was applied to the rear and front webs for all blades considered. The first reason for this design choice was to eliminate variations between composite rotors with different layups. Secondly, it was found that introducing an antisymmetric layup to the left and right webs of the spar did not strongly effect the strength of the coupling.

4.4.1 Coarse Mesh

A coarse rotor mesh was used for multiple cases: uncoupled layup, nominally coupled layup, and the homogenized hygrothermally stable layups. For all, each blade cross section contained 37 elements and 177 nodes. The rotor mesh is made up of 16 radial cross sections with a total of 5841 nodes and 592 elements.

4.4.1.1 Uncoupled Composite

In the uncoupled spar all four sides of the spar were built with a homogenized [0°/90°] layup. Because carbon fiber is significantly lighter than titanium, in order to maintain blade mass and c.g. location the material density of the spar webs was artificially increased. Table 4-1 shows what material densities were used on each side of the box beam

spar. The same values used for the spar web density were also used in all other rotor designs, as only the ply angles, not the material, was changed in the top and bottom flanges.

Table 4-1. Material density definitions for the modified composite spar in the UH-60A-like rotor meshes.

	COMPOSITE SPAR DENSITY (KG/M^3)
TRAILING EDGE WEB	23000
LEADING EDGE WEB	23000
TOP FLANGE	1580
BOTTOM FLANGE	1580

Figure 4-12 shows approximately how big the weights would have to be. If tungsten is used, see in Figure 4-12 (d), there is little difference between the current thickness of the spar webs and the increased thickness including the balancing weights. In this work, inclusion of the weight is modeled by simply increasing the density of the spar webs. Note that the increase in weight is not *additional* weight but simply what was required to keep the blade mass the same as the titanium blade and not change the top level inertial properties of the rotor (effecting autorotation index, ground resonance, rotor start-up and shut-down, etc.). This is not a weight penalty, but merely a compensation to bring it back to the baseline.

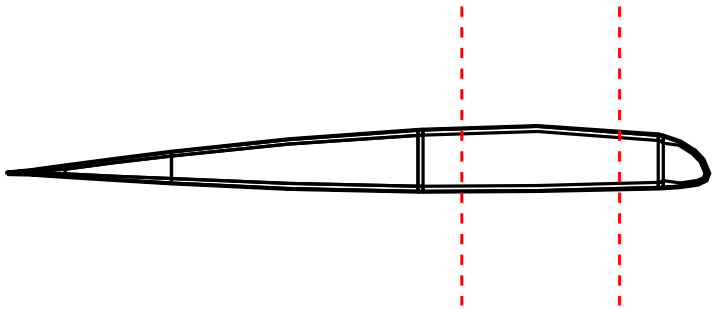

(a) Approximate inner dimension of spar with aluminum balancing weights

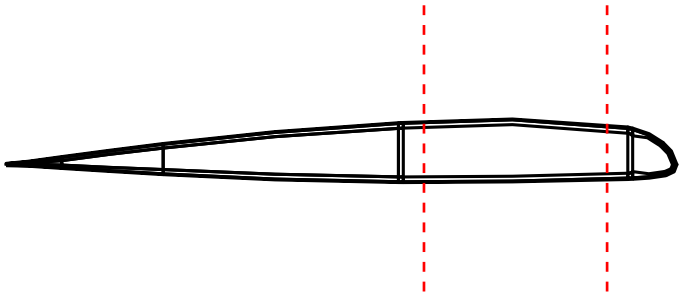

(b) Approximate inner dimensions of spar with titanium balancing weights

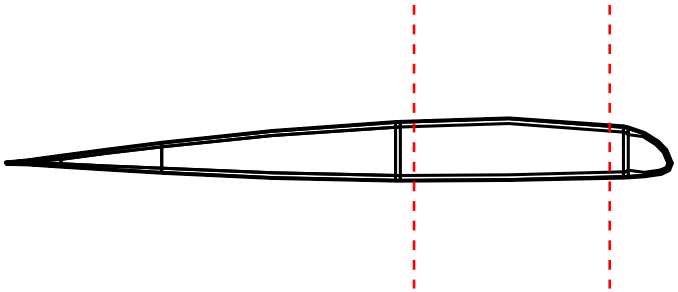

(c) Approximate inner dimension of spar with stainless steel balancing weights

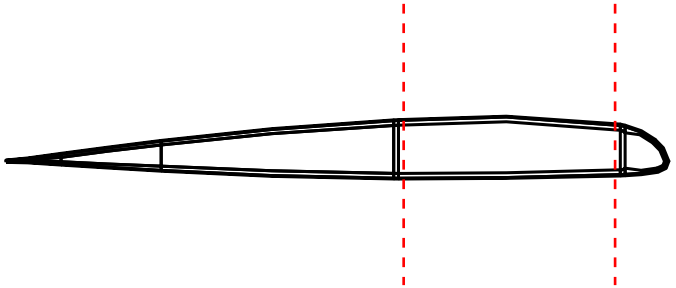

(d) Approximate inner dimensions of spar with tungsten balancing weights

Figure 4-12. Web balancing weights for composite coupled rotor to maintain original blade mass and mass properties

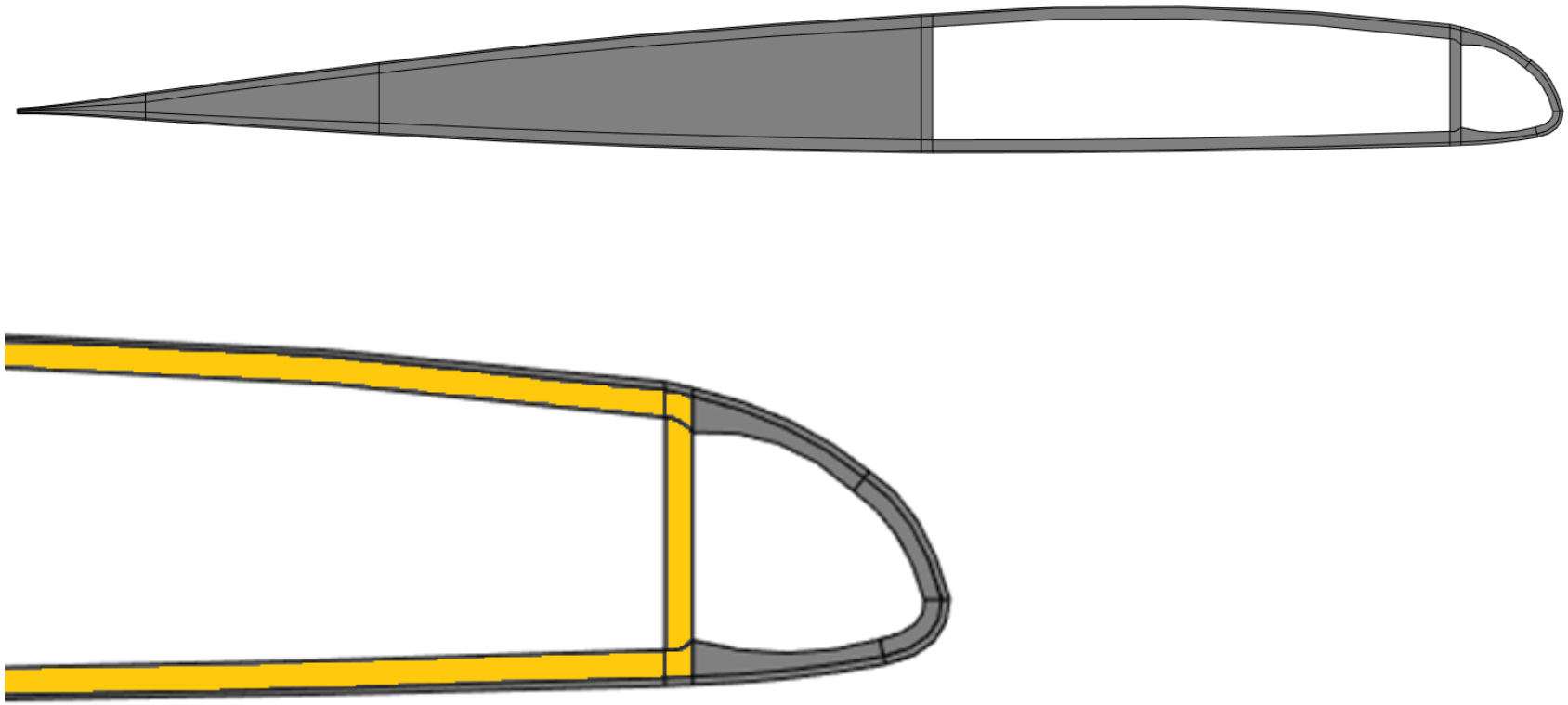

Figure 4-13. Coarsest rotor mesh cross section. Note that there is only one element through the spar thickness.

4.4.1.2 Nominal Coupled Composite

The mesh for the nominal coupled composite rotor is the same as the uncoupled mesh, but with updated material definitions. Rather than a $[0°/90°]$ layup, two different layups were considered based on the experimental work conducted by Chandra and Chopra: $[\theta]_n$ and $[0°/\theta]_n$. To determine which layup should be chosen, a simple study of the effect of ply angle and layup scheme was conducted.

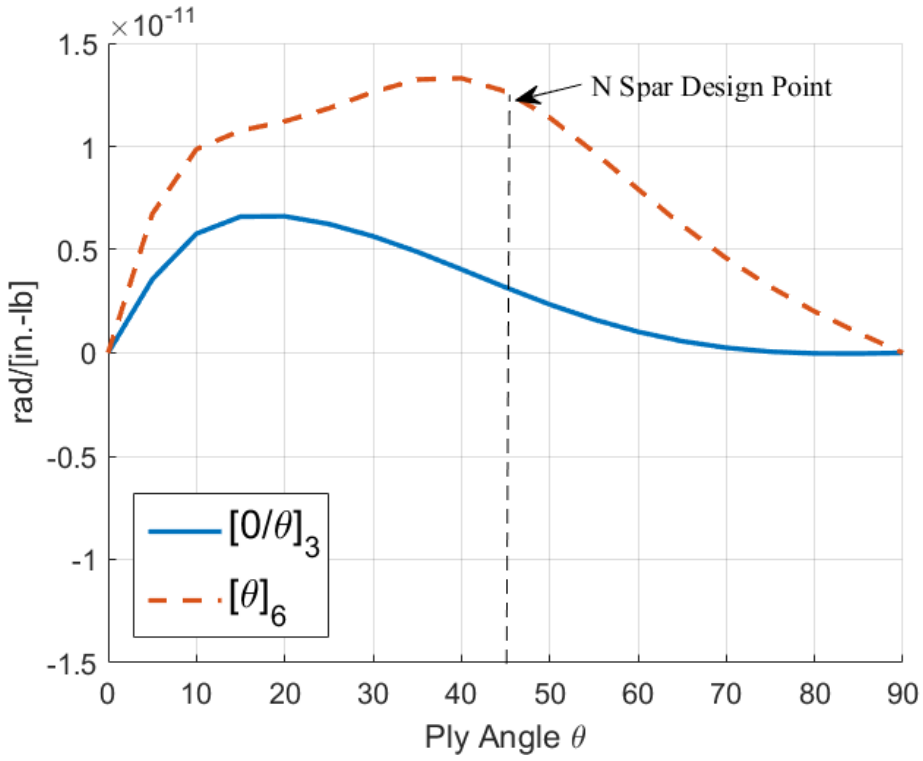

Figure 4-14. Twist sensitivity due to unit axial force as a function of ply angle θ for nominal coupled box beams

Figure 4-14 shows the twist sensitivity (Equation 4-2) for the Chandra-Chopra box beams validated in Figure 3-3 for $\theta = 0$ to 90°. It is clear that the twist sensitivity of all $[\theta]_6$ layups is higher than the mixed $[0°/\theta]_3$ layups – which is why the $[15°]_6$ case

achieved more twist than the $[0°/30°]_3$ or $[0°/45°]_3$ cases. High twist sensitivity is desired for the purpose of this work so a $[\theta]_n$ layup with $\theta = 45°$ was chosen for the rotor spar. This layup is designated as the nominal coupled spar.

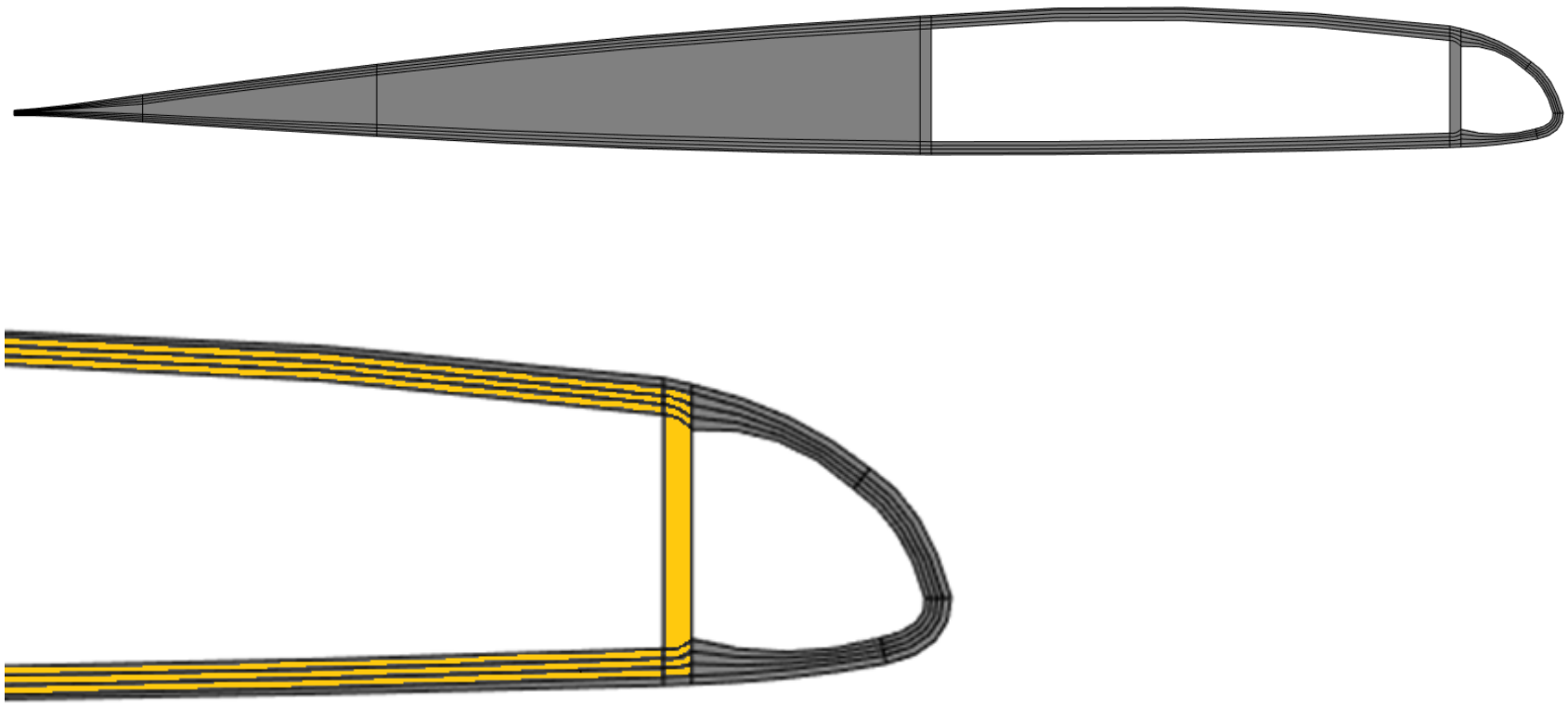

Figure 4-15. Fine rotor mesh cross section for the Haynes layup. Note that there are three elements through the spar thickness.

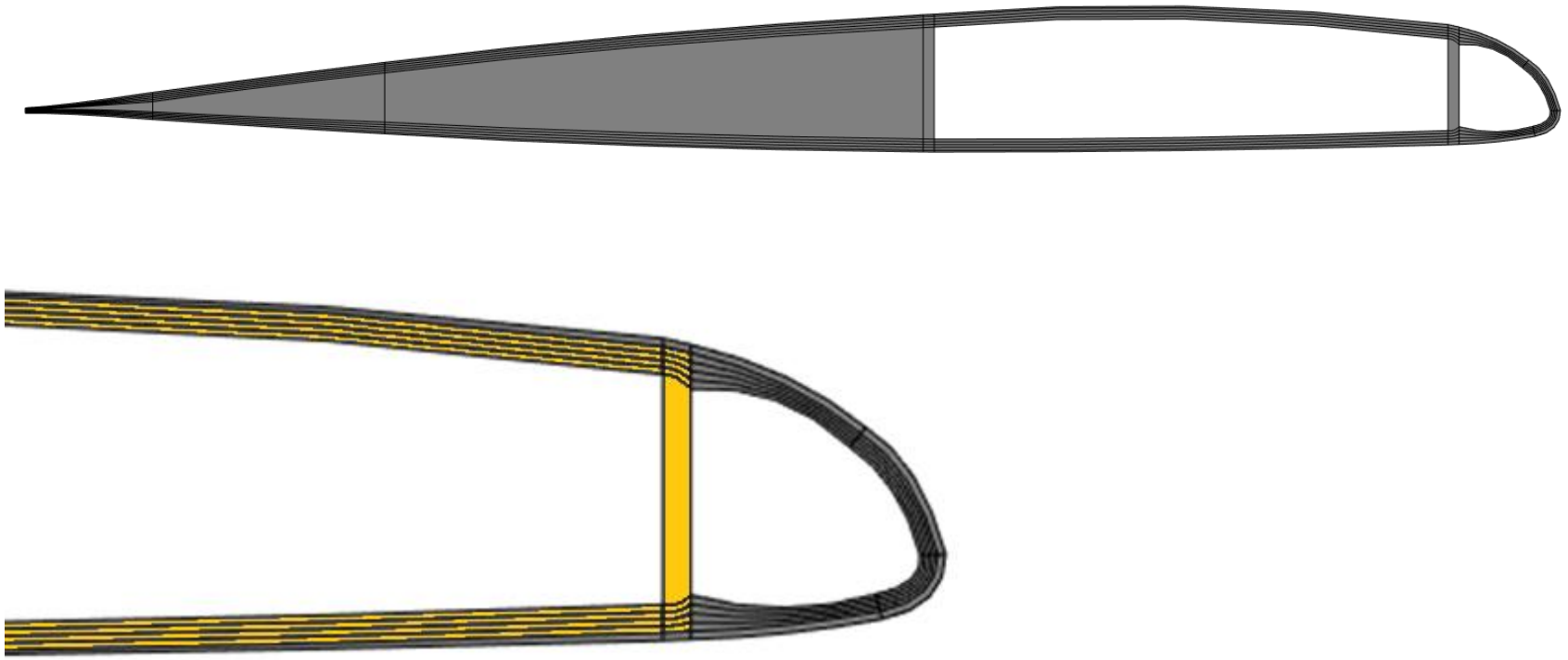

Figure 4-16. Fine rotor mesh cross section for Winckler layup. Note that there are four elements through the spar thickness.

4.4.2 Hygrothermally Stable Layups

A nominal layup can swell, warp, and lose its material properties and structural integrity under humidity and temperature fluctuations (that might be encountered by rotor blades over the span lifetime). It also has manufacturing limitations under conventional high temperature curing. Hygrothermally stable layups attempt to avoid these limitations. Here, the top and bottom flanges still a mirror image of each other like the nominal layup, but consist of multiple ply orientations that are meant to provide stability from thermal or moisture fluctuations.

Two hygrothermally stable families of layups were proposed by Winckler [8] and Haynes [9]. Both combined two layups with extension-shear coupling that were individually hygrothermally stable, in opposite directions. The opposing shears, caused by axial loading acting at equivalent distances from the full layup's centerline, provide a purely torsional moment, as illustrated in Figure 1. In this paper the Winckler and Haynes layups are denoted by 'W' and 'H' respectively.

Winckler and Haynes applied their layups to thin, solid, plates built of 6 and 8 plies, respectively. In this research, the same principle is applied to a box beam, i.e., the layup chosen for the top and bottom of the box were both individually hygrothermally stable and provide extension-shear coupling.

The layups are summarized in Table 4-2. In order to maintain the same mass and minimize any inertial differences between each blade examined in this study, the rotor spar wall thickness was kept constant and then divided into elements representative of each ply orientation for a given layup. Table 4-2 shows that a Winckler layup requires a minimum

of 4 plies on either the top or bottom to achieve hygrothermal stability, compared the Haynes layup requirement of 3.

As was done with the Chandra-Chopra beam models in Section 3.3.2, multiple rotor meshes were created in order to verify the homogenization of the spar materials. Two finer meshes were created: one for the Haynes layup (with three ply orientations), and one for the Winckler layup (with four ply orientations). If the spar was to be designed with the correct ply thickness (as was done with the Haynes and Winckler experiments) there would be differences between the spar dimensions for each blade design. Instead, the spar wall thickness, t_{spar}, was held constant and the thickness of the individual ply, t_{ply}, was varied to fit within the rotor spar dimension. As an example, Figure 4-17 shows how the Winckler layup was applied to the rotor spar. Here the element with spar thickness t_{spar} has been divided into four elements with equal thickness ($t_{ply} = t_{spar}/4$). If fewer plies were needed for the layup, the ply thickness would be larger.

Table 4-2. Layup definition for composite spar designs used in this study

	Top Layup	**Bottom Layup**
U	$[0°/90°]$	$[0°/90°]$
N	$[\theta]$	$[-\theta]$
H	$[21.2°/-63.8°/-48.7°]$	$[-21.2°/63.8°/48.7°]$
W	$[\theta/(\theta + 90°)_2/\theta]$	$[-\theta/(-\theta + 90°)_2/-\theta]$

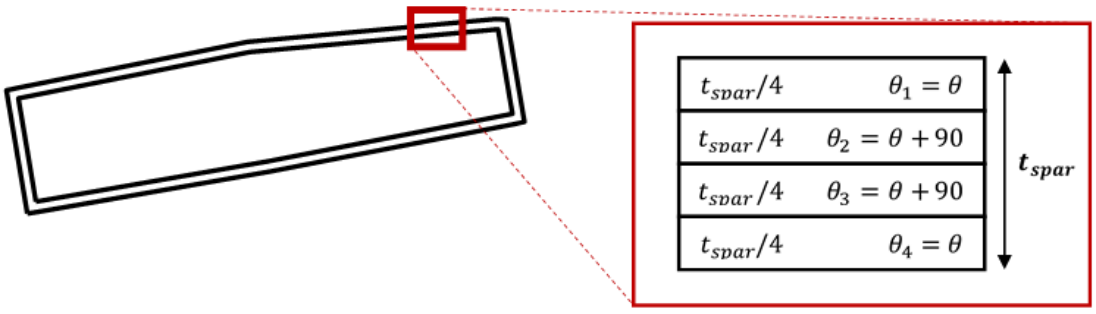

Figure 4-17. Application of a Winckler layup to the UH-60A box beam like spar

4.4.2.1 Winckler

Winckler [92] determined that there was a family of layups that would maintain extension-torsion coupling while remaining hygrothermally stable. The full laminate had to satisfy two conditions: (1) the extension-torsion coupling term had to be nonzero and (2) the curvature due to thermal or hygral fluctuations remained zero ($\kappa^{TH} = 0$).

The laminate can also be considered as two symmetric halves, which on their own have no extension-torsion coupling. These halves allow us to consider a partial solution where each laminate must satisfy three conditions: (1) the laminate is symmetric ($[B] = 0$), (2) the thermal shear strain is zero ($\varepsilon_6^{TH} = 0$), and (3) there is a non-zero extension-shear coupling ($A_{16} \neq 0$). These requirements allowed for the laminate to shear in response to an applied load, but not to changing thermal conditions. The two halves are designed to shear in opposite directions so that when bonded together provide the bi-moment required to twist the beam. These requirements led to the following hygrothermally stable extension-torsion coupled laminate:

$$[\theta/(\theta + 90°)_2/\theta/-\theta/(-\theta + 90)_2/-\theta]$$

where θ is any arbitrary ply angle.

There are many variations of this layup that will still maintain hygrothermal stability. The one most pertinent to this research, as shown in the bottom of Figure 1-2, is:

$$[\theta/(\theta + 90°)_2/\theta/\ CORE\ /-\theta/(-\theta + 90°)_2/-\theta]$$

In this layup, core refers to any isotropic material that does not interfere with the symmetry of the layup or could represent empty space. As was done with the nominal coupled layup, it was important to determine what angle θ to use in order to maximize the extension-torsion coupling. Again using Equation 4-2 the twist sensitivity was calculated for this layup and is shown in Figure 4-18. Any value between 10° and 25° would provide a high sensitivity. Based on these results, a value of $\theta = 25°$ was chosen.

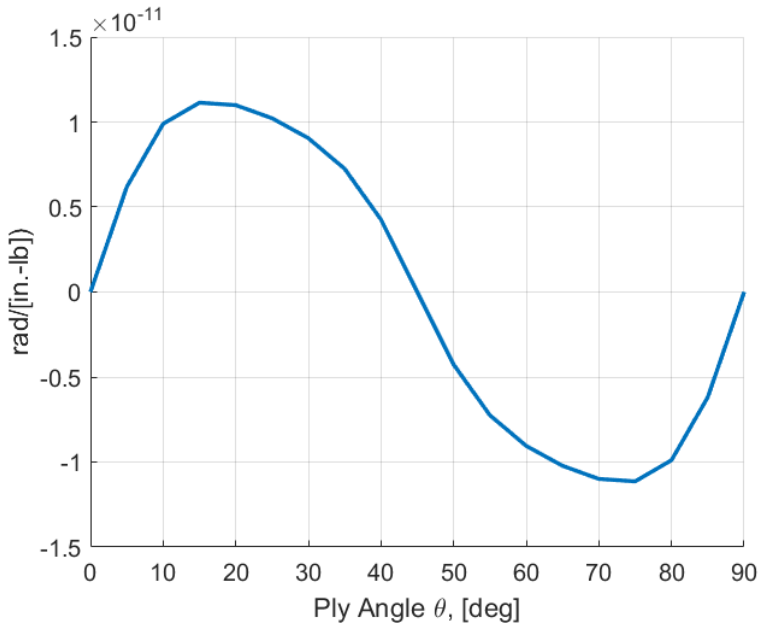

Figure 4-18. Twist sensitivity due to unit axial force as a function of ply angle for a Winckler, hygrothermally stable layup

For the rotor, because the Winckler layup contains 4 layers of equal thickness on the top and similarly on the bottom of the beam, the Winckler spar blade mesh was designed with four elements through the spar thickness, as shown in Figure 4-16. The final

blade mesh contained 12,375 nodes and 1,360 elements. The cross section has 375 nodes and 85 elements.

4.4.2.2 Haynes and Armanios

In 2009, Haynes and Armanios sought to expand on the families of hygrothermally stable, extension-torsion coupled laminates. Numerical optimization showed that a 6-ply layup (3 plies on the top and bottom respectively) improved the extension-torsion coupling capabilities of the Winckler layups. This claim was verified by Haynes and Armanios experimentally, and validated using X3D, as shown in Figure 4-19. For these experiments, two laminates were constructed from T300/976 graphite/epoxy sheets based on the layup of Winckler (where $\theta = 25°$) and the Haynes layup discussed here. The material properties of this material are listed in Table 2-1.

Each laminate was cut into slender beams (1.0” by 7.0” or 2.54 cm by 17.78 cm), an increasing tip load was applied, and the resulting twist at the tip of the beam was recorded. Here it can be seen that the 6 ply laminate designed by Haynes achieves more twist than the Winckler laminate at all blade loads. The large range of force required a nonlinear (geometric) solution, where the strains are no longer small nor a linear function of displacement.

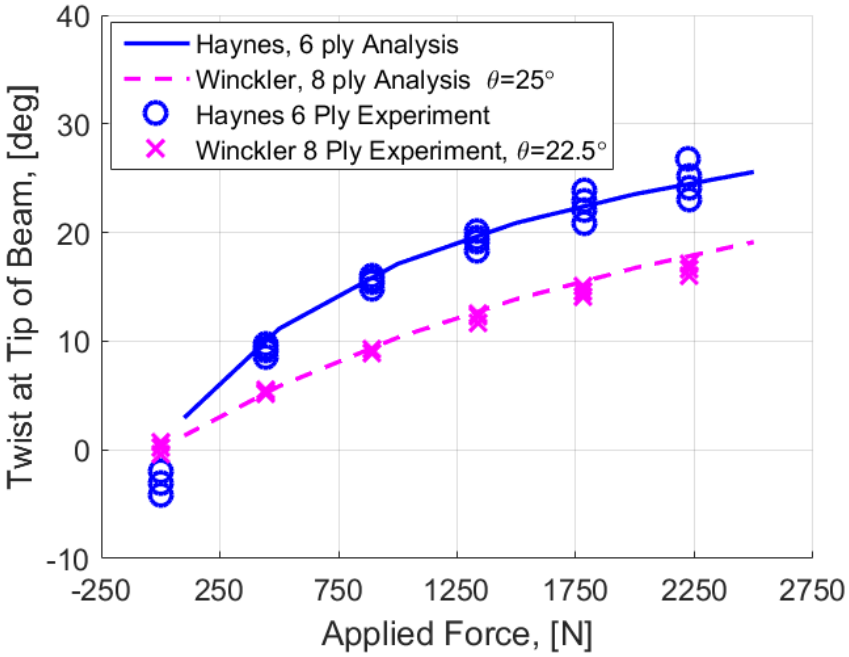

Figure 4-19. Experimental vs. analytical results for twist as a function of applied axial loading for a Winckler and Haynes beam

It should be noted that because a different number of plies was required for both laminates, the thickness of the beam varied from 0.912 mm (0.04") for the Haynes laminate to 1.216 mm (0.048") for the Winckler laminate. However, as mentioned earlier, to keep the rotor geometry and meshes as similar as possible, the thickness of the spar for the composite blade was not altered. Instead, it was divided into three elements through the spar thickness, as indicated in Figure 4-15. This mesh contains 10,197 nodes and 1,104 elements. The cross section contains 309 nodes and 69 elements.

4.4.2.3 Hygrothermally Stable Coarse Mesh

The use of the Winckler and Haynes rotor meshes was time consuming and inefficient. To improve run time and demonstrate feasibility, the coarse mesh, used earlier for the uncoupled and nominal cases, was also used for the hygrothermally stable layups.

Accordingly the spar material definition in the upper and lower flanges of the spar were calculated based on the homogenization procedure given earlier in Section 653.1.1.

The material definition for the homogenized matrices are included in Appendix II.

Chapter 5: Results and Discussion

The main objective of this research was to improve a helicopter rotor's efficiency in high speed forward flight. The effect of extension-torsion composite coupling on rotor performance was studied by examining the following:

1. Effect of composite coupling on radial twist distribution as a function of rotor rotational speed (rotor RPM in hover is considered 100% nominal rotation speed or 100NR)
2. Comparison of uncoupled to nominal coupled layup rotor at 100NR
3. Comparison of uncoupled to nominal coupled layup rotor at reduced rotation speed (85NR, 65NR)
4. Effect of hygrothermally stable layups on rotor performance

Each layup considered was first studied in vacuum to obtain the desired twist distribution (described above) and blade frequencies. Then consideration of the overall rotor performance was followed by analysis of sectional aero-environment. Finally, consideration of the blade strains was attempted. The lift to drag ratio, L/D_e, is considered the metric for overall rotor performance. Changes in L/D_e are studied for the various layups for identical trim conditions. The underlying aeromechanics behind the changes are explained by changes in rotor frequencies and the aerodynamic environment. The resulting

changes in blade strain are also investigated. All of these phenomena are part of a single integrated analysis. When layups change, there is no extra requirement to constrain the frequencies to reproduce the same dynamics and loads. When the loads change, there is no uncertainty in the trim solution or strains. A unified analysis allows changes in material properties to flow into the blade dynamics, aerodynamics, trim, and strains.

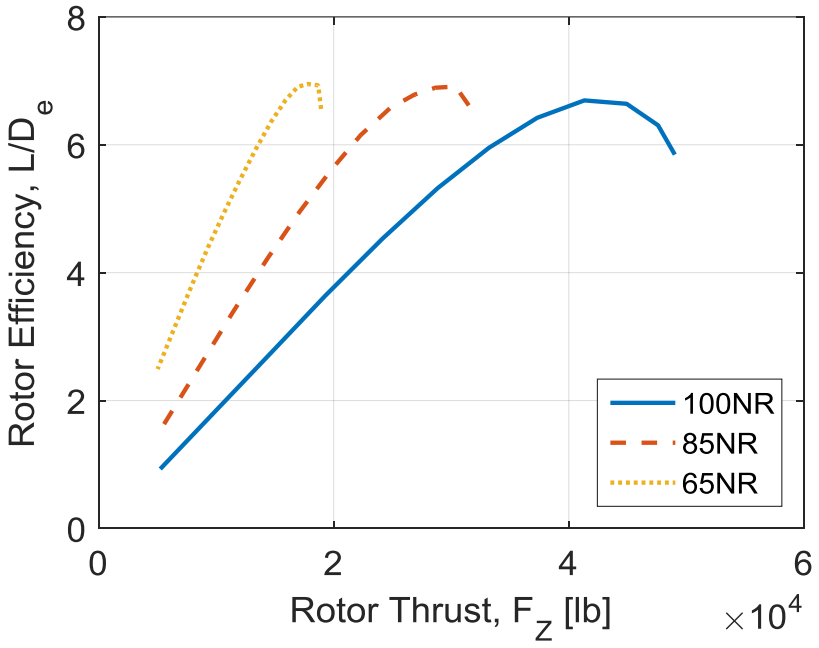

Figure 5-1. Rotor efficiency as a function of thrust for an uncoupled composite rotor at three different RPMs. Note that the overall rotor thrust range decreases as the rotor slows.

Variation in rotor twist was calculated in vacuum. This twist is then the "built-in" twist at any rotor speed. Analysis of the rotor in forward flight was carried out at a speed of 157 kts and a constant rotor shaft tilt of $\alpha = 0°$. This is a stringent flight condition both due to the asymmetry of the flow field and due to the fact that the inflow is entirely induced. As such, a free-wake is required. Gains, if any, are expected to be higher than those seen in more normal conditions. Problems, too, if any, are more likely to appear under these conditions and allows for us to study and address them in advance.

It is well understood that as the rotor RPM is decreased, the rotor naturally will produce less (dimensional) lift, as shown in Figure 5-1. It was therefore reasonable to assume, for this research, that if greater than 70% RPM reduction will eventually be accomplished with a supplementary lifting body such as a wing and a thruster such as a propeller to ensure full vehicle equilibrium. Therefore the focus of this research is entirely on the rotor.

5.2 Effect of Coupling on Radial Twist Distribution

To ensure that the composite coupled rotors matched the built-in twist of the baseline titanium-spar rotors at 100NR, and that they untwisted as the rotor RPM was slowed, the following method was employed:

1. Apply the composite coupling to the baseline spar with layup opposite to what is actually intended in the final rotor (so the top is now $[-\theta]$ and bottom is $[\theta]$)
2. Spin this blade in vacuum at 100NR and record the twist distribution
3. Now re-define the blade geometry (composite mesh) with the 100NR twist distribution (from Step 2), and correct the direction of composite coupling (top returns to $[\theta]$ and bottom to $[-\theta]$)
4. Verify that the correct twist is achieved by spinning the new blade at 100NR and compare the twist distribution to that of the baseline titanium spar blade

The twist distribution along the blade span at varying RPM is shown in Figure 5-2. In black is the original built-in twist of the UH-60A rotor. When the above methodology was used,

a new twist built-in twist distribution was determined for an extension-torsion coupled rotor, shown in purple. In the context of this research, a nominal coupled rotor (denoted by **N**) is defined by a classical antisymmetric layup (see Section 1.3.1.1 for details) with the ply angle defined by θ.

In Figure 5-2 it can be seen that as the rotor RPM is increased (65NR in yellow, 85NR in red) the rotor twists towards the titanium rotor distribution. At 100NR, the coupled rotor distribution, shown in blue, matches well with the titanium rotor twist distribution. It can also be seen from this figure that as the rotor is slowed, the natural reduction in centrifugal forcing allows the rotor to return to its cold shape twist.

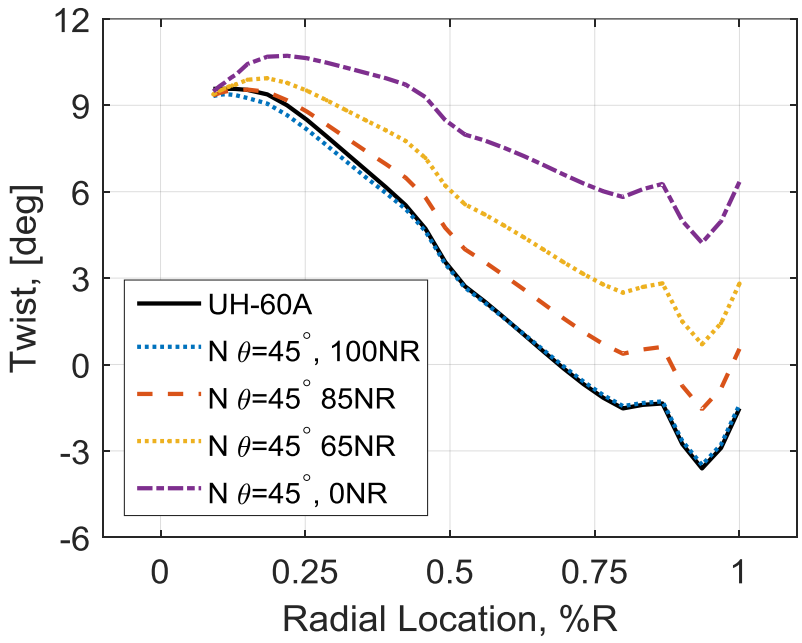

Figure 5-2. Twist as a function of radial location for baseline titanium spar UH-60A blade compared to twist of rotor with a nominal layup composite spar at 100NR, 85NR, and 65NR. Calculated in vacuum.

5.3 Rotor Dynamics

Because the present analysis is unified, there is no extra requirement for the new composite blade to match the original titanium blade frequencies. However, it was still important to understand whether modifications to the blade structure are likely to cause resonance crossings at the reduced operational speeds, and if they do, know where so that they can be avoided. Figure 5-3 shows how the new uncoupled composite rotor frequencies compare to the titanium spar rotor frequencies (shown by the black dashed lines for reference). For both the uncoupled and coupled rotors, the first three structural modes match closely with the titanium model. The biggest difference in these modes can be seen in the 2nd flap mode, in yellow, which is slightly higher for the uncoupled rotor and slightly lower for the nominally coupled rotor.

Significant differences can be seen in the next three modes. These modes, although designated by their dominant motions, are highly coupled. For the coupled rotor, all three higher mode frequencies are significantly reduced when compared to both the titanium and uncoupled rotors. This is to be expected as introducing extension-torsion coupling is designed to soften the torsional stiffness of the rotor.

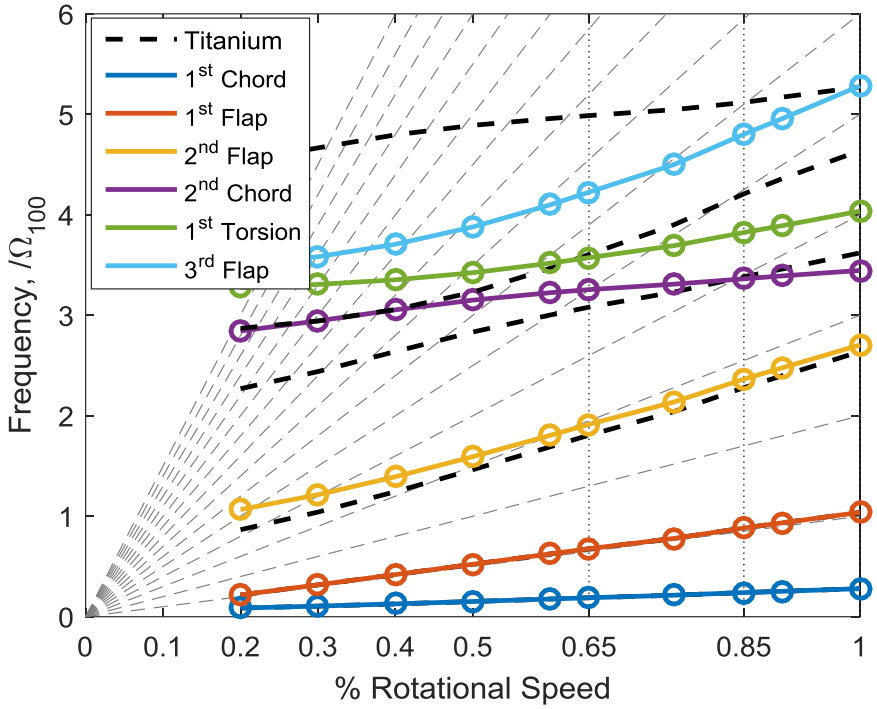

Figure 5-3. Fanplot for a UH-60A-like rotor with an uncoupled composite spar compared to the titanium spar

Table 5-1. Frequencies of the first 6 modes of the uncoupled composite spar blade nondimensionalized with operating RPM

Mode	Type	100NR $/\Omega_{100}$	85NR $/\Omega_{85}$	65NR $/\Omega_{65}$
1	Lag	0.280	0.283	0.290
2	Flap	1.038	1.039	1.041
3	Flap	2.705	2.782	2.946
4	Lag (coupled*)	3.446	3.957	5.008
5	Torsion (coupled)	4.036	4.499	5.497
6	Flap (coupled)	5.284	5.649	6.500

*coupled: these are coupled flap-lag-torsion modes designated by their principle (dominant) motions

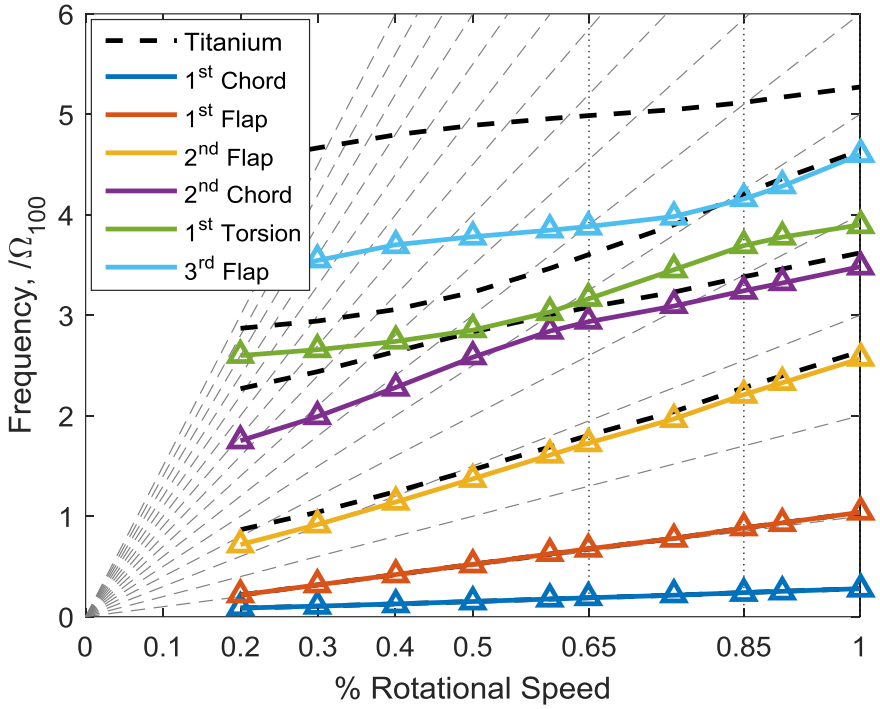

Figure 5-4. Fanplot for a UH-60A-like rotor with a nominally coupled composite spar compared to original titanium spar

Table 5-2. Frequencies of the first 6 modes of the nominal coupled composite spar blade nondimensionalized with operating RPM

Mode	Type	100NR $/\Omega_{100}$	85NR $/\Omega_{85}$	65NR $/\Omega_{65}$
1	Lag	0.279	0.282	0.290
2	Flap	1.038	1.039	1.041
3	Flap	2.567	2.600	2.661
4	Lag (coupled*)	3.483	3.816	4.518
5	Torsion (coupled)	3.900	4.345	4.870
6	Flap (coupled)	4.599	4.892	5.975

*coupled: these are coupled flap-lag-torsion modes designated by their principle (dominant) motions

As indicated by the vertical dotted lines in Figure 6-3 and 6-4, two slowed operating RPMs were considered: 85NR and 65NR. As established by Snyder et al., current helicopter engines are capable of slowing by 15% with minimal specific fuel consumption (SFC) degradation [2]. This research considered 85NR as one of the slowed operational speeds in order to take advantage of this. Improvement at this RPM would only require design modification to the rotor system without the needs for complex variable drive systems. The other slowed operational speed of 65NR was chosen in order to consider the potential for future advancements in engine technology beyond current capabilities.

5.4 Performance

As indicated in Section 4.2, the measure of rotor efficiency is the L/D_e ratio. To determine the maximum rotor performance, a collective sweep was carried out. For each point, the rotor was set to a fixed collective, θ_0, and trimmed to zero cyclic flapping (β_{1c} and β_{1s}) measured at the flap hinge. Each point in Figure 5-5 shows the performance for a different collective, ranging from 0° to 14°.

Each point had a forward flight speed of $V_\infty = 157\ kts$ ($\mu = 0.37$ for 100NR). Additionally, the shaft tilt was kept constant at $\alpha = 0°$.

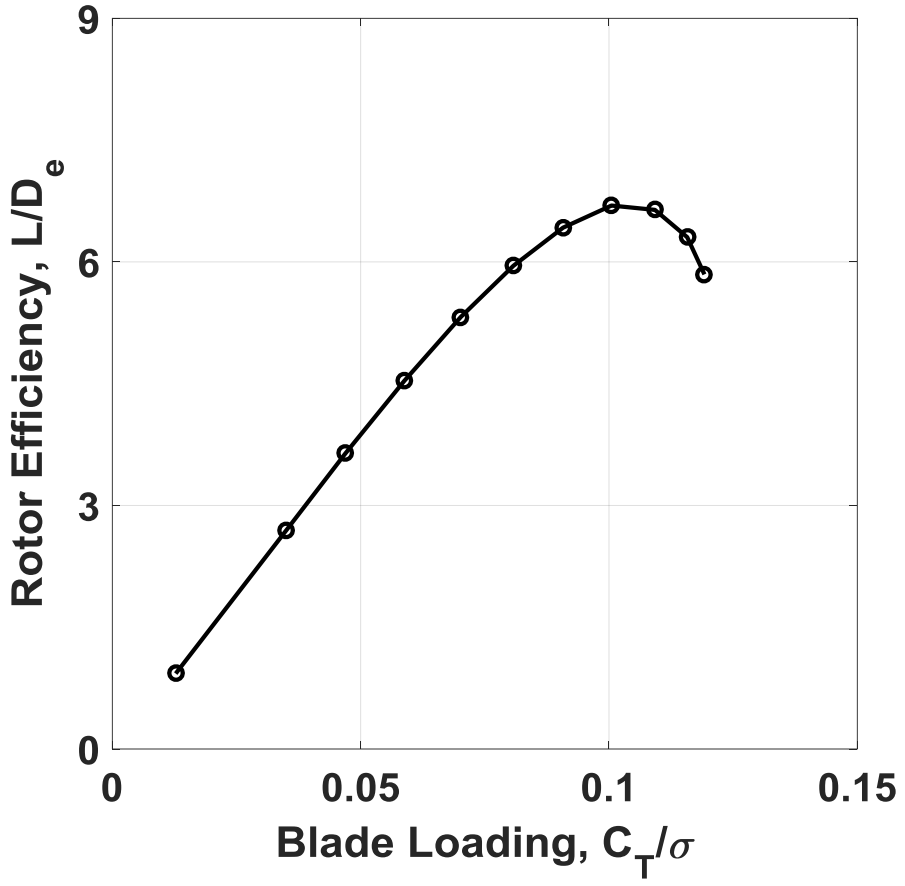

Figure 5-5. Rotor efficiency as a function of blade loading for a UH-60A-like rotor with titanium spar. Each point along the curve represents a different collective setting with $V_\infty = 157\ kts$, $\mu = 0.37$

5.5 Effect of Nominal Layup on Performance at 100NR, 85NR, and 65NR

In order to make a consistent comparison, the results for the coupled composite rotor spar are compared to a blade with an uncoupled composite spar, instead of the baseline titanium spar. This ensures that any performance differences found subsequently are due entirely to coupling and not the substitution of composite materials per se.

At the hover RPM, 100NR (27 rad/s), the efficiency of all blades must remain the same. This was ensured by reproducing the UH-60A twist distribution at 100NR, as well as maintaining the baseline titanium spar's rotor mass and sectional c.g. locations. As can be seen in Figure 5-6 (a), the L/D_e for both the uncoupled and nominal coupled rotors has been maintained at 100NR for all blade loadings, C_T/σ.

When the rotor RPM is slowed to 85NR, see Figure 5-6 (b), while both rotors see an increase in efficiency it is clear that the coupled rotor outperforms the uncoupled rotor at all blade loadings, reaching a maximum L/D_e of 8.2 compared to the uncoupled rotor's maximum of 6.9 (at $C_T/\sigma \approx 0.1$), an improvement of 20%.

When the RPM is slowed further to 65NR (Figure 5-6 (c)), the coupled rotor again outperforms the uncoupled rotor but only at lower blade loadings (up to $C_T/\sigma \approx 0.075$). The coupled and uncoupled rotors at 65NR only reach a peak L/D_e ratio of 6.9; there is no improvement in maximum efficiency at this RPM. The greatest improvement in efficiency occurs at $C_T/\sigma \approx 0.025$ where we see a 15% improvement over the uncoupled rotor efficiency.

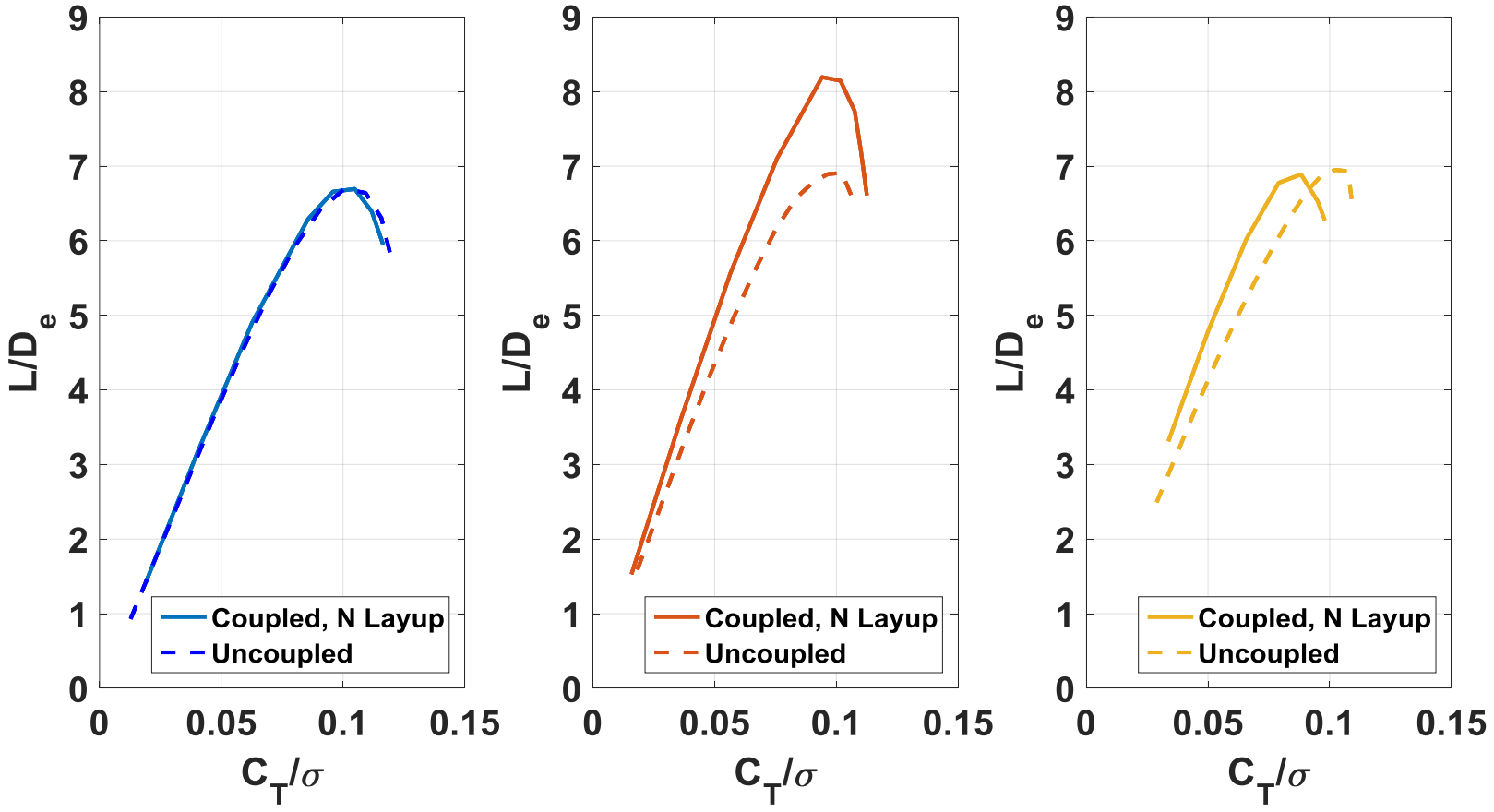

(a) 100NR, $\mu = 0.37$ (b) 85NR, $\mu = 0.46$ (c) 65NR, $\mu = 0.57$

Figure 5-6. L/D_e ratio for uncoupled and nominal coupled rotors for (a) 100NR, (b) 85NR, and (c) 65NR

5.6 Aeromechanics of composite rotor

To understand the cause of the performance change between the uncoupled and coupled rotors, Figure 5-7 considers lift versus drag at two different radial locations (75%R and 89%R) and three different RPMs. Although there are differences between the three RPM at 75%R (a and c), the effects are more clearly observed outboard at 89%R (b and d). Two conclusions can be drawn from this figure: 1) the drag has more distinct variation as the rotor RPM is varied and 2) there is variation in negative lift between the uncoupled and coupled rotors.

First, we consider the drag in more detail. Figure 5-8 shows the azimuthal variation of drag. For both the uncoupled and coupled rotor, a reduction in RPM from 100NR to 85NR yields a very large reduction in drag along the advancing side of the rotor. Further RPM reduction to 65NR yields a relatively smaller reduction. For the uncoupled rotor, a significant drag spike appears on the retreating side of the rotor at 85NR. For the coupled rotor, this spike is eliminated. At 65NR the uncoupled rotor shows a rapid increase in drag along the advancing side. For the coupled rotor this increase is eliminated, but a spike on the retreating side appears instead.

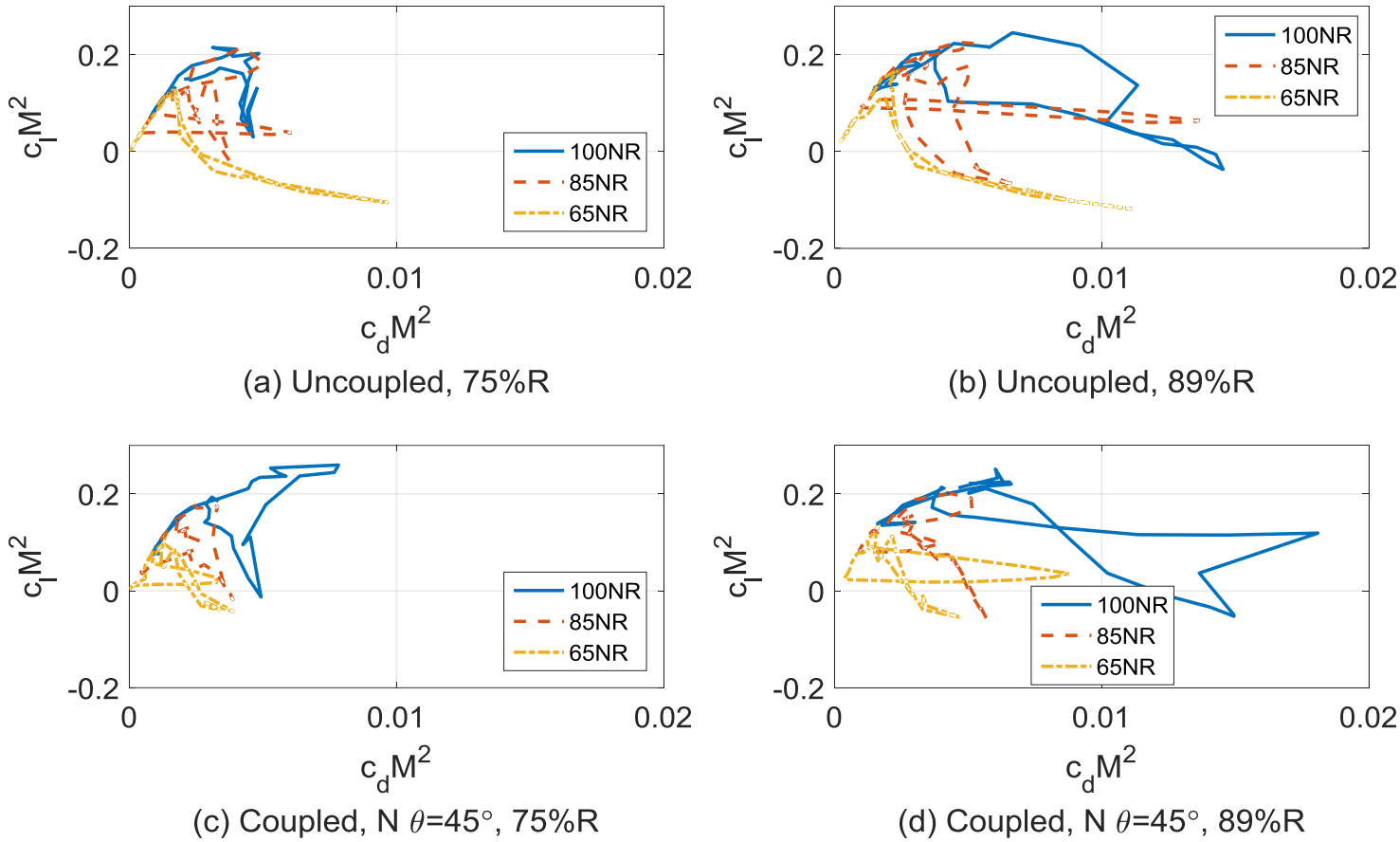

Figure 5-7. Lift vs drag for the uncoupled and nominal coupled rotor at two radial locations (75%R and 89%R) and three nominal RPM (100NR, 85NR, and 65NR). Calculated in vacuum.

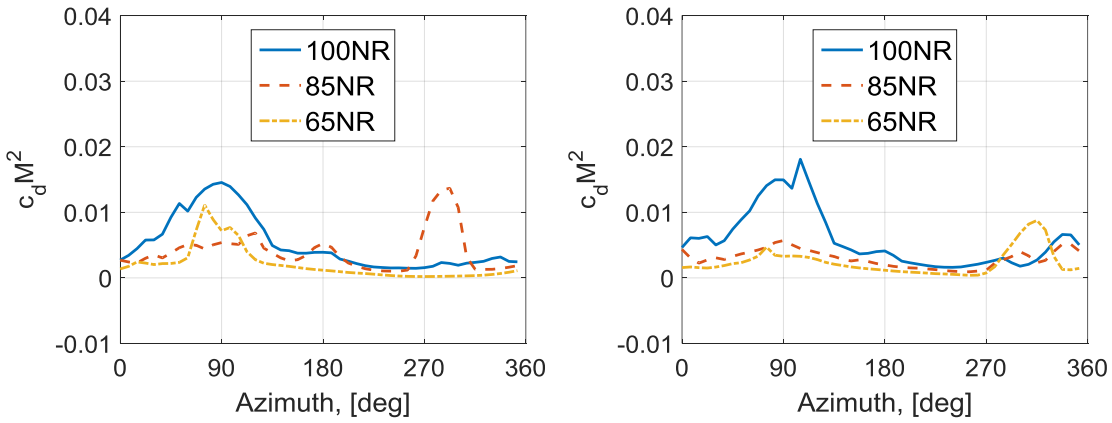

(a) Uncoupled, 89%R **(b) Coupled N ($\theta = 25°$), 89%R**

Figure 5-8. Drag as a function of azimuth at $C_T/\sigma \approx 0.1$ for uncoupled and nominal coupled rotors at 89%R for 100NR, 85NR, and 65NR

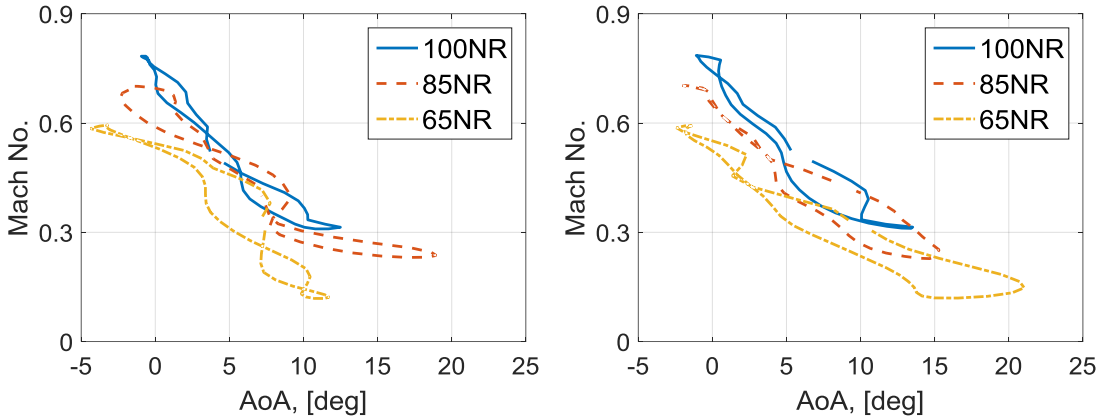

(a) Uncoupled, 89%R **(b) Coupled N ($\theta = 25°$), 89%R**

Figure 5-9. Mach number as a function of angle of attack at $C_T/\sigma \approx 0.1$ for uncoupled and nominal coupled spar rotors at 100NR, 85NR, and 65NR

As the rotor RPM is reduced from 100NR to 85NR the advancing tip Mach number decreases from $M_{ADV} = 0.89$ to $M_{ADV} = 0.80$, so the blade tip leaves the transonic region when the rotor is slowed. This change in operating environment alone, with or without composite coupling in the blade spar, would result in a substantial reduction in drag, which is what was observed on the advancing side of the rotor. In addition to this change in M_{ADV},

the coupled rotor is also untwisted (as shown in Figure 5-2). This reduces the drag on the advancing side of the rotor. As the rotor RPM is further reduced to 65NR, the overall change in drag around the azimuth is not as significantly affected, as the aerodynamic environment does not change fundamentally from an $M_{ADV} = 0.80$ to $M_{ADV} = 0.66$ (both are in the high subsonic region, but below transonic).

To understand drag behavior Figure 5-9 shows how Mach number and angle of attack (denoted as AoA) vary along the azimuth. At any given RPM, between uncoupled and coupled, the Mach number range does not change. This is an indication that compressibility is not a factor in the rotor efficiency change from composite coupling. The main factor is the change in angle of attack distribution. This figure shows that the uncoupled rotor at 85NR and the coupled rotor at 65NR enter stall ($AoA > 15°$) along the retreating side of the rotor. This accounts for the spikes in the drag coefficient at 85NR and 65NR, seen previously in Figure 5-8.

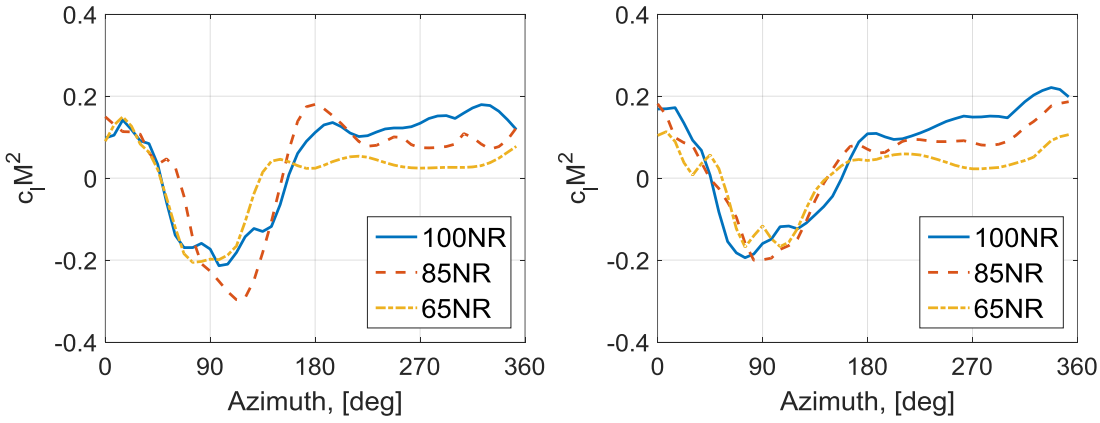

(a) Uncoupled, 89%R **(b) Coupled N ($\theta = 25°$), 89%R**

Figure 5-10. Lift as a function of azimuth at $C_T/\sigma \approx 0.1$ for uncoupled and nominal coupled rotors at 89%R for 100NR, 85NR, and 65NR

The second observation made from Figure 5-7 was that there were variations in the negative lift between the uncoupled and coupled rotors. These have a significant impact on rotor performance. Figure 5-10 shows the azimuthal variation of lift. Again, both the uncoupled and coupled rotor have very similar distributions at 100NR. When the rotor RPM is reduced to 85NR, however, the uncoupled rotor generates significantly more negative lift on the advancing side of the rotor, whereas the coupled rotor does not. This is an important effect that occurs outboard of 90%R. With an increase in negative lift comes a need to make up the lift somewhere else around the azimuth in order to maintain the same blade loading. This leads to an increase in angle of attack (to the point of stall in this case) and therefore an increase in the drag.

It should be noted that the choice of the nominal layup with $\theta = 45°$ for this study was made to achieve maximum untwisting of the rotor blade, but was not optimized to maximize the aerodynamic performance at multiple slowed RPMs. It is possible that a different layup angle could have provided an increase over the uncoupled rotor L/D_e ratio at 85NR *and* 65NR if the change in twist was less extreme.

Figure 5-11 shows the pitching moment at the 89% radial location, just inboard of the swept portion of the rotor. Here it can be seen that there are no differences between the uncoupled and coupled rotor other than the retreating side stall that was also seen in the drag plots for the uncoupled rotor at 85NR and the nominal coupled rotor at 65NR. The lack of difference in the pitching moment tells us that there is minimal difference in the dynamic twist. This indicates that the change in negative lift is, in fact, from the static untwisting of the rotor (changing the "built-in" twist due to composite coupling) and not from any resulting change in the torsion (dynamic twist) from the changing pitching

moments. Near the blade tip there are greater differences, but a lifting line analysis is inadequate for concrete conclusions.

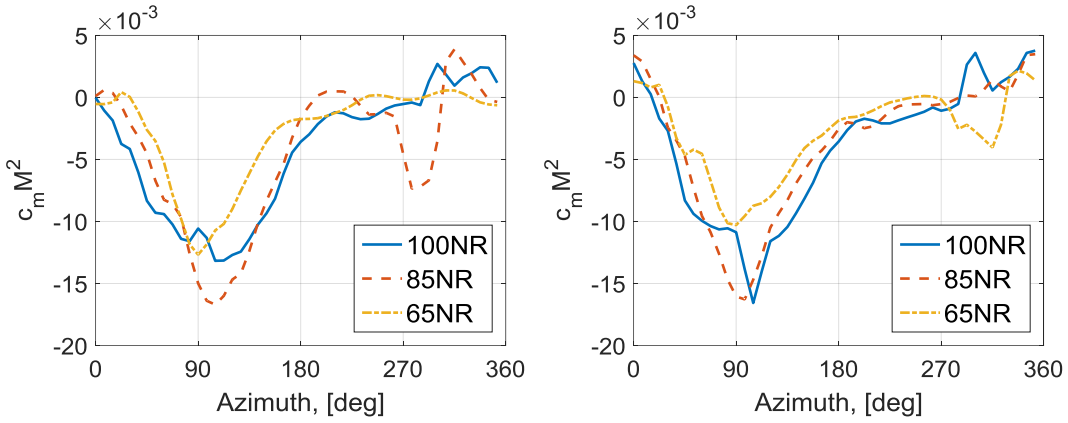

(a) Uncoupled, 89%R **(b) Coupled N ($\theta = 25°$), 89%R**

Figure 5-11. Pitching moment as a function of azimuth at $C_T/\sigma \approx 0.1$ for uncoupled and nominal coupled rotors at 89%R for 100NR, 85NR, and 65NR

Moving outwards closer to the tip of the blade, Figure 5-12 shows the pitching moments at 95%R, in the swept portion of the blade where the Mach number is higher. Again both blades perform similarly at 100NR, ignoring the uncoupled rotor local stall (due to negative AoA) on the advancing side (90° azimuth). When the rotor is slowed to 85NR the coupling reduces the nose down pitching moment along the advancing and the retreating side. At 65NR the Mach number is already low enough that there is not a dramatic influence by the coupling on the pitching moment.

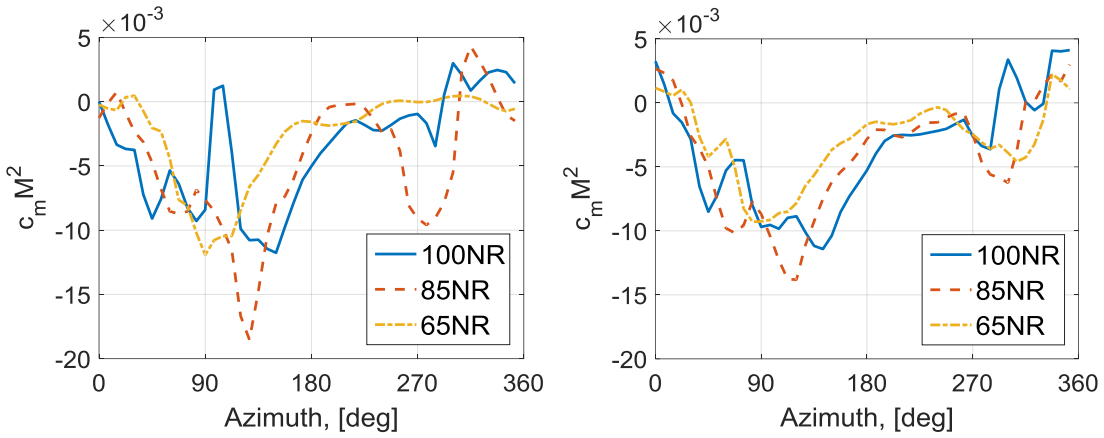

(a) Uncoupled, 95%R **(b) Coupled N ($\theta = 25°$), 95%R**

Figure 5-12. Pitching moment as a function of azimuth at $C_T/\sigma \approx 0.1$ for uncoupled and nominal coupled rotors at 95%R for 100NR, 85NR, and 65NR

A more accurate calculation of the magnitude of pitching moments requires CFD to capture 3-D transonic effects. In future work it would be advantageous to use CFD to accurately characterize this phenomenon, but the calculations here allow us to understand the basic trends. With larger negative pitching moments from CFD, the benefits of untwisting the rotor at these high μ conditions are expected to be greater.

As previously mentioned, the pitching moment has a strong influence on the elastic or dynamic twist of the rotor. As shown in Figure 5-13 the uncoupled rotor experiences elastic twist excursions much larger than that experienced by the coupled rotor when the RPM is reduced, however this is not due to pitching moments. As shown in Table 5-1, the uncoupled rotor has a mode near 4/rev (3.96/rev). The introduction of coupling shifts this frequency away from resonance at 85NR. Similarly, at 65NR the uncoupled rotor has a mode near 3/rev (2.95/rev) and again the coupling shifts this mode away from resonance. Thus, as previously stated, there are significant dynamic and aerodynamic coupled phenomena, that are tied to the changing blade frequencies, that call for an integrated

analysis, such as the one conducted here. An isolated structural analysis would not be sufficient as it would not capture these coupled aeromechanical phenomena and artificially constraining the blade frequencies and cross-sectional properties would not reveal the benefits of this coupling.

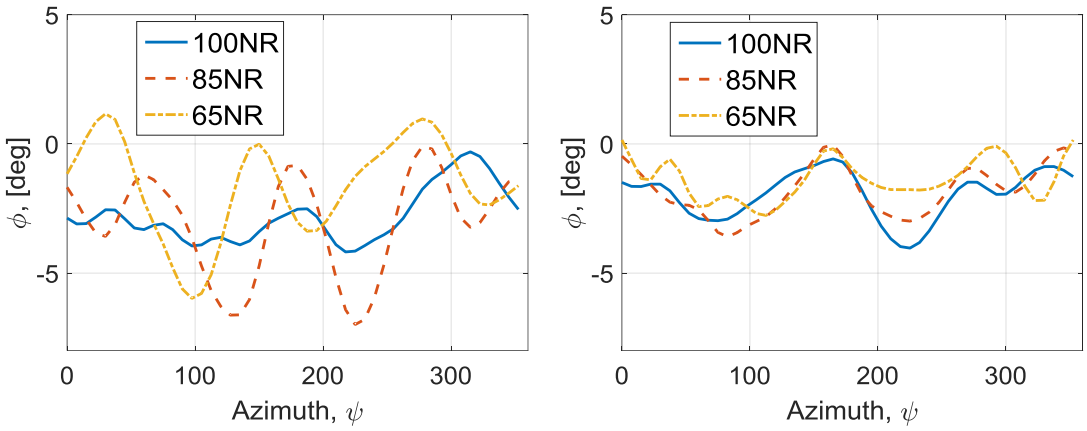

(a) Uncoupled, 95%R **(b) Coupled N ($\theta = 25°$), 95%R**

Figure 5-13. Elastic twist as a function of azimuth at $C_T/\sigma \approx 0.1$ for uncoupled and nominal coupled rotors at 95%R for 100NR, 85NR, and 65NR

5.6.1 Aeromechanics of Hygrothermally Stable Composite Rotors

The hygrothermally stable layups, when applied to the same box beam spar, once again affected the built-in twist of the rotor strongly, as shown in Figure 5-14. The Winckler layup achieved twist very similar to the nominal layup at the slowed rotor speeds; the Haynes layup twisted relatively less. As should be apparent by now, these mean nothing by themselves; an aeromechanical analysis is required to compare their relative merit.

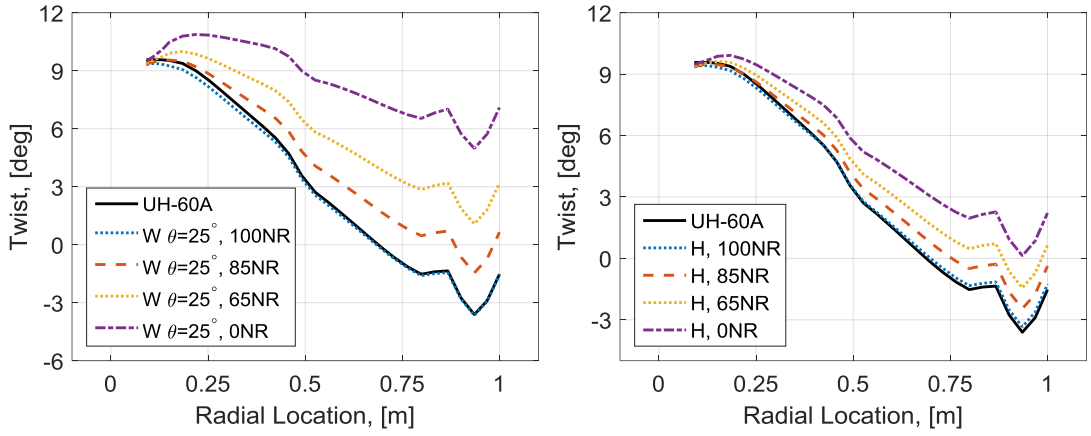

(a) Winckler Layup **(b) Haynes Layup**

Figure 5-14. Twist as a function of radial location in vacuum for (a) Winckler layup spar with θ=25° and (b) Haynes layup spar

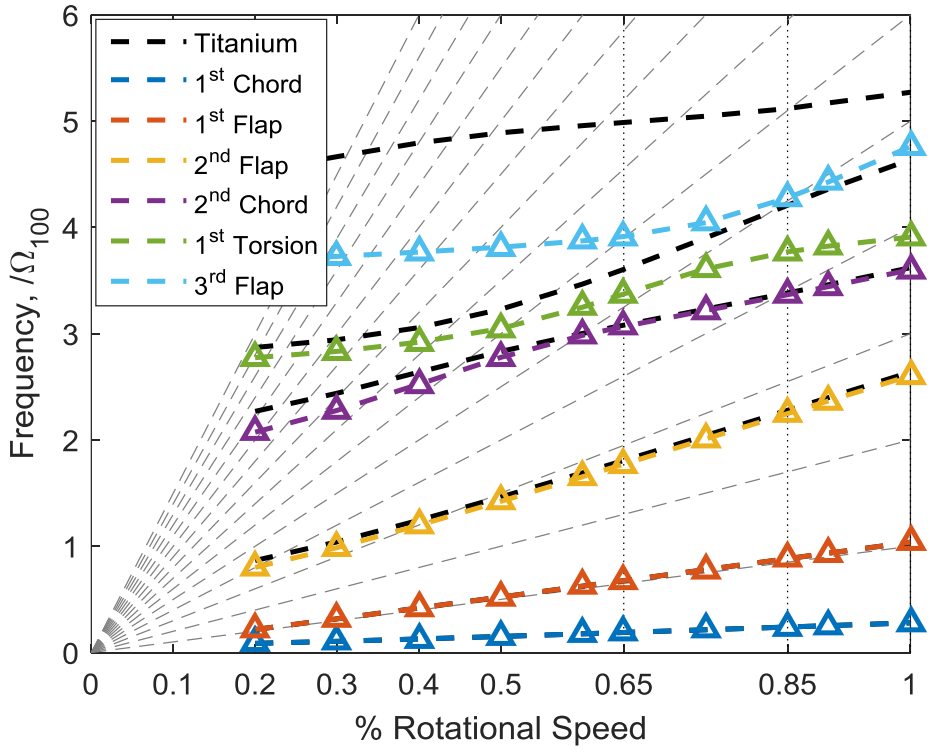

Figure 5-15. Fanplot for a UH-60A-like rotor with a hygrothermally stable Haynes layup composite spar compared to titanium spar

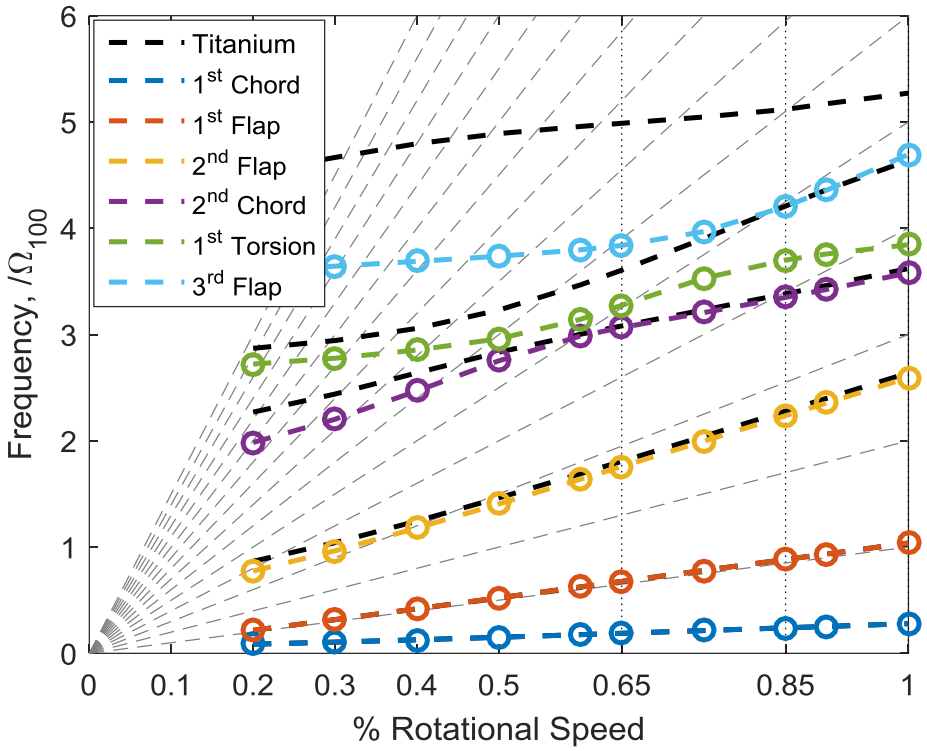

Figure 5-16. Fanplot for a UH-60A-like rotor with a hygrothermally stable, Winckler layup, composite spar compared to titanium spar for $\theta = 25°$

Table 5-3. Nondimensionalized frequencies (/rev) of the first 6 modes as a function of the percentage change in the nominal RPM for a rotor with a hygrothermally stable composite coupling

Mode	Type	100NR ($/\Omega_{100}$)		85NR ($/\Omega_{85}$)		65NR ($/\Omega_{65}$)	
		Haynes	Winckler	Haynes	Winckler	Haynes	Winckler
1	Lag	0.279	0.279	0.282	0.282	0.290	0.290
2	Flap	1.038	1.038	1.039	1.039	1.041	1.041
3	Flap	2.606	2.594	2.645	2.630	2.727	2.704
4	Lag (coupled*)	3.601	3.579	3.961	3.940	4.719	4.716
5	Torsion (coupled)	3.909	3.844	4.436	4.354	5.190	5.039
6	Flap (coupled)	4.760	4.695	5.034	4.947	6.022	5.904

*coupled: these are coupled flap-lag-torsion modes designated by their principle (dominant) motions

Figure 5-15 and Figure 5-16 show the frequencies of the hygrothermally stable composite rotors compared to the titanium spar rotor. There is little difference between the first four modes with maximum differences in the two higher modes (5 and 6), as shown in Table 5-3. In general, the hygrothermally stable composite spar blades are softer than the titanium, again shown in the dashed black lines.

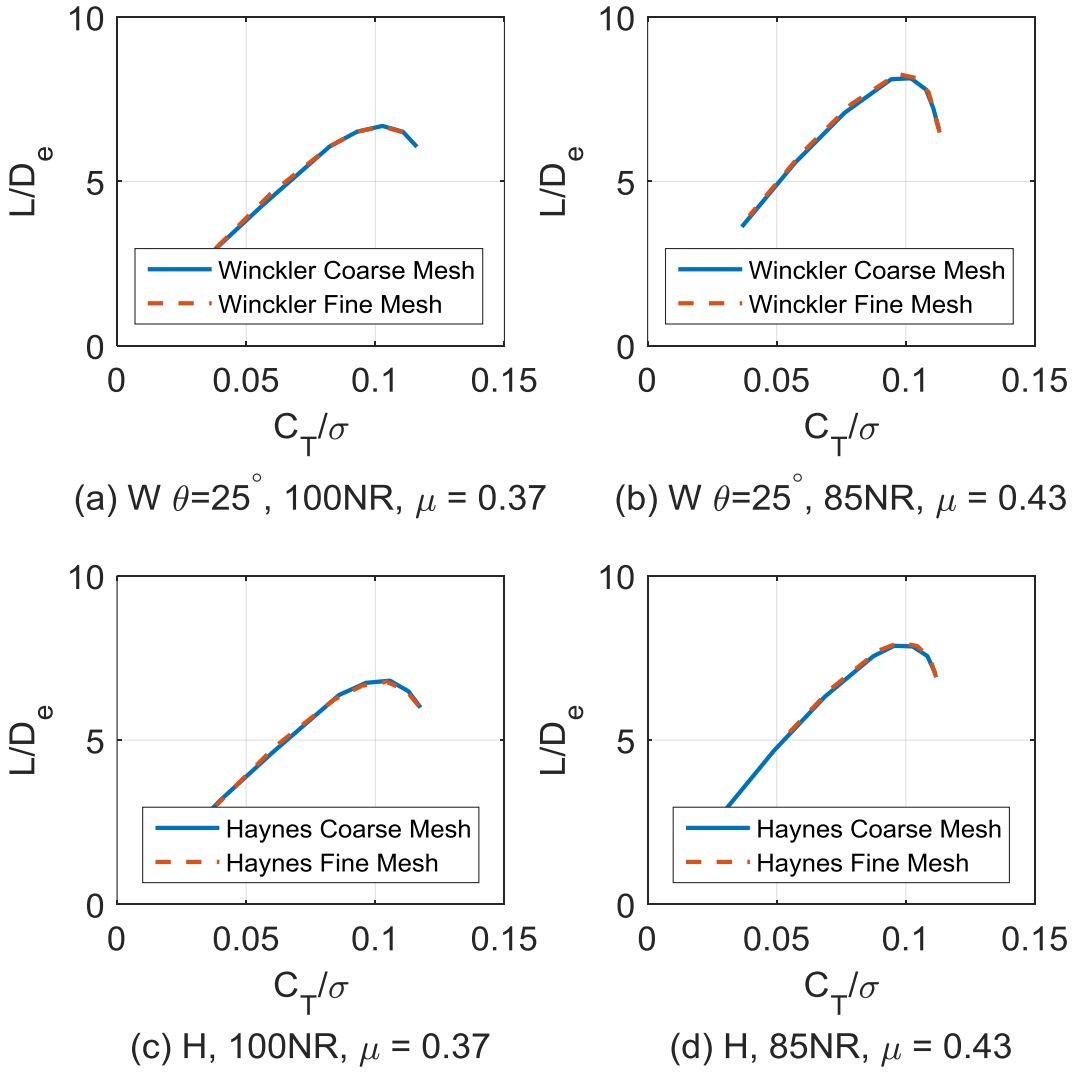

Figure 5-17. Comparing performance of coarse, homogenized material mesh to fine, ply resolved mesh for Winckler layup ($\theta = 25°$) and Haynes layup at 100NR

As indicated in Section 4.4.2.3, homogenized material properties were applied to the coarse mesh brick in the Winckler and Haynes layups. It was important to first validate that this simplification did not impact the rotor performance. Figure 5-17 (a) and (b) show the performance results for both the coarse and fine mesh Winckler rotor at two different rotor RPMs. Figure 5-17 (c) and (d) show the same, but for the Haynes layup. It is apparent that the mesh size does not have an impact on the rotor performance, regardless of layup applied or rotor RPM. These results reinforced confidence in the homogenization method and accuracy for this spar design and allowed us to continue our investigation using only the coarse mesh.

It only remains to be seen whether the Winckler and Haynes layups provide similar improvements as the nominal coupling or whether hygrothermal stability imparts a penalty in performance. At 100NR, shown in Figure 5-18 (a), there are no discernable differences between the rotor performances of the three coupled rotors. When the rotor RPM is reduced to 85NR ($\mu = 0.46$), see Figure 5-18 (b), the Winckler layup with $\theta = 25°$ and the nominal layup with $\theta = 45°$ outperform the Haynes layup, with a maximum L/D_e difference of 0.3 at $C_T/\sigma \approx 0.1$. When the RPM is slowed further to 65NR ($\mu = 0.57$) the Winckler layup outperforms both the nominal and Haynes blades by 0.3 and 0.5 respectively, at their peak ($C_T/\sigma \approx 0.09$). Based on these results it was determined that the Winckler blade was the most desirable design.

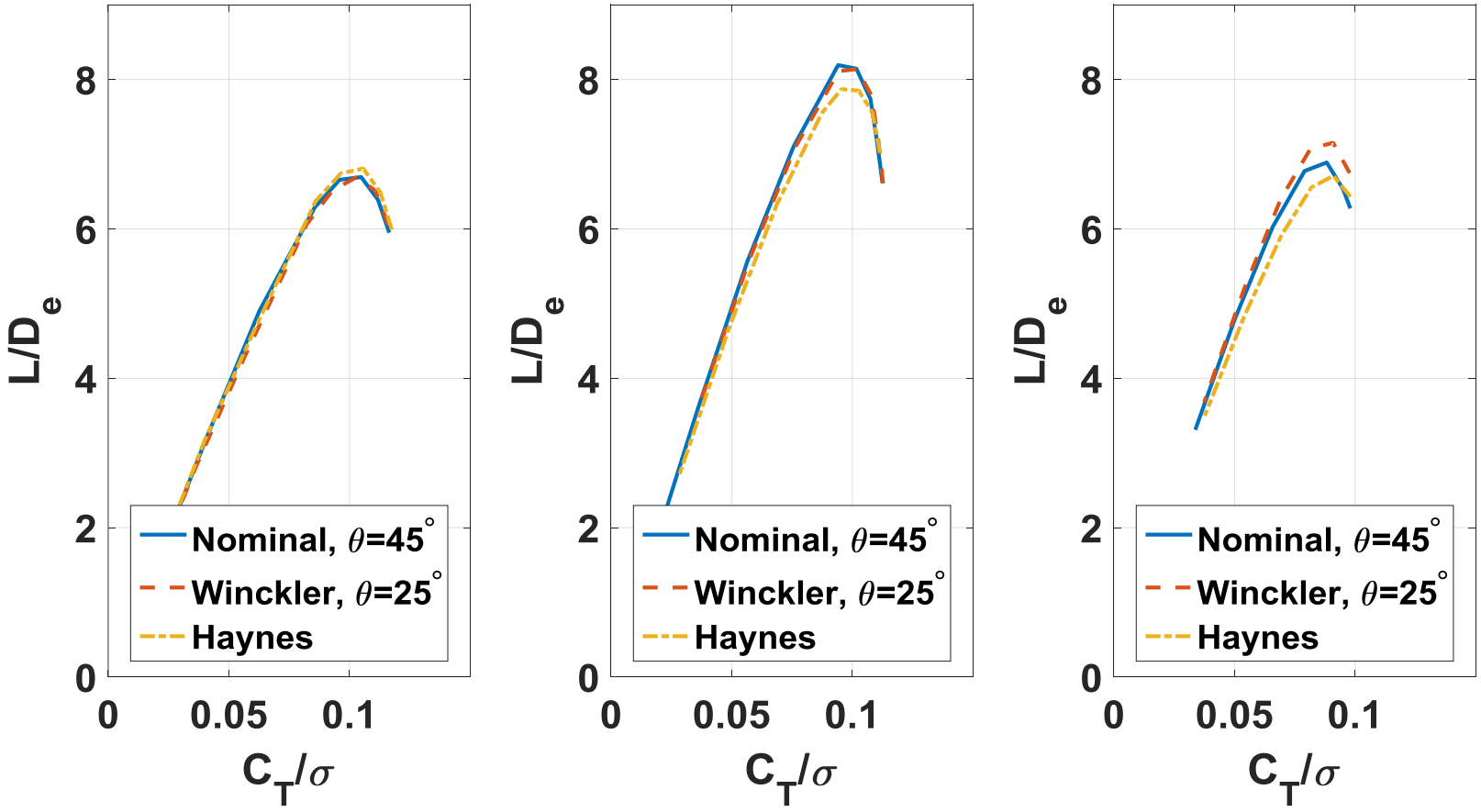

(a) 100NR, μ=0.37 85NR, μ=0.46 (c) 65NR, μ=0.57

Figure 5-18. L/D_e ratio vs. blade loading for Chandra-Chopra composite spar design compared to the hygrothermally stable designs of Winckler and Haynes at (a) 100NR, (b) 85NR, and (c) 65NR

Figure 5-19 and Figure 5-20 show the drag and lift variations of the Winckler blade compared to the nominal blade. The differences between the two are hardly discernible, which indicates that including hygrothermal stability does not significantly alter the rotor behavior. Investigation of lift, pitching moment, and elastic twist (as shown earlier for the nominal coupled blade) revealed the same and consistent patterns and are not repeated here. Of the three layups studied the Winckler layup provides the best performance, improving L/D_e at both slowed RPMs, relative to the uncoupled blade.

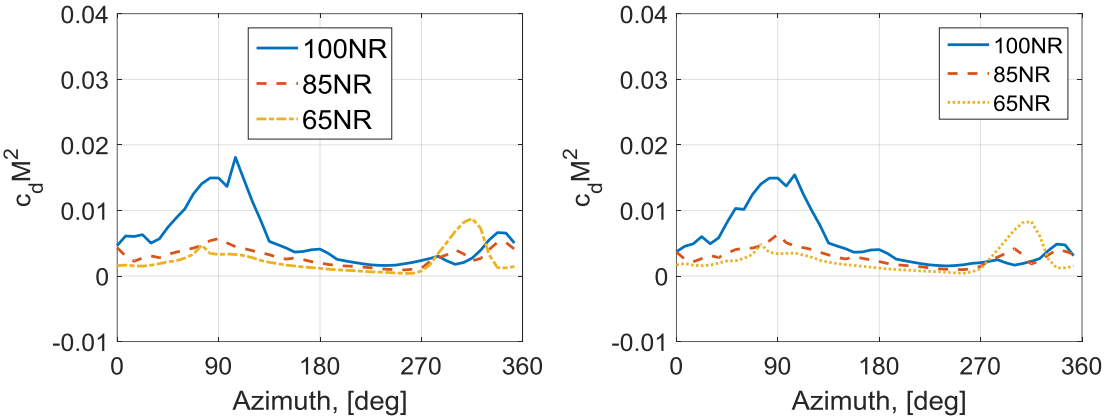

(a) Nominal ($\theta = 25°$), 89%R **(b) Winckler ($\theta = 25°$), 95%R**

Figure 5-19. Drag as a function of azimuth comparing the nominal coupled spar design to the Winckler layup (where $\theta = 25°$) for 100NR, 85NR, and 65NR

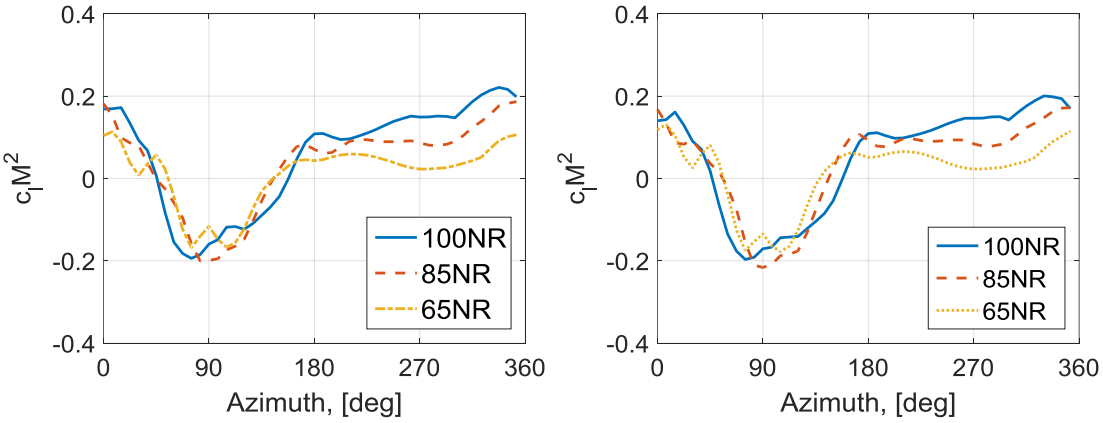

(a) Nominal ($\theta = 25°$), 89%R **(b) Winckler ($\theta = 25°$), 95%R**

Figure 5-20. Lift as a function of azimuth comparing the nominal coupled spar design to the Winckler layup (where θ=25°) for 100NR, 85NR, and 65NR

5.7 Rotor Hub Loads

Reduction of rotor RPM could possibly lead to substantial changes to the loads experienced at the rotor hub. Figure 5-21 shows that for the Winckler rotor this is not the case. There is in fact an overall reduction in the 4/rev vertical shear force, F_z, as the rotor RPM is reduced. At 85NR a more distinct 8/rev response is introduced. Slowing the rotor further to 65NR, the magnitude of this 8/rev content is diminished and the hub load returns to a similar loading to that of 100NR. Removing the mean of the hub vertical shear, (Figure 5-22), shows clearly that there is also a phase shift in the loading between 100NR and the 85NR and 65NR cases.

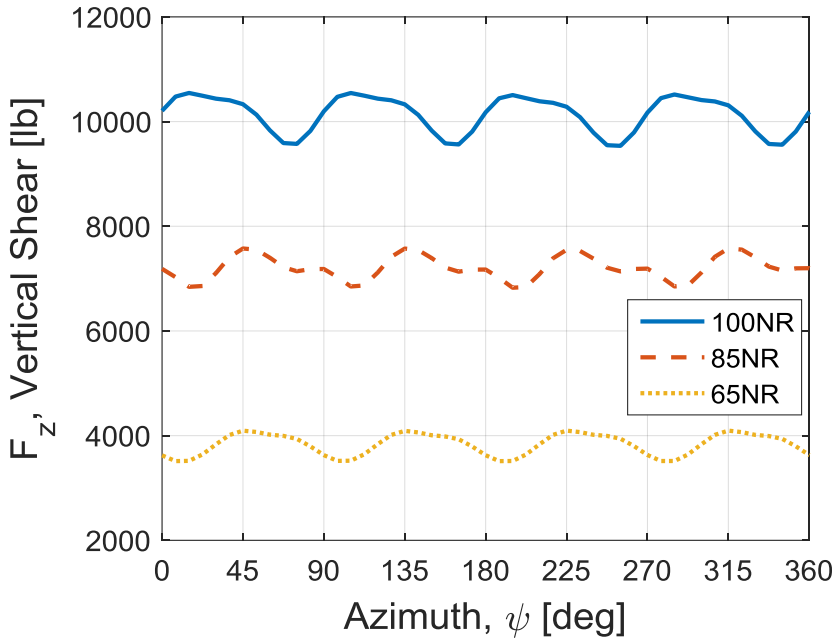

Figure 5-21. Vertical hub shear for a four bladed Winckler rotor at peak blade loading, $C_T/\sigma \approx 0.01$

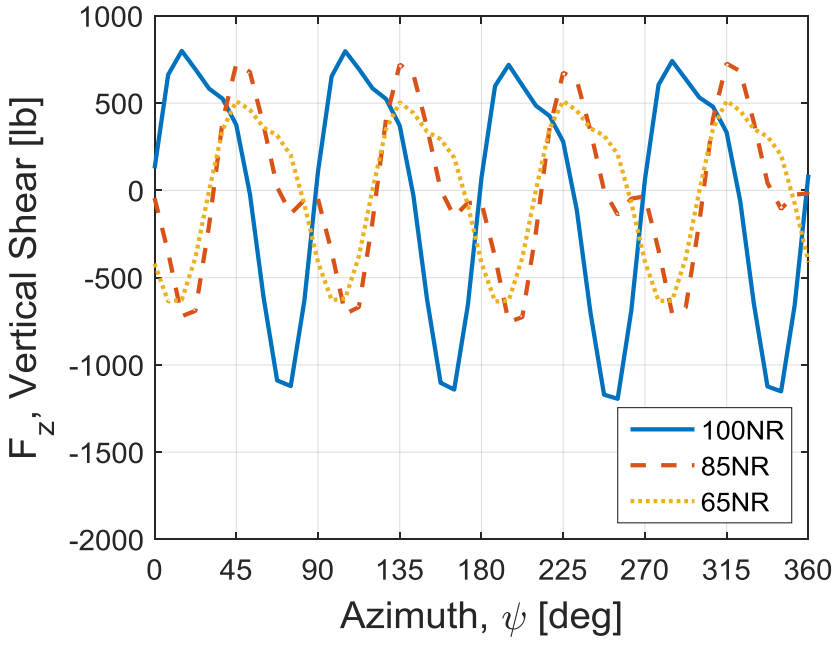

Figure 5-22. Mean removed vertical hub shear for a four bladed Winckler rotor at peak blade loading, $C_T/\sigma \approx 0.01$.

Figures 5-23 and 5-24 show how the change in rotor RPM effects the hub rolling (M_x) and pitching (M_y) moments, respectively. Figure 5-23 shows that there is an increase of about 27% in the peak-to-peak rolling moment when the RPM is reduced from 100NR to 85NR. However, there is a reduction in moment when the RPM is further reduced to 65NR, back down to the 100NR level. This is perhaps an indication that the increase from 100NR to 85NR is due to the change in blade natural frequencies (change in response) and not an increase in flow asymmetry due to increasing advance ratio, μ (change in/greater airloads). Similarly, for M_y, there is a 20% increase in peak-to-peak pitching moment when the RPM is reduced to 85NR. Further reduction in RPM to 65NR, however, decreases the moment significantly to benign levels (a 66.6% decrease from the 100NR peak-to-peak moment). As for rolling moment, some higher frequency content (8/rev) is also introduced in the pitching moment down at 65NR.

So overall, there is no dramatic detrimental effect on the hub loads – the 4/rev vertical shear generally drops below the 100NR level with about a 27% increase in hub rolling moment.

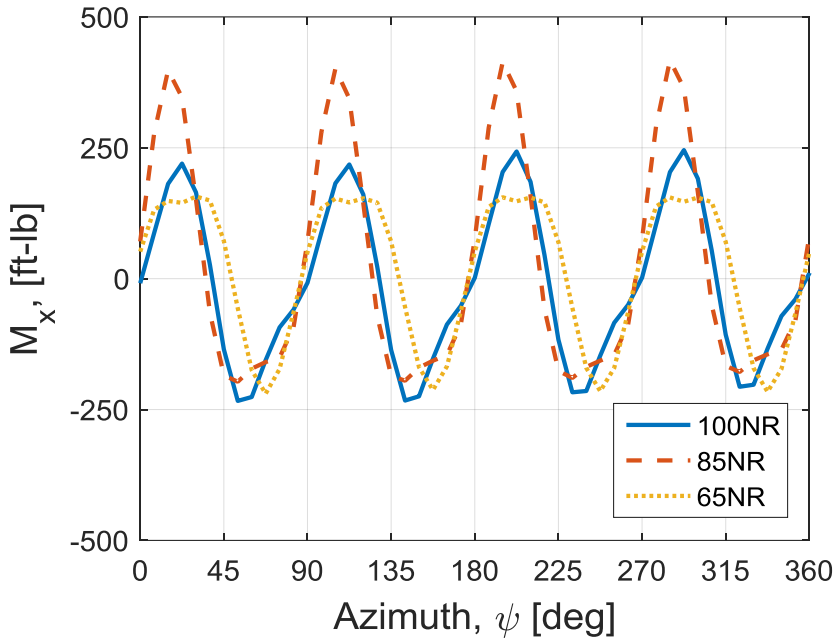

Figure 5-23. Hub roll moment (positive roll left, advancing side up), M_x, for a four bladed Winckler rotor at peak blade loading, $C_T/\sigma \approx 0.01$

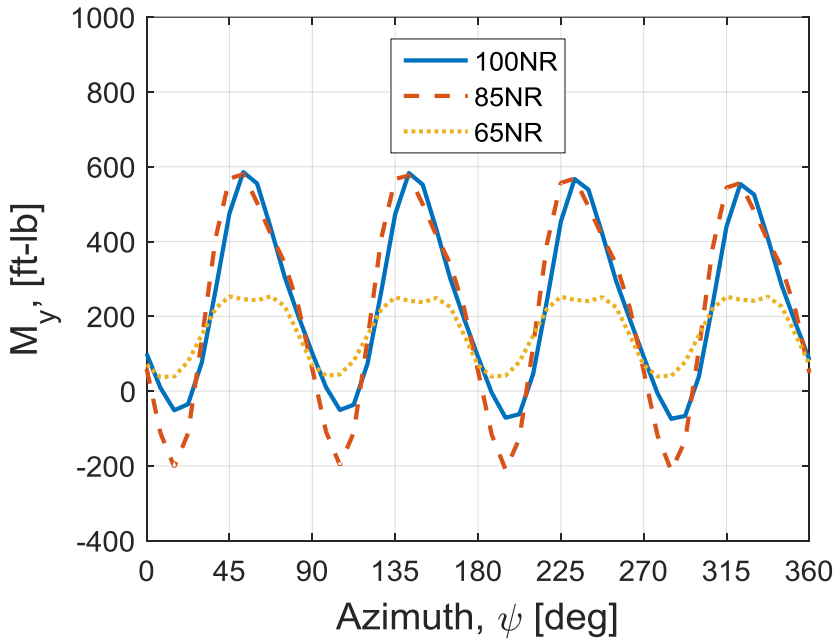

Figure 5-24. Hub pitching moment (positive pitch up), M_y, for a four bladed Winckler rotor at peak blade loading, $C_T/\sigma \approx 0.01$

5.8 Composite Spar Strains

Practical design requires that strength constraints of the materials be met. The material considered here, IM7/8552, has strain allowables of approximately 6000 microstrain (με) in tension, 4500 $\mu\varepsilon$ in compression, and 3000-4500 $\mu\varepsilon$ under cyclic loading [1] in the fiber direction. Figure 5-25 through Figure 5-27 show axial strains in the radial direction that the uncoupled and Winckler blade experiences at 100NR (E11 in the legend refers to ε_{11} or ε_x). Transformation of strain from the blade frame to the fiber direction can be carried out using Equation 5-1.

$$\varepsilon_x' = \varepsilon_x \cos^2\theta + \varepsilon_y \sin^2\theta + \varepsilon_{xy}\sin(\theta)\cos(\theta) \qquad 5\text{-}1$$

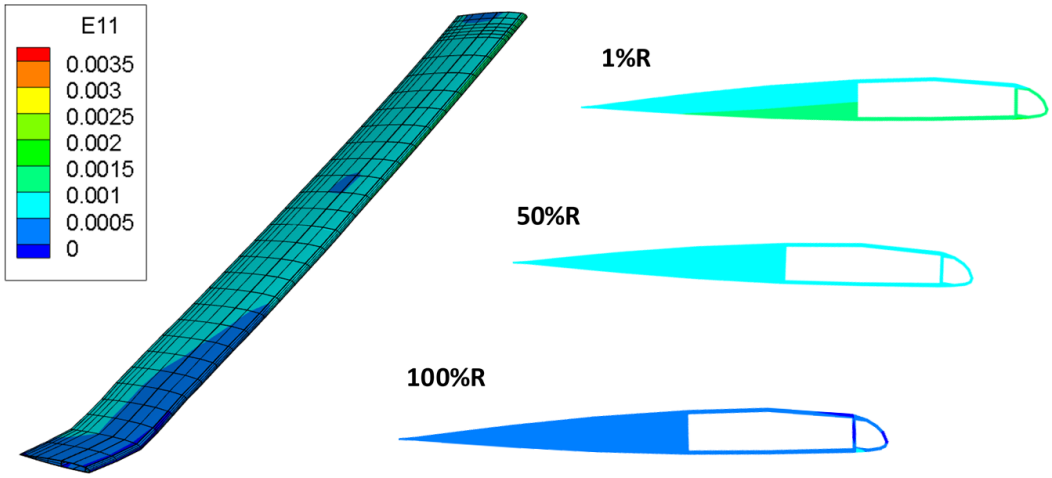

Figure 5-25. Axial strain in uncoupled rotor at 100NR, ψ = 0°

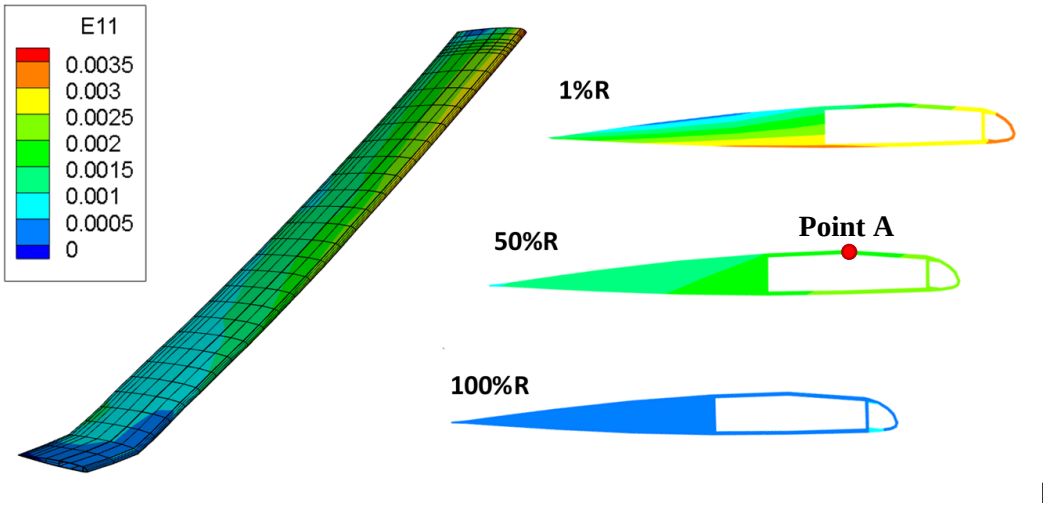

Figure 5-26. Axial strain in a Winckler coupled rotor at 100NR, $\psi = 0°$

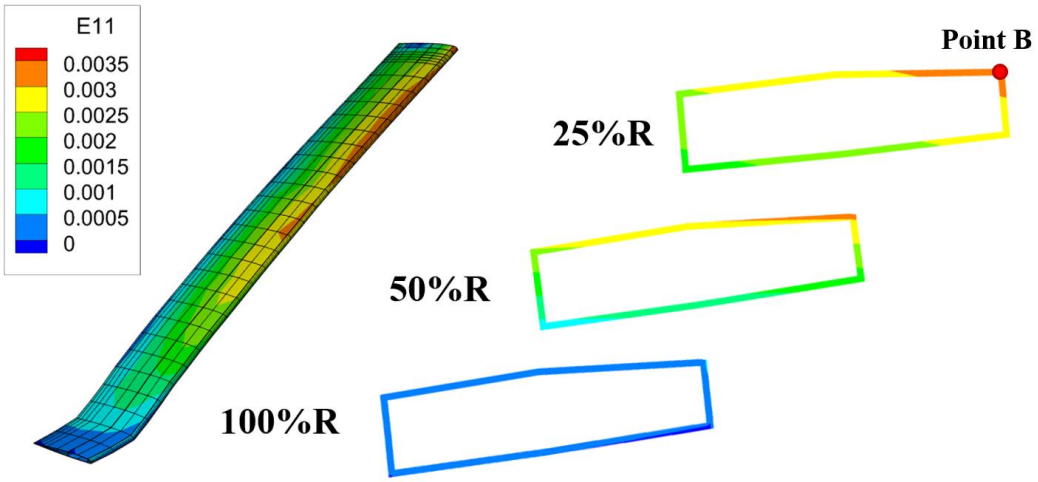

Figure 5-27. Axial strain in a Winckler coupled rotor at 100NR, $\psi = 97.5°$ where large axial strain in the spar is found

For the homogenized spar meshes there is no applied ply angle between the global and fiber frame, as the calculated material properties already include the appropriate ply orientations. The Winckler blade utilizes four different ply orientations to ensure hygrothermal stability. When both the fine and coarse global strain results were

transformed into the coordinate's corresponding ply direction, Figure 5-28 (a) and (b), were obtained. These show that the difference in the fiber strain between both is minimal, with the fine mesh naturally providing greater resolution.

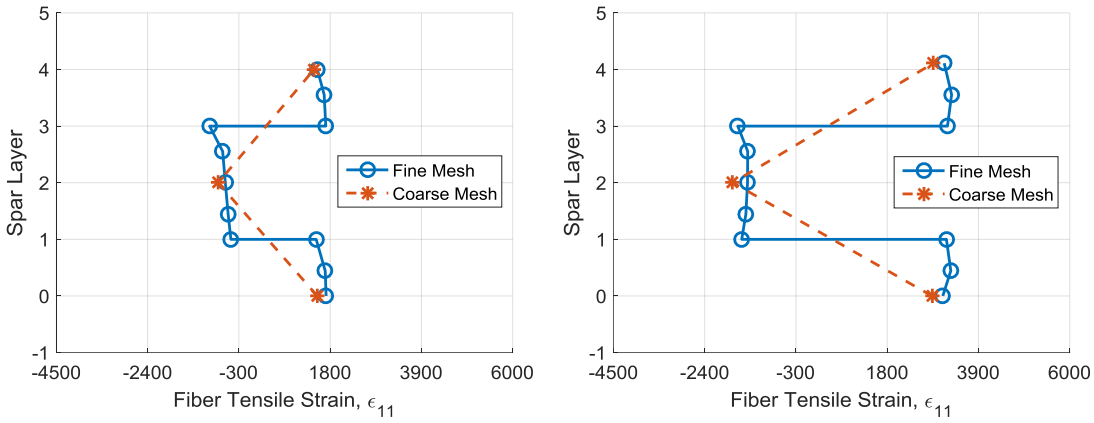

(a) Strain at at 50%R, Point A, and azimuth $\psi = 0°$

(b) Strain at 25%R, Point B, and azimuth $\psi = 97.5°$

Figure 5-28. Fiber tensile strain, ε_{11}, for ply resolved (fine mesh) and homogenized (coarse mesh) blades with a Winckler layup of [25°/115°/115°/25°]

Note the fiber strain is well within the allowable strain for IM7/8552. A margin of safety of about 1.9 tension and 2.6 in compression is found. Figure 5-28 (b) shows the fiber

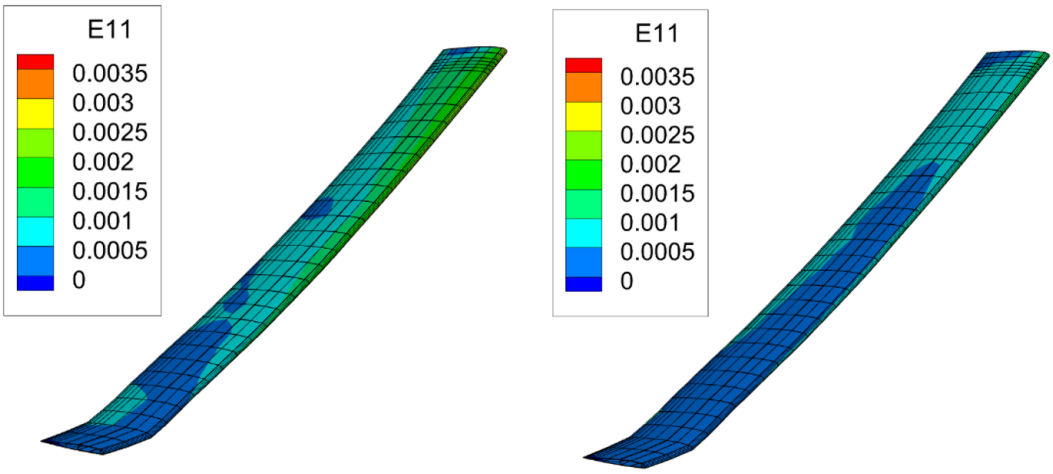

(a) 85NR

(b) 65NR

Figure 5-29. Reduced axial strain for the Winckler rotor at 85NR and 65NR, at $\psi = 0°$

strain at 25%R, along the advancing side of the rotor, and at a leading edge corner of the spar (reference Point B in Figure 5-27). At this area of high strain concentration it can be seen that the fiber direction strains still do not exceed the allowables.

Extension-torsion coupling is brought into play by extensional strain, so naturally the Winckler blade encounters higher strains at higher RPM. Figure 5-26 shows generally that there is greater axial strain towards the blade root compared to the uncoupled rotor, in Figure 5-25. In order to achieve the same twist as the uncoupled rotor at 100NR, the coupled rotor goes through a change of approximately 10° twist at the tip. As the rotor RPM is decreased, and the coupled blade begins to return to its cold shape (reduces the built-in twist), the large strains disappear, as shown in Figure 5-29.

This is further illustrated by Figure 5-30 (a) and (b). In this figure the maximum and minimum ε_{11} value in the blade spar was plotted as a function of azimuth. It should be noted that these values do not all occur at the same node, but are clustered: at two points at the root end of the blade for extension, and at three points at the tip for compression. Figure 5-30 (a) highlights magnitude difference in extensional strain experienced by the rotor as the rotor RPM, and therefore the centrifugal load, is reduced. Figure 5-30 (b) highlights how the reduction in RPM also reduces centrifugal stiffening. It can be seen here that as the RPM is reduced, the spar experiences much stronger spikes of compressive strain. This figure also illustrates, however, that regardless of location, the maximum and minimum strains experienced by the rotor fall with the allowable ranges for IM7/8552.

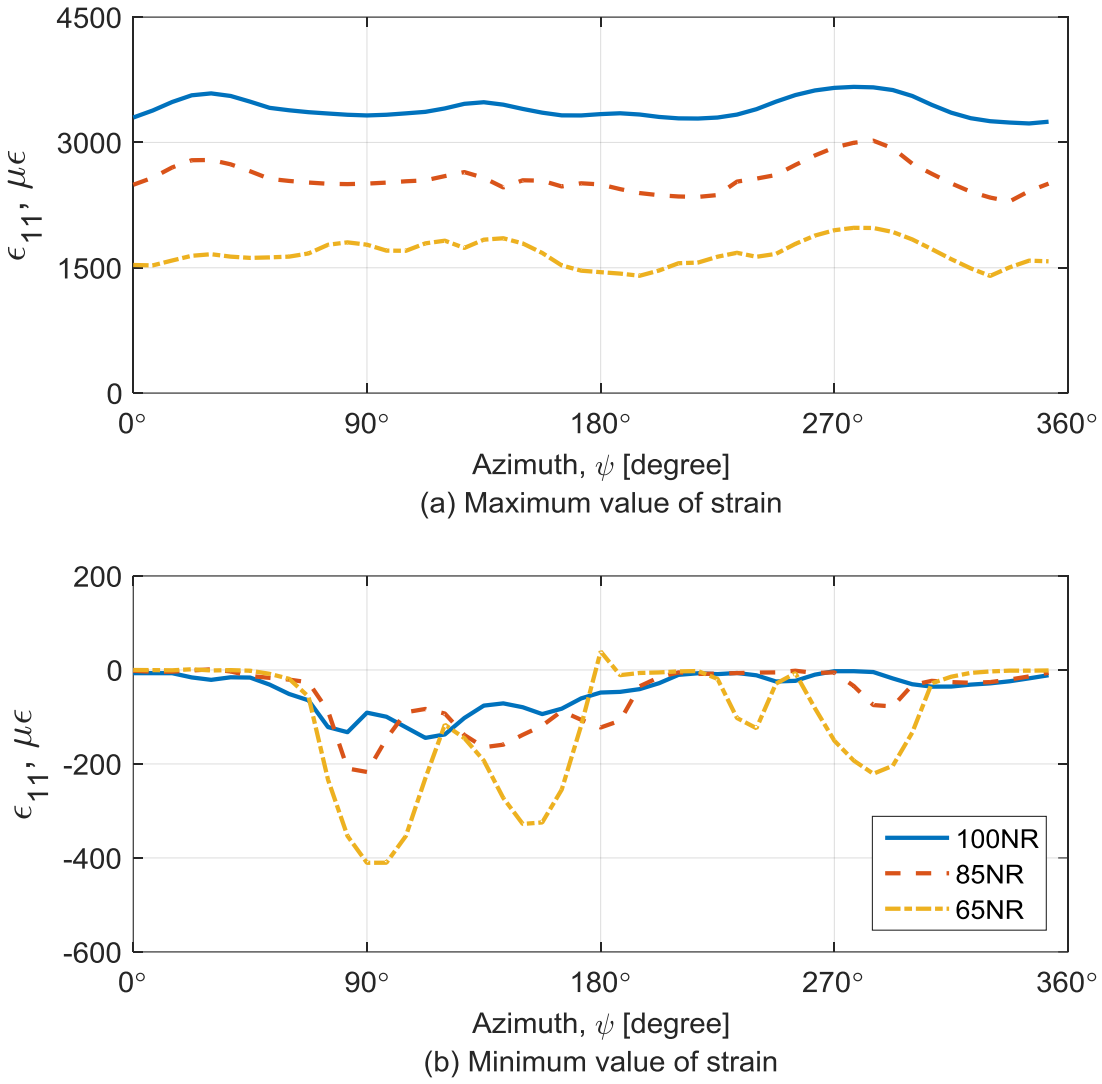

Figure 5-30. Maximum and minimum strain ε_{11} experienced by the Winckler spar at various RPMs

It is also industry practice to consider the potential for rotor overspeed up to 15% of the nominal RPM. Figure 5-31 shows that at 115NR, the Winckler spar rotor strains fall within the allowable strains for IM7/8552. As expected, with an increase in centrifugal loading, there is an increase in the axial strain. While it is not recommended to continuously operate at this speed, the composite material is able to withstand it.

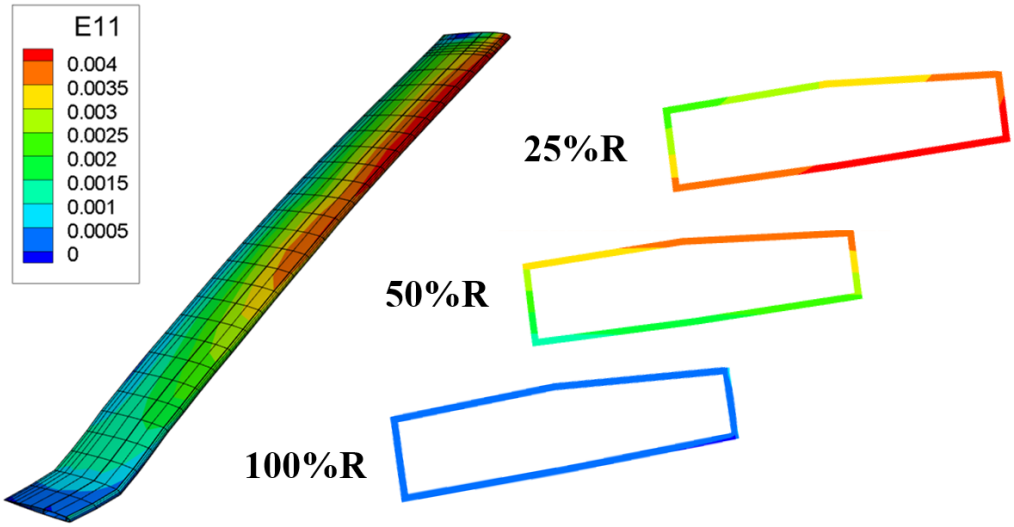

Figure 5-31. Increased axial strain for the Winckler rotor in oversped conditions (115NR, at $\psi = 112.5°$)

Chapter 6: Conclusions

6.1 Summary

The goal of this research was to investigate the variation of built-in twist in a helicopter rotor blade during flight due to the inclusion of composite coupling, in particular extension-torsion coupling, and characterize its effects on the efficiency of an articulated rotor in high-speed flight. To study this, a UH-60A-like rotor with a metallic spar was used as the baseline blade as it is the only production rotor that has undergone extensive wind tunnel testing at slowed RPMs, down to 40NR, and high advance ratios, up to $\mu = 1.0$. This baseline blade was validated using the UH-60A test data from the Ames high-μ, 40 ft x 8ft full-scale wind tunnel in 2010, including analytical compensation for the highly instrumented, non-aerodynamic blade shank.

The UH-60A blade was then modified, replacing the spar material with composite, IM7/8552 ply layups. The baseline inertial properties, such as c.g. and mass, were maintained to ensure proper comparisons could be made. Three extension-torsion coupled layups were analyzed: one with a purely academic antisymmetric layup, and two that were hygrothermally stable. To provide reliable comparisons, all composite blades were designed to have the same twist at 100NR, or the hover RPM. The composite coupling allowed for the blades to de-twist towards the built in twist (cold shape) as the RPM was reduced.

The benefits of coupling were studied in detail. Departure from the baseline titanium spar performance and the relative differences in the aerodynamic operating envelopes of all the blades was characterized. Additionally, as a preliminary step in characterizing the manufacturability of the rotor, strains were analyzed to determine whether they remained within the allowable limits for IM7/8552. This provided key information on where a more detailed strain analysis should be conducted for accurate characterization of possible failure modes.

6.2 Specific Conclusions

Based on the current study, the following specific conclusions are drawn:

(i) To account for the non-aerodynamic, highly instrumented blade shank that was used in the experimental testing of the UH-60A blade, validation of an analytical shank drag coefficient was conducted. It was determined that a shank drag coefficient of 0.75 across 8-20%R was sufficient to provide an acceptable correlation of L/D_e, including drag, power, and thrust, up to an advance ratio of $\mu = 0.6$. As most rotors do not have such highly instrumented, non-aerodynamic sections, it is assumed that this correction will not be needed for the analysis of future rotor designs.

(ii) When the rotor is slowed to 85NR, the extension-torsion coupling from the nominal layup, with $\theta = 45°$, provides enough twist differential from the 100NR case to provide an increase in rotor aerodynamic efficiency. As the uncoupled rotor does not untwist as the rotor slows it is well established that the twist plays a large role in this efficiency gain. The maximum value of rotor efficiency

improvement seen was 20% over the uncoupled blade, occurring at a blade loading of $C_T/\sigma = 0.1$. Additionally, coupling provided an improvement in aerodynamic efficiency over the entire range of blade loading.

(iii) Though a highly coupled phenomenon, the improvement in rotor efficiency was shown to be due to a decrease in negative lift along the advancing side of the rotor. This reduction was shown to play a role in the reduction in drag and alleviation of stall.

(iv) The nominal composite coupling can only provide a performance boost for a limited range of operating RPMs and blade loading combinations. At 65NR it was shown that the *maximum* rotor efficiency was not affected by the change in rotor twist, however at blade loadings below $C_T/\sigma = 0.09$ the composite coupled rotor outperformed the uncoupled rotor by a maximum of 15%.

(v) It was shown that the use of hygrothermally stable extension-torsion coupled layups does not negatively impact rotor performance and provides practical manufacturability to the design. At 85NR the Winckler layup performed equally as well as the nominal layup with an L/D_e of 8.14 at $C_T/\sigma \approx 0.1$. The Haynes layup performed marginally worse than the Winckler rotor, but still better than the uncoupled rotor.

(vi) When the rotor RPM was reduced to 65NR, the Winckler rotor outperformed both the nominal and Haynes rotors by a maximum L/D_e of 0.3 and 0.5 respectively, at $C_T/\sigma \approx 0.09$, showing an improved performance range over the nominally coupled rotor.

(vii) The axial strain seen in the Winckler rotor falls within the allowable strain for IM7/8552 for RPMs up to 100NR. This strain was not found in the uncoupled rotor at 100NR (where there was no change in twist) and was reduced as the rotor RPM slowed (less change in twist). The elastic twist and the extension needed to induce it play a key role in axial strain.

6.3 Recommendations for Future Work

The research presented in this dissertation is the first step in proving the benefits of designing future slowed-rotor designs with composite coupling. However, significant work needs to be done in order to make these design choices a reality in future generations of high speed rotorcraft. There are two areas specifically that are recommended for future work: experimentation and analysis.

Unfortunately, with the exception of the experimental tests conducted by Ames, there are no data sets to validate high-speed, slowed rotor designs with composite coupling. To validate the results shown in Chapter 5, it would be prudent to build and test a Mach scaled rotor with no coupling, and an identically constructed blade with a Winckler layup. As the spar and ply thickness was idealized based on a simplified UH-60A model, a more formal design optimization should be conducted to achieve the desired coupling at this scale. Additionally, there must be careful consideration of manufacturing techniques avoid delamination at material junctures or locations of changing ply orientation. The design of a clean blade is also crucial as it would eliminate the shank drag uncertainty that had to be accounted for (via analytical tuning) as discussed in Section 4.3.

The strength of an integrated analysis tool like X3D is in its capability to conduct formal optimizations. Therefore, a study should be conducted to determine the optimum slowed RPM and the required layup to achieve the ideal spanwise twist distribution in both hover and cruise conditions.

As X3D is capable of coupling with Helios, the aerodynamics should also be upgraded to CFD for further study of the 3-D aeromechanics of the morphing system. This would provide a more accurate prediction of the dynamic pitching, especially towards the rotor tip. However, while the framework exists, modifications are required to CFD software tools to enable true compatibility with the 3-D structural dynamics provided by X3D.

Another modification to X3D that would be beneficial is the need for a scheme that allows the solver to orient the composite ply properties based on undeformed mesh shapes. The current version of this tool cannot rotate the material properties to follow the twist of the rotor and so must be done by the problem designer manually. Automation of this process would allow for easier application of composites and a more streamlined process.

Finally, a detailed analysis of interlaminar stresses/strains should be conducted. While the current results provided gross trends and are helpful in identifying key areas of possible failure, it does not provide the ply resolved stresses and strains that would define specific failure modes. This requires an automated process for three-dimensional interpolation of stress/strain values at known mesh nodes to ply interfaces, which are not necessarily located at discrete nodes.

Appendix I

Recall from Section 2.1.2 the strain-displacement relations based on kinematics:

$$\varepsilon_{xx}^{0} = U_{,x} - yV_{,xx} - zW_{,xx} + \psi\phi_{,xx}$$
$$\gamma_{xs}^{0} = \left(\psi_{,s} + r\right)\phi_{,x} \qquad \text{2-12}$$

where $\left(\psi_{,s} + r\right) = \dfrac{2A_e}{\oint \dfrac{ds}{A_{66}}}\left(\dfrac{1}{A_{66}}\right)$

The shear strain γ_{xs}^{0} in Equation 1a is obtained from kinematic and displacement considerations using equilibrium of displacements.

A.1 Shear strain from stress equilibrium of an element

The shear strain can also be obtained from force balance. Consider a simple rectangular element, depicted in Figure A1 below.

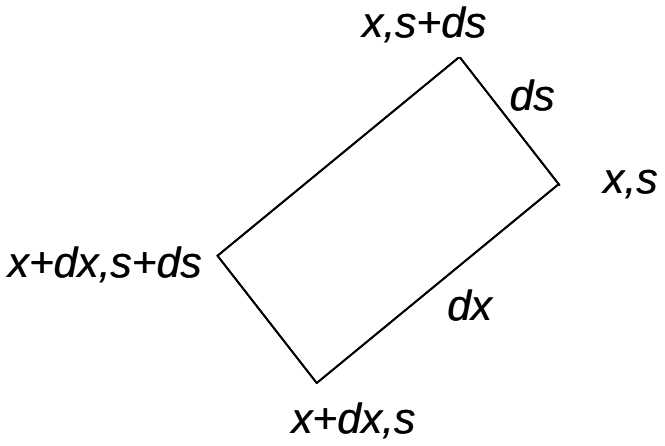

A1. Simple rectangular element

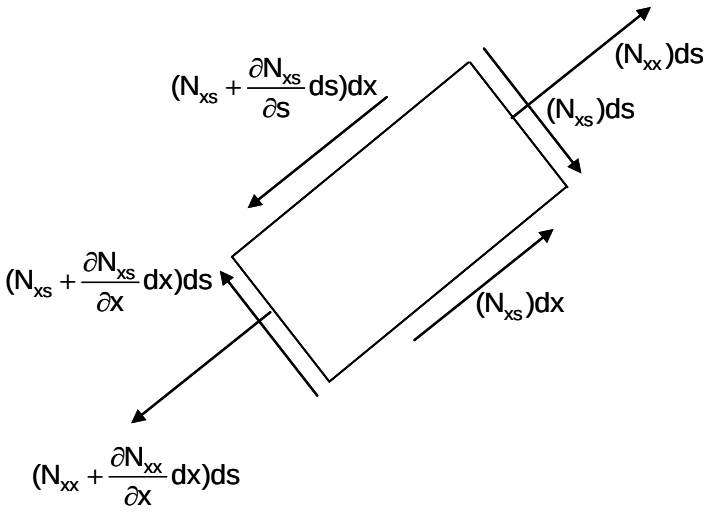

Forces on each face

A2. Forces experienced by rectangular element's faces

Figure A2 shows the forces acting on the four faces of the element. The balance of forces in the $x-$ and $s-$ directions yields the following equations:

$$N_{xx}ds - \left(N_{xx} + \frac{\partial N_{xx}}{\partial x}dx\right)ds + N_{xs}dx - \left(N_{xs} + \frac{\partial N_{xs}}{\partial s}ds\right)dx = 0$$

$$N_{xs}dx - \left(N_{xs} + \frac{\partial N_{xs}}{\partial x}ds\right)dx = 0$$

Simplifying this we get:

$$\frac{\partial N_{xx}}{\partial x} + \frac{\partial N_{xs}}{\partial s} = 0 \qquad \text{A-1}$$

$$\frac{\partial N_{xs}}{\partial x} = 0 \qquad \text{A-2}$$

The first of the equilibrium equations, Equation A-1, defines the shear flow as:

$$N_{xs} = N_{xs}^0 - \int_0^s \frac{\partial N_{xx}}{\partial x} ds \qquad \text{A-3}$$

where N_{xs}^0 is a constant.

The second of the equilibrium equations, Equation A-2, indicates that N_{xs} is independent of x and therefore has the same value at all cross-sections.

A.2 Solve for N_{xs}^0

Equation A-4 relates the stress flow (in units of force per unit length) to the strains through a stiffness matrix. It is assumed that we know the strains which will enable us to find the corresponding stresses. This expression can also be written in semi-inverted form, as shown by Equation A-5.

$$\begin{Bmatrix} N_{xx} \\ N_{xs} \end{Bmatrix} = \begin{bmatrix} A_{11} & A_{16} \\ A_{16} & A_{66} \end{bmatrix} \begin{Bmatrix} \varepsilon_{xx}^0 \\ \gamma_{xs}^0 \end{Bmatrix} \qquad \text{A-4}$$

$$\begin{Bmatrix} N_{xx} \\ \gamma_{xs}^0 \end{Bmatrix} = \begin{bmatrix} A_{11} - \frac{A_{16}^2}{A_{66}} & \frac{A_{16}}{A_{66}} \\ -\frac{A_{16}}{A_{66}} & \frac{1}{A_{66}} \end{bmatrix} \begin{Bmatrix} \varepsilon_{xx}^0 \\ N_{xs} \end{Bmatrix} \qquad \text{A-5}$$

In Equation A-5 it is assumed that the direct strain, ε_{xx}^0, and the shear flow, N_{xs}^0, are known. The name "Mixed Method" comes from the fact that we know one displacement and one force. Expanding Equation A-5 yields:

$$\begin{aligned} N_{xx} &= \left(A_{11} - \frac{A_{16}^2}{A_{66}} \right) \varepsilon_{xx}^0 + \frac{A_{16}}{A_{66}} N_{xs} \\ \gamma_{xs}^0 &= -\frac{A_{16}}{A_{66}} \varepsilon_{xx}^0 + \frac{1}{A_{66}} N_{xs} \end{aligned} \qquad \text{A-6}$$

Substituting the relation for N_{xx} into Equation A-3 we get:

$$
\begin{aligned}
N_{xs} &= N_{xs}^0 - \int_0^s \frac{\partial N_{xx}}{\partial x} ds \\
&= N_{xs}^0 - \int_0^s \left(A_{11} - \frac{A_{16}^2}{A_{66}}\right)\left(\frac{\partial \varepsilon_{xx}^0}{\partial x}\right) ds \\
&= N_{xs}^0 - \int_0^s \left(A_{11} - \frac{A_{16}^2}{A_{66}}\right)\left(U_{,xx} - yV_{,xxx} - zW_{,xxx} + \psi\phi_{,xxx}\right) ds
\end{aligned}
\qquad \text{A-7}
$$

The second term of Equation A-7 contains $U_{,xx}$, $V_{,xxx}$, $W_{,xxx}$, and $\phi_{,xxx}$ which represent (higher order) shear related terms. For first approximation, these are neglected and Equation A-7 collapses to a constant. Now that $N_{xs} = N_{xs}^0$, it can be substituted into Equation A-5 to express the shear strain as:

$$
\gamma_{xs}^0 = -\frac{A_{16}}{A_{66}}\varepsilon_{xx}^0 + \frac{1}{A_{66}}N_{xs}^0 \qquad (Force\ equilibrium) \qquad \text{A-8}
$$

There are now two relations for γ_{xs}^0: Equation 2-12, which was obtained from displacement and kinematic considerations and Equation A-8, which was obtained from force-equilibrium conditions. The shear strain from Equation 2-12 will not, in general, satisfy the force equilibrium conditions. It is possible to obtain a better approximation for γ_{xs}^0 by equating the two expressions and requiring that the integral of the difference over the contour is zero.

$$
\oint \left[\left(\psi_{,s} + r\right)\phi_{,x} + \frac{A_{16}}{A_{66}}\varepsilon_{xx}^0 - \frac{1}{A_{66}}N_{xs}^0\right] ds = 0 \qquad \text{A-9}
$$

Equation A-9 is solved for the shear flow:

$$N_{xs}^{0} = \frac{\oint \frac{A_{16}}{A_{66}} \varepsilon_{xx}^{0}\, ds}{\oint \frac{1}{A_{66}} ds} + \frac{\oint (\psi_{,s} + r)\phi_{,x}\, ds}{\oint \frac{1}{A_{66}} ds}$$

$$= \frac{\oint \frac{A_{16}}{A_{66}}\, ds}{\oint \frac{1}{A_{66}} ds} U_{,x} - \frac{\oint y \frac{A_{16}}{A_{66}} ds}{\oint \frac{ds}{A_{66}}} V_{,xx} - \frac{\oint z \frac{A_{16}}{A_{66}} ds}{\oint \frac{ds}{A_{66}}} W_{,xx} + \frac{\oint \psi \frac{A_{16}}{A_{66}} ds}{\oint \frac{ds}{A_{66}}} \phi_{,xx} + \frac{2A_e}{\oint \frac{ds}{A_{66}}} \phi_{,x} \qquad \text{A-10}$$

The stress-strain relations can now be expressed as follows:

$$N_{xx} = \left(A_{11} - \frac{A_{16}^2}{A_{66}}\right) \varepsilon_{xx}^{0} + \frac{A_{16}}{A_{66}} N_{xs}$$

$$= \left(A_{11} - \frac{A_{16}^2}{A_{66}}\right) \left(U_{,x} - y V_{,xx} - z W_{,xx} + \psi \phi_{,xx}\right) + \frac{A_{16}}{A_{66}} N_{xs}$$

$$N_{xs} = N_{xs}^{0} = \frac{\oint \frac{A_{16}}{A_{66}} ds}{\oint \frac{1}{A_{66}} ds} U_{,x} - \frac{\oint y \frac{A_{16}}{A_{66}} ds}{\oint \frac{ds}{A_{66}}} V_{,xx} - \frac{\oint z \frac{A_{16}}{A_{66}} ds}{\oint \frac{ds}{A_{66}}} W_{,xx} + \frac{\oint \psi \frac{A_{16}}{A_{66}}\, ds}{\oint \frac{ds}{A_{66}}} \phi_{,xx} + \frac{2A_e}{\oint \frac{ds}{A_{66}}} \phi_{,x} \qquad \text{A-11}$$

Equation A-11 is in mixed form. N_{xx} is expressed in terms of the displacements and also N_{xs}. In the displacement method, N_{xs} would have contained only the final term. Because N_{xs} is expressed in terms of displacements, Equation A-11 has both N_{xx} and N_{xs} in terms of displacements and can now be used for calculation of the stiffness matrix.

A.3 Derivation of the cross-section stiffness matrix (Newtonian Method)

1. Axial Force

$$
\begin{aligned}
N &= \oint N_{xx} ds = \oint \left[\left(A_{11} - \frac{A_{16}^2}{A_{66}} \right) \left(U_{,x} - y V_{,xx} - z W_{,xx} + \psi \phi_{,xx} \right) + \frac{A_{16}}{A_{66}} N_{xs} \right] ds \\
&= U_{,x} \oint \left(A_{11} - \frac{A_{16}^2}{A_{66}} \right) ds - W_{,xx} \oint z \left(A_{11} - \frac{A_{16}^2}{A_{66}} \right) ds - V_{,xx} \oint y \left(A_{11} - \frac{A_{16}^2}{A_{66}} \right) ds \\
&\quad + \phi_{,xx} \oint \psi \left(A_{11} - \frac{A_{16}^2}{A_{66}} \right) ds + \frac{\left(\oint \frac{A_{16}}{A_{66}} ds \right)^2}{\oint \frac{1}{A_{66}} ds} U_{,x} \\
&\quad - \frac{\oint \frac{A_{16}}{A_{66}} ds \oint y \frac{A_{16}}{A_{66}} ds}{\oint \frac{ds}{A_{66}}} V_{,xx} - \frac{\oint \frac{A_{16}}{A_{66}} ds \oint z \frac{A_{16}}{A_{66}} ds}{\oint \frac{ds}{A_{66}}} W_{,xx} \\
&\quad + \frac{2A_e \oint \frac{A_{16}}{A_{66}} ds}{\oint \frac{ds}{A_{66}}} \phi_{,x} + \frac{\oint \frac{A_{16}}{A_{66}} ds \oint \psi \frac{A_{16}}{A_{66}} ds}{\oint \frac{ds}{A_{66}}} \phi_{,xx}
\end{aligned}
$$

2. Bending Moment about z-axis:

$$
\begin{aligned}
M_y &= -\oint N_{xx} z \, ds \\
&= -\oint \left[\left(A_{11} - \frac{A_{16}^2}{A_{66}} \right) \left(z U_{,x} - yz V_{,xx} - z^2 W_{,xx} + z \psi \phi_{,xx} \right) + \frac{A_{16}}{A_{66}} z N_{xs} \right] ds \\
&= -U_{,x} \oint \left(A_{11} - \frac{A_{16}^2}{A_{66}} \right) z ds + W_{,xx} \oint z^2 \left(A_{11} - \frac{A_{16}^2}{A_{66}} \right) ds \\
&\quad + V_{,xx} \oint yz \left(A_{11} - \frac{A_{16}^2}{A_{66}} \right) ds - \phi_{,xx} \oint \psi z \left(A_{11} - \frac{A_{16}^2}{A_{66}} \right) ds \\
&\quad - \frac{\oint \frac{A_{16}}{A_{66}} ds \oint z \frac{A_{16}}{A_{66}} ds}{\oint \frac{ds}{A_{66}}} U_{,x} + \frac{\oint z \frac{A_{16}}{A_{66}} ds \oint y \frac{A_{16}}{A_{66}} ds}{\oint \frac{ds}{A_{66}}} V_{,xx} \\
&\quad + \frac{\left(\oint z \frac{A_{16}}{A_{66}} ds \right)^2}{\oint \frac{ds}{A_{66}} W_{,xx}} W_{,xx} - \frac{2A_e \oint z \frac{A_{16}}{A_{66}} ds}{\oint \frac{ds}{A_{66}}} \phi_{,x} \\
&\quad - \frac{\oint z \frac{A_{16}}{A_{66}} ds \oint \psi \frac{A_{16}}{A_{66}} ds}{\oint \frac{ds}{A_{66}}} \phi_{,xx}
\end{aligned}
$$

3. Bending Moment about y-axis

$$M_z = -\oint N_{xx} y \, ds$$

$$= \oint \left[\left(A_{11} - \frac{A_{16}^2}{A_{66}} \right) \left(-yU_{,x} + y^2 V_{,xx} + yzW_{,xx} - y\psi\phi_{,xx} \right) - \frac{A_{16}}{A_{66}} y N_{xs} \right] ds$$

$$= -U_{,x} \oint \left(A_{11} - \frac{A_{16}^2}{A_{66}} \right) y \, ds + W_{,xx} \oint yz \left(A_{11} - \frac{A_{16}^2}{A_{66}} \right) ds$$

$$+ V_{,xx} \oint y^2 \left(A_{11} - \frac{A_{16}^2}{A_{66}} \right) ds - \phi_{,xx} \oint y\psi \left(A_{11} - \frac{A_{16}^2}{A_{66}} \right) ds$$

$$- \frac{\oint y \frac{A_{16}}{A_{66}} ds \oint \frac{A_{16}}{A_{66}} ds}{\oint \frac{ds}{A_{66}}} U_{,x} + \frac{\left(\oint y \frac{A_{16}}{A_{66}} ds \right)^2}{\oint \frac{ds}{A_{66}}} V_{,xx}$$

$$+ \frac{\oint y \frac{A_{16}}{A_{66}} ds \oint z \frac{A_{16}}{A_{66}} ds}{\oint \frac{ds}{A_{66}}} W_{,xx} - \frac{2A_e \oint y \frac{A_{16}}{A_{66}} ds}{\oint \frac{ds}{A_{66}}} \phi_{,x}$$

$$- \frac{\oint y \frac{A_{16}}{A_{66}} ds \oint \psi \frac{A_{16}}{A_{66}} ds}{\oint \frac{ds}{A_{66}}} \phi_{,xx}$$

4. Torsion:

$$M_x = \oint N_{xs} (\psi_{,s} + r) ds = 2A_e N_{xs}^0$$

$$= 2A_e \frac{\oint \frac{A_{16}}{A_{66}} ds}{\oint \frac{ds}{A_{66}}} U_{,x} - 2A_e \frac{\oint y \frac{A_{16}}{A_{66}} ds}{\oint \frac{ds}{A_{66}}} V_{,xx} - 2A_e \frac{\oint z \frac{A_{16}}{A_{66}} ds}{\oint \frac{ds}{A_{66}}} W_{,xx}$$

$$+ 2A_e \frac{\oint \psi \frac{A_{16}}{A_{66}} ds}{\oint \frac{ds}{A_{66}}} \phi_{,xx} + \frac{4A_e^2}{\oint \frac{ds}{A_{66}}} \phi_{,x}$$

5. Vlasov bi-moment:

$$
\begin{aligned}
M_{\omega} &= \oint N_{xx}\psi ds \\
&= \oint \left[\left(A_{11} - \frac{A_{16}^2}{A_{66}}\right)\left(\psi U_{,x} - y\psi V_{,xx} - \psi z W_{,xx} + \psi^2 \phi_{,xx}\right) + \frac{A_{16}}{A_{66}}\psi N_{xs}\right] ds \\
&= U_{,x}\oint \left(A_{11} - \frac{A_{16}^2}{A_{66}}\right)\psi ds - W_{,xx}\oint z\psi\left(A_{11} - \frac{A_{16}^2}{A_{66}}\right) ds \\
&\qquad - V_{,xx}\oint y\psi\left(A_{11} - \frac{A_{16}^2}{A_{66}}\right) ds + \phi_{,xx}\oint \psi^2\left(A_{11} - \frac{A_{16}^2}{A_{66}}\right) ds \\
&\qquad + \frac{\oint \psi \frac{A_{16}}{A_{66}} ds \oint \frac{A_{16}}{A_{66}} ds}{\oint \frac{ds}{A_{66}}} U_{,x} - \frac{\oint y \frac{A_{16}}{A_{66}} ds \oint \psi \frac{A_{16}}{A_{66}} ds}{\oint \frac{ds}{A_{66}}} V_{,xx} \\
&\qquad - \frac{\oint \psi \frac{A_{16}}{A_{66}} ds \oint z \frac{A_{16}}{A_{66}} ds}{\oint \frac{ds}{A_{66}}} W_{,xx} + \frac{2A_e \oint \psi \frac{A_{16}}{A_{66}} ds}{\oint \frac{ds}{A_{66}}} \phi_{,x} \\
&\qquad + \frac{\left(\oint \psi \frac{A_{16}}{A_{66}} ds\right)^2}{\oint \frac{ds}{A_{66}}} \phi_{,xx}
\end{aligned}
$$

Rehfield Method	Mixed Method
$\boldsymbol{K(1,1) = \oint A_{11} ds}$	$K(1,1) = \oint \left(A_{11} - \frac{A_{16}^2}{A_{66}}\right) ds + \frac{\left(\oint \frac{A_{16}}{A_{66}} ds\right)^2}{\oint \frac{ds}{A_{66}}}$
$\boldsymbol{K(1,2) = \oint z\, A_{11}\, ds}$	$K(1,2) = -\oint z \left(A_{11} - \frac{A_{16}^2}{A_{66}}\right) ds - \frac{\oint \frac{A_{16}}{A_{66}} ds \oint z \frac{A_{16}}{A_{66}} ds}{\oint \frac{ds}{A_{66}}}$
$\boldsymbol{K(1,3) = \oint y\, A_{11}\, ds}$	$K(1,3) = -\oint y \left(A_{11} - \frac{A_{16}^2}{A_{66}}\right) ds - \frac{\oint \frac{A_{16}}{A_{66}} ds \oint y \frac{A_{16}}{A_{66}} ds}{\oint \frac{ds}{A_{66}}}$
$\boldsymbol{K(1,4) = \frac{2A_e}{\oint \frac{ds}{A_{66}}} \oint \frac{A_{16}}{A_{66}} ds}$	$K(1,4) = \frac{2A_e}{\oint \frac{ds}{A_{66}}} \oint \frac{A_{16}}{A_{66}} ds$
$\boldsymbol{K(1,5) = \oint A_{11} \psi\, ds}$	$K(1,5) = \oint \psi \left(A_{11} - \frac{A_{16}^2}{A_{66}}\right) ds + \frac{\oint \frac{A_{16}}{A_{66}} ds \oint \psi \frac{A_{16}}{A_{66}} ds}{\oint \frac{ds}{A_{66}}}$
$\boldsymbol{K(2,2) = \oint A_{11} z^2\, ds}$	$K(2,2) = \oint z^2 \left(A_{11} - \frac{A_{16}^2}{A_{66}}\right) ds + \frac{\left(\oint z \frac{A_{16}}{A_{66}} ds\right)^2}{\oint \frac{ds}{A_{66}}}$
$\boldsymbol{K(2,3) = -\oint A_{11} yz\, ds}$	$K(2,3) = \oint yz \left(A_{11} - \frac{A_{16}^2}{A_{66}}\right) ds + \frac{\oint y \frac{A_{16}}{A_{66}} ds \oint z \frac{A_{16}}{A_{66}} ds}{\oint \frac{ds}{A_{66}}}$
$\boldsymbol{K(2,4) = \frac{2A_e}{\oint \frac{ds}{A_{66}}} \oint z \frac{A_{16}}{A_{66}}\, ds}$	$K(2,4) = -\frac{2A_e}{\oint \frac{ds}{A_{66}}} \oint z \frac{A_{16}}{A_{66}} ds$
$\boldsymbol{K(2,5) = \oint A_{11} z\psi\, ds}$	$K(2,5) = -\oint \psi z \left(A_{11} - \frac{A_{16}^2}{A_{66}}\right) ds - \frac{\oint \psi \frac{A_{16}}{A_{66}} ds \oint z \frac{A_{16}}{A_{66}} ds}{\oint \frac{ds}{A_{66}}}$

$\boldsymbol{K(3,3) = \oint A_{11} y^2\, ds}$	$K(3,3) = \oint y^2 \left(A_{11} - \frac{A_{16}^2}{A_{66}}\right) ds + \frac{\left(\oint y \frac{A_{16}}{A_{66}} ds\right)^2}{\oint \frac{ds}{A_{66}}}$
$\boldsymbol{K(3,4) = -\frac{2A_e}{\oint \frac{ds}{A_{66}}} \oint y \frac{A_{16}}{A_{66}} ds}$	$K(3,4) = -\frac{2A_e}{\oint \frac{ds}{A_{66}}} \oint y \frac{A_{16}}{A_{66}} ds$
$\boldsymbol{K(3,5) = \oint -A_{11} y\, \psi\, ds}$	$K(3,5) = -\oint y\psi \left(A_{11} - \frac{A_{16}^2}{A_{66}}\right) ds - \frac{\oint y \frac{A_{16}}{A_{66}} ds \oint \psi \frac{A_{16}}{A_{66}} ds}{\oint \frac{ds}{A_{66}}}$
$\boldsymbol{K(4,4) = \frac{4A_e^2}{\oint \frac{ds}{A_{66}}}}$	$K(4,4) = \frac{4A_e^2}{\oint \frac{ds}{A_{66}}}$
$\boldsymbol{K(4,5) = 0}$	$K(4,5) = \frac{2A_e \oint \psi \frac{A_{16}}{A_{66}} ds}{\oint \frac{ds}{A_{66}}}$
$\boldsymbol{K(5,5) = \oint \psi^2\, A_{11}\, ds}$	$K(5,5) = \oint \psi^2 \left(A_{11} - \frac{A_{16}^2}{A_{66}}\right) ds + \frac{\left(\oint \psi \frac{A_{16}}{A_{66}} ds\right)^2}{\oint \frac{ds}{A_{66}}}$

Appendix II

[0°/90°] material input for all spar sides:

C11 = 8.4964824e+10, C12 = 3.4095141e+09, C13 = 2.4671402e+09, C14 = 1.0791216e-07, C15 = 0.0000000e+00, C16 = 0.0000000e+00,
C22 = 8.4964824e+10, C23 = 2.4671402e+09, C24 = 4.5273753e-06, C25 = 0.0000000e+00, C26 = 0.0000000e+00,
C33 = 9.2648354e+09, C34 = 5.7703760e-08, C35 = 0.0000000e+00, C36 = 0.0000000e+00,
C44 = 4.6900000e+09, C45 = 0.0000000e+00, C46 = 0.0000000e+00,
C55 = 4.2800173e+09, C56 = 2.5104202e-08,
C66 = 4.2800173e+09,

Winckler material input, spar bottom:

C11 = 6.0533389e+10, C12 = 2.3295247e+10, C13 = 3.8592107e+09, C14 = 1.5040564e+10, C15 = 0.0000000e+00, C16 = 0.0000000e+00,
C22 = 6.0533389e+10, C23 = 3.8592107e+09, C24 = -1.5040564e+10, C25 = 0.0000000e+00, C26 = 0.0000000e+00,
C33 = 1.0439325e+10, C34 = 1.0033361e-07, C35 = 0.0000000e+00, C36 = 0.0000000e+00,
C44 = 2.3923186e+10, C45 = 0.0000000e+00, C46 = 0.0000000e+00,
C55 = 5.0221459e+09, C56 = 3.0100084e-07,
C66 = 5.0221459e+09,

Winckler material input, spar top:

C11 = 6.0533389e+10, C12 = 2.3295247e+10, C13 = 3.8592107e+09, C14 = -1.5040564e+10, C15 = 0.0000000e+00, C16 = 0.0000000e+00,
C22 = 6.0533389e+10, C23 = 3.8592107e+09, C24 = 1.5040564e+10, C25 = 0.0000000e+00, C26 = 0.0000000e+00,
C33 = 1.0439325e+10, C34 = 0.0000000e+00, C35 = 0.0000000e+00, C36 = 0.0000000e+00,
C44 = 2.3923186e+10, C45 = 0.0000000e+00, C46 = 0.0000000e+00,
C55 = 5.0221459e+09, C56 = 1.0033361e-07,
C66 = 5.0221459e+09,

Haynes material input, spar bottom:

C11 = 5.7413434e+10, C12 = 2.6404196e+10, C13 = 3.8589661e+09, C14 = -1.2872736e+09, C15 = 0.0000000e+00, C16 = 0.0000000e+00,
C22 = 5.7435446e+10, C23 = 3.8594552e+09, C24 = -2.3871905e+10, C25 = 0.0000000e+00, C26 = 0.0000000e+00,
C33 = 1.0439325e+10, C34 = -5.5904230e+08, C35 = 0.0000000e+00, C36 = 0.0000000e+00,
C44 = 2.7032135e+10, C45 = 0.0000000e+00, C46 = 0.0000000e+00,
C55 = 5.0223039e+09, C56 = -3.6115455e+08,
C66 = 5.0219879e+09,

Haynes material input, spar top:

C11 = 5.7413434e+10, C12 = 2.6404196e+10, C13 = 3.8589661e+09, C14 = 1.2872736e+09, C15 = 0.0000000e+00, C16 = 0.0000000e+00,
C22 = 5.7435446e+10, C23 = 3.8594552e+09, C24 = 2.3871905e+10, C25 = 0.0000000e+00, C26 = 0.0000000e+00,
C33 = 1.0439325e+10, C34 = 5.5904230e+08, C35 = 0.0000000e+00, C36 = 0.0000000e+00,
C44 = 2.7032135e+10, C45 = 0.0000000e+00, C46 = 0.0000000e+00,
C55 = 5.0223039e+09, C56 = 3.6115455e+08,
C66 = 5.0219879e+09,

References

[1] W. Johnson, G. K. Yamauchi and M. E. Watts, "NASA Heavy Lift Rotorcraft Systems Investigation," NASA TP-2005-213467, Moffett Field, CA, December 1, 2005.

[2] C. A. Snyder, M. Robuck, J. Wilkerson and C. Nordstrom, "Summary of the Large Civil TiltRotor (LCTR2) Engine Gearbox Study," in *American Helicopter Society International Powered Lift Conference*, Philidelphia, PA, Oct. 2010.

[3] I. Chopra and P. Chen, "Hover Testing of Smart Rotor with Induced-Strain Actuation of Blade Twist," *AIAA Journal*, vol. 35, no. 1, pp. 6-16, 1997.

[4] J. P. Rodgers and N. W. Hagood, "Design, Manufacture, and Testing of an Integral Twist-Actuated Rotor Blade," in *Proceedings of the 8th International Conference on Adaptive Structures and Technology*, Nagoka, Japan, Oct. 1997.

[5] J. Riemenschneider, S. Keye, P. Wierach and H. Mercier des Rochettes, "Overview of the Common DLR/ONERA Project 'Active Twist Blade'," in *30th European Rotorcraft Forum*, Marseille, France, Sept. 2004.

[6] J. Riemenschneider, S. Opitz, M. Schulz and V. Plassmeier, "Active Twist Rotor for Wind Tunnel Investigations," in *ASME 2010 Conference on Smart Materials, Adaptive Structures, and Intelligent Systems*, Philadelphia, PA, Sept. 2010.

[7] A. Kovalovs, E. Barkanov, S. Ruchevskis and M. Wesolowski, "Optimisation Methodology of a Full-Scale Active Twist Rotor Blade," *Procedia Engineering*, vol. 289, pp. 85-95, 2017.

[8] T. Oktay and F. Sal, "Combined Passive and Active Helicopter Main Rotor Morphing for Helicopter Energy Save," *Journal of the Brazilian Society Mechanical Sciences and Engineering*, vol. 38, no. 6, pp. 1511-1525, Aug. 2016.

[9] S. J. Shin, C. E. S. Cesnik and S. R. Hall, "Design and Simulation of Integral Twist Control for Helicopter Vibration Reduction," *International Journal of Control: Automation and Systems*, vol. 5, no. 1, pp. 24-34, 2007.

[10] P. C. Chen, J. D. Baeder, R. A. D. Evans and J. Niemczuk, "Blade-Vortex Interaction Noise Reduction with Active Twist Smart Rotor Technology," *Smart Materials and Structures*, vol. 10, no. 1, pp. 77-85, 2001.

[11] R. L. Foye, "Evolution of the Application of Composite Materials to Helicopter," *Journal of the American Helicopter Society,* vol. 26, no. 4, pp. 5-15, Oct. 1981.

[12] F. D'Ambra, "The Impact of New Materials on the Development of Rotary Wing Aircraft," *Journal of the American Helicopter Society,* vol. 26, no. 4, pp. 16-23, Oct. 1871.

[13] S. Varanay and M. Ozier, "Advanced Composite Application for Structures and Housing," in *Proceedings of the American Helicopter Society 60th Annual Forum,* Baltimore, MD, June 7-10, 2004.

[14] L. W. Rehfield, D. H. Hodges and A. Atligan, "Some Considerations on the Non-Classical Behavior of Thin-Walled Composite Beams," in *American Helicopter Society National Technical Specialists' Meeting on Advanced Rotorcraft Structures*, Oct. 1988.

[15] L. W. Rehifeld, "Design Analysis Methodology for Composite Rotor Blades," in *Seventh DoD/NASA Conference on Fibrous Composites in Structural Design*, Denver, Colorado, Jun, 1985.

[16] D. H. Hodges, M. W. Nixon and L. W. Rehfield, "Comparison of Composite Rotor Blade Models: A Coupled Beam Analysis and and MSC NASTRAN Finite Element Model," NASA Technical Memorandum, 1987.

[17] O. Bauchau, B. S. Coffenberry and L. W. Rehfield, "Composite Box Beam Analysis: Theory and Experiments," *Journal of Reinforced Plastics and Composites,* vol. 6, pp. 25-35, 1987.

[18] M. W. Nixon, "Extension-Twist Coupling of Composite Circular Tubes with Application to Tilt-Rotor Blade Design," in *Proceedings of the 28th Structures, Structural Dynamics, and Materials Conference*, Monerey, CA, Apr., 1987.

[19] A. Bauchau and C. Hong, "Nonlinear Composite Beam Theory," *Journal of Applied Mechanics,* vol. 55, no. 1, pp. 156-163, March 1988.

[20] E. Smith and I. Chopra, "Aeroelastic Response, Loads, and Stability of a Composite Rotor in Forward Flight," *AIAA Journal,* vol. 31, no. 7, pp. 1265-1273, July 1993.

[21] S. N. Jung and S. J. Kim, "Effect of Transverse Shear on Aeroelastic Stability of a Composite Rotor Blade," *AIAA Journal,* vol. 33, no. 8, pp. 1541-1543, Aug. 1993.

[22] C.-H. Hong and I. Chopra, "Aeroelastic Stability Analysis of a Composite Bearingless Rotor Blade," in *International Conference on Rotorcraft Basic Research*, Feb. 1985.

[23] W. H. Mansfield and A. J. Sobey, "The Fiber Composite Helicopter Blade, Part 1: Stiffness Properties, Part 2: Prospects for Aeroelastic Tailoring," *Aeronautical Quarterly,* May, 1979.

[24] N. T. Sriniveri and I. Chopra, "Dynamic Stability of a Rotor Blade Using Finite Element Analysis," *AIAA Journal,* vol. 20, no. 2, May 1982.

[25] R. Chandra, A. D. Stemple and I. Chopra, "Thin-Walled Composite Beams Under Bending, Torsional, and Extensional Loads," *Journal of Aircraft,* vol. 27, no. 7, pp. 619-626, July 1990.

[26] M. Nixon, *Analytical and Experimental Investigations of Extension-Twist Coupled Structures,* M.S. Thesis, NASA Langley/George Washington University, 1989.

[27] E. C. Smith and I. Chopra, "Formulation and Evaluation of an Analytical Model for Composite Box-Beams," *Journal of the American Helicopter Society,* vol. 36, no. 3, pp. 23-35, July 1991.

[28] D. H. Hodges, Nonlinear Composite Beam Theory, Reston, VA: American Institute of Aeronautics and Astronautics, 2006.

[29] O. A. Bauchau, R. G. Loewy and P. S. Bryan, "An Approach to Ideal Twist Distribution in Tilt Rotor VTOL Blade Designs," in *Rensselaer Polytecnic Institute Rotorcraft Technology Center Report No D-86-2,* July 1986.

[30] M. W. Nixon, "Improvements to Tilt Rotor Performance Through Passive Blade Twist Control," NASA Technical Memorandum 100583, Hampton, VA, April 1988.

[31] R. C. Lake, M. W. Nixon, M. L. Wilbur, J. D. Singleton and P. H. Mirick, "Demonstration of an Elastically Coupling Twist Control Concept for Tilt Rotor Blade Application," *AIAA Jounal*, vol. 32, no. 7, pp. 1549-1551, July, 1994.

[32] J. B. Kosmatka and R. C. Lake, "Extension-Twist behavior of Initially Twisted Composite Spars for Tilt-Rotor Applications," in *AIAA/ASME/ASCE/AHS/ASC Structures, Structural Dynamics and Materials Conference and Exhibit*, Salt Lake City, UT, Apr. 1996.

[33] O. Soykasap and D. Hodges, "Performance Enhancement of a Composite Tilt-Rotor Using Aeroelastic Tailoring," *Journal of Aircraft*, vol. 37, no. 5, pp. 850-858, August 2000.

[34] S. Ozbay, O. Bauchau, S. D. Dancila and E. A. Armanios, "Stability analysis of extension-twist coupled composite rotor blades," in *in 61st Annual Forum Proceedings - AHS International*, Grapevine, TX, June 1-3, 2005.

[35] L. Peng, S. Prothin, F. Mohd-Zawawi, E. Benard, J. Morlier and J.-M. Moschetta, "Performance Improvement of Small-Scale Rotors by

Passive Blade Twist Control," *Journal of Fluids and Structures,* vol. 55, pp. 25-41, 2015.

[36] S.-Y. Oh, O. Song and L. Librescu, "Effects of pretwist and presetting on coupled bending vibrations of rotating thin-walled composite beams," *International Journal of Solids and Structures,* vol. 40, pp. 1203-1224, 2003.

[37] L. W. Rehfield, A. R. Atilgan and D. H. Hodges, "Nonclassical behavior of thin walled composite beams with closed cross sections," *Journal of the American Helicopter Society,* vol. 35, no. 2, pp. 42-51, 1990.

[38] R. Chandra and I. Chopra, "Experimental-theoretical investigation of the vibration characteristics of rotating composite box beams," *Journal of Aircraft,* vol. 29, no. 3, pp. 657-664, 1992.

[39] S. N. Jung, V. T. Nagaraj and I. Chopra, "Refined structural dynamics model for composite rotor blades," *AIAA Journal,* vol. 39, no. 2, pp. 339-348, 2001.

[40] S. Mahadev and D. Dancila, "Extension-Twist-Coupled Star-Beam Composite Rotor Blade Tip Concept," in *in 18th International Conference on Composite Materials,* December 1, 2011.

[41] W. de Goeij, M. van Tooren and A. Beukers, "Implementation of Bending-Torsion Coupling in the Design of a Wind-Turbine Rotor-Blade," *Applied Energy*, vol. 63, no. 3, pp. 191-207, July 1999.

[42] C. L. Bottasso, F. Campagnolo, A. Croce and C. Tibaldi, "Optimization-based study of bend-twist coupled rotor blades for passive and integrated passive/active load alleviation," *Wind Energy*, vol. 16, no. 8, pp. 1149-1166, 2013.

[43] V. Federov and C. Berggreen, "Bend-Twist Coupling Potential of Wind Turbine Blades," *Journal of Physics: Conference Series*, vol. 524, no. 1, 2014.

[44] A. R. Stablein, "Analysis and Design of Bend-Twist Coupled Wind Turbine Blades," in *New Materials and Reliability in Offshore Wind Turbone Technology*, Springer, 2016, pp. 67-80.

[45] J. Bao, V. Nagaraj, I. Chopra and A. P. F. Bernhard, "Wind Tunnel Test of Five Sets of Mach Scale Composite Tailored Rotor with Flap-Bending/Torsion Couplings for Vibration Reduction," *Journal of the American Helicopter Society*, vol. 53, no. 3, pp. 215-225, July 2008.

[46] E. C. Smith and I. Chopra, "Air and Ground Resonance of Helicopters with Elastically Tailored Rotor Blades," *Journal of the American Helicopter Society*, vol. 30, no. 2, pp. 57-67, July 1985.

[47] A. P. F. Bernhard and I. Chopra, "Analysis of a bending-torsion coupled actuator for a smart rotor with active blade tips," *Smart Materials and Structures*, vol. 10, no. 1, pp. 35-52, 2001.

[48] A. Bernhard and I. Chopra, "Hover Test of Mach-Scaled Active-Twist Rotor Using Piezo-Bending-Torsion Actuators," *Journal of Aircraft*, vol. 39, no. 4, pp. 678-688, July 2002.

[49] H. A. Koratkar and I. Chopra, "Wind Tunnel Testing of a Smart Rotor Model with Trailing-Edge Flaps," *Journal of the American Helicopter Society*, vol. 47, no. 4, pp. 263-272, Oct. 2002.

[50] F. K. Straub, D. K. Kennedy, D. B. Domzaolski, A. A. Hassan, H. Ngo, V. Anand and T. Birchette, "Smart Material-Actuated Rotor Technology - SMART," *Journal of Intelligent Material System and Structures*, vol. 15, no. 4, pp. 249-260, Apr. 2004.

[51] C. E. S. Cesnik, S. J. Shin, W. K. Wilkie, M. L. Wilbur and P. H. Mirick, "Modeling, Design, and Testing of the NASA/ARMY/MIT Active Twist Rotor Prototype Blade," in *AHS International 55th Annual Forum Proceedings*, Montral, Canada, May 25-27, 1999.

[52] J. E. White and F. A. Angona, "Elastic Wave Velocities in Laminated Media," *Journal of the Acoustical Society of America*, vol. 27, p. 311, 1955.

[53] G. W. Postma, "Wave Propogation in a Stratified Medium," *Geophysics,* vol. 20, p. 780, 1955.

[54] S. M. Rytov, "Acoustical Properties of a Thinly Laminated Medium," *Soviet Phys. Acoustics,* vol. 2, p. 68, 1956.

[55] E. Behrens, "Sound Propogation in Lamellar Composite Materials and Averaged Elastic Constants," *Journal of the Acoustical Society of America,* vol. 42, p. 378, 1967.

[56] M. D. G. Salamon, "Elastic Moduli of Stratified Rock Mass," *International Journal of Rock Mechanics Mineral Science,* p. 519, 1968.

[57] P. C. Chou, J. Carleone and C. M. Hsu, "Elastic Constants of Layered Media," *Journal of Composite Materials,* vol. 6, no. 1, pp. 80-93, January 1972.

[58] T. A. Bogetti, C. P. R. Hoppel and W. H. Drysdale, "Three-Dimensional Effective Property and Strength Prediction of Thick Laminated Composite Media," Army Research Laboratory, Newark, DE, Oct. 1995.

[59] C. T. Sun and S. Li, "Three-Dimensional Effective Elastic Constants for Thick Laminates," *Journal of Composite Materials,* vol. 24, pp. 629-639, 1988.

[60] C. T. Sun and S. Liao, "Three-Dimensional Effective Elastic Constants for Thick Laminates," *Journal of Composite Materials,* vol. 22, no. 7, pp. 629-639, July, 1988.

[61] N. J. Pagano and F. G. Yuan, "The Significance of Effective Modulus Theory (Homogenization) in Composite Laminate Mechanics," *Composite Science and Technology,* vol. 60, no. 12, pp. 2471-2788, Sept. 2000.

[62] H. Glauert, "The Theory of the Autogyro," *The Journal of the Royal Aeronautical Society,* vol. 31, no. 198, pp. 483-508, June 1927.

[63] J. Houbolt and G. Brooks, "Differential Equations of Motion for Combined Flapwise Bending, Chordwise Bending, and Torsion of Twisted Nonuniform Rotor Blades," NACA TN 3905, 1957.

[64] D. Hodges and E. Dowell, "Nonlinear Equations of Motion for the Elastic Bending and Torsion of Twisted Nonuniform Rotor Blades," NASA TN D-7818, 1974.

[65] R. Ormiston and D. Hodges, "Linear Flap-Lag Dynamics of Hingeless Helicopter Rotor Blades in Hover," *Journal of the American Helicopter Society,* vol. 17, no. 2, pp. 2-14, April 1972.

[66] R. Kvaternik and R. Kirshna, "Nonlinear Curvature Expressions for Combined Flapwise Bending, Chordwise Bending, Torsion, and Extension of Twisted Rotor Blades," NASA TM X-73997, 1976.

[67] A. Rosen and P. Friedmann, "Nonlinear Equations of Equilibrium for Elastic Helicopter or Wind Turbine Blades Undergoing Moderate Deformation," NASA CR-159478, 1978.

[68] W. Johnson, "Aeroelastic Analysis for Rotorcraft in Flight or in a Wind Tunnel," NASA TN D-8515, 1977.

[69] S. P. Timoshenko, "On the Correction for Shear of the Differential Equation for Transverse Vibrations of Prismatic Bars," *Philosophical Magazine,* vol. 41, no. 245, 1921.

[70] V. H. Cortinez and M. T. Piovan, "Vibration and Buckling of Composite Thin-Walled Beams with Shear Deformability," *Journal of Sound and Vibration,* vol. 258, no. 4, pp. 701-723, Dec. 2002.

[71] P. P. Friedmann and D. H. Hodges, "Rotary Wing Aeroelasticity - A Historical Perspective," *Journal of Aircraft,* vol. 40, no. 6, pp. 1019-1046, Dec. 2003.

[72] Y. Bazilevs, M. C. Hsu, J. Kiendl, R. Wuchner and K. U. Bletzinger, "3-D Simulation of Wind Turbine Rotors at Full Scale. Part II: Fluid-

Structure Interaction Modeling with Composite Blades," *International Journal for Numerical Methods in Fluids,* vol. 34, no. 3, pp. 211-242, 2015.

[73] O. Bauchau and N. Kang, "A Multibody Formulation for Helicopter Structural Dynamic Analysis," *Journal of the American Helicopter Society,* vol. 38, no. 2, pp. 3-14, April 1993.

[74] H. Kang, C. Chang, H. Saberi and R. Ormiston, "Assessment of Beam and Shell Elements for Modeling Rotorcraft Blades," *Journal of Aircraft,* vol. 51, no. 2, pp. 520-531, Mar.-Apr. 2014.

[75] A. Datta and W. Johnson, "Three-Dimensional Finite Element Formulation and Scalable Domain Decomposition for High Fidelity Rotor Dynamic Analysis," *Journal of the American Helicopter Society,* vol. 56, no. 2, pp. 1-14, April 2011.

[76] A. Datta and W. Johnson, "A Multibody Formulation for Three Dimensional Brick Finite Elements Based Parallel and Scalable Rotor Dynamic Analysis," in *American Helicopter Society 66th Annual Forum*, Phoenix, AZ, May 11-13, 2010.

[77] A. Datta and W. Johnson, "Integrated Aeromechanics with Three-Dimensional Solid-Multibody Structures," in *American Helicopter Society 70th Annual Forum Proceedings*, Montreal, QC, May 20-22, 2014.

[78] A. Datta, H. Yeo and T. R. Norman, "Experimental Investigation and Fundamental Understanding of a Slowed UH-60A Rotor at High Advance Ratios," *Journal of the American Helicopter Society*, vol. 58, no. 2, pp. 1-17, April 2013.

[79] T. Blacker, S. Owen, M. Staten, R. Quadros, B. Hanks and et al., "CUBIT Geometry and Mesh Generation Toolkit 15.2 User Documentation," Sandia National Laboratories, SAND2016-1649 R, Albuquerque, New Mexico, May, 2016.

[80] W. Staruk, I. Chopra and A. Datta, "Three-Dimensional CAD-Based Structural Modeling for Next Generation Rotor Dynamic Analysis," in *American Helicopter Society 70th Annual Forum Proceedings*, Montreal, QC, May 22-24, 2014.

[81] W. Staruk, E. Ward and I. Chopra, "CAD-Based 3-D Structural Dynamic Modeling of the Tilt Rotor Aeroacoustic Model (TRAM) Proprotor," in *American Helicopter Society 71st Annual Forum Proceedings*, Virginia Beach, VA, May 5-7, 2015.

[82] W. Staruk, I. Chopra and A. Datta, "Coupled Aerodynamics and 3-D Structural Dynamics of the Tilt Rotor Aeroacoustic Model (TRAM) Proprotor," in *AHS International Technical Meeting on Aeromechanics Design for Vertical Lift*, San Francisco, CA, Jan. 20-22, 2016.

[83] W. Staruk, I. Chopra, A. Datta and B. Jayaraman, "Validation of Aeromechanics Predictions for a Full 3-D Structural Analysis Model of the Tilt Rotor Aeroacoustic Model (TRAM) Proprotor," in *42nd European Rotorcraft Forum*, Lille, France, September 6-8, 2016.

[84] W. Staruk and A. Datta, "Fundamental Understanding, Prediction, and Validation of Tiltrotor Dynamic Loads in Transition Flight Using RANS/FEA," in *58th AIAA/ASCE/AHS/ASC Structures, Structural Dynamics, and Materials Conference, AIAA Science and Technology Forum and Exposition 2017*, Grapevine, TX, January, 2017.

[85] W. Staruk, I. Chopra and A. Datta, "Loads Prediction for a Gimbaled Tiltrotor in Conversion Flight Using CAD-Based 3-D Structural Analysis Models," in *American Helicopter Society 73rd Annual Forum Proceedings*, Fort Worth, TX, May 8-11, 2017.

[86] E. Ward, I. Chopra and A. Datta, "RPM Driven Extension-Torsion Coupled Self-Twisting Rotor Blades," in *American Helicopter Society 72nd Annual Forum*, West Palm Beach, FL, May 2016.

[87] E. Ward, I. Chopra and A. Datta, "Design of Self-Twisting Rotor Blades for High Speed Compoud Rotorcraft," in *25th AIAA/AHS Adaptive Structures Conference, AIAA Science and Technology Forum and Exposition 2017*, Grapevine, TX, Jan. 9-13, 2017.

[88] E. Ward, I. Chopra and A. Datta, "RPM Driven Extension-Torsion Coupled Self-Twisting Rotor Blades," in *American Helicopter Society 73rd Annual Forum*, Fort Worth, TX, May 9-11, 2017.

[89] E. Ward, I. Chopra and A. Datta, "Realistic Structural Design of Self-Twisting Rotors for High-Speed Compound Rotorcraft," in *43rd European Rotorcraft Forum*, Milan, Italy, Oct. 12-14, 2017.

[90] A. Bagai and J. G. Leishman, "Rotor Free-Wake Modeling Using a Pseudo Implicit Technique - Including Comparisons with Experimental Data," *Journal of the American Helicopter Society*, vol. 40, no. 13, pp. 29-41, July 1995.

[91] R. Chen, "A Survey of Nonuniform Inflow Models for Rotorcraft Flight Dynamics and Control Applications," 1989.

[92] S. Winckler, "Hygrothermally Curvature Stable Laminates with Tension-Torsion Coupling," *Journal of the American Helicopter Society*, vol. 30, no. 3, pp. 56-58, July 1985.

[93] R. Haynes and E. Armanios, "Overview of Hygrothermally Stable Laminates with Improved Extension-Twist Coupling," in *17th International Conference on Composite Materials, ICCM-17*, Edinburgh, GBR, July 2009.

[94] E. Makai, "A Proof of Saint-Venant's Theorem on Torsional Rigidity," *Acta Mathematica Academiae Scientarium Hungarica*, vol. 17, no. 3-4, pp. 419-422, Sept. 1966.

[95] B. Popescu and D. Hodges, "On asymptotically correct Timoshenko-like anisotropic beam theory," *International Journal of Solids and Structures*, vol. 37, no. 3, pp. 535-558, 2000.

[96] O. A. Bauchau and D. H. Hodges, "Analysis of Nonlinear Multibody Systems with Elastic Couplings," *Multibody System Dynamics*, vol. 3, no. 2, pp. 163-188, May 1999.

[97] CMH-17 Composite Materials Handbook Volumes 1, 2, and 3, SAE International, 2012.

[98] W. Staruk, I. Chopra and A. Datta, "Coupled Aerodynamic and 3-D Structural Dynamics of the Tilt Rotor Aeroacoustic Model (TRAM) Proprotor," in *AHS International Technical Meeting on Aeromechanics Design for Vertical Lift*, San Francisco, CA, Jan. 20-22, 2016.

[99] A. Datta, "X3D - A 3-D Solid Finite Element Multibody Dynamic Analysis for Rotorcraft," in *Aeromechanics Specialists Conference*, San Francisco, CA, January 22, 2016.

[100] A. Datta and I. Chopra, "Validation of Structural and Aerodynamic Modeling Using UH-60A Airloads Program Data," *Journal of the American Helicopter Society*, vol. 51, no. 1, pp. 43-58, Jan. 2006.

[101] H. Yeo, "Investigation of UH-60A Rotor Performance and Loads at High Advance Ratios," *Journal of Aircraft*, vol. 50, no. 2, pp. 576-589, March-April 2013.

[102] R. A. Ormiston, "Revitalizing Advanced Rotorcraft Research - and the Compound Helicopter," *Journal of the American Helicopter Society*, vol. 61, no. 1, pp. 1-23, January 2016.

[103] M. Potsdam, H. Yeo and R. Ormiston, "Performance and Loads Predictions of a Slowed UH-60A Rotor at High Advance Ratios," in *39th European Rotorcraft Forum*, Moscow, Russia, Sept. 2013.

[104] L. A. Young, "Tilt Rotor Aeroacoustic Model (TRAM): A New Rotorcraft Research Facility," in *AHS International Meeting on Advanced Rotorcraft Technology and Disaster Relief*, Gifu, Japan, 1998.

[105] J. J. Totah and J. F. I. Madden, "Rotor and Control System Loads Analysis of the XV-15 With the Advanced Technology Blades," NASA TM 102876, April 1991.

[106] J. J. Totah and W. Patterson, "Control of a Human-Powered Helicopter in Hover," NASA Technical Memorandum 101029, November, 1988.

[107] R. Strawn, "High-Performance Computing for Rotorcraft Modeling and Simulation," *Computing in Science and Engineering,* vol. 12, no. 5, pp. 27-35, Sep-Oct 2010.

[108] V. Srinivas and I. Chopra, "Validation of a Comprehensive Aeroelastic Analysis for Tiltrotor Aircraft," *Journal of the American Helicopter Society,* vol. 43, no. 4, pp. 333-341, October 1998.

[109] V. Srinivas, I. Chopra and M. W. Nixon, "Aeroelastic Analysis of Advanced Geometry Tiltrotor Aircraft," *Journal of the American Helicopter Society,* vol. 43, no. 3, pp. 212-221, July 1998.

[110] R. Sopher, "The AHS Igor Sikorsky Human Powered Helicopter Competition," *Vertiflite,* vol. 43, no. 3, pp. 32-34, 1997.

[111] J. Sitaraman, M. Potsdam, A. Wissink, B. Jayaraman, D. Mavriplis and H. Saberi, "Rotor Loads Prediction Using Helios: A Multisolver Framework for Rotorcraft Aeromechanics," *Journal of Aircraft,* vol. 50, no. 2, pp. 478-492, March 2013.

[112] M. Potsdam and R. Strawn, "CFD Simulations of Tiltrotor Configurations in Hover," *Journal of the American Helicopter Society*, vol. 50, no. 1, pp. 82-94, January 2005.

[113] M. W. Nixon, D. J. Piatak, L. M. Corso and D. A. Popelka, "Aeroelastic Tailoring for Stability Augmentation and Performance Enhancements of Tiltrotor Aircraft," *Journal of the American Helicopter Society*, vol. 45, no. 4, pp. 270-279, October 2000.

[114] J. G. Leishman, Principles of Helicopter Aerodynamics, New York: Cambridge University Press, 2008.

[115] W. Johnson, "Milestones in Rotorcraft Aeromechanics," *Alexander A. Nikolsky Honorary Lecture, Journal of the American Helicopter Society*, vol. 56, no. 3, pp. 1-24, July, 2011.

[116] W. Johnson, B. H. Lau and J. V. Bowles, "Calculated Performance, Stability, and Maneuverability of High-Speed Tilting-Prop-Rotor Aircraft," NASA TM 88349, 1986.

[117] G. M. Hoffman and C. J. Tomlin, "Quadrotor Helicopter Flight Dynamics and Control: Theory and Experiment," in *AIAA Guidance, Navigation, and Control Conference*, Hilton Head, SC, 2007.

[118] T. J. Hawkins, "Aerodynamic & Power Considerations for Human Powered Helicopter in Vertical Flight," PhD Thesis, Stanford, 1996.

[119] B. M. Govindarajan and J. G. Leishman, "Prediction of Rotor and Rotor/Airframe Configurational Effects on Brownout Dust Clouds," *Journal of Aircraft*, Vols. (Yet to appear, doi: 10.2514/1.C033447), 2015.

[120] I. Fejtek and L. Roberts, "Navier-Stokes Computation of Wing/Rotor Interaction for a Tilt Rotor in Hover," *AIAA Journal*, vol. 30, no. 11, pp. 2595-2603, November 1992.

[121] S. A. Bruce, E. R. Wood and R. M. Howard, "Human-Powered Helicopter: A Program for Design and Construction," Naval Postgraduate School Masters Thesis, 1991.

[122] S. Brown, "Determination of Human Powered Helicopter Stability Characteristics Using Multi-Body System Simulation Techniques," California Polytechnic State University Masters Thesis, 2012.

[123] J. M. Bilger, R. L. Marr and A. Zahedi, "In-Flight Structural Dynamic Characteristics of the XV-15 Tilt Rotor Research Aircraft," *Journal of Aircraft*, vol. 19, no. 11, pp. 1005-1011, November 1982.

[124] S. M. Barkai and O. Rand, "The Influence of Composite Induced Couplings on Tiltrotor Whirl Flutter Stability," *Journal of the American Helicopter Society*, vol. 43, no. 2, pp. 133-145, April 1998.

[125] J. Bao, *Development of Mach Scale Rotors with Composite Tailored Couplings for Vibration Reduction,* Department of Aerospace Engineering, University of Maryland, 2004.

[126] A. Alexander and J. T. Tzeng, "Three Dimensional Effective Properties of Composite Materials for Finite Element Applications," *Journal of Composite Materials,* vol. 31, no. 5, pp. 466-485, 1997.

[127] UC Structural Dynamics Research Lab, [Online]. Available: http://www.sdrl.uc.edu/sdrl/referenceinfo/universalfileformats/file-format-storehouse/universal-file-datasets-summary. [Accessed 22 March 2016].

[128] AHS International, "Human Powered Helicopter Regulations," [Online]. Available: http://vtol.org/awards-and-contests/human-powered-helicopter/hph-rules. [Accessed 4 Aril 2013].

[129] D. Hodges, "Geometrically Exact, Intrinsic Theory for Dynamics of Curved and Twisted Anisotropic Beams," *AIAA Journal,* vol. 41, no. 6, pp. 1131-1137, June 2003.

[130] G. Jelenić and M. Crisfield, "Geometrically Exact 3D beam Theory: Implementation of a Strain-Invariant Finite Element for Statics and Dynamics," *Computer Methods in Applied Mechanics and Engineering,* vol. 171, no. 1-2, pp. 141-171, March 1999.

[131] W. Johnson, Helicopter Theory, New York: Dover Publications, Inc., 1980.

[132] W. Johnson, "Calculation of the Aerodynamic Behavior of the Tilt Rotor Aeroacoustic Model (TRAM) in the DNW," in *American Helicopter Society 57th Annual Forum Proceedings*, Washington, DC, May 9-11, 2001.

[133] D. Hodges, "A Mixed Variational Foundation Based on Exact Intrinsic Equations for Dynamics of Moving Beams," *International Journal of Solids and Structures,* vol. 26, no. 11, pp. 1253-1273, December 1990.

[134] W. Johnson, "Airloads and Wake Geometry Calculations for an Isolated Tiltrotor Model in a Wind Tunnel," in *27th European Rotorcraft Forum*, Moscow, Russia, September, 2001.

[135] D. Hodges, R. Ormiston and D. Peters, "On the Nonlinear Deformation Geometry of Euler–Bernoulli Beams," NASA TP 1566, 1980.

[136] J. L. R. Kosmatka, "Passive approach of controlling twist in composite tilt-rotor blades," in *SPIE Proceedings Vol. 2717*, May 1, 1996.

[137] Z. Kaler, P. Koliais and J. Schmaus, "Gamera IID: Expanding the Flight Envelope of Human Powered Helicopters," in *69th Annual Forum of the American Helicopter Society*, Phoenix, AZ, 2013.

[138] J. Schmaus, B. Berry, G. Bowen-Davies, B. Bush, C. Friedman, M. Gilad, A. Sridharan, W. Staruk and B. Woods, "Design and Development of

Gamera: A Human Powered Helicopter from the University of Maryland," in *American Helicopter Society Future Vertical Lift Aircraft Design Conference*, San Francisco, CA, January 2012.

[139] J. Schmaus, B. Berry, W. Gross and P. Koliais, "Experimental Study of Rotor Performance in Deep Ground Effect with Application to a Human-Powered Helicopter," in *68th Annual Forum of the American Helicopter Society*, Fort Worth, TX, 2012.

[140] A. Datta, M. Nixon and I. Chopra, "Review of Rotor Loads Prediction with the Emergence of Rotorcraft CFD," *Journal of the American Helicopter Society*, vol. 52, no. 4, pp. 287-317, October 2007.

[141] B. Berry, G. Bowen-Davies, K. Gluesenkamp, Z. Kaler, J. Schmaus, W. Staruk, E. Weiner and B. Woods, "Design Optimization of Gamera II: a Human Powered Helicopter," in *68th Annual Forum of the American Helicopter Society*, Fort Worth, TX, 2012.

[142] R. Derham and N. Hagood, "Rotor Design Using Smart Materials to Actively Twist Blades," in *52nd Annual Forum of the American Helicopter Society*, Washinton, D.C., 1996.